NTNU

Norwegian University of
Science and Technology

Experimental and Numerical Investigations of Global Motions and Slamming Loads on an Aquaculture Feed Barge

Yuyang Zang

Marine Technology
Submission date: June 2018
Supervisor: Trygve Kristiansen, IMT
Co-supervisor: David Kristiansen, SINTEF Ocean

Norwegian University of Science and Technology
Department of Marine Technology

Preface

This thesis is submitted to Norwegian University of Science and Technology (NTNU) as a part of the Master of Science degree at the Department of Marine Technology. This work is carried out in spring 2018 and is a continuation of the project thesis from autumn 2017, under the supervision of Professor Trygve Kristiansen.

The idea of the topic in this thesis is suggested by David Kristiansen. The reader should have basic knowledge about hydrodynamics.

Yuyang Zang
Trondheim, June 2018

Acknowledgement

The work in this thesis is carried out under the supervision of Professor Trygve Kristiansen. His professional suggestions during the experiments and his guidance are most appreciated.

I would also like to thank my co-supervisor, David Kristiansen, for giving me this interesting topic. A special thanks to Terje Rosten, Trond Innset and Ole-Erik Vinje for solving practical issues about the equipment during the experiments, building the model, and fixing the mechanical issues in order to make the laboratory exercises possible. Last but not least, I would like to thank my family and my friends for the support during my work of this thesis.

Abstract

Local slamming on an aquaculture barge will occur on a deck that is located lower than the main deck. The problem is dependent on the global motions of the structure. If the structure has decks that are located at the port- and starboard side, then the global roll motions will be essential for the problem. By obtaining correct global motions, the relative velocities of the structure and the waves can be calculated, which is further used in the slamming analysis. This consists of estimating correct global motions of a floating barge structure, conducting laboratory work, and making a similar numerical model in the potential solver, *WADAM*.

An estimation of roll damping ratio to a barge with sharp edges is conducted. The results are compared with experiments where linear waves with different wave periods and wave steepness are tested. The experiments are conducted in a small towing tank, "*Lilletanken*", at the Center of Marine Technology at NTNU. A rectangular shaped model with a scale of 1:25 is built, and a plate made by aluminum is used to act as the small platform. Between the attachment point of the platform, a force sensor is used to measure the slamming force from the global motions and from the waves. A decay test is performed in all six global motions, and the natural period in heave and roll are approximately $7.6s$ and $12.05s$ respectively in full scale. This corresponds well with the results from the potential solver.

Two laboratory experiments are conducted. One in *January* and one in *April*. The tests from *January* consist of different regular waves with many various steepness, but few wave periods. It is observed that the global motions are largest at the steepest waves, and the slamming forces at the platform are largest when the structure is moving in heave. Furthermore, from the analysis of the results, it is decided to run more tests with more wave periods. Therefore, another experiment in *April* is conducted. The results from *April* show that the model is exposed to parametric instability when an incoming regular wave with full scale wave periods $6.0s$ up to $6.4s$ are tested. This instability is observed to be greater for large wave steepness.

Comparison of the results from the experiments and the numerical simulations show that the method for estimating the damping ratio is conservative. The results from the experiments are more damped at the resonance region than the simulated results. With an exception at the resonance region, the global roll motions obtained from the experiments correspond well with the numerical results. The wall effects are simulated by using mirroring techniques, and show consistent results with the experimental results.

Time series of the slamming forces are demonstrated. It is observed that the time duration of the high impact force is short, while there exist forces with negative values that have longer time duration after the impact. A sensitivity test of the frequency range for the

filtering process of the measured slamming forces is conducted. The results show that the filter type should be a low-pass filter with a cut-off frequency at $200Hz$. The measured slamming forces are compared with the analytic results calculated from Wagner model. Due to large uncertainties of the deadrise angle, the analytic results did not correspond well to the experimental results. However, the estimated slamming forces show an upper and lower limit of the measured time series.

From the results of slamming force obtained from the experiments, it is shown that the slamming forces are dependent on various parameters. The main parameters that change the slamming forces are wave steepness, relative velocity, water density, added mass and global motions.

A perforated plate with same dimensions as the solid plate is tested. The results of the slamming forces are compared to each other, and they show that the peaks of the impact force are much lower for the perforated plate.

Sammendrag

Lokal slamming på en havbruksfôrflåte vil inntreffe på et sidedekk som er plassert lavere enn hoveddekket på fôrflåten. Dette problemet er avhengig av globale bevegelser av strukturen. Hvis strukturen har dekk som er plassert på styrbord og babord side, vil rullebevegelser være essensielle i analysen. Ved å få estimert korrekte globale bevegelser kan den relative hastigheten mellom strukturen og bølgen bli beregnet, og brukes videre i slammingkraftanalyse. Dette innebærer å estimere korrekte globale bevegelser på fôrflåten, gjennomføre laboratorieforsøk og lage en numerisk modell i programmet, *WADAM*.

Dempingsforhold til rullbevegelse av en lekter med skarpe hjørner er estimert. Resultatene er sammenlignet med forsøksresultatene hvor lineære bølger med forskjellige bølgeperioder og bølgesteilheter er testet. Forsøkene er gjennomført i den lille slepetanken, *"Lilletanken"*, hos Marinteknisk Senter på NTNU. En rektangulær modell med skala 1:25 er brukt, og en plate laget av aluminium er brukt som platformen på lekteret under forsøkene. Mellom festepunktet på platformen finnes det en kraftsensor som måler slammingkreftene. Dempingstester er gjennomført for alle seks frihetsgrader, og den naturlige perioden i hiv og rull er henholdsvis tilnærmelsesvis $7.6s$ og $12.05s$ i fullskala. Dette stemmer godt med resultatene beregnet fra *WADAM*.

To forsøksrunder har blitt gjennomført, en i *januar* og en i *april*. Testene fra *januar* består av forskjellige regulære bølger med mange bølgesteilheter, men med få bølgeperioder. Det er observert at globale bevegelser er størst i bølgene med størst steilhet, og slammingkreftene på plattformen er størst når lekteren beveger seg i hiv. Fra analysene av resultatene er det bestemt å kjøre flere tester i *april*. Resultatene i *april* viser at modellen er utsatt for parametrisk ustabilitet når en bølge med fullskala perioder fra $6.0s$ til $6.4s$ er testet. Denne ustabiliteten er større for store bølgesteilheter.

Sammenligningen av resultatene fra forsøkene og de numeriske simuleringene viser at metoden for rulldemping er konservativ. Resultatene fra forsøkene er mer dempet i resonansområdet. Globale rullebevegelser målt i forsøkene stemmer godt med de numeriske resultatene, men med unntak i resonansperiodene. Veggeffekter er simulert ved bruk av speilingsteknikk, og simuleringsresultatene er konsistente med de målte dataene.

Tidsserier av slammingkreftene er presentert. Det er observert at tidsvarigheten for slagkraften er svært kort, og det er krefter med negative verdier som har en lenger tidsvarighet etter slaget. En sensitivitetstest av filtreringsprosessen av slammingkreftene er gjennomført. Resultatene viser at for en lavpassfiltrering, bør verdien for den øverste grensefrekvensen være $200Hz$. De målte slammingkrefene er sammenlignet med de analytiske resultatene som er beregnet ved å bruke Wagner modell. På grunn av en stor usikkerhet på innfallsvinkelen, samsvarer ikke de analytiske resultatene godt med

forsøksresultatene, men de viser en øvre og nedre grense på slammingkreftene. Slammingkreftene fra forsøkene viser at slammingkrefter er avhengig av ulike parameter som bølgesteilhet, relativ hastighet, tettheten på fluidet, tilleggsmasse, og globale bevegelser.

En perforert plate med like dimensjoner som den massive platen er testet med samme bølgeserier. Resultatene er sammenlignet, og viser at kraftamplituden på den perforerte platen er lavere enn den massive platen.

Contents

Nomenclature

Abbreviations

BM	Buoyancy to Metacenter, distance from Buoyancy center to Metacenter
CFD	Computational Fluid Dynamics
GM	Gravity center to Metacenter, distance from center of Gravity to Metacenter
KB	Keel to Buoyancy, distance from Keel to Buoyancy center
KC	Keulegan Carpenter Number
KG	Keel to Gravity center, distance from Keel to center of Gravity
ODE	Ordinary Differential Equation
PSD	Power Spectrum Density
RAO	Response Amplitude Operator
$WADAM$	Wave Analysis by Diffraction and Morrison Theory
2D	Two-Dimensional
3D	Three-Dimensional
BVP	Boundary Value Problem

Greek Symbols

β	Deadrise Angle in Wagner Model
$\beta_{\eta 4}$	Estimated Damping Ratio
$\ddot{\eta}_{ij}$	Acceleration of a body
Δ	Dry Weight
$\dot{\eta}_{ij}$	Velocity of a body
η_{ij}	Motion Response of a body
λ	Wave Length
λ_s	Scaling Factor
μ	Dynamic Viscosity
∇	Displaced Volume

ν Kinematic Viscosity

ω Angular Frequency

ω_d Damped Natural Frequency

ω_e Encounter Frequency

ω_n Natural Frequency

ϕ Velocity Potential

ρ Water Density

ξ Damping Ratio in Mathieu Equation

ζ Wave Elevation

Roman Symbols

$\overline{Re}$ Modified Reynolds Number

A_{ij} Added mass

B Breadth

B_e Equivalent Damping Coefficient

B_L Linear Damping Coefficient

B_N Nonlinear Damping Coefficient

B_{e0} Estimated Eddy Damping

B_{f0} Estimated Friction Damping

B_{ij} Damping

C_B Block Coefficient

C_f Friction Coefficient

C_{ij} Restoring Force

D Draught

F_n Froude Number

F_{ij} Excitation Force

g Gravitational Constant

H Wave Height

I_{ij} Inertia

k Wave Number

L Length

L_m Length in Model scale

L_s Length in Full scale

M_{ij} Mass

R_0 RAO calculated without external Damping

Re Reynolds Number

S Wetted Surface Area

t Time

U Velocity

Subscripts

i Denotes the six degrees of freedom

j Denotes the six degrees of freedom

L Denotes Linear

m Denotes the model scale

N Denotes Nonlinear

n Denotes the natural frequency

s Denotes the full scale

Other Symbols and Mathematical Operators

Σ Summation

$U(s)$ Laplace Transformed Variable

$Y(s)$ Laplace Transformed Variable

1 Background

1.1 Introduction

The salmon industry has been growing in the recent years, and Norway has become one of the leading countries in aquaculture of Atlantic salmon according to [Lekang, 2017]. The increase of the world population has caused the need of larger, and more efficient fish farms in order to meet the global demand. Today many suitable sites for fish farming are in use, and it has been difficult to find more approved sites. Therefore, it has been suggested to move aquaculture into exposed locations. One of the advantages is that the fish will gain an optimal growth. If aquaculture takes place at a sheltered area, the bottom area will have accumulation of decomposition from the fish, which will result an anaerobic environment in the water. This effect will harm fish growth.

In exposed water, the weather and environment are expected to be harsher. Therefore, higher standards and stricter rules for the equipment are required. Feed barge is one of the main important tools used in fish farming, and it is considered as the brain of the cage farming system. A vulnerable area of an aquaculture feed barge can be the side deck that is mounted on the main hull. On this deck, pumps that transport the fish food into the fishing nets can be installed. These decks lie lower than main deck, and hence the chance for local slamming damage is large. Damages on the decks will cause the pumps to slide off, or the pumps may even break off from the feed barge. This will give severe consequences.

A feed barge's main task is to store fish food and to provide the crew a place to stay when they are working at the farm. Therefore, safety and comfort are two important design requirements. The barges that are constructed today are said to be able to store 750 tons of fish food in addition to providing a control room and living quarter for the crew. According to [Steinsvik, 2017], feed barges are classified into classic and modern barges. Typical geometry of the feed barge is a rectangular shaped floating structure which is moored on the sea bed. A few design concepts are shown in figure 1.1 and 1.2.

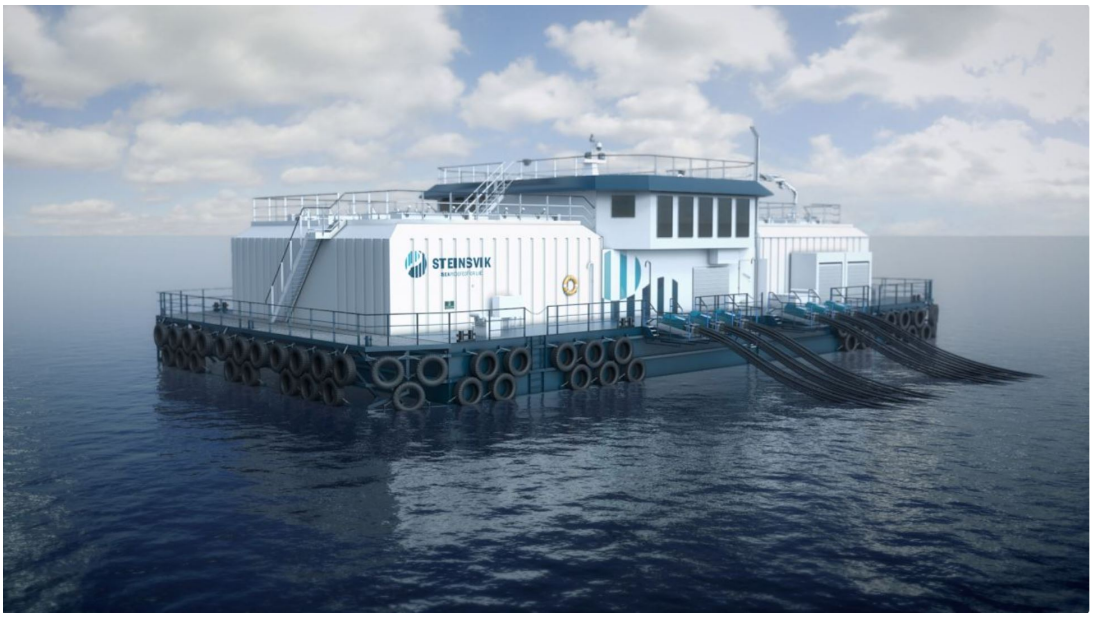

Figure 1.1: Classic feed barge designed by [Steinsvik, 2017]

In recent years, more modern design of the feed barge has been made. The shape is still rectangular, but the compartments on the main deck are improved due to the need for more efficient operations. This can be seen from the concept design of [Steinsvik, 2017] in figure 1.2. As the figure shows, the design concept contains side decks that will be vulnerable to slamming loads.

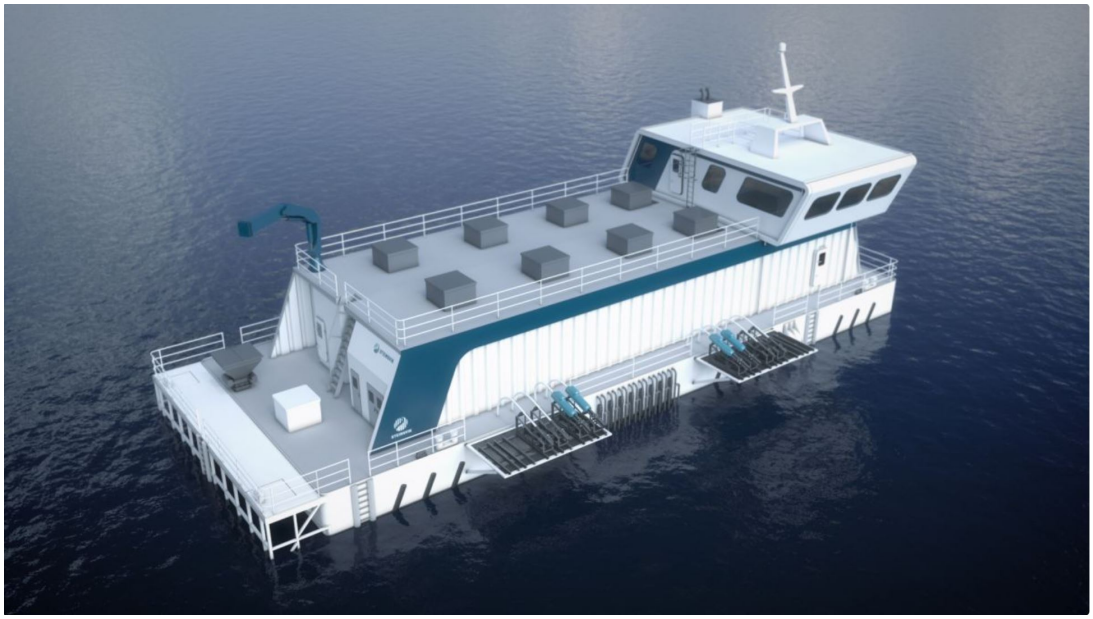

Figure 1.2: Modern concept design for a feed barge

Since early 2018, it is reported that side decks of active feed barges have been knocked off in harsh weather conditions. However, no serious consequences occured with only small local damages.

1.2 Previous related studies

Various practical slamming problems for ships and ocean structures are summarized in [Faltinsen et al., 2003]. The paper first discusses water entry problems on an initially calm water free surface, followed by other topics such as wet-deck slamming, green water slamming and sloshing. Challenges and current research status of the related topic are discussed in detail. In the conclusion, it is stated clearly that the general slamming phenomenon is a major concern for marine operations and applications. Furthermore, the slamming may be caused by breaking waves, which can cause impact loads on ship hulls and offshore platforms. The run-up of the waves can cause local damage on the platform deck, and this can in addition cause free surface effect due to increased fluid. The latter case is referred as green-water slamming. The slamming phenomenon can furthermore be caused by unexpected large waves, which leads to the importance of stochastic analysis of a sea state.

Slamming can often be connected to a sloshing problem, which is a non-linear behaviour of the fluid. If violent fluid motion occurs, there is chance that large slamming load may take place. A sloshing problem is usually related to a partially filled tank. However, it can be related to ship motions when surge, sway, roll, pitch and yaw motions are within the frequency range of the lowest natural frequency of the fluid motions. Therefore, it is important to estimate the global motions. However, the main interest related to sloshing is the highest natural period of the fluid motions. The tools for the analysis of the problem are mainly based on the Computational Fluid Dynamics (CFD). The solution will be in the time domain due to the non-linearities that are associated with the free surface conditions. There are varieties of numerical methods to provide the solutions. The common used CFD method is based on the so-called Reynolds-Averaged Navier-Stokes Equations (RANSE). However, the drawback is that it is costly and time consuming. Other methods, such as the Finite Volum Methods (FVM), Finite Difference Methods (FDM) and Finite Element Methods (FEM) are also common to use, and they are used to solve field equations. There are methods that are based on field discretization to handle a nonlinear free-surface motion. Boundary Element Methods (BEM) are also used for such problems, and they are based on a velocity potential that satisfies the Laplace equation. In recent years, Smoothed Particle Hydrodynamics (SPH) has been used for solving sloshing problems, and results presented in [Faltinsen et al., 2003] show good greement with the solution obtained from BEM. The SPH is proved to be more robust than BEM when the simulation involves wave breaking phenomenon after long time simulations.

1.2.1 Water entry on an initially calm free surface

The first contribution to analytic slamming analysis and impact problems was done by von Kármán (1929). His work is about stress analysis on seaplane floats. The objective in his work [Karman, 1929], was to determine the maximum pressure that acted on the floats during a plane's landing process. A theoretical formula for the maximum pressure during the landing was developed and checked with experimental results. The conclusion states that the results coincide with the experimental results except for the flat bottom impact. The theory can be applied to different bodies with different velocities.

The formula of impact pressure is established in detail in [Karman, 1929] where the model is considered as a horizontal cylindrical body in wedge shape with a deadrise angle. A deadrise angle is the angle of the inclination of the wedge shown in figure 1.3, and denoted as β. The established mathematical formulas give an analytic expression for the impact force acting on the body. The basis of the derivation is the momentum theory with some approximations. It is assumed that the momentum theory for a long plate with a specific width is used. This leads to that the mass of the plate is equal to the fluid mass that is contained in the cylinder with a diameter that is equal to the width of the plate. This cylinder will be composed with half water and half of air, which leads to an effect of the seaplane float to accelerate the water particles before it, and suck in the air behind it. However, the effect of the air can be neglected as its density is small compared to water density. Therefore, it is assumed that only half of the apparent mass is increased. This is why the added mass is only half of the apparent mass. It is important to note that the effect of buoyancy decreases the momentum, but it is neglected in this case. With this, the force of the impact can be expressed as in [Karman, 1929] along with the formula of the average pressure. It is noted that the formula can only be applied in two dimensional cases.

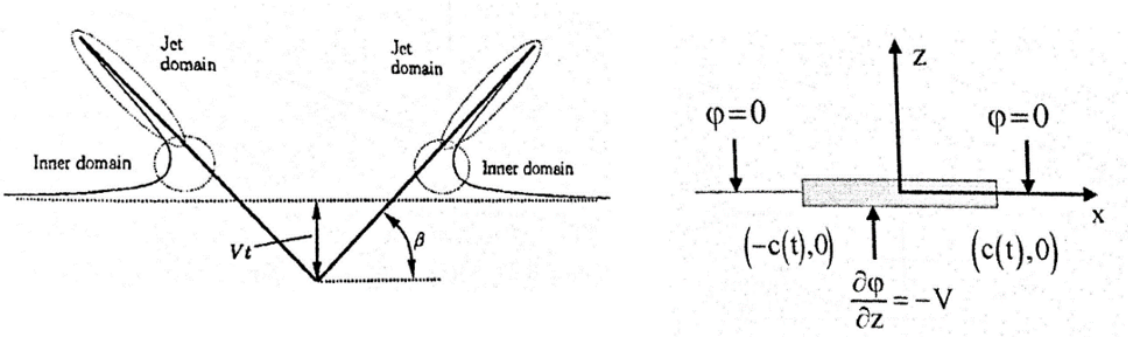

Figure 1.3: Parameters used in the Wagner model for an edge impact problem

The effect of the hydroelasticity due to compressible fluid has been studied in water entry problems. In [Faltinsen et al., 2003], it is stated that an important parameter that governs the hydroelasticity is the ratio between the loading time and the highest natural period for the local structural vibration in the impact area. By considering the wedge shaped cross section as shown in figure 1.3, it is stated that the hydroelasticity should be considered if the deadrise angle is less than 5 degrees. However, this effect is not important in the analysis of the maximum structural stress in general. On the other hand, there has been research about the air cushion effect that may be important if there are several dominant natural periods of the structural vibrations. All the findings are related to analysis in two dimensional flow. In reality three dimensional effects may reduce or increase the effects estimated in the 2D flow.

The edge impact problem shown in figure 1.3 is described by the Wagner model (1932). The theory assumes that no hydro-elastic effects are present during the impact, and the potential theory is applied where no air influence is considered. Wagner considered the effect of the spray roots during the impact, which was different from the work done by von Kármán (1929) who assumed no water rise after the impact. Wedge theory by Wagner

(1932) may be considered as an extension of the von Kármán theory by taking the local jet analysis into consideration.

1.2.2 Plate impact

Further investigation of the water entry problem is followed by the plate impact problem. This problem is similar to the case of the edge impact, and the study of a bottomed float from [Karman, 1929]. It is shown that a plate impact will give an infinite impact pressure due to the assumption of incompressible fluid. In [Karman, 1929], it has been suggested that the compressibility must be taken into consideration for this case. A possible formula of an approximated maximum pressure from the impact can be derived as a function of the velocity at the moment of the first contact of the body and the water, and the sound in the fluid.

Research of an early stage for floating plate impact was done by [Korobkin and Iafrati, 2017], where the initial flow close to the plate edges is approximately self-similar. The research was first used to investigate the rough landing of airplanes, but the theory can be applied to impact problems in liquids. The study is closely followed by the edge impact problem. The main differences are the free surface elevation areas. From the edge impact problem, the free surface elevations will not detach abruptly from the body surface. Whereas in the plate impact, the plate edges act as the separation point. This may cause the flow to be unsteady. The solution of the problem is to solve a boundary value problem. However, this solution cannot satisfy the conditions at the plate edges.

1.2.3 Violent sloshing problem

The current impact problem on the side deck of the feed barge is similar to a tank sloshing problem as illustrated in figure 1.4. The current local slamming problem is considered as a rigidly fixed deck to the barge with analogy to a sloshing problem where the water is violently moving near the corner of the tank roof. The flow caused by the roof impact due to sloshing can be modelled by a Wagner approach as proposed in [Faltinsen et al., 2003]. During the impact, the free surface is assumed to be in a parabolic shape that has an impact velocity which varies with time. The energy of the jet flow consists of kinetic and potential energy with the assumption that the energy are dissipated during the impact moment. Other important assumptions are standing waves of the resonant fluid motion and a rigid tank.

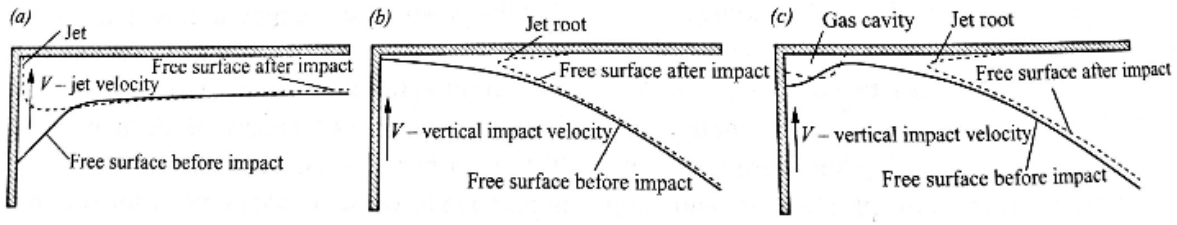

Figure 1.4: Three cases for tank roof slamming related to a tank sloshing problem presented in [Faltinsen and Timokha, 2009]

In [Faltinsen and Timokha, 2009], the problems listed in figure 1.4 are related to cases of flat impact with oscillating air cavity that is associated with a finite depth of tank filling. This problem can be related to a deck slamming with finite water depth. It is suggested that the high slamming pressure might be the cause of small distance of the impact free surface and the tank surface. Furthermore, the slamming pressure is sensitive to the details of the impact free surface. The experimental results presented in [Faltinsen and Timokha, 2009] show a stochastic manner of the slamming pressure, even if the excited waves are harmonic. From the structure point of view, the stresses may not have a similar behaviour as the pressure during the impact. Therefore, it is concluded that the slamming pressure is not a good measurement parameter for the analysis of the slamming phenomenon. This is because the measurement of the slamming pressure is usually high, and it is normally limited in space and time. The slamming force is a more reliable parameter from the experiments, even though the accuracy is not very high.

Model tests are usually performed for assessment of slamming loads. Based on the similarity requirement of the model and the full scale, many of the flow parameters should ideally be the same. The sloshing is also associated with gravity waves, which requires Froude scaling. However, Reynolds scaling should be considered if there are dominating viscous effects.

Computational methods such as CFD, that has been mentioned earlier, is a common tool to assess the slamming loads and sloshing problems. However, experiences from [Faltinsen and Timokha, 2009] show some difficulties to use this method in the initial impact stage if the angle between the impact surface and the tank surface is small, because the CFD is usually based on the Wagner model (1932). This will give the program a crash when the deadrise angle is small, because the solution gives an infinite rate of change of the wetted surface. However in 2007, a stretched coordinate system was introduced and it may be used to solve this problem.

The slamming problem cannot be solved by theoretical study alone. In [Faltinsen and Timokha, 2009], it is stated that the state of art of the methods do not permit a purely theoretical analysis. It is recommended that model tests should be a basis of the structural design and analysis.

1.3 Present study

In this thesis, the global motions and the local slamming forces of a feed barge are investigated. This is done by conducting both experiments and numerical calculations with a free floating barge structure. Scale effects of the experiments are considered to be a minor concern, as the main focus is the global motions and the local slamming forces. The numerical simulations are carried out based on the experiments. This means that mooring line pretensions, mass properties and loading conditions are modelled as the set up in the laboratory.

1.3.1 Motivation

Slamming can be considered as an initial phase of a water entry problem. By water entry, it means that the moment when a body enters the water and the wetted surface area of the body increases with time. Slamming is characterized by a very small time scales and initial impact loads, and the slamming load is a concern to structure integrity. If slamming occurs when a ship has forward speed, the vessel may experience a speed loss. Slamming can in addition excite a whipping phenomenon, which is a global elastic transient resonance oscillations. Furthermore, fatigue is also a problem if the impact forces are periodic. This is a consequence of impacts that will not lead to serious damage after one impact, but result to a fatigue failure and cause small local damages. For ships, periodic slamming might in addition give concern for carrying out operations and on-board comfort. If hydroelasticity occurs during an impact, this will result in cavitation and ventilation. To summarize, the slamming phenomena is a concern and it is undesired. It is important to have a proper method to predict slamming and learn the characteristics related to the problem.

1.3.2 Objectives

The purpose of this thesis is to estimate the global motions of a feed barge with a loading condition, and establish the characteristics for the local slamming analysis on the deck. Experiments are carried out relating to the topic and for the validation of the numerical simulations. The main objective of this project is described in the following steps:

1. Use the potential solver, *WADAM*, to obtain the global motions numerically
2. Investigate roll damping of the barge, and obtain correct roll motion characteristics
3. Carry out laboratory experiment, and post-process measured data
4. Compare the measured experimental results with the simulation results
5. Study the impact problem of a wedge-shaped structure, and use the analogy for the current problem
6. Establish simple characteristics for the slamming force of the side deck, and find out parameters that are essential for the slamming force

Simple experiments will be carried out in the small towing tank, *Lilletanken*, at the Centre of Marine Technology. The experiment will be based on a box shaped model with 1:25 scale. Responses of the model in regular waves with different steepness and periods will be tested. The measured global motions will be compared with the responses calculated from *WADAM*, where estimated roll damping is applied.

Time series of slamming forces on the side deck will be studied. The analytic method for slamming analysis will be compared with the results obtained from the experiments. The aim is to understand the basic characteristic of the slamming force and find a method to estimate it.

1.3.3 Assumptions

Based on a report written by [Moran, 1965], in order to simplify the mathematical problem of the flow around the body, assumptions are used in this thesis. In this report, the problems for water-exit and -entry are discussed. As slamming can be considered as an initial phase of a water entry problem, it is reasonable to utilize the assumptions related to these topics.

The main assumptions are the requirements to make the potential theory valid. This means that the flow has to be irrotational, incompressible and inviscid. The assumption of an irrotational flow is justified in [Moran, 1965] as the viscous effect on the pressure during the impact is generally small. The incompressible flow is based on the speed of the body when it enters the water, which is generally well below the speed of the sound in water. This leads to a negligible effect of compressibility of the water. By applying these assumptions to the mass continuity equation, the well-known Laplace equation is defined. However, the assumption of the incompressible fluid should be used with caution. It is stated in [Faltinsen et al., 2003] that it cannot be used in all cases that are related to slamming problems, as the fact that the water is a compressible fluid that can cause hydroelasticity, air bubbles and air cushions, which will affect the results. It should be noted that in cases with small effect of these elements, it is valid to neglect the interaction effect between water and air. However, there are some specific cases listed in [Faltinsen et al., 2003] where air cushion is formed, and compressibility should be taken into consideration in the analysis.

The air density and the surface tension are neglected. This is due to that the factors are generally unimportant during the slamming analysis. However, according to the report by [Moran, 1965], they have a small significance, but not an essential role in an analytic solution.

It is assumed that the gravity can be neglected. This means that the Froude number is infinite. This is justified as the gravitation will not be essential during very short impact time frame. Furthermore, it is assumed that no cavitation takes place during the impact. However, this might be questionable during the initial impact phase of a water entry problems as there is clear chance that the cavitation might occur. [Moran, 1965] has stated that neglecting cavitation is one of the major defects of the theory about water exit- and -entry. This is due to that there will be two free surfaces and the flow will be unsteady. Unfortunately, there are currently no techniques that are capable to cope with these two effects.

1.3.4 Approach

The problem of the side deck impact is caused by the global motions of the barge. The motion of the barge can be solved by the potential solver program in frequency domain, *WADAM*. This program is based on potential theory applied to a panel model. The interactions of the waves and the rigid body are calculated as body motion response amplitude operators and panel pressure responses.

Because the location of the side deck is usually on the starboard and portside of the structure, one of the most important motions out of the six global motions is the roll.

It is therefore essential to have a good estimate of the roll damping. According to [Dhavalikar and Negi, 2009], additional damping is needed in the numerical simulations. A method for estimating the nonlinear roll damping has been suggested, and experiments have been carried out in order to validate of this method. The exact roll damping can be obtained form the experiments by comparing the roll response with the numerical simulations.

The slamming is caused by the rate of change of the added mass. Hence, it is important to obtain the added mass during the slamming events. However, this is not possible with the test set up and equipment of the experiments conducted related to this thesis. From the time series of slamming forces in the experiments, it is shown that the slamming forces are largest when the body experiences a blunt impact. This means that the heave response will be more crucial than roll.

There are some waves that cannot be made during the experiments. This is due to the limitations of the wave maker. It is known that too large accelerations will cause errors which instantly stop the wave maker from working. This is usually related to long and high waves with large periods and large steepness. Due to this limitation of the wave maker, the maximum flap motion is limited to $0.3m$ from its zero position, and it has later been taken to be $0.2m$.

1.3.5 Structure of the thesis

This thesis focuses on the linear responses of a floating barge and the slamming responses on the deck. In Chapter 2, the basic theory is outlined. The procedure of the numerical simulations in *WADAM* is explained in detail in Chapter 3, and the input parameters and mass properties of the numerical panel model used in the simulations are presented.

The experimental results and the data processing of the measured quantities are presented in Chapter 4. The comparisons and discussions of the results obtained from the simulations and experiments, and the list of further work are presented in the last two chapters.

2 Theory

2.1 Scaling

Scaling is important when a physical model is to be used in experiments. This means that the physics on the model size should be similar as in full scale. According to [J.Kirkegaard et al., 2011], many considerations should be taken into account in the scaling process. The process shall be based on past experiments, and the dominant forces must be well represented.

From the past experiences, Froude scaling is used, because the main concern is the wave induced motions. [Faltinsen and Michelsen, 1974] carried out an experiment of a box shaped model with 1:100 scale. The objective was to find the wave excitation force and moment, and the motions in the six degrees of freedom. The results were stated to correspond well with the theoretical predictions. As the waves are gravity driven forces, Froude scaling is a suitable scaling parameter. This is given by the Froude number, which is the relationship between the inertia and gravity forces as given in equation 2.1.

$$F_n = \frac{U}{\sqrt{gL}} \tag{2.1}$$

By using Froude scaling, it is required to have same Froude number for both model and full scale. By using this procedure, the relationship of the different parameters and the scaling factor can be obtained as shown in table 2.1.

Table 2.1: Scaling factors relationship

Parameter	Scaling factor	Parameter	Scaling factor
Length	λ_s	Mass	λ_s^3
Surface	λ_s^2	Force	λ_s^3
Volume	λ_s^3	Density	1
Time	$\sqrt{\lambda_s}$	Kinematic viscosity	$\lambda_s^{3/2}$
Velocity	$\sqrt{\lambda_s}$	Dynamic viscosity	$\lambda_s^{3/2}$
Acceleration	1		

2.2 Motion response

The motion response of a floating body is based on the linear theory. The incoming waves are assumed to be regular waves with different frequencies that can be superimposed to give an irregular sea state. The transient effect is neglected, therefore the response of the body will consist the same oscillation frequency as the incoming waves. According to [Faltinsen, 1993], the hydrodynamic problem of a body with incoming waves can be separated into two sub-problems. The two different force components can be found independently. Due to the linearity, superposition can be used to obtain the total force. The two force components are the excitation forces and the hydrodynamic forces.

The excitation forces are the forces and moments on the body from the incident waves when it is restrained from moving. In other words, it is a sum of Froude-Kriloff and diffraction forces. The hydrodynamic forces are forces from added mass, damping and restoring when the body is free to oscillate in all rigid body modes in the incident wave frequency. This is illustrated in figure 2.1.

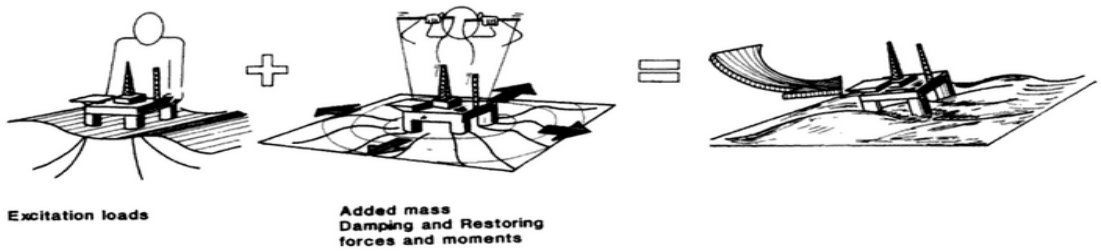

Figure 2.1: Superposition of the excitation forces and hydrodynamic forces from [Faltinsen, 1993]

By superimposing the two forces, the equation of motion in all rigid body modes can be obtained as in equation 2.2.

$$\sum_{j=1}^{6}[(M_{ij}+A_{ij})\ddot{\eta}_j + B_{ij}\dot{\eta}_j + C_{ij}\eta_j] = F_i e^{-i\omega_e t} \qquad (i=1,...,6) \tag{2.2}$$

ω_e denotes the encounter frequency, and it is the same as the frequency of the incident waves if the forward speed of the body is zero. The indices i and j refer to the motion modes of the rigid body motions, which are translations and rotations about different axis. An overview of the motions are shown in table 2.2.

Table 2.2: Overview of the 6 rigid body motions

Axis	Translation		Rotation	
x	η_1	Surge	η_4	Roll
y	η_2	Sway	η_5	Pitch
z	η_3	Heave	η_6	Yaw

Solution of equation 2.2 gives the motion at any point of the body as expressed in formula 2.3.

$$\mathbf{s} = \eta_1\mathbf{i} + \eta_2\mathbf{j} + \eta_3\mathbf{k} + \boldsymbol{\omega} \times \mathbf{r} \tag{2.3}$$

In the equation, $\boldsymbol{\omega} \times \mathbf{r}$ indicates the contribution from the rotations by cross multiplying the rotations with the position vector. The values of the vector $\boldsymbol{\omega}$ and $\mathbf{r}$ are described as following:

$$\boldsymbol{\omega} = \eta_4\mathbf{i} + \eta_5\mathbf{j} + \eta_6\mathbf{k} \qquad \mathbf{r} = x\mathbf{i} + y\mathbf{j} + z\mathbf{k} \tag{2.4}$$

Thus, the motion at any point on the body can be written as equation 2.5.

$$\mathbf{s} = (\eta_1 + z\eta_5 - y\eta_6)\mathbf{i} + (\eta_2 - z\eta_4 + x\eta_5)\mathbf{j} + (\eta_3 + y\eta_4 - x\eta_5)\mathbf{k} \tag{2.5}$$

If the incident waves are assumed to be sinusoidal, the response will be in the form as expressed in equation 2.6.

$$\eta_j = \eta_{aj}\sin(\omega t + \epsilon_j) \tag{2.6}$$

Where η_{aj} is the amplitude of the response in motion j, and ϵ_j is the corresponding phase between the wave and the response.

2.3 Mass-spring-damper relation

The ordinary differential equation (ODE) described in equation 2.2 in Chapter 2.2 is a mass-spring-damper system. The origin of the equation is based on from Newton's second law. If the initial conditions are assumed to be zero, by the Laplace transform, the ODE can be transformed into a polynomial equation as shown in equation 2.7.

$$[M_{ij} + A_{ij})s^2Y(s) + B_{ij}sY(s) + C_{ij}Y(s) = U(s) \tag{2.7}$$

Here, $Y(s)$ is the Laplace transform of the output signal and in this case it is the body motion, η_{ij}. Similarly, $U(s)$ is the Laplace transform of the input signal. The transfer function, often taken as the response amplitude operator (RAO), is the ratio of the output signal and the input signal. For a mass-spring-damper system, the transfer function is expressed as in equation 2.8.

$$\frac{Y(s)}{U(s)} = \frac{F_j}{[M_{ij} + A_{ij}]s^2 + B_{ij}s + C_{ij}} \tag{2.8}$$

2.4 Ordinary differential equation

The motions of a floating body are obtained by solving the boundary value problem described in Appendix A.2, which is a second order differential equation (ODE). Many numerical solver are designed to solve a first order ODE. Conversion of the higher order ODE into a set of first order ODE is therefore necessary. The response in one motion will be in a form as expressed in formula 2.2 in Chapter 2.2. This can be converted into two first order ODE by introducing two state variables, η_{jk_1} and η_{jk_2}. Following derivations and replacement of the two states must be carried out:

$$\begin{aligned} \eta_{jk_1} &= \eta_{jk} \rightarrow \dot{\eta_{jk_1}} = \dot{\eta_{jk}} \\ \eta_{jk_2} &= \dot{\eta_{jk}} \rightarrow \dot{\eta_{jk_2}} = \ddot{\eta_{jk}} \end{aligned} \tag{2.9}$$

This gives a set of first order ordinary differential equation expressed as in formula 2.10.

$$\begin{aligned} \dot{\eta_{jk_1}} &= \eta_{jk_2} \\ \dot{\eta_{jk_2}} &= -\frac{B_{jk}}{(M_{jk}+A_{jk})}\dot{\eta_{jk}} - \frac{C_{jk}}{(M_{jk}+A_{jk})}\eta_{jk} + \frac{F_j}{(M_{jk}+A_{jk})}e^{-i\omega_e t} \end{aligned} \tag{2.10}$$

2.5 Roll motion

Motions in all 6 degrees of freedom will naturally be coupled to each other. However, due to the structure symmetry the motions can be decoupled if the reference point is taken at the center of the symmetry plane. If the roll motion is decoupled with sway and yaw, the equation is reduced to formula 2.11.

$$(I_4 + A_{44})\ddot{\eta_4} + B_{44}\dot{\eta_4} + C_{44}\eta_4 = F_4 \tag{2.11}$$

As mentioned, the damping can be non-linear. Consider a non-linear roll damping, the equation for roll motion can be written as following according to [Zhao et al., 2016]:

$$(I_4 + A_{44})\ddot{\eta_4} + B_L\dot{\eta_4} + B_N\dot{\eta_4}|\dot{\eta_4}| + C_{44}\eta_4 = F_4 \tag{2.12}$$

Where B_N and B_L denote non-linear and linear damping coefficients respectively. The non-linear term of damping can be important in some cases. From the experiments performed by [Vugts, 1968], it is observed that the linear damping differs from the calculations of the experimental results for models with a certain beam and draught ratio. The results of the two dimensional roll wave damping are plotted against the beam-draught ratio for a rectangular cross section. This is shown in figure 2.2.

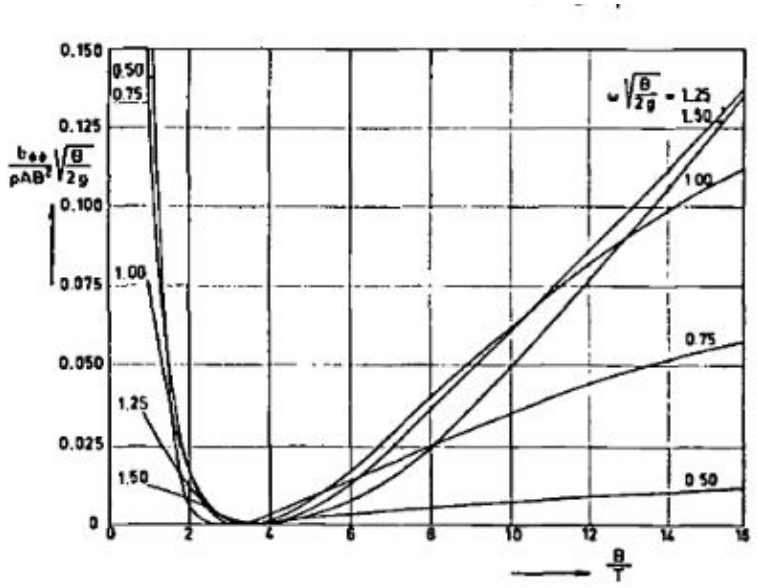

Figure 2.2: Results obtained from experiments in [Vugts, 1968] where two dimensional wave damping $B_{44}^{(2D)}$ is plotted against a rectangular cross section with different beam-draught ratio in infinite water depth. The roll axis is taken at the mean free surface

The non-linear damping coefficient can be estimated with a method which replaces it with an equivalent linearized damping coefficient. This method assumes that the energy dissipated during a half cycle of roll motion is equal to the damping. From the lecture notes in *Marine Operations* [Nielsen and Berg, 2007], the equivalent linearized damping coefficient is expressed as following:

$$B_e = B_1 + \frac{16x_n}{3T_n}B_2 = B_1 + \frac{8}{2\pi}\omega_n x_n B_2 \tag{2.13}$$

Where T_n is the time between two roll peak motions, and x_n is the roll motion amplitude of interest. The linear and non-linear damping coefficients can be found by plotting B_e against the average roll amplitude by linear regression.

Roll natural frequency is dependent on the metacentric height which is expressed in equation 2.14. The value is the distance from the center of gravity to the metacenter.

$$GM = KB + BM - KG \tag{2.14}$$

In formula 2.14, KB denotes the distance from keel to buoyancy center of the structure, and KG the center of gravity measured from the keel. BM is the distance from buoyancy center to metacenter, which is the ratio of the second moment area, I, and the displaced volume, ∇. The natural period in roll is a function dependent on GM_T in transverse direction. From [Faltinsen, 1993], the natural period in roll is expressed as in 2.15.

$$T_{n4} = 2\pi\sqrt{\frac{Mr_{44}^2 + A_{44}}{\rho g \nabla G M_T}} \tag{2.15}$$

Where r_{44} is the roll radius of gyration with respect to x-axis through the center of gravity.

2.6 Damping

The barge is modelled as a rectangular box with sharp edges. This will create nonlinear viscous damping and must be treated as an additional external damping in the potential solver, *WADAM*. The external damping is usually taken as a certain percentage of the critical damping in the respective rigid body motion. This is the damping ratio, and the method presented in this chapter is used to estimate the quantity of this ratio.

2.6.1 Estimation from the decay test

The damping can be estimated from a decay test as stated in [Steen, 2014]. The solution for a dynamic system which takes form as $M\ddot{x} + b\dot{x} + kx = F$ is expressed as in equation 2.16.

$$x = e^{-\frac{b}{2M}t \pm i\omega t} \tag{2.16}$$

By writing only the real part of equation 2.16, the solution will be as following:

$$x = e^{-\frac{b}{2M}t} \cos \omega t \tag{2.17}$$

Equation 2.17 illustrates that the motion amplitudes follows an exponential function, and hence the damping coefficient can be estimated as expressed in formula 2.18.

$$\beta = \frac{b}{b_{crit}} = \frac{1}{2\pi n} ln \frac{x_1}{x_2} \tag{2.18}$$

Where n is the number of oscillations for average value of the damping. x_1 and x_2 are two peaks from the amplitudes of the oscillations from the decay test. The first peak with the largest value is x_1, and x_2 is the value of the last peak in n periods. The damping estimated from this method is the linear damping.

For a non-linear damping model as mentioned in equation 2.12 in Chapter 2.5, the quadratic damping can be estimated by assuming that the decay oscillation is reasonably harmonic over each half cycle according to [Zhao et al., 2016]. The non-linear term can be linearized by a Fourier series expansion, and the results can be formulated as in equation 2.19.

$$\dot{x}|\dot{x}| = \frac{8}{3\pi} \omega_n x_i \dot{x} \tag{2.19}$$

With this relation, the dynamic system will have different equation which gives the relationship for the two peaks from the decay test as following:

$$\frac{1}{\pi} \frac{lnx_{i-1} - lnx_{i+1}}{2} = B_1 + \frac{4}{3\pi} x_i B_2 \tag{2.20}$$

Equation 2.20 is a linear function with the coefficients B_1 and B_2 representing the linear and non-linear damping coefficients respectively. The values of the left hand side and x_i are plotted and fitted with linear regression.

With the damping ratio known, the natural frequency of the damped, freely oscillating system will have a natural frequency ω_d as expressed in equation 2.21.

$$\omega_d = \omega_n \sqrt{1 - \beta^2} \tag{2.21}$$

2.6.2 Estimation of roll damping

This chapter is based on the paper written by [Dhavalikar and Negi, 2009], which describes the empirical method used for roll damping. A *MATLAB* script has been made. The method is empirical and is accurate if the resonance frequency is close to unity. The method can be used to estimate the damping ratio. The critical damping for a system is expressed as in equation 2.22.

$$B_{crit} = 2\sqrt{C_{jk}(M + A_{jk})} \tag{2.22}$$

The method for estimating of roll damping is a sum of skin friction damping, eddy making damping, free surface wave damping, lift force damping and bilge keel damping. It is stated in the paper, that the main contributions of the roll damping are hull skin friction damping and the hull eddy shedding damping for a barge with sharp corners.

Friction damping

The formula of the friction damping is given as an empirical formula expressed in equation 2.23.

$$B_{f0} = \frac{4}{3\pi} \rho S r_e^3 R_0 \omega C_f \tag{2.23}$$

Here, C_f is the friction coefficient and is given by formula 2.24.

$$C_f = 1.328 \Big[\frac{2\pi\nu}{3.22 r_e^2 R_0^2 \omega} \Big]^{0.5} \tag{2.24}$$

In formula 2.23, r_e denotes bilge keel radius. Since the barge does not have bilge keel installed, the value is set equal to 1. R_0 is the value of the response amplitude operator (RAO) calculated without external damping, and is given in radians for rotation motions. S is the wetted surface area and is given by the following formula:

$$S = L(1.7D + C_B B) \tag{2.25}$$

C_B in formula 2.25 denotes the block coefficient of the structure. The barge is perfectly rectangular, which gives the block coefficient equal to 1.

Eddy making damping

Due to sharp edges of the barge, the suggested empirical formula for eddy making damping is expressed as in formula 2.26.

$$B_{e0} = \frac{2}{\pi}\rho L D^4 (H_0^2 + 1 - \frac{OG}{D})\big[H_0^2 + (1 - \frac{OG}{D})^2\big] R_0 \omega \tag{2.26}$$

Where H_0 and OG are given as in equation 2.27.

$$H_0 = \frac{B}{2D} \qquad OG = D - KG \tag{2.27}$$

Methodology

The sections above give two equations of the estimation for the two different roll damping components. The total non-dimensional damping ratio is given in expression 2.28, with B_{44}^* as the sum of frictional damping and eddy making damping.

$$\beta_{\eta_4} = \frac{B_{44}^*}{2\sqrt{(g\Delta\overline{GM_t})(I_{44} + A_{44})}} \tag{2.28}$$

In the equation, the added mass A_{44} is frequency dependent. Therefore, β_{η_4} will also be frequency dependent. The undamped solution from a potential solver must be performed first, and the damping ratio for all wave frequencies is calculated by using formula 2.28. A value β' must be computed as shown in formula 2.29 for all frequencies.

$$\beta' = \frac{1}{2\beta_{\eta_4}} \tag{2.29}$$

The difference between the estimated ratio and the undamped RAO can be calculated as shown in formulae 2.30. This must be done for all wave frequencies.

$$\Delta\beta = \beta' - \text{undamped RAO in roll [deg]} \tag{2.30}$$

Next step is to determine the value for the last positive number before the sign of $\Delta\beta$ changes from positive to negative, and the minimum value of $\Delta\beta$. This is the range where the values for β_{η_4} are plotted against $\Delta\beta$. The plot is fitted with least square regression, and the estimated damping ratio is the intersect point in x-axis of the fitted line. To summarize, a chart in figure 2.3 gives an overview of the method. This method is used for all roll damping estimation in the numerical model.

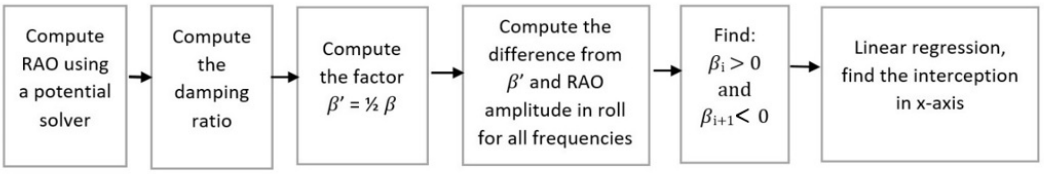

Figure 2.3: The procedure of the roll damping ratio estimation

2.7 Parametric roll

Parametric roll is defined as a spontaneous rolling motion which can cause a great amplitification of roll motions. This is usually related to ships with a forward speed in head or following seas which causes dynamic instabilities. Parametric roll motion in ships was first discovered in late 1930s [Sheikh, 2008]. However, it is believed that this phenomenon was a result of a byproduct and related to small ships with forward speed in following seas until a few incidents with container ships in 1990. The APL CHINA container ship was exposed to the parametric roll and was heavily damaged. This brought the attention to this topic.

Parametric roll is initially triggered by a small disturbance in roll motion. This disturbance can cause oscillatory motion that grows large over a few cycles. For ships, it is defined that the parametric roll occurs when the ship's encounter frequency is approximately twice of the natural roll frequency with a damping that is insufficient to dissipate the roll energy as described in the assessment document by ABS [ABS, 2004]. There has been large attention which focused on the trigger conditions that causes the instability in order to prevent this. Some mitigating methods listed in [Sheikh, 2008] are suggested by adjusting the forward speed, changing direction of the ship, or by installing active fins or other devices.

The estimation can be done according to [Faltinsen, 2012] by using the classical Mathieu equation. The theory considers a type of instability that occurs in the same manner as the parametric roll instability. There are similar requirements for this instability to occur. As described in [Faltinsen, 2012], it is required that the waves should not change much in amplitude or period. Due to this, it is expected to be easier to demonstrate this instability in the experiments with regular and linear waves, rather than irregular waves. Furthermore, it is required that the ratio between the natural frequency in roll and the encounter frequency should be approximately 0.5, 1.0, 1.5, 2.0 etc. with a low roll damping in these regions.

The Mathieu equation is obtained when a damping ratio ξ is set to zero in equation 2.31.

$$\frac{d^2\eta_4}{dt^2} + 2\xi\omega_n\frac{d\eta_4}{dt} + \omega_n^2(1 + \frac{\delta GM}{GM_m}\sin(\omega_e t + \beta))\eta_4 = 0 \tag{2.31}$$

The stability as shown in figure 2.4 is dependent on the ratio of the natural frequency and the encounter frequency, ω_n/ω_e, $\delta\overline{GM}/\overline{GM}$ and the damping ratio ξ. Here, $\delta\overline{GM}$ is the amplitude of the harmonically oscillating part of the metacentric height. It is shown

in figure 2.4 that the region for instability lies when $\omega_n/\omega_e = 0.5, 1.0, 1.5, 2.0$ and so on, when the ratio of $\delta\overline{GM}/\overline{GM}$ is small.

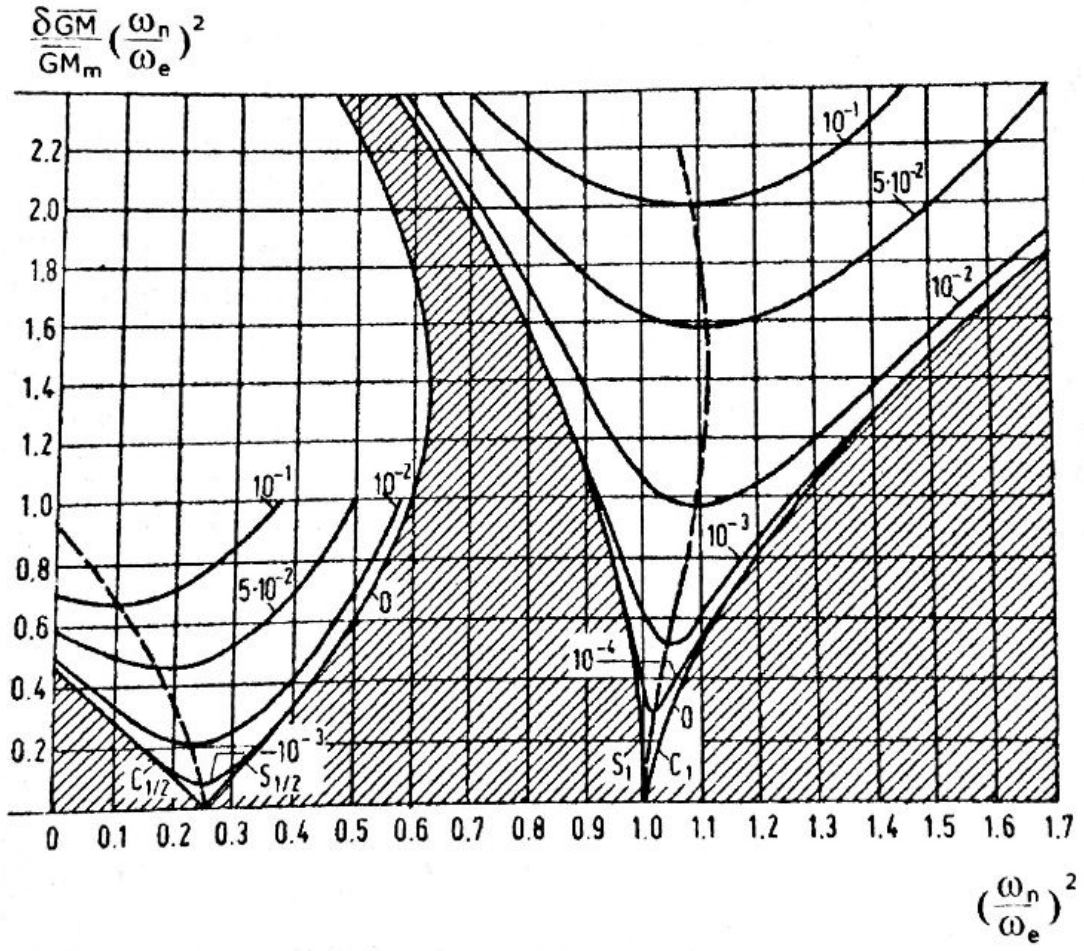

Figure 2.4: Stability diagram for the Mathieu equation for ship rolling motion. The shaded area represents the stable region when the damping ratio is zero

2.8 Slamming

There have been reviews of the theories for the two cases of slamming with Wagner theory and Korobin theory. These two methods have been used to express the slamming phenomena in deep- and shallow-water, and especially impacts with small or zero deadrise angles. This is reviewed in [Howison et al., 2002] where the two theories have been analyzed and tested.

Slamming are impulse loads with high pressure that occur during an impact between a body and water. The characteristic of this phenomena is that the impact loads usually appear in a very short time. According to [Faltinsen, 1993], slamming has the highest probability when the relative velocity between the body and the waves is largest. In addition, the duration of the slamming pressure measured is usually of the order of milliseconds. The pressure from slamming are sensitive to how the water hits the structure. From an experiment measuring the slamming pressure presented by [Kim et al., 2015], it

shows that the harmonic oscillations do not give a pressure variation which is also harmonic. It is observed that the magnitude and the duration of the pressure peaks tend to vary. This trend is also described by [Faltinsen, 1993].

2.8.1 Analytic studies

It is stated that the first analytic approach of the slamming problem is based on the work of von Kármán (1929). His method is used to analyze a horizontal cylinder that is forced through an infinity calm water surface with a constant velocity. Further assumptions made are that the body has small submergence and that the form is blunt. The potential theory can in addition be used as the flow is simplified to be irrotational and incompressible. Details of the analytic slamming theory can be found in Appendix A.4.

Wagner model

This chapter is based on Chapter 11.3.1 in the book *Sloshing*, written by *O.M. Faltinsen* and *A.N. Timokha* [Faltinsen and Timokha, 2009]. The theory is based on the tank roof impact inside a tank regarding a sloshing problem. The problem can be theoretically modelled after the Wagner's method (1932) with assumption that there is no hydroelasticity. Other assumptions are that the liquid is incompressible with no air influence. The method also requires that the geometry of the free surface is known at the instant time of the impact. This can be done by the particle image velocimetry measurements. The Wagner model is generalized by taking the profile of the tank roof as the edge impact. This is illustrated in figure 2.5 which is taken from [Faltinsen and Timokha, 2009].

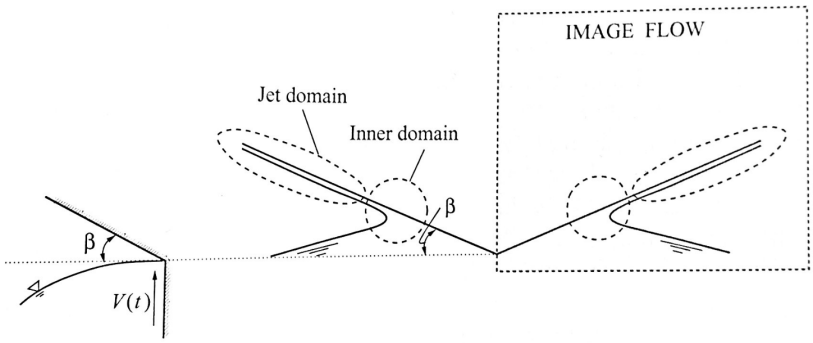

Figure 2.5: Wagner theory applied to the tank roof impact illustrated from [Faltinsen and Timokha, 2009]

The focus of the method lies on the outer flow domain, which is located below the inner and jet domains that is illustrated in figure 2.5. The details about the inner domain is unknown due to the rapid variation of the flow at the spray roots.

The Wagner model presents a symmetric wedge body with edge impact as illustrated in figure 2.6. The body impacts the free surface with a constant uniform speed $V(t)$ which comes from the assumption that the case is a local scenario. The vertical velocity of the

free surface is approximately constant on the length scale of the wetted body due to the impact.

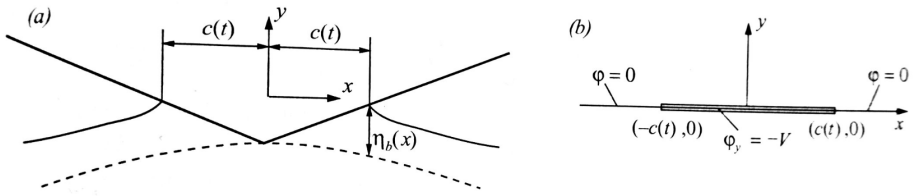

Figure 2.6: Wagner model of outer flow domain solution and the boundary value problem of the outer domain analysis. The boundary value problem is represented in the right hand side figure with a velocity potential $\phi_y = \partial\phi/\partial y$

It should be noted that y is used as the vertical coordinate, which should not be confused with the usual notation as z. The reason for this is that the value z is denoted as a complex variable in this analysis. The boundary value problem in figure 2.6 must be solved at each time instant to find the velocity potential ϕ due to the impact. The body boundary condition is transferred to a straight line between $x = -c(t)$ and $x = c(t)$ by using Taylor expansion with the respect to the penetration depth and ignoring the higher order terms. The endpoints where $x = \pm c(t)$ correspond to the instantaneous intersections between the outer flow free surface and the body surface. This is shown in right hand side of figure 2.6.

The free surface condition where $\phi = 0$ at $y = 0$ is because the liquid has an acceleration that are much larger than the gravitational acceleration during the impact. Furthermore the free surface geometry is changed to a straight line by neglecting the higher order terms.

For experimental measurements, it is convenient to represent the slamming force as a dimensionless coefficient. From experiments conducted by [Smith et al., 1997] with aluminum plates dropped in waves, a slam force coefficient expressed in equation 2.32 is used. The coefficient is based on neglegible effect of gravitational acceleration, water and air compressibility.

$$C_s = \frac{F_s}{0.5\rho V^2 l b} \qquad \text{where} \qquad l = \sqrt{\frac{m}{\rho b}} \tag{2.32}$$

Where l is a length scale of the hydrodynamic impact at the time of the maximum deceleration, b is the plate width and m is the mass. From the various experiments in [Smith et al., 1997], slamming force is a function of the parameters as shown below:

$$F_s = F_s(\rho, m, V, \beta, g, H, \lambda) \tag{2.33}$$

Where H and λ are the wave height and wave length respectively, and β is deadrise angle of the plate.

The theoretical slamming force results for a wedge are shown in figure 2.7 taken from [Faltinsen, 2012]. The results are based on a constant vertical velocity during the water entry stage. Wagner's flat plate approximation is good for structures with small deadrise

angles, whereas the general method is good for large angles. It is shown that von Karman solution underpredicts the force.

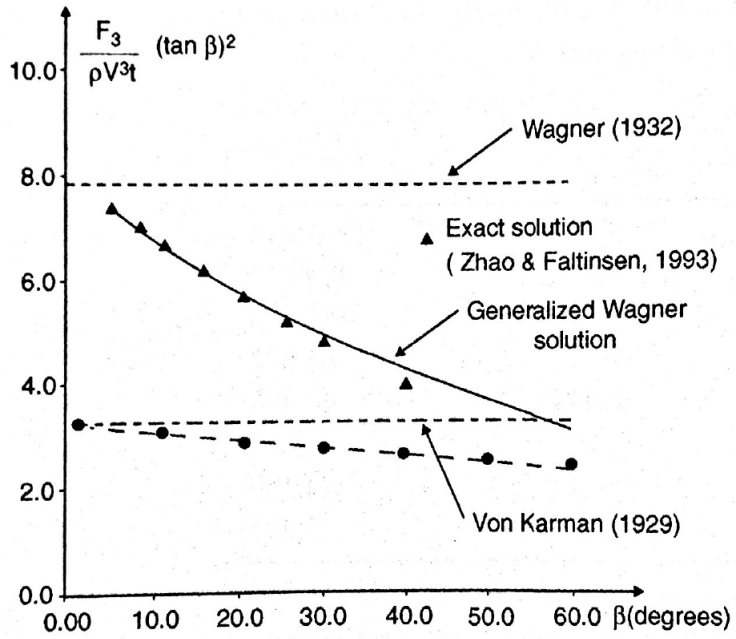

Figure 2.7: The force prediction distribution during water entry of a rigid wedge with a constant velocity taken from [Faltinsen, 2012] for different deadrise angles

2.8.2 Added mass effect

The added mass theory is based on the *DNV*'s recommended practice *DNV-RP-H103* [DNV, 2011]. In the proceedings of *DNV*, the slamming is modelled as an added mass effect. The slamming force is a result of the rate of change of the added mass. It is expressed as a function of the rate of change of the instantaneous high frequency limited added mass in heave, A_{33}^{∞}, and the slamming velocity v_s, that is assumed to be positive as expressed in equation 2.34.

$$F_s(t) = \frac{d(A_{33}^{\infty} v_s)}{dt} = v_s \frac{dA_{33}^{\infty}(t)}{dt} \tag{2.34}$$

The slamming force can be directly expressed as the slamming coefficient, C_s, and is expressed as in equation 2.35 for the added mass effect.

$$C_s = \frac{2}{\rho A_p v_s} \frac{dA_{33}^{\infty}}{dt} = \frac{2}{\rho A_p} \frac{dA_{33}^{\infty}}{dh} \tag{2.35}$$

where dA_{33}^{∞}/dh is the rate of change of added mass with submergence, A_p is taken as the horizontal projected area of the object and h is the submergence that is relative to the wave elevation.

Related to water entry that takes place in waves, the relative velocity between the lowered object and the sea surface must be used. The slamming force can be expressed as in

formula 2.36.

$$F_s(t) = \frac{1}{2}\rho C_s A_p(\dot{\zeta} - \dot{\eta})^2 \tag{2.36}$$

Where $\dot{\zeta}$ and $\dot{\eta}$ are the vertical velocity and the vertical motion of the object respectively, and A_p is the projected area during the impact. When measuring the vertical force on an object during water entry, the buoyancy force and viscous force will be a part of the measurement. However, during the initial water entry, the dominant force will be slamming force which is why the effect of the buoyancy and the viscosity can be neglected.

3 Numerical Simulations

A numerical model has been made in *WADAM* in order to calculate the barge motion characteristics. The response amplitude operator (RAO) of the barge can be obtained, and the wall effects from the experiment has been modelled in the simulations by using mirroring technique. A sensitivity test of the mass center has been performed.

3.1 WADAM

Potential solver program, *WADAM*, for Wave Analysis by Diffraction and Morrison Theory, is a program in *DNV GL*'s sesam package. According to the user manual for the program, [WAD, 2015], the program uses a calculation method based on the potential theory to calculate the first order radiation and diffraction effects on large volumes.

Two analysis are carried out in *WADAM*. One with finite water depth and one with infinite water depth. This is because the experiment has a set up with finite water depth waves. The simulations are first carried out with deep water configurations. However, the effect of the finite water depth is significant which will affect the results. This is shown in the comparisons of the results of the added mass, damping coefficients, and the results of the motions in terms of response amplitude operator.

3.1.1 Numerical model

In *WADAM*, a panel model made by four patches is used in order to solve the boundary value problem, and obtain the global motion responses of the barge. *WADAM* runs in the batch mode together with *HydroD* as a graphical user interface. Wave and structure interaction simulations are simulated, and the results can be presented in a graphical post-process program, *Postresp*.

The modeling in *WADAM* is executed for a model in full scale, and the properties are listed in table 3.1. The global axis system in *WADAM* is set to be at the center of the model. The loading condition is based on the loading condition carried out during the experiments. It is first considered to have a loading condition with a center of gravity (COG) located in the same plane as the buoyancy center (COB). However, this is not possible in the experiments, and hence the loading condition is changed. By changing the gravity center, the natural frequency of the roll motion will also change due to the dependency of GM. In order to compare the results from the experiments, the numerical model is modified to be consistent with the physical model.

Table 3.1: Input parameters used in the numerical model in *WADAM*

COG	R_{44}	R_{55}	L	B	D	∇	COB	Δ in tonnes
(0, 0, 4.75)	$0.338B$	$0.25L$	20	12.5	7	1750	(0, 0, 3.5)	1793.75

The total mass (Δ) of the structure can be calculated within the program, and the stability calculation is performed. The main goal with this numerical model is to determine the global motions characteristics. The panel model generated in *WADAM* with the properties in table 3.1 is shown in figure 3.1.

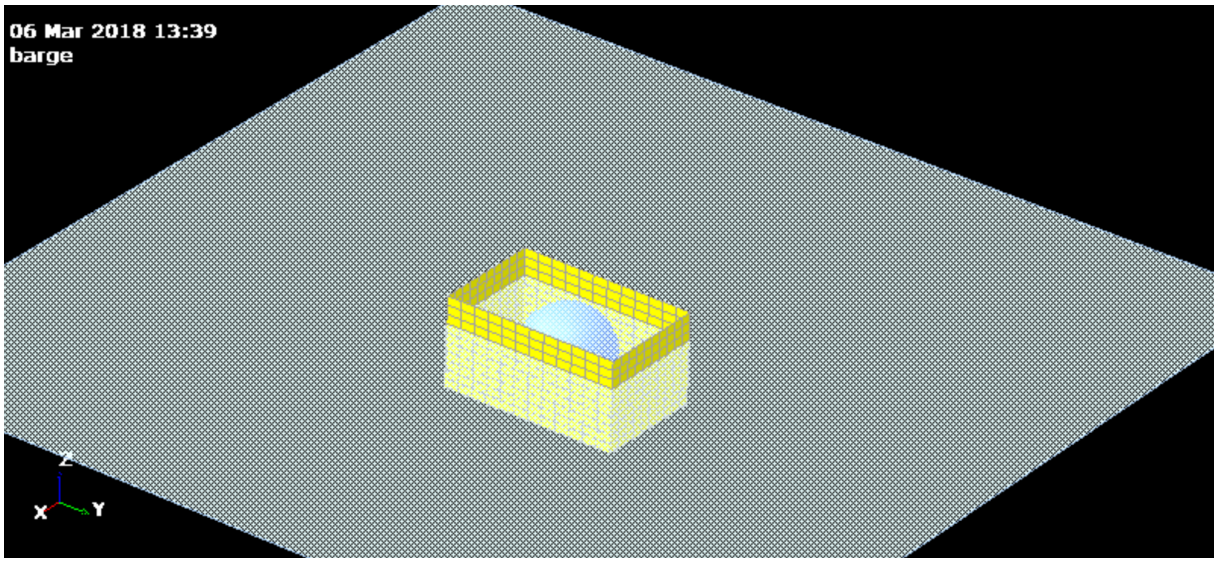

Figure 3.1: Panel model used for simulations in *WADAM* in open sea configurations. Wall reflection effects which will be discussed in following chapter are simulated based on this panel model

As shown in the figure, the side deck is not modelled. This is because the potential solver only takes the wet part of the structure into account. The dry part of the structure is not taken into account in the linear potential solver. The mass is set to be uniformly distributed in the body, and the center of gravity is indicated in figure 3.1 as a sphere at the center of the model. This model is furhter used for wall reflection simulation which will be discussed in the following chapter.

3.1.2 Additional matrices

As mentioned in Chapter 2.6, viscous damping is needed in order to simulate roll motions. In *WADAM*, it is possible to add external damping matrix as a percentage of the critical damping. As the body is moored during the experiments, external restoring matrix must be taken into account.

Some viscous damping for heave motions is found due to the sharp edges of the body which create vortices that contribute to heave damping. The heave damping is taken as 3% of the critical damping as expressed in equation 3.1.

$$B_{33} = 0.032\sqrt{C_{33}(M + A_{33})} \tag{3.1}$$

The model is moored with four springs that represents the mooring lines in the experiments. This effect is included as an additional stiffness in surge and pitch. The stiffness of the springs is approximately $28N/m$ in model scale, and attached with an angle of 45 degrees to the model. This gives a total restoring forces, $C_{11} = 4.9496 \cdot 10^4 N$ in full scale in uncoupled surge direction. Due to the restoring in surge, a stiffness in uncoupled pitch direction will also be affected. By using the geometry relation of the model, the stiffness in pitch was found to be the pretension of the mooring lines multiplied with the breadth of the model. A side view of the model is shown in figure 3.2, where two springs act as the mooring system with a pretension as $F_{pretension}$.

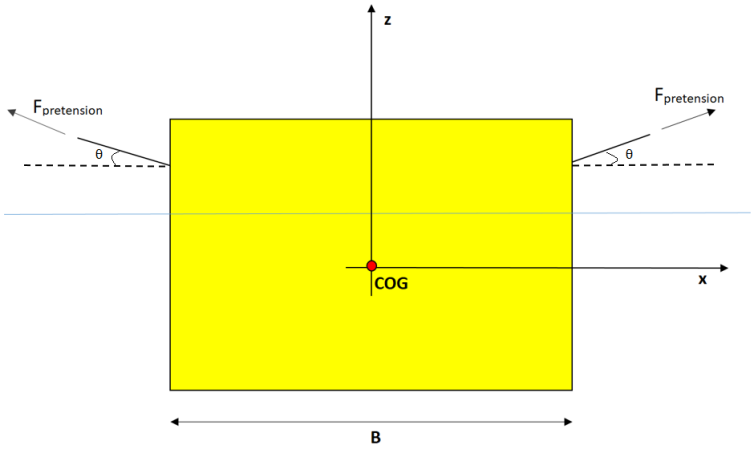

Figure 3.2: Geometry of the model to determine the pitch restoring forces, C_{55}

By decomposing the pretension in the springs, the initial force in pitch, $F_{0,pitch}$, about the mass center is expressed as in equation 3.2 due to small angle approximation ($\sin(\theta) \approx \theta$).

$$F_{0,pitch} = F_{pretension}\theta\frac{B}{2} \tag{3.2}$$

For the two mooring lines on both port and starboard side, the final expression of the initial pitch force is expressed as in formula 3.3.

$$F_{0,pitch} = F_{pretension}B\theta \quad \text{with} \quad C_{55} = F_{pretension}B \tag{3.3}$$

The stiffness in pitch motion is added to the numerical simulations for the comparison of the results.

Because of the orientation of the model with the coordinate system as shown in figure 3.1, roll motion in beam sea is equivalent to pitch motion in head sea. Hence, the roll motion of the barge is actually the pitch motion in the numerical model. The damping considered for the pitch motions is applied in the model. To summarize, the values of the added parameters for the mooring forces and viscous damping in the numerical simulations are presented in table 3.2.

Table 3.2: Values for external matrices used in the numerical model analysis

Value	Magnitude	Description
C_{11}	49497.47 [N]	Mooring line stiffness in surge
C_{55}	636328.125 [N]	Mooring line pretension
B_{33}	3% of critical damping in heave	Heave damping
B_{55}	$1.6633 \cdot 10^7$ [N]	Estimated pitch damping with 19 mirroring bodies

3.2 Wall effects

As the experiments are executed in a towing tank, the wall reflections may affect the results. This comes from that the model is relatively large compared to the tank width. In order to include the wall effect in the numerical simulations, the mirroring technique is used. The distance between the two consecutive bodies is the distance of the model to the tank wall in full scale. Figure 3.3 shows the modelling for the wall effect with 19 bodies rigidly connected.

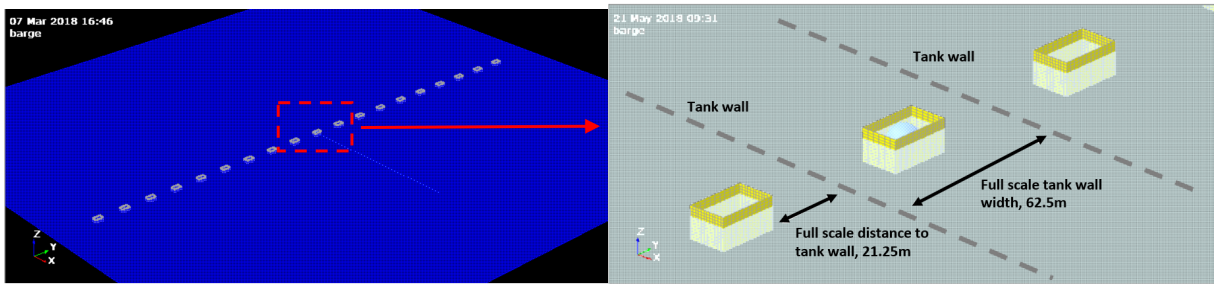

Figure 3.3: Panel model to account for the wall effects. Left: 19 bodies rigidly connected to each other. Right: Zoomed in view of three panel models

The multiple bodies are considered as one body rigidly connected. Therefore, there will be only one response amplitude operator from the results. The parameters for the mooring, the mass property, and viscous damping are similarly applied to each of the body. The estimated pitch damping ratio is shown in table 3.3 for different number of bodies in deep water.

Table 3.3: External damping estimation results for a model in infinite water depth

No. boxes	damping ratio	No. boxes	damping ratio	No. boxes	damping ratio
1 Box	3.95%	9 Box	7.74%	17 Box	10.57%
3 Box	6.42%	11 box	8.70%	19 Box	11.13%
5 Box	8.10%	13 Box	9.36%	21 Box	12.18%
7 Box	7.12%	15 Box	9.99%	23 Box	11.68%

3.2.1 Convergence test

It is believed that with more bodies added, the tank wall reflection effects will be better simulated. However, this will lead to a longer computational time. In order to find an optimal number of the bodies with sufficient accuracy, a convergence test is performed

in both damped and undamped cases where the motions in surge, heave and pitch are evaluated. The standard deviations of the response amplitudes in the three motions are calculated and plotted against number of the bodies. This is shown in figure 3.4 for all three motions. It can be seen that heave motions are most unstable. The results are presented in more detail in Appendix C.2.

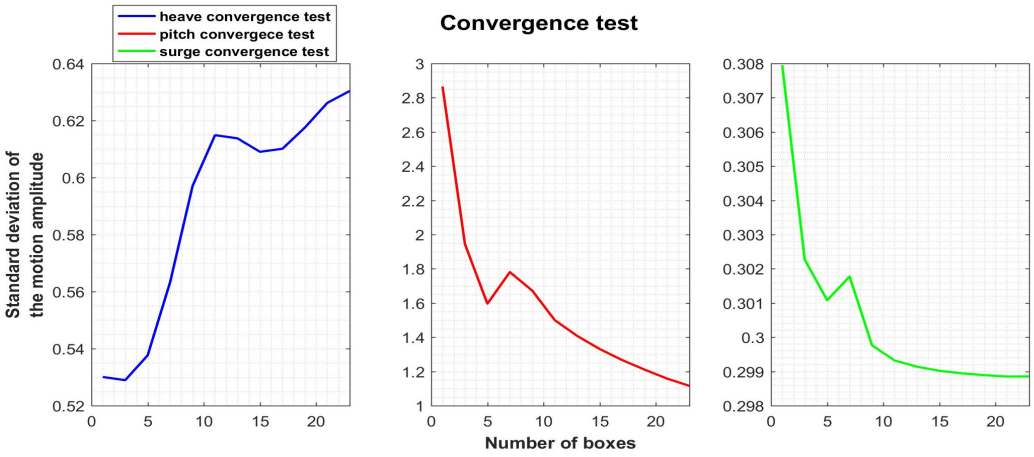

Figure 3.4: Convergence test results in infinite water depth analysis with the estimated damping calculated from the method presented in Chapter 2.6.2

3.3 Consideration of water depth

The previous simulations have considered an infinite water depth. However, in the experiments, the water depth is finite due to the scale factor and a relatively large body. This can be corrected in *WADAM* by defining the water depth in the environmental conditions. It is observed that water depth may affect the results significantly. This can be seen by the comparison of the experimental results, with the numerical simulated results. Furthermore, the added mass and the potential damping are different in different water depths which is shown in figure 3.5.

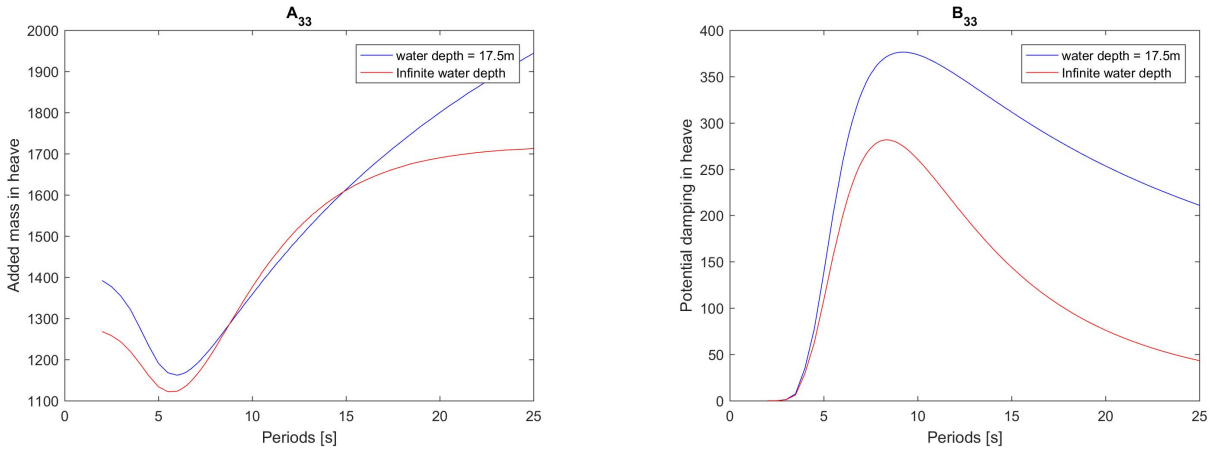

(a) Added mass in heave

(b) Potential damping in heave

Figure 3.5: Added mass and potential damping in heave for infinite and finite water depth

Figure 3.5a shows that the added mass does not differ much in the resonance region, but

not for the large periods. The reason for an increase of added mass in finite water depth is because the sea bottom creates a reflection in longer waves.

There is a significant increase in potential damping in resonance region for the finite water depth case. This is caused by the difference in the velocity potential of infinite water depth and finite water depth. In finite water depth analysis, the body displaces more water, which makes it easier to make waves due to the sea bottom. The waves will then contribute to the damping in the mass-spring system.

Due to the large difference between the results of finite and infinite water depth, analysis for finite water depth with $17.5m$ has been conducted. This depth is the full scale value of the largest water depth in the small towing tank during the experiments. The purpose of this is to check and compare simulations with the experimental results.

3.3.1 Finite water analysis

As shown in figure 3.5, the potential damping is different. This leads to a different damping that must be added to the numerical model. The results for pitch damping estimation for finite water depth analysis are listed in table 3.4. Furthermore, the responses of the body will be different with different water depth. Thus, a new convergence test and new pitch damping estimation need to be carried out. All results of the convergence test in finite water depth can be found in Appendix C.1.

The heave response amplitude operator (RAO) from the finite water analysis shown in the Appendix differs from the results from infinite water analysis. In the heave RAO from the finite water depth analysis, there is a second peak for the cases with more bodies. This is the effect of the wall reflection, and has been checked with the experimental results.

Table 3.4: Viscous damping for finite water depth analysis

No. boxes	damping ratio	No. boxes	damping ratio	No. boxes	damping ratio
1 Box	3.4017%	9 Box	5.1704%	17 Box	6.7176%
3 Box	3.6858%	11 box	5.5281%	19 Box	7.0618%
5 Box	4.1909%	13 Box	5.9581%	21 Box	6.9198%
7 Box	4.7736%	15 Box	6.3531%	23 Box	7.2042%

The results for the convergence test in the finite water depth are presented in figure 3.6 with a water depth of $17.5m$. The results show that the optimal number of bodies is 19, similar to the results obtained from the convergence test in the case with infinite water depth. It is shown that heave motion is most unstable compared to the other two motions.

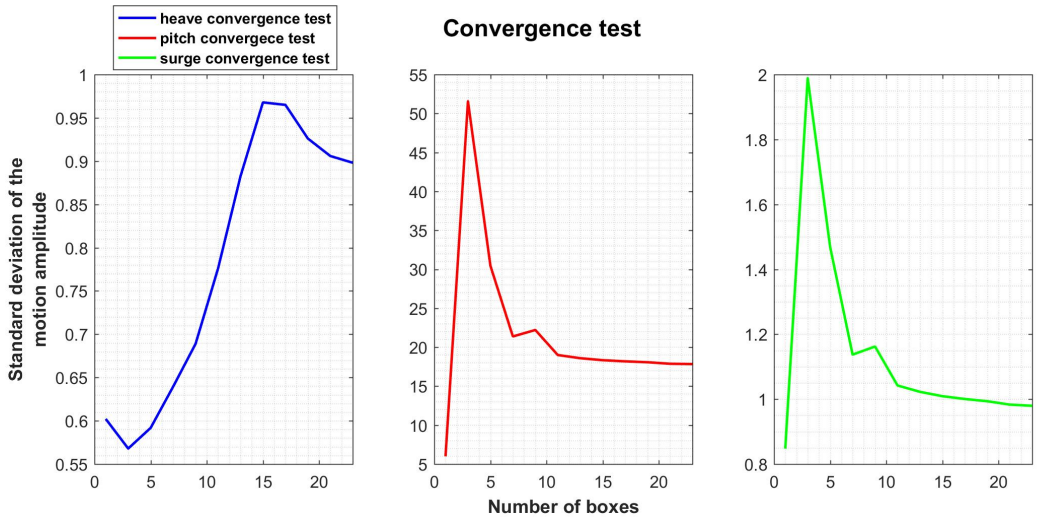

Figure 3.6: Convergence test result for finite water depth analysis with a water depth of $17.5m$ and external damping estimated from the method presented in Chapter 2.6.2

3.4 Sensitivity test of the center of gravity

The mass center will change with different loading conditions. It is shown that pitch motion is most sensitive of the change of the gravity center. The heights of the center of gravity used in the sensitivity test are $3.75m, 4.45m, 4.55m, 4.65m, 4.75m$ and $6m$. The results are shown in figures 3.7 and figure 3.8.

In the simulations, the wall effects are included with 19 bodies and a finite water depth of $17.5m$. As expected, the location of the peak in pitch response for head sea waves is moving further to the right due to the decreasing value of GM_T. The surge response is coupled with the pitch motions, and surge response gives different RAOs for different height of the center of gravity

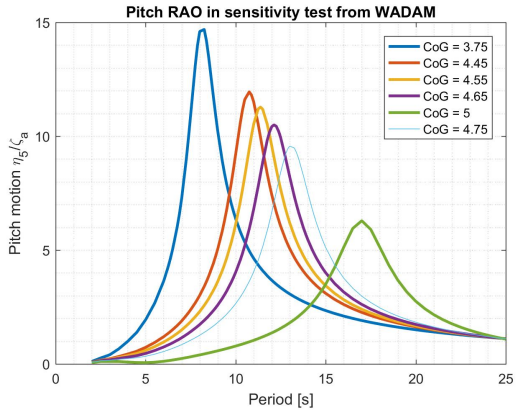

(a) Plot of pitch RAO obtained from *WADAM* during the sensitivity test

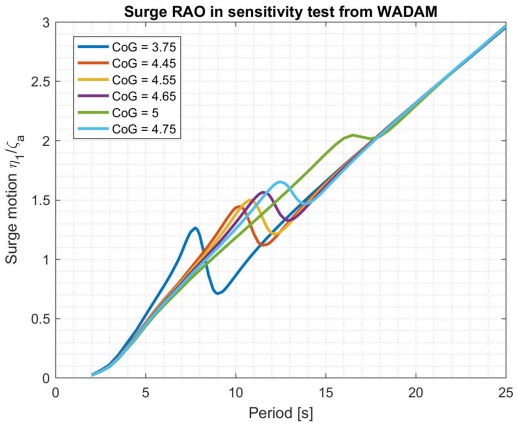

Plot of pitch RAO obtained from *WADAM* during the sensitivity test

Figure 3.7: Results of the sensitivity test of pitch and surge motion from *WADAM* with 19 mirroring bodies. The heights of center of gravity considered are $COG = 3.75m, 4.45m, 4.55m, 4.65m, 4.75m, 5m$

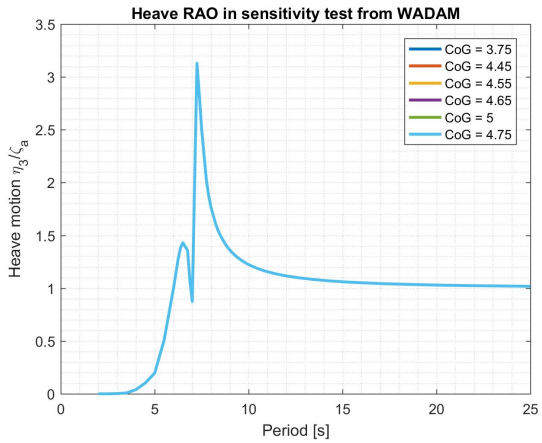

Figure 3.8: Result of the sensitivity test of heave motion. The height of center of gravity varies from $COG = 3.75m, 4.45m, 4.55m, 4.65m, 4.75m$, 5m and with 19 bodies

It can be seen in figure 3.8 that the heave motion is not affected by the change of the gravity center.

4 Experimental Modeling

The main goal of the experiment is to verify the method for the damping estimation, and to establish slamming characteristics. This chapter describes how the experiment is conducted, regarding the model test set up and instrumentation, and how the measured data are post-processed. The model has a symmetric mooring system, which is modelled by springs. The side deck is mounted on the model, and the height of the plate can be adjusted. However, in most of the tests, the height of the side deck is set to be in the middle of the free board height. A force sensor is attached at the attachment point, in order to measure the slamming force. Global motions will be measured by four accelerometers mounted at the main deck.

Two experiments are carried out. One in *January* and one in *April*. During the laboratory work in *January*, it is observed that there are large reflections due to the large body, and too few wave periods had been tested. It is then decided in *April* to run a test without a model in the tank in order to get better result for the waves. In the tests with more wave periods, parametric instability is observed. During the second experiment, some modifications are made in order to measure how the waves are moving up to the deck.

4.1 The model and the instrumentation

The physical model has a wall thickness of $8cm$, and is constructed by wood, which is later polished by polyester by Trond Innset from NTNU. The loading condition of the model is different from the expected. It was first decided that the physical model should have a center of gravity located at the same level as the buoyancy center, and the radius of gyration in roll at beam sea should be 35% of the beam length. However, when the model was ballasted, the desired center of gravity and the radius of gyration in roll cannot be achieved at the same time. This is the main reason why the numerical model is modified, and it is tested for different locations of mass center. The properties of the model are listed in table 4.1, for a global axis system with origin at the keel and in the aft perpendicular of the model.

Table 4.1: Data for the physical model used in experiment

COG	R_{44}	R_{55}	∇	Δ in [kg]	COB	L	B	D	H	*thic*
(0.25, 0, 0.19)	$0.338B$	$0.25L$	0.112	112	(0.25, 0, 0.14)	0.8	0.5	0.28	0.4	0.08

On the deck, the model is mounted with a small weight for fine adjustment of trim, and four accelerometers. Accelerometers are used to measure the vertical and horizontal acceleration of the body. Two accelerometers are mounted to measure the horizontal

accelerations which are attached in transverse direction. The last two accelerometers are mounted in longitudinal direction and measure the vertical accelerations. The arrangement of the equipment on the main deck is shown in figure 4.2.

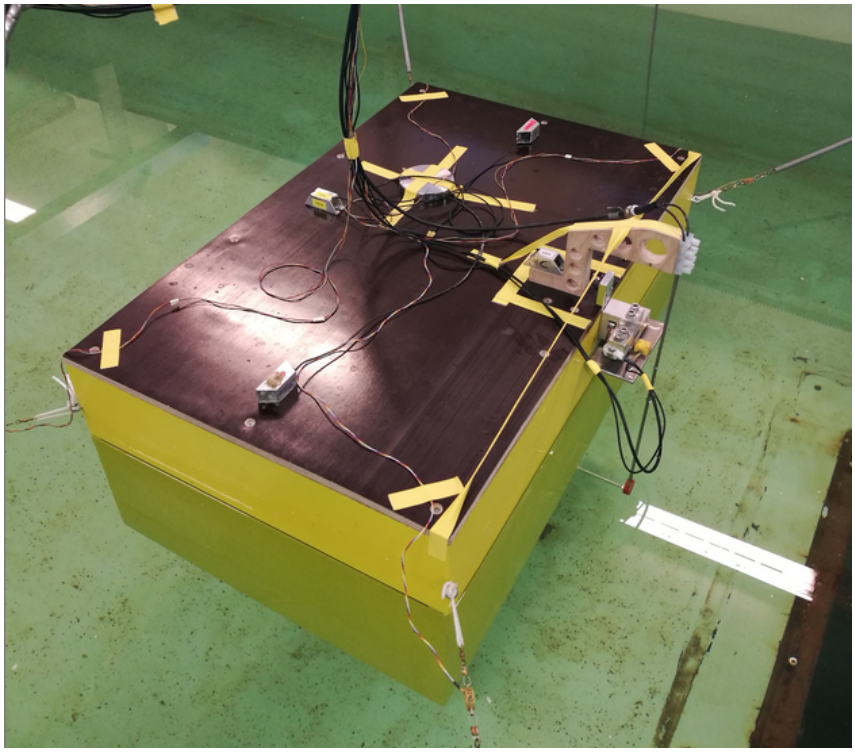

Figure 4.1: The physical model ballasted and moored in the small towing tank

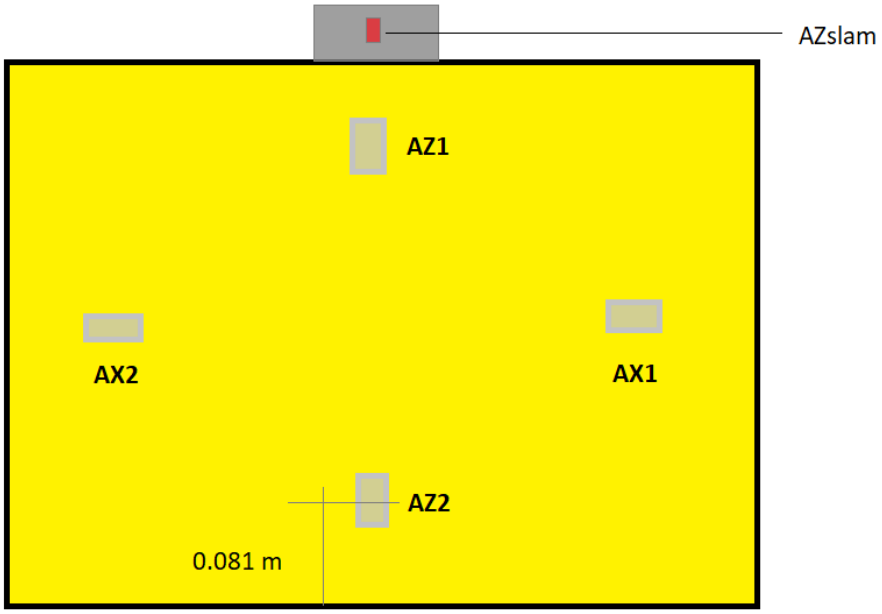

Figure 4.2: Arrangement of the equipment attached to the model viewed from above

In figure 4.1, it can be seen that a wave probe is mounted on the main deck. This

is to measure the incoming wave when it hits the model. Since it is attached to the model, it can also be used to measure the relative motion of the model and the waves. On the side deck, there is an accelerometer attached in order to measure the vibrations and hydroelasticity effects when slamming occurs. A force transducer is fixed on the platform in order to measure the slamming force. The model is moored with four springs on each corners. This is to prevent the model from drifting away. The forces from the springs are measured by a force sensor. To summarize, the different equipment with the corresponding properties used in the experiment are listed in table 4.2.

Table 4.2: Measured quantities and equipment used during the experiments

Sensor name		Quantity measured
Accelerometers		Acceleration
Quantity	Unit	Description
AX1	m/s^2	Horizontal acceleration in starboard side
AX2	m/s^2	Horizontal acceleration in port side
AZ1	m/s^2	vertical acceleration in forward section
AZ2	m/s^2	Vertical acceleration in rear section
AZslam	m/s^2	Vertical acceleration in deck
Forces transducer		Forces
Quantity	Unit	Description
slamForce	N	Slamming force on deck
F1	N	Mooring line force in starboard side in forward section
F2	N	Mooring line force in port side in forward section
F3	N	Mooring line force in port side in rear section
F4	N	Mooring line force in starboard in rear section
Wave probes		Wave elevation
Quantity	Unit	Description
WP1 - WP10	m	wave elevation of the incident waves from the wave maker

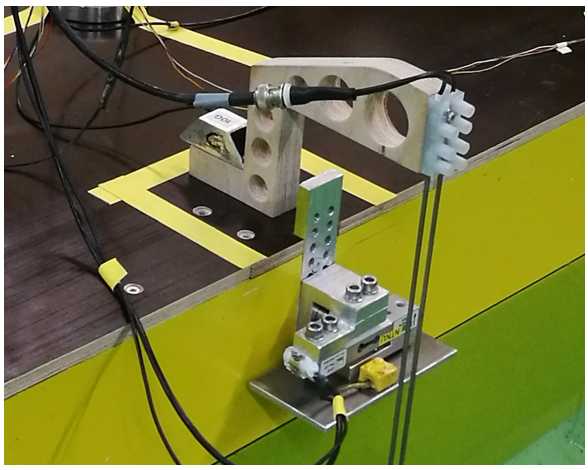

(a) Solid plate mounted on the model with the force sensor, an accelerometer and one wave probe

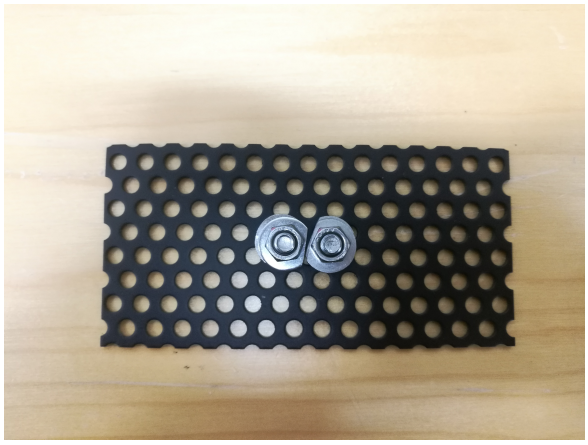

(b) The perforated plate that is used in few tests

Figure 4.3: Snapshots of the solid and perforated plate

The plate attached to the model is solid and made of aluminum with the dimensions

$L \times B \times D = 0.12m \times 0.06m \times 0.004m$. This is shown in figure 4.3a. The weight of the solid plate is $90g$ excluding the weight of the sensor. If the weight of the sensor is accounted, the total weight is $255g$ for the solid plate. In addition to the solid plate for modeling the side deck, a few tests are carried out with a perforated plate as the side deck and this is shown in figure 4.3b. The data of the perforated plate are listed in table 4.3.

Table 4.3: Data of the perforated plate

Length	Width	Thickness	Perforate rate	Weight
0.12 [m]	0.06 [m]	0.0025 [m]	34.5%	65 [g]

4.2 Calibration

The zero reference has to be determined before the calibration takes place. This is due to the variations of different parameters that the sensors are sensitive of. After the zero reference has been found, the sensors can be calibrated. By calibration, [Steen, 2014] defines it that there should be an agreement of the the output signals and the known physical properties. The relationship of the input and output signal should be linear. If the relationship becomes non-linear, there will be some complications in handling the non-linearities in the data acquisition and the post-processing process. The procedure of the calibration is the same for all sensors, and the steps are described as following:

1. Find a set of known values of the specific parameters that is going to be measured
2. Measure the parameters by the sensors. Analyze the measured values, and get the linear relationship between the input and output signal
3. The calibration factor can be obtained, as the trend line from step 2 will give a linear function expressed as in formula 4.1. The formula gives a factor a, which is the calibration factor and it is used in the logging program. Linear regression can be used to obtain this factor.

$$y = ax + b \tag{4.1}$$

4.3 Set up

The experiments are conducted in "*Lilletanken*" at the Center of Marine Technology. They are carried out twice with different test set ups and arrangements described in this chapter.

4.3.1 *January* tests

Nine wave probes are placed in the tank as shown in figure 4.4, to measure the wave elevations. The 10th wave probe is placed on the model in order to measure the relative motion of the body and the waves. Due to the test set up in the global axis system as shown in the same figure, the roll motion in beam sea will correspond to the pitch motion

in head sea. The parabolic beach in the tank is acting as a damper for the waves, and the waves are made by a piston wave maker.

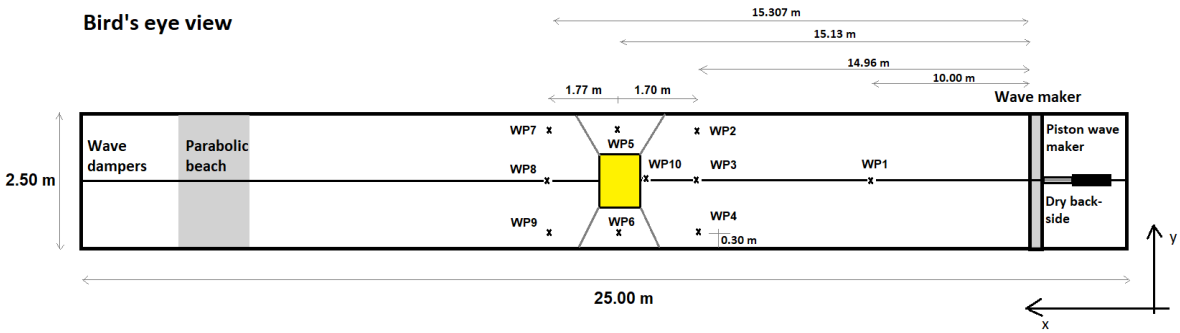

Figure 4.4: Test set up viewed from the top

A side view of the test set up is shown in figure 4.5. The tank is filled up to the deepest water depth possible and was taken to be $0.7m$. However, the water depth is not constant at all time due to the small leakage behind the piston wave maker. There is a pump which pumps the water from the leakage behind the wave maker, which keeps the water depth approximately the same level.

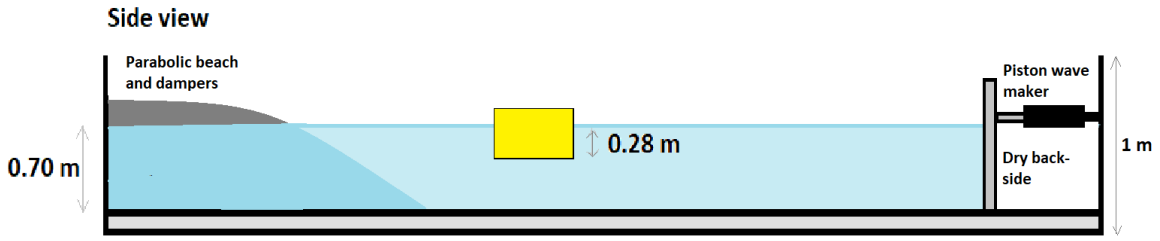

Figure 4.5: Side view of test set up

The full scale water depth is supposed to be infinite. This cannot be achieved with the current scaling factor. Therefore, the finite water depth analysis in the numerical simulation is considered. In the experiments, some modifications are made. This is done under the supervision of professor Trygve Kristiansen. The parabolic beach is raised higher at later stage in the experiment in order to damp out the incoming waves and prevent reflection. The beach is raised to a level as shown in figure 4.5.

4.3.2 *April* tests

The test set up for the second experiment has different arrangement for the wave probes in the tank. The model used is the same, and the arrangement of the accelerometers on the main deck is not altered. The main difference is the arrangement of the wave probes in the tank and on the main deck. Three wave probes are attached to the model as shown in figure 4.7a in order to measure the wave profile when the waves hit the plate. The arrangement of the wave probes placed in the tank is shown in figure 4.6.

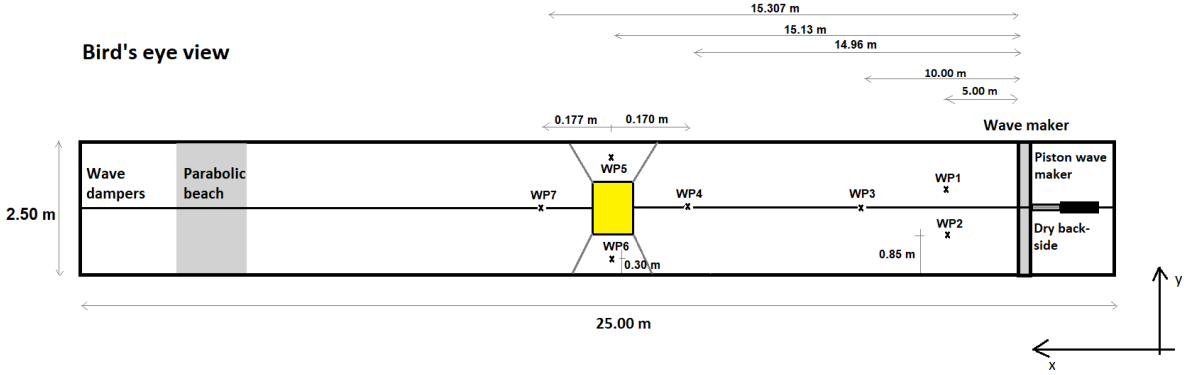

Figure 4.6: Test set up viewed from the top during second lab visit

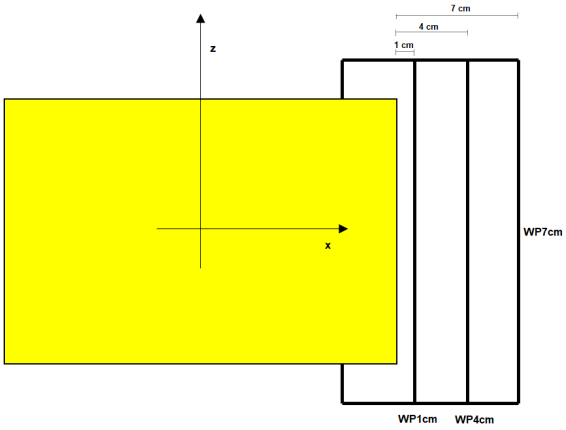

(a) Arrangement of the wave probes viewed from the side without the side deck

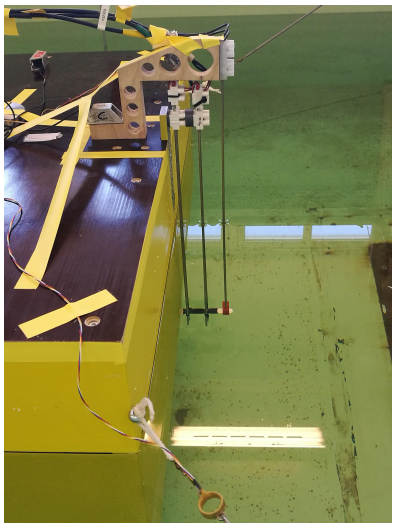

(b) Snapshot of the three wave probes attached to the model

Figure 4.7: Model mounted with three wave probes instead of the side deck

As mentioned, there are significant reflections from the experiment carried out in *January*. In order to obtain proper measurements of the waves, a few wave probes have been subjected in the tank without model. The same wave series have been used for testing the model and the deck slamming afterwards. The procedure of the second experiment is described as following:

1. Wave probes 1 to 4 are used to measure the wave elevation of undisturbed waves without body in the tank

2. The body is placed in the tank, but the deck is not mounted on the hull. Instead, three wave probes are mounted on the model

3. The deck is mounted on the body with one wave probe

4.4 Test matrix

The test matrices used in the experiments are made by a *MATLAB* script called *generateRegular.m* created by professor Trygve Kristiansen. The script gives the output data file in binary that the wave maker uses to make the desired waves. The main focus of the tests is different for the two experiments. The first test focused more on different wave steepness, and less wave periods are tested. In the second experiment, more wave periods are tested with less wave steepness.

4.4.1 *January* tests

The input for the test matrix of first laboratory work is presented in table 4.4. It shows the input for the *MATLAB* scripts to generate the data file for the test with a sampling frequency of $200Hz$. The input show that the wave amplitude is ramped up to full amplitude in 5 periods. Between two wave tests, there is a 240 second pause in order for the water to calm down.

Table 4.4: Test matrix inputs for test series *200* and *7000*

Test serie	T_{min}	T_{max}	T_{step}	$Steep_{min}$	$Steep_{max}$	$Steep_{step}$	water depth	n_{period}	n_{ramp}	t_{zero}
200	6	13	1	40	15	1	17.5	60	5	240
7000	5	13	0.5	60	24	18	17.5	60	5	240

In order to capture the slamming forces in more detail, two test series are conducted with a sample frequency of $1200Hz$. The results of the two test series are merged together in post-processing. The input data for the two series are presented in table 4.5.

Table 4.5: Test matrix inputs for test series *80000* and *90000*

Test series	T_{min}	T_{max}	T_{step}	$Steep_{min}$	$Steep_{max}$	$Steep_{step}$	water depth	n_{period}	n_{ramp}	t_{zero}
80000	6	8	1	30	15	3	17.5	60	5	240
90000	8	11	1	30	15	3	17.5	60	5	240

4.4.2 *April* tests

The input data for test series used in the second experiment are presented in table 4.6, where the data are all sampled with a sampling frequency of $200Hz$. More periods with smaller step size are tested with short pause time.

Table 4.6: Test matrix for second laboratory visit

Test series	T_{min}	T_{max}	T_{step}	$Steep_{min}$	$Steep_{max}$	$Steep_{step}$	water depth	n_{period}	n_{ramp}	t_{zero}
401003	3	15	0.5	50	50	1	17.5	60	5	120
4090011	2	15	0.2	40	40	1	17.5	60	5	120
4012003	3	10	0.2	60	30	10	17.5	60	5	120
4012002	5	10	0.2	26	22	2	17.5	60	5	120

4.5 Analysis procedures

The procedure for processing the measured data is very important. The measured test data from the test equipment are discrete numbers. The data are recorded and sampled at an equal interval of time. The sampling frequency must be sufficiently to capture all variations of the measured quantity. However, too high sampling frequency will give too much data which is a challenge to the digital memory. On the other hand, too low sampling frequency may give poor resolution in the measured data. This is illustrated in figure 4.8.

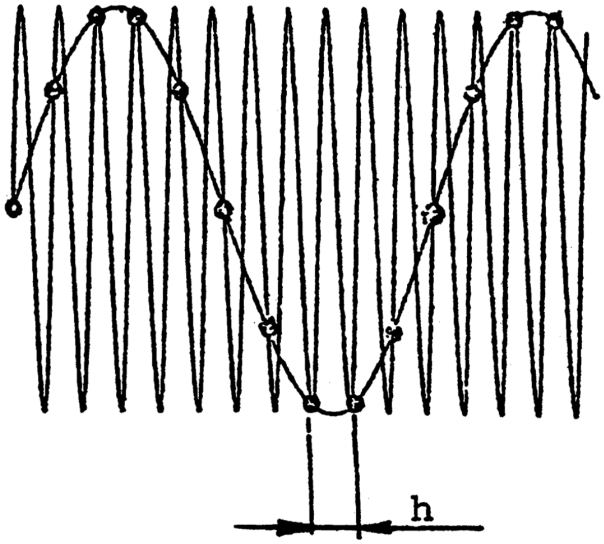

Figure 4.8: Example where the sampling frequency is too low and capture the wrong picture of the observed data illustrated from [Steen, 2014]

According to [Steen, 2014], it is necessary to at least have two samples per wave period in order to properly represent the wave in the digitized data, and more samples per period is necessary to capture a good representation. If the signals are sampled less than two times per wave period, it will give false representations as shown in figure 4.8. The default sampling frequency during the experiments is taken as $200Hz$. This sampling frequency is good enough to have a proper measurement for the global motion of the body. However, the slamming is a phenomenon that occurs in a very short time duration, which requires higher sampling frequency. Thus, a few tests with a sampling frequency up to $1200Hz$ are conducted.

As mentioned in Chapter 4.4, wave amplitude is ramped up in 5 oscillations. The measured data in the transient phase should not be taken into account. Figure 4.9 shows the data of a selected time series window that are used in the post-processing of the measured data.

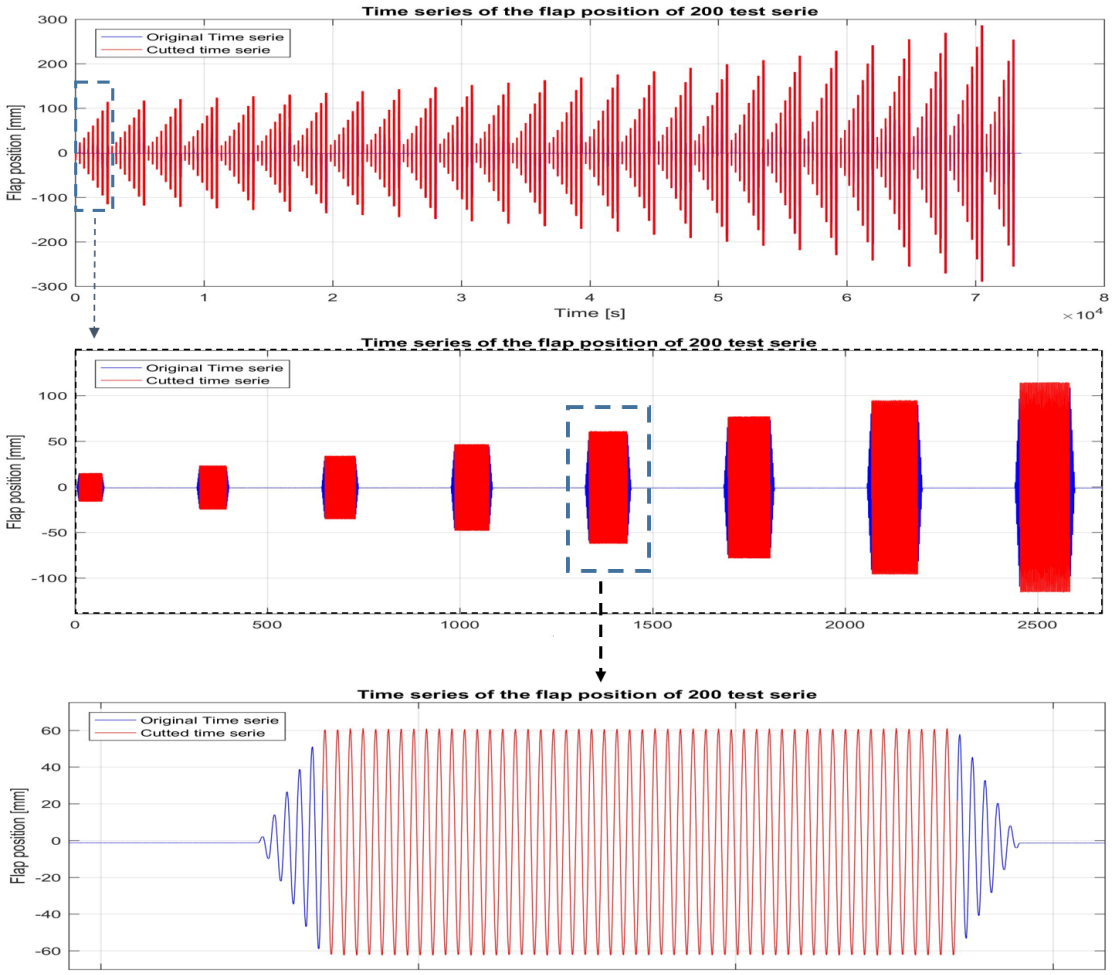

Figure 4.9: Selected time series window for the steady state data of the flap motion for the piston wave maker. The red lines are the selected time series, and blue line are the original recorded time series

The quantity shown in figure 4.9 is the flap position of the piston wave maker. This is used as a reference for selecting the relevant time series window for other quantities. The waves will take some time to reach the wave probes and the model that are placed in the tank. Therefore, the distance and the group velocity of the incoming waves must be calculated, and thus the time for the waves to reach the different equipment can be obtained.

4.5.1 Accelerometers

The sign of the accelerometers must be checked in order to interpret the measured data. This can be determined from a decay test in pitch. The accelerometers are supposed to measure a positive acceleration upwards and the component is shown in figure 4.10 along with the definition of the local axis system that is defined for the analysis. The accelerometer will not measure any gravitation acceleration after the zero setting. This means that the only recorded measurement is the vertical acceleration.

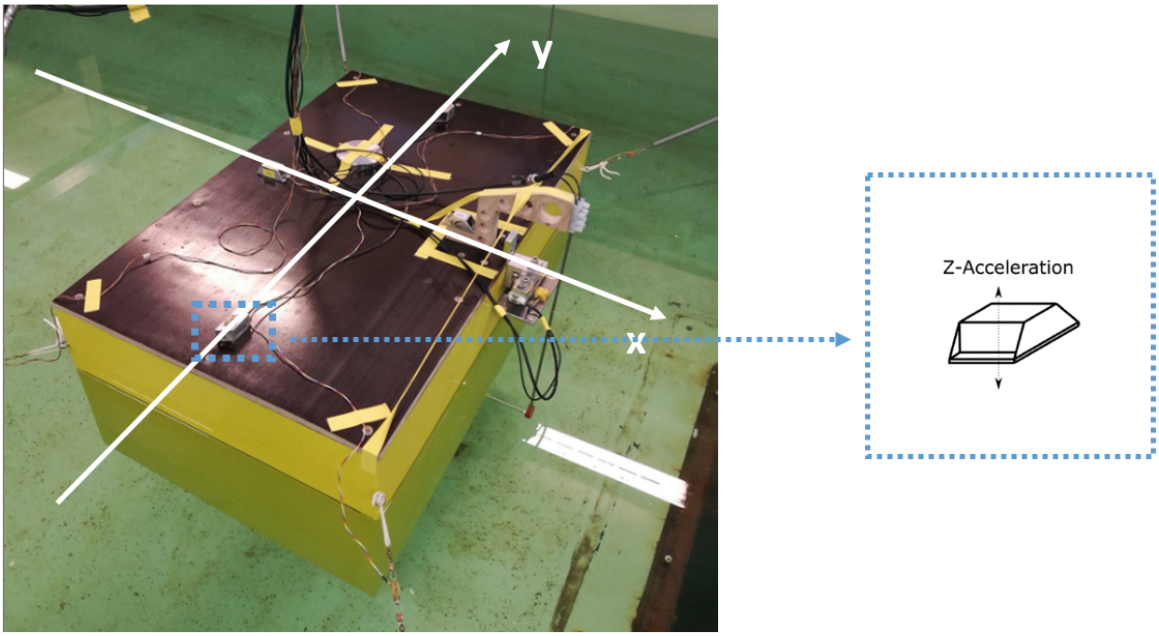

Figure 4.10: Model with local axis system and the accelerometer

In the decay test, all measured data from the four accelerometers are plotted in figure 4.11. It shows that the horizontal accelerometers have similar measurements. This is expected as the horizontal accelerometers are located at symmetric locations. For the accelerometers used to measure vertical accelerations, they should measure same value but with opposite signs. When the body is inclined, the horizontal accelerometers will measure the contribution of the gravity acceleration. This can be verified by taking an initial pitch angle for the decay test.

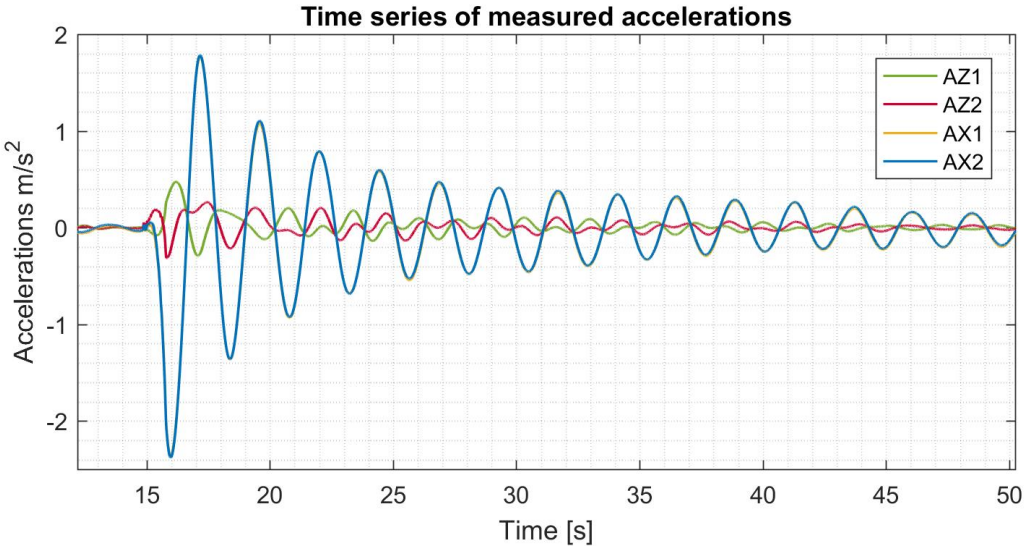

Figure 4.11: Time series of the accelerations during the pitch decay test

The inclination angle during the decay test was approximately 15 degrees. This gives a measured horizontal acceleration as expected as $AX1 = AX2 = g\sin(15)$, which is $2.53m/s^2$. If it is assumed that the positive pitch angle is counter clockwise as shown in

figure 4.12, the accelerometer that measures the vertical acceleration at the right hand side should measure a positive acceleration and the opposite with approximately same value for the accelerometer on the left. Furthermore, the accelerometer that measure the horizontal acceleration should both measure a negative value that is approximately $2.53 m/s^2$. This is proved to be correct in the time series of the pitch decay test.

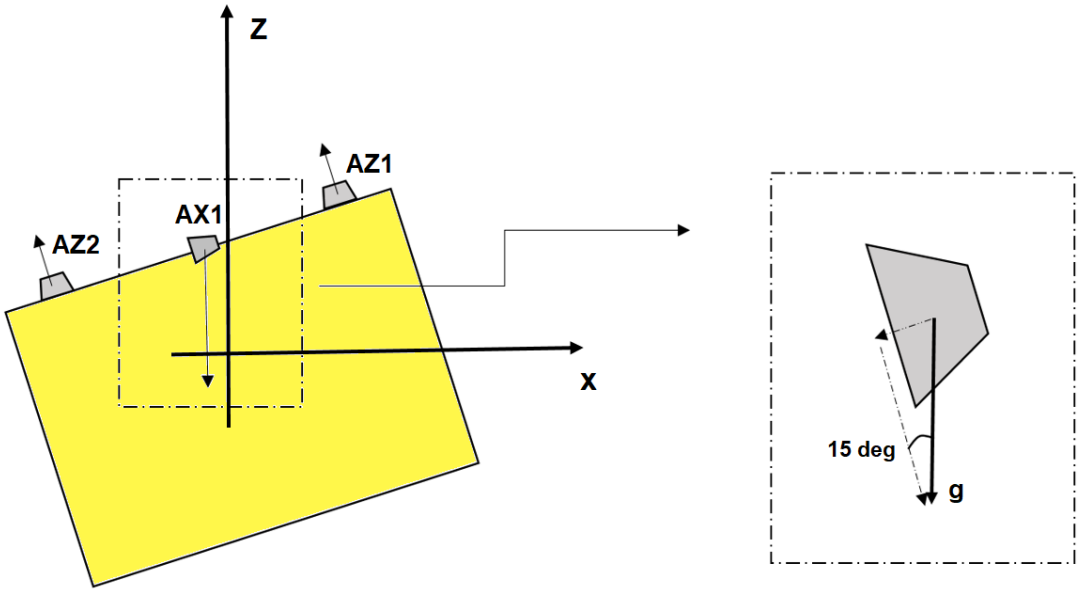

Figure 4.12: Illustration of the measured accelerations on the model during a pitch decay test according to the local axis system

4.5.2 Mooring line pretension

As mentioned in Chapter 3.1.2, mooring lines in the numerical model which represent the springs in the experiments will affect the global motions. This is because surge motion and pitch motion are coupled. During the test set up in *January*, the pretension of the mooring lines is set to be approximately equal to each other in order for the model to stay at the symmetry plane. The values of the pretension and the spring stiffness of the four springs are listed in table 4.7 for the tests conducted during *January*.

Table 4.7: Pretension of the springs and the spring stiffness during experiments in *January*

Mooring line no.	H	Mooring line no.	H
1	3.0797 N	3	3.3547 N
4	3.4036 N	2	3.1939 N
Average pretension			
3.258 [N]			
Spring stiffness			
28 [N/m]			

From the experiences of the first experiment in *January*, it is observed that the pretension is too small as the spring went slack for large and steep waves. This causes a drift force

as the model is pushed backwards. In order to prevent this in the second experiment in *April*, the pretensions are changed to largest possible value which are listed in table 4.8. The pretension used in the numerical simulations is the average value of the pretensions in this table.

Table 4.8: Pretension of the springs during experiments in *April*

Mooring line no.	H	Mooring line no.	H
1	4.8 N	3	5.6 N
4	4.6 N	2	5.1 N
Average pretension			
5.025 [N]			

4.5.3 Filtering

Before filtering, the data has to be cleaned in order to remove sample points that are measured incorrectly. According to lecture notes by [Chabaud, 2015], missing data points can occur of a test series with a long duration, and this will affect the results even if the mean value is small. The script for data cleaning is based on the linear interpolation between the sampling points after the outliers are removed.

During the experiments, there will be some unwanted noise and interference that will be recorded and captured by the sensors. It is then necessary to post-process the data and filter out the unnecessary measurements. This is also relevant to filter away the second order effect for the analysis of the linear wave theory. In addition, the reflected waves will disturb the incident waves from the wave maker. The filter used in this case is a band pass filter where the low and high frequency limit must be specified.

The time series for the waves must be corrected with the group velocity since the wave probes are placed some distance away from the wave maker. The consequence of this is that the time series window will be delayed than the time series window measured for the wave flap. Figure 4.13 shows the time series for the data measured in wave probe 3 during the tests in *January*. The correct time interval is taken as the group velocity divided by the distance of the selected wave probe from the wave flap. In the same figure, it shows that the transient phase is cut out from the selected time interval at the start of the time series. As a result, only the steady state time series are selected for the post processing.

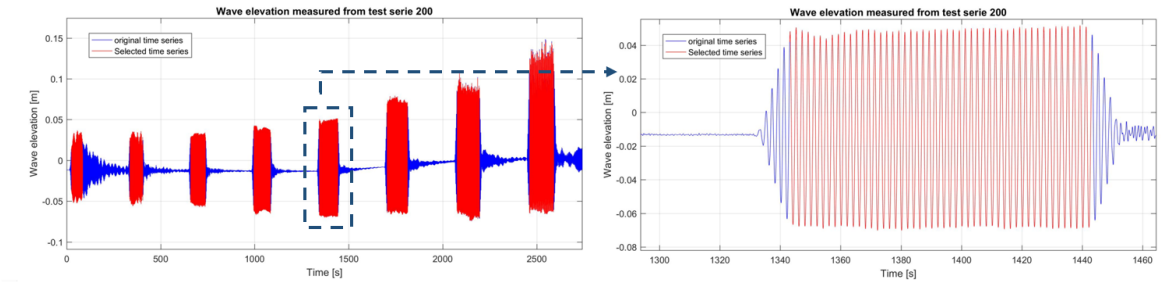

Figure 4.13: Selected time series of the measured waves during experiments in *January*. The red lines are the selected time series window, and the blue lines are the originally recorded data

Figure 4.13 shows that the water level is not constant. However, this will not affect the body motions, as the structure is freely floating in the water. The band pass filter used in the data analysis is a *MATLAB* script called *bpass2.m* made by professor Trygve Kristiansen. This filter is applied to the selected time series window. The frequency of interest is the same frequency of the incoming waves, because most of its energy will be concentrated here. An illustration of the filtering is shown in figure 4.14 for a wave with a period of 2 seconds. As the result of the band pass filter, the power spectrum density plot shows that the relevant data that have been in the filtering range are concentrated at a frequency of $0.5Hz$ with $\pm$ $0.2Hz$ for a wave with period of $2s$ in model scale.

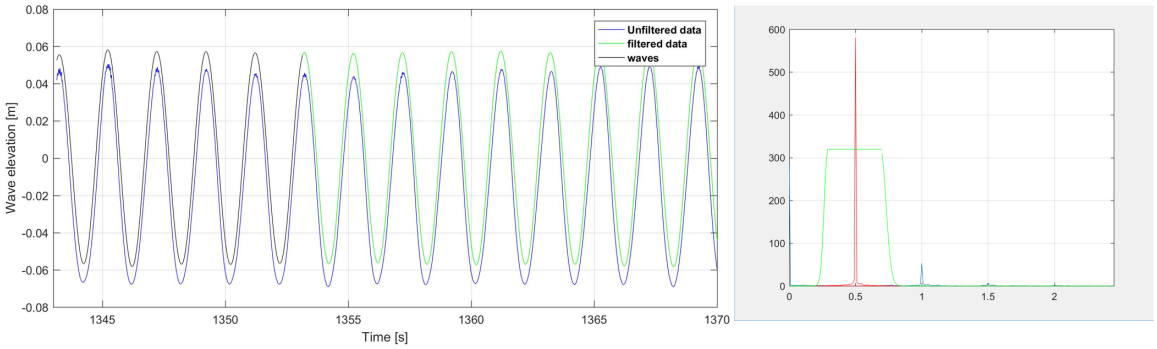

Figure 4.14: Illustrating of the filtering process of the experimental data. PSD plot on the right with the green line as the band pass filter window, red line as the filtered signal and blue as the unfiltered signal from tests conducted in *January*

In figure 4.14, it is shown in the time series that 5 oscillations from the selected time interval are selected and plotted in black. This is the selected time window for the waves that are used for calculation of the response amplitude operator (RAO). Due to the large disturbance from the model, it is necessary to only select the first 5 oscillations from the wave elevation time series.

4.5.4 Converting measured quantities

As mentioned, the measured quantities related to the body motions are the accelerations. In order to obtain the motions of the model, it is necessary to integrate the measured accelerations into the motions. This is done by another *MATLAB* code written by Professor Trygve Kristiansen, called *acc2pos.m*, where the sampled data of the acceleration are integrated to the corresponding motions. The method used is the Fourier transform. In order to obtain the results for the pitch motion, the data are obtained from the difference of the measured vertical accelerations. According to [Mukhlas, 2017], the pitch motion about the center of the gravity can be as expressed in equation 4.2.

$$\ddot{\eta_5} = \frac{\ddot{\eta_{3,1}} - \ddot{\eta_{3,2}}}{L_{acc}} \tag{4.2}$$

The positive of the pitch motion is defined as in figure 4.15. L_{acc} is the length between the centers of the accelerometers which measure the vertical acceleration of the body.

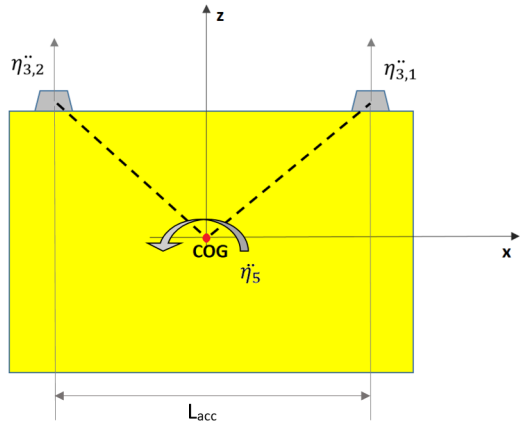

Figure 4.15: Definition of the positive pitch and the measured accelerations

For heave motion, the results are obtained by considering the average of the measured vertical acceleration. Thus the heave and pitch motion can be compared with the results obtained from *WADAM* which is calculated from the reference point at the center of gravity.

However, for surge, the local horizontal acceleration is measured in the experiment. The surge motion is coupled with pitch, and it will be different depending on reference. In order to compare the results with the numerical calculation with the reference point at the mass center, the data measured from the experiments must be adjusted. Equation 4.3 shows the formula used for this adjustment, where $\eta_{1,local}$, $\eta_{5,meas}$ and $\eta_{1,meas}$ are the local surge motion, measured pitch angle and measured surge motion respectively. The overdots represent the time derivative of the parameters. The basis of the adjustment is illustrated in figure 4.16. Furthermore, the horizontal accelerometers will measure the contribution of the gravity acceleration as mentioned in Chapter 4.5.1. This must be considered by subtracting the product of the gravitational acceleration and the corresponding pitch angle from the measured horizontal accelerations. Second part of equation 4.3 shows the horizontal acceleration before the integration takes place.

$$\eta_1 = \eta_{1,local} - 0.21\eta_{5,meas} \qquad \text{and} \qquad \ddot{\eta}_{1,local} = \ddot{\eta}_{1,meas} - g\eta_{5,meas} \tag{4.3}$$

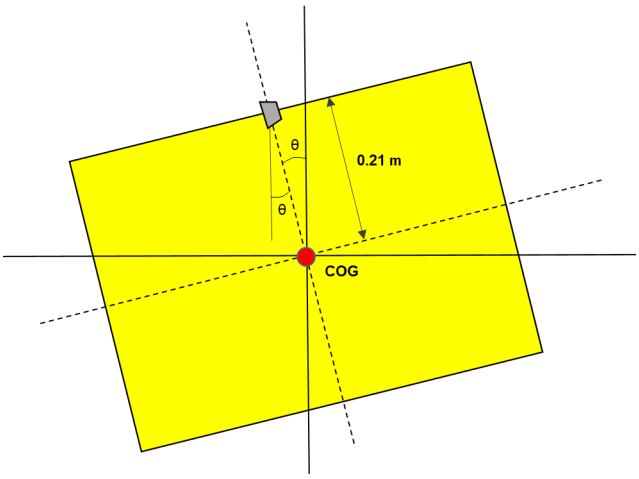

Figure 4.16: Body with a pitch angle θ adjusted for surge motion

4.5.5 Motion response amplitude operator

The response amplitude operator (RAO) for surge, heave and pitch are calculated from the measured data obtained from the experiments. The concept of RAO is introduced in Chapter 2.3, by using the relationship between the input and output signal. In [Steen, 2017], it is recommended that the standard deviation for a regular wave test should be used to quantify the oscillation amplitudes. If the maximum and minimum values for the measured peaks are used instead, it will be considered as the instantaneous response. Therefore, the standard deviations of the results for the motions and the undisturbed incoming waves are used for representation of RAO.

The pitch RAO calculated from *WADAM* is normalized. This is done by taking the pitch amplitude in radians and dividing it by the wave number k. A sinusoidal wave can be defined as a function of wave elevation expressed by $\zeta = \zeta_a \sin(\omega t - kx)$. Thus, the slope of the wave elevation is mathematically $k\zeta_a$ by differentiation of the function. Normalization of the pitch response from the experiments can be done in a similar manner. By taking the measured pitch amplitude divided by the product of the corresponding wave steepness and π, the pitch motion is normalized. Since the wave height is the same as the twice of the wave amplitude, the product of the wave steepness and π is same as the slope $k\zeta_a$ from the differentiation of the wave elevation function. Heave and surge RAOs obtained from the experiments will be presented in the same manner as the *WADAM* calculated RAOs.

4.5.6 Slamming forces

Based on the water entry analysis presented in Chapter 2.8.1, the slamming force obtained from the experiments are compared with the results in figure 2.7 for Wagner solutions. By using the equations, the expression of the vertical force at a given deadrise angle can be given as following:

$$F_3 = \frac{A\rho V^3 t}{\tan^2 \beta} \tag{4.4}$$

Where A is the factor presented in y-axis in figure 2.7 for wedge structure with different deadrise angles. The deadrise angle can be estimated from the experiments for different periods, and the time must be defined. This can be done by studying the local wave profile during the impact. A sketch of the plate during the impact is shown in figure 4.17.

The time expression can be expressed as in equation 4.5 based on the body geometry from figure 4.17. This can be explained by assuming that time variable t can be expressed as $t = t_1 - t_0$, where t_0 is the time when the plate is dry and and t_1 is the time when the body is wetted.

$$t_1 = \frac{l_{plate} \tan \beta}{V} + t_0 \tag{4.5}$$

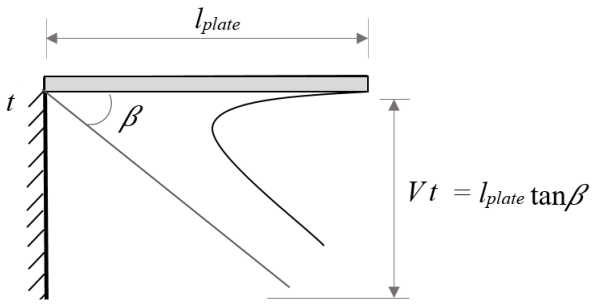

Figure 4.17: Local analysis of the impact. The plate is viewed from the side. β is the angle between the water and the plate during the impact, l_{plate} is the plate width, V is the local vertical velocity, and t is the time during the impact

5 Results and discussion

In numerical estimations, the peak in heave and pitch response in the response amplitude operator appear at $T = 7s$ and $13s$ respectively. From the results obtained from the experimental work, the RAO is in good agreement with the results obtained from *WADAM* with respect to the natural periods.

In this chapter, results from the experiments and *WADAM* are compared, and the wave heights estimated from the linear wave theory are compared with the waves measured from the experiments. Discussions about the time series and the slamming forces are followed.

5.1 Experimental results and discussion

The results from the experiments are presented in this chapter, where they are post-processed with the methods presented in previous chapters.

5.1.1 Decay tests

Before the model is exposed to the incoming waves, it is important to obtain the natural periods of the system. Decay tests are carried out for all six motions, and the plate that is mounted on the barge is also tested by hitting it gently with a hammer. The decay test can give useful information about the natural frequencies, added mass and the damping of a dynamic system according to [Steen, 2014].

Motions

The results of the natural periods in all six motions are listed in table 5.1 for the experiments that are conducted in *January*. The natural periods are obtained by converting the decay test time series into a power spectrum density (PSD) function by using the fast Fourier transformation. The plot of the PSD shows at least one peak, which gives the natural frequency. The result of a plotted PSD with the corresponding time series of the pitch decay test is shown in figure 5.1. The rest of the results from decay tests can be found in Appendix B.1.

Table 5.1: Result of the decay test in model and full scale from tests in *January*

Motion	η_1	η_2	η_3	η_4	η_5	η_6
Natural period in model scale	15.57 s	15.77 s	1.59 s	1.41 s	2.50s	6.49 s
Natural period in full scale	77.85 s	78.85 s	7.95 s	7.05 s	12.50 s	32.45 s

The decay test results for the second experiment with a model mounted with three wave probes, and with the deck are shown in table 5.2. It can be seen that the two results are slightly different. This is because the deck that is mounted on the model contributes an additional weight which changes the mass property.

In the set up shown in Chapter 4.3, the only accelerometers that measures the horizontal acceleration are in surge direction. In order to obtain the time series and the decay test results in sway direction, the measured spring forces are used instead. The time series in sway are shown in Appendix B.1, and they are obtained by utilizing the simple mass-spring relation.

Table 5.2: Result of the decay test in model and full scale from the laboratory experiments in *April*

		η_1	η_2	η_3	η_4	η_5	η_6
Model without deck	Model scale	19.45 s	14.48 s	1.54 s	1.39 s	2.33 s	5.47 s
	Full scale	97.25 s	72.40 s	7.70 s	6.95 s	11.65 s	27.35 s
Model with deck	Model scale	19.60 s	13.75 s	1.52 s	1.41 s	2.41 s	5.60 s
	Full scale	98.00 s	68.75 s	7.6 s	7.05 s	12.05 s	28.00 s

The damping can be estimated by using the method in Chapter 2.6.1. The linear damping can be calculated from the decay test time series. The damping ratio can be estimated by using equation 2.18, and the results for the linear damping are listed in table 5.3 for all six motions. It should be noted that the linear damping listed in table 5.3 is the average damping in 5 oscillations (n = 5). This will be different from the damping ratio estimated by using the method in Chapter 2.6.2. The analytic method for damping estimating will give the damping related to the resonance area. From the results for pitch motion calculated from *WADAM*, it is observed that the pitch RAO without external additional damping has a peak up to 120 degrees, which is too large to perform in the decay test. Therefore, it is not possible to estimate the corresponding damping at the resonance area from the decay test.

Table 5.3: Linear damping from the decay test in model and full scale, averaged by taking 5 oscillations ($n = 5$) from the time series

	η_1	η_2	η_3	η_4	η_5	η_6
January test with deck	0.1137	0.0655	0.01916	0.0132	0.047	0.07177
April test with deck	0.076	0.06	0.019	0.01813	0.029	0.0529
April test without deck	0.1009	0.0799	0.0217	0.01842	0.0363	0.0727

However, the exact damping can be estimated from the decay test for specific amplitudes. Assume a case where the amplitude of the pitch motion is 5 degrees from the potential solver. The decay test from the experiments gives a time series of the pitch motion as

shown in figure 5.1. Then, the total damping for pitch with an amplitude of 5 degrees can be estimated from equation 2.18. The two amplitudes that are taken into the calculations are the ones that are closest to 5 degrees, and $n = 1$ for one oscillation. The estimated damping ratio is 9.23%. This is very different if a pitch amplitude of 3 degrees is considered, where the estimated damping ratio is 4.9%.

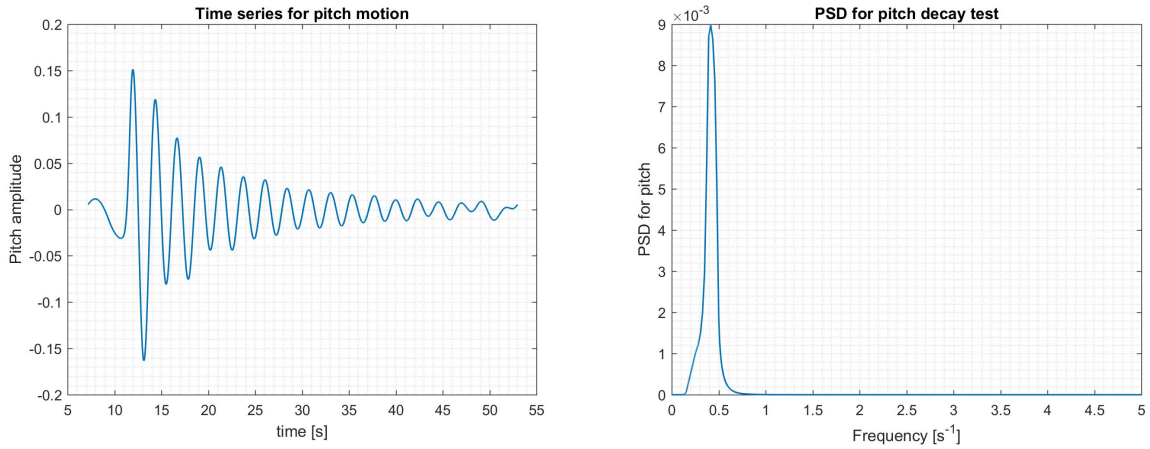

Figure 5.1: Time series and the power spectrum of a pitch decay test with side deck mounted performed in *April*

Another possible method to calculate the damping is to use the model for nonlinear damping. According to [Steen, 2014], one should avoid using the results from the first oscillation and the last oscillations from the time series of the decay test. This is due to to the transient effects for the first few oscillations, and questionable accuracy for the small amplitudes. The nonlinear damping is obtained by plotting the logarithmic decrements of the peaks as expressed in equation 2.18 against the mean amplitude of two successive amplitudes. The results of the nonlinear damping in pitch motion are shown in figure 5.2. The damping coefficients obtained from the corresponding figure is 0.47 and 0.017 for nonlinear and linear damping coefficient respectively.

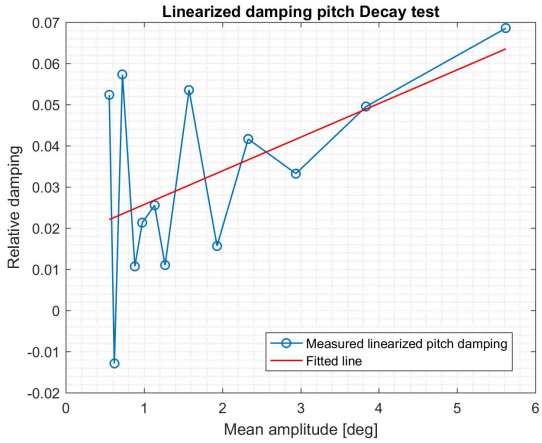

Figure 5.2: Measured damping in pitch decay test using linearized damping equation for a model with the side deck mounted. Pitch angle is given in degrees

The plate

In order to find the natural period of the platform, a pluck test is performed five times for both the perforated and solid plate. The procedure for finding the natural period is same as for the global motions. The results are shown in table 5.4, and the time series and the corresponding power spectrum density (PSD) plot are shown in figure 5.3 for the first test with the solid plate.

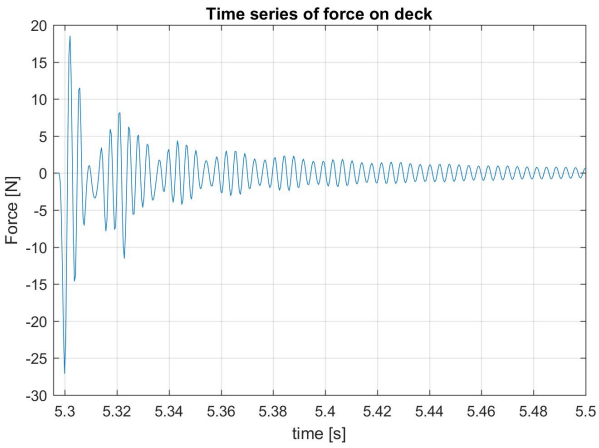

(a) Time series for pluck test no. 1

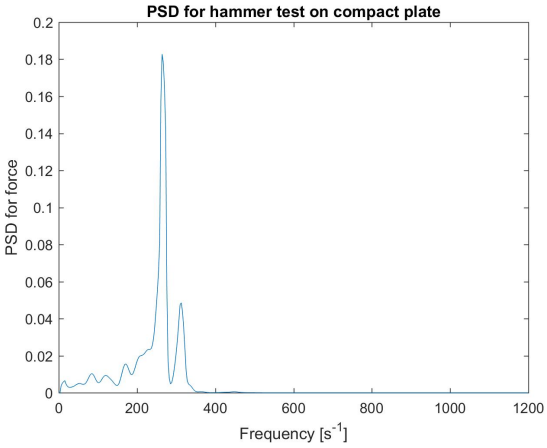

(b) Power spectrum density of the plutck test no. 1

Figure 5.3: Pluck test results for test no. 1 for a solid plate

As the PSD plot in figure 5.3 shows, there are two large peaks. The second peak may possibly be due to a different modal motion. When the hammer hits the deck, it might not be exactly in the middle of the plate. This can trigger other vibrations that are not from the plate center. The decay test is repeated five times in order to have reliability of the results. All plots of the power spectrum density and the time series can be found in Appendix B.2.

Table 5.4: Natural frequencies for solid and perforated plate of same dimensions obtained from the pluck test

		Test no.				
Plate type		**1**	**2**	**3**	**4**	**5**
Solid plate	**1st peak**	263.9 Hz	266.0 Hz	279.0 Hz	268.2 Hz	266.4 Hz
	2nd peak	313.0 Hz	314.0 Hz	N/A	320.4 Hz	316.5 Hz
Perforated plate	**1st peak**	268.7 Hz	271.2 Hz	271.5 Hz	267.4 Hz	272.2 Hz
	2nd peak	324.8 Hz	323.1 Hz	337.8 Hz	307.7 Hz	324.1 Hz

The natural frequency obtained from the pluck test is considered as the natural frequency of the plate where the force sensor is mounted. This is useful with respect to the measured slamming forces to filter out the system oscillations which are not the actual responses of the structure.

5.1.2 Measured waves

The measured waves in experiments are compared with the estimated wave height. The calculated waves are linear waves in finite water depth. The test results from the experiment in *January* are shown in figure 5.4. The measured results are obtained by taking first five oscillations after the transient phase of the waves from wave probe 1 in test set up from *January*.

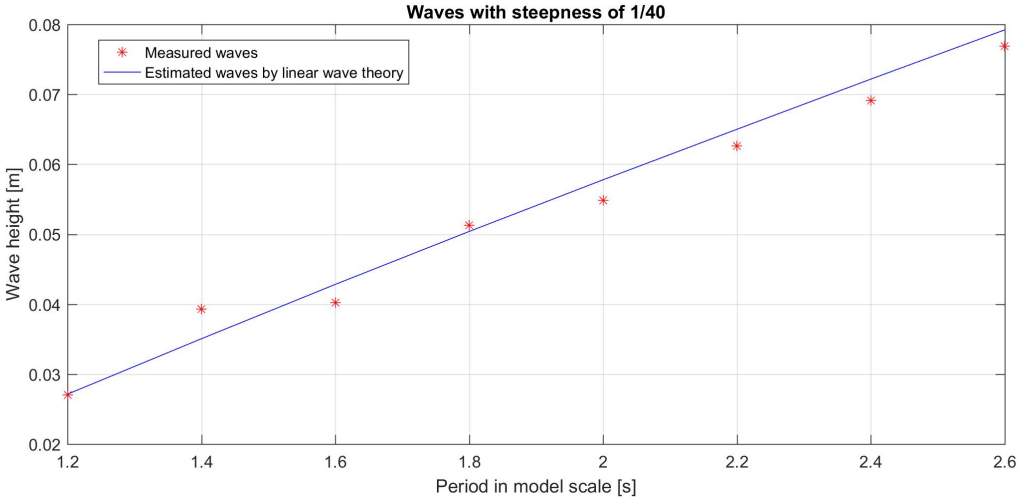

Figure 5.4: Measured wave height plotted against estimated wave height for a wave series with steepness 1/40. The wave height is measured when the model is present in the tank

The error is estimated to be about 10%. This might be due to the reflection of the parabolic beach in the towing tank. However, the error is expected to be greater as the wave steepness increases due to the validity of the linearization of the wave propagation theory, which is mentioned in Appendix A.3. With increased wave steepness, the second order effect becomes more important, and thus the waves described by the linear wave theory gives larger deviations. The error of the measured waves from each period and the analytically calculated wave height for wave steepness of 1/40 can be found in table 5.5.

Table 5.5: Relative error of all waves with steepness 1/40 in test series *200* from *January* by using linear wave theory with the model present in the tank

Wave period [s]	Absolute error [%]
1.2	7.99
1.4	8.44
1.6	6.45
1.8	2.89
2.0	1.44
2.2	0.65
2.4	1.54
2.8	0.92

The group velocity and phase velocity are calculated based on the linear wave theory for finite water depth. The measured waves from the experiments conducted in *April* without

the model show a better agreement with the linear wave theory with an error less than 2.3%. This small error may be due to the leakage of the piston wave maker behind the tank. The plot of the measured waves and the estimated waves from test series in *April* is shown in figure 5.5.

Figure 5.5 shows that there are larger deviations at the longer wave periods. This may possibly be due to the reflection from the parabolic beach at the end of the tank. For large and long waves, there are more reflections from the beach. Therefore, it is better to utilize the test results of period below $12s$ in full scale. In this region, heave and pitch have the natural frequencies where the slamming on the deck occurs.

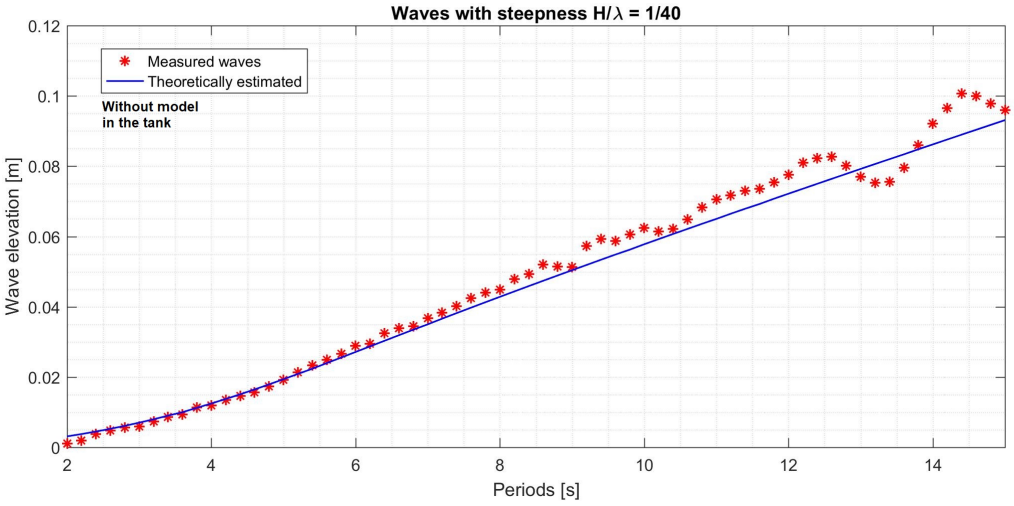

Figure 5.5: Measured waves with steepness 1/40 from test series *4090011* without the model in the tank, plotted against the linear wave theory for finite water depth. Dots are the measured data, the solid line is the theoretically results

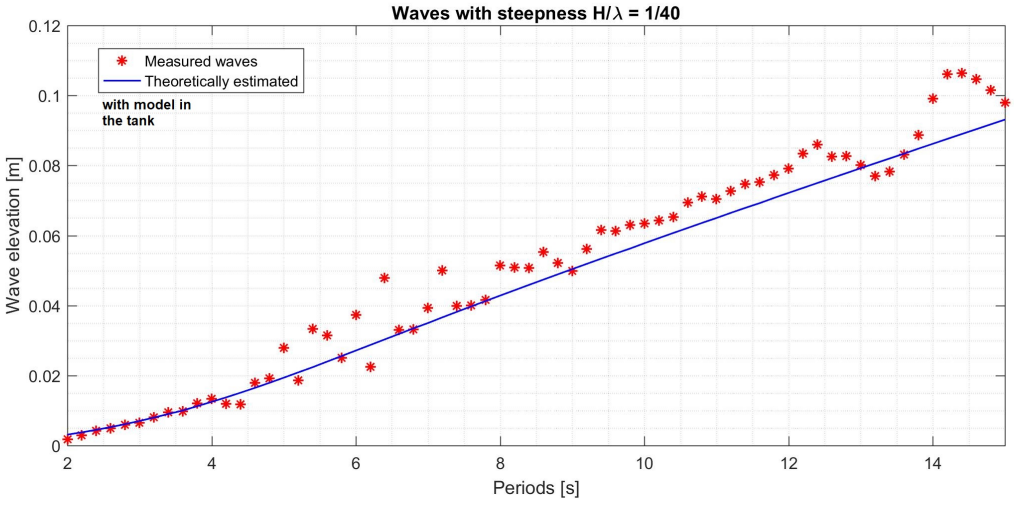

Figure 5.6: Measured wave elevation with reflections when a model is present in the towing tank for the same test series as in figure 5.5

The reflection of the waves can be clearly observed when the model is present in the tank. This is shown in figure 5.6, where the measured waves deviate from the linear wave theory. The waves are tested with the same test series as in figure 5.5, and the deviations are large from $T = 5s$ up to $T = 9s$. This is due to the large body motions within these periods.

From the decay tests, it is seen that heave resonance is 7.6s and pitch is at 12.05s in full scale. It should be noted that parametric pitch occurs approximately at $T = 6.025s$ which also increases reflections that disturb the incoming waves.

5.1.3 Response Amplitude Operator

The response amplitude operator obtained by using the normalization method described in Chapter 4.5.5 for heave, surge and pitch for test no. *4012003* are shown in figures 5.7, 5.8 and 5.9 respectively. It can be seen that for larger wave steepness, the RAO will have lower value. A peak at $T = 6.2s$ from the experimental results can be seen, and it might be the consequences of parametric instability, which will be discussed later.

From a report on closed fish farms written by [Kristiansen et al., 2018], it is stated that the wall effects have most influence on heave motions. The results of the RAO in heave, surge and pitch show that pitch motion gives less influence than the other two motions. From figure 5.7 for heave RAO, it can be seen that the wall effects simulated in *WADAM* show a good agreement with the experimental results.

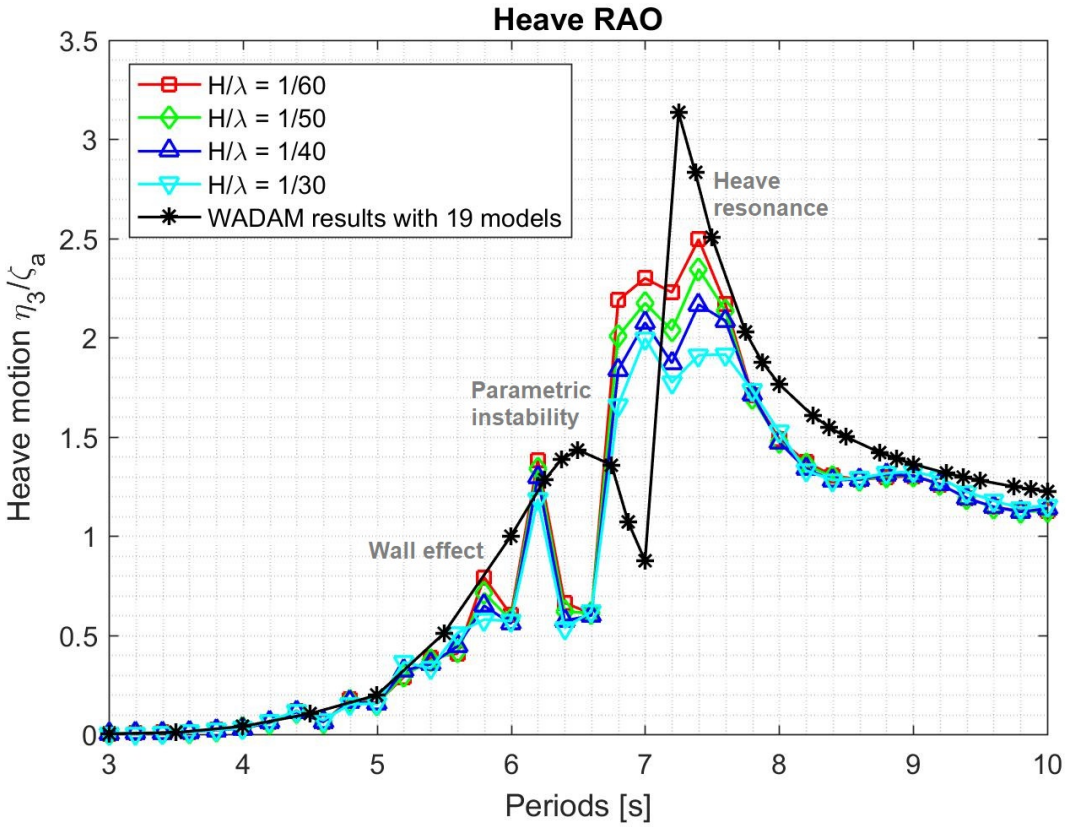

Figure 5.7: Heave RAO calculated from *WADAM* results with wall effects implemented by 19 bodies, plotted with wave steepness $H/\lambda = 1/60, 1/50, 1/40$ and $1/30$ from the experiments. Peak at $T = 6.2s$ can be due to parametric instability

The reason that heave motion is more influenced by the wall effects is because the water particles are prevented from moving outwards when the body is oscillating in heave. The wall from the towing tank prevents the water from moving, and reflects the radiated waves back to the model. This can cancel or amplify the heave motion.

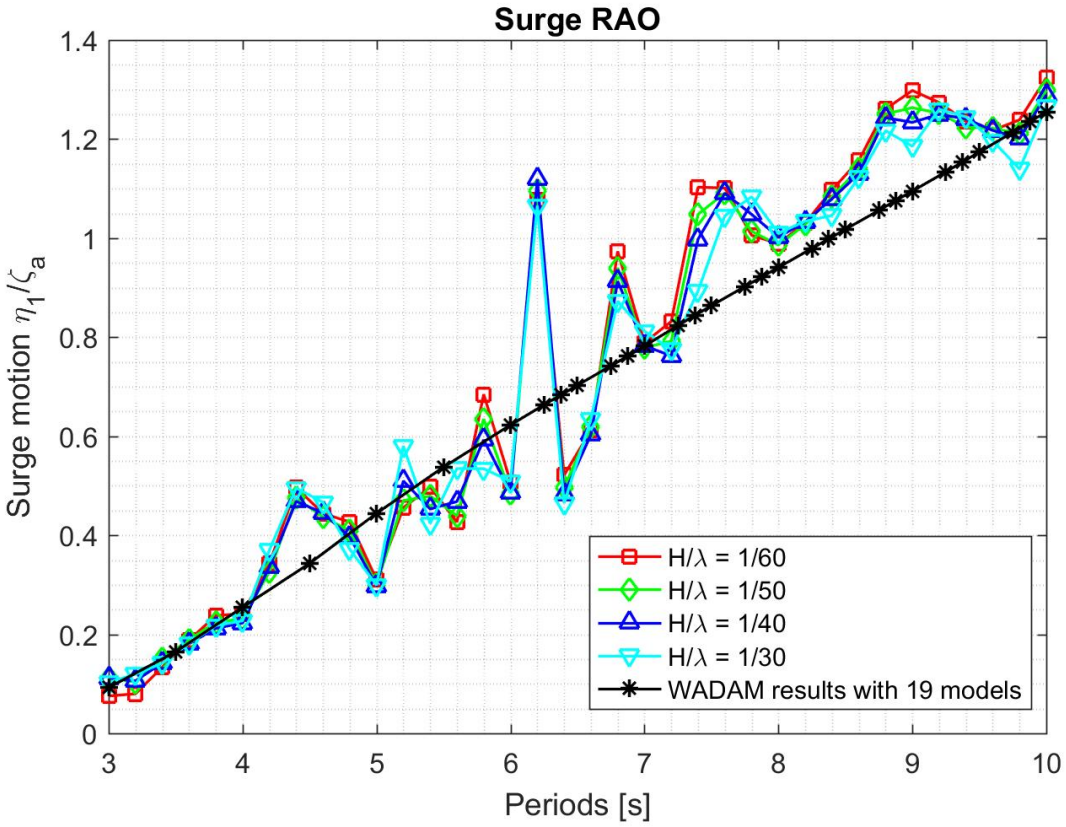

Figure 5.8: Surge RAO plotted with the results simulated from *WADAM*

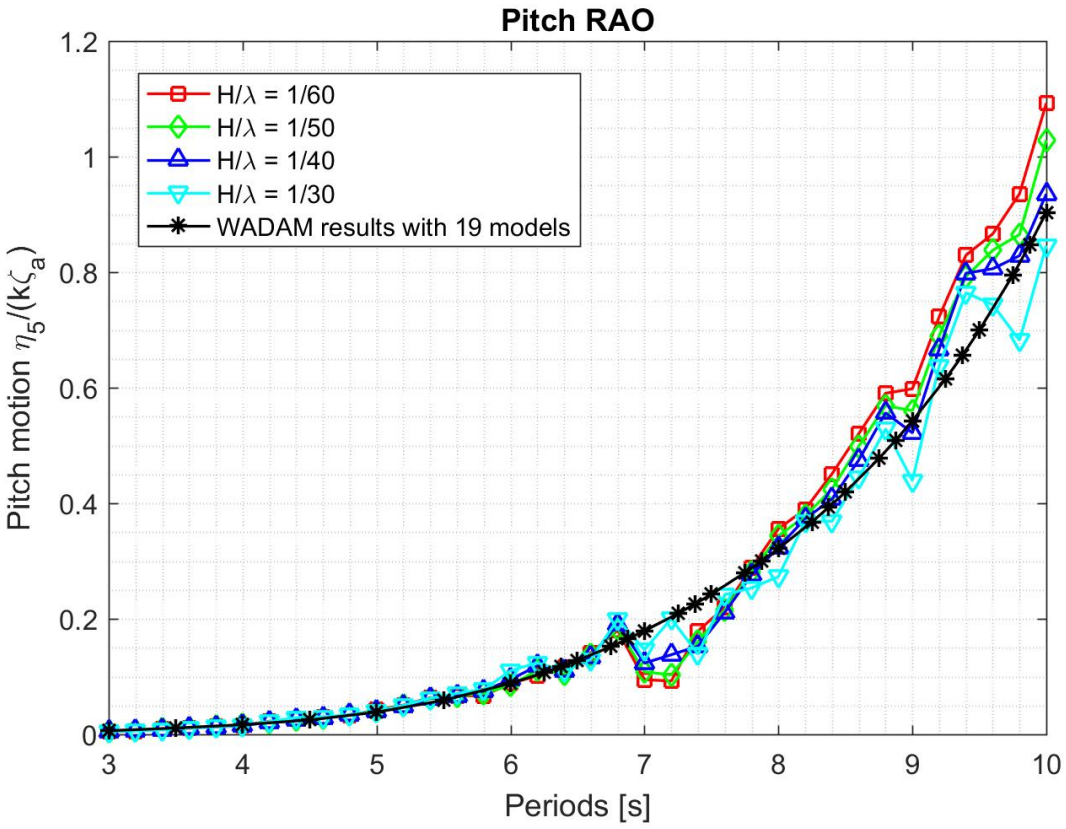

Figure 5.9: Normalized pitch RAO with different wave steepness plotted with *WADAM* results for 19 mirroring images where external damping is added

Figure 5.8 shows the surge motion RAOs for experiment and *WADAM* calculations. The lower periods show good agreement, but not for higher periods. This is possibly due to the coupling effect between surge, heave and pitch motions. The pitch response shows an agreement between the numerical and experimental results. In general, the results show a good agreement. At $T = 6.8s$, a peak appears from the experimental results in pitch RAO. This is possibly a result from the parametric instability as the natural period of pitch is at $T = 12.05s$. Furthermore, it can be seen that the pitch motion in the resonance region is heavily damped compared to the estimated damping. The estimated natural period for pitch is at $12.05s$ and $12.50s$ from the decay test, dependent if the model is mounted with the deck or not. Using the calculated RAO from test series *4090011* in figure 5.10, it can be seen that the pitch RAO from the experiments is lower than the *WADAM* results. This is possibly due to the viscous damping in the experiment. In addition, the method used for damping estimation from [Dhavalikar and Negi, 2009] stated that the results are more accurate for a structure with natural angular frequency near unity. In this case the pitch natural frequency is $2.60 rad/s$. Therefore, some deviations are expected.

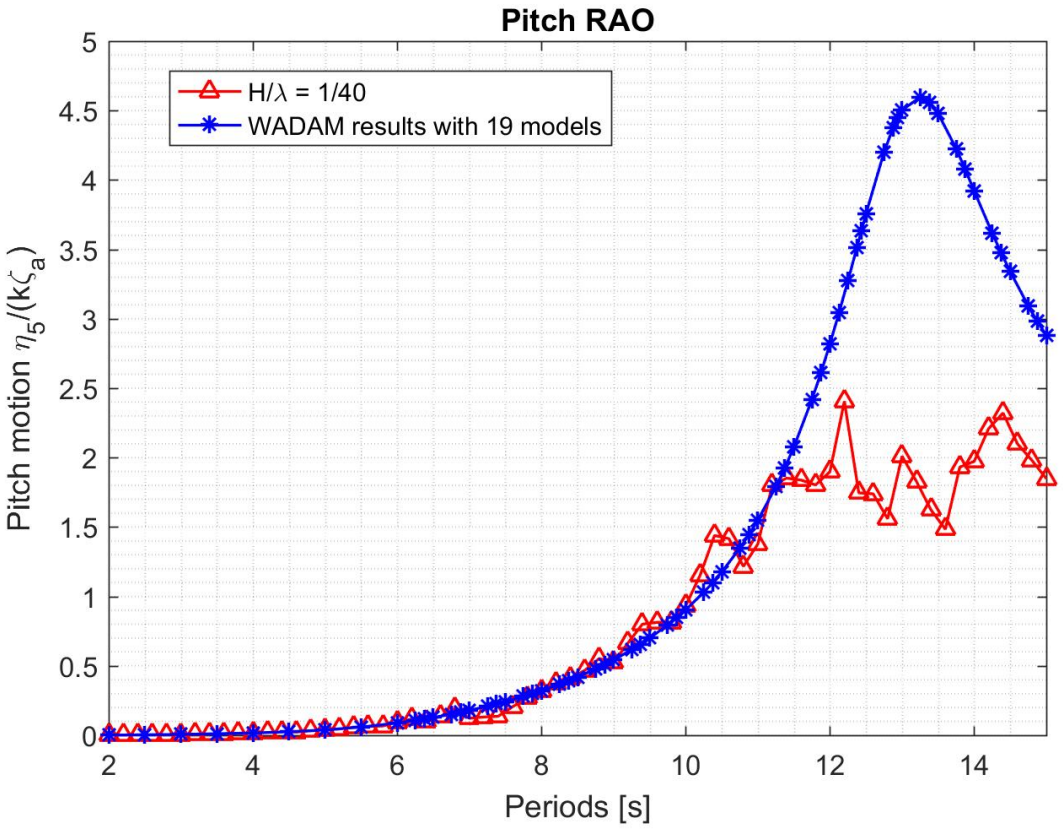

Figure 5.10: Normalized pitch RAO from test series *4090011* plotted against *WADAM* results with 19 bodies from wave periods $T = 2s$ to $T = 15s$ in full scale with external damping

5.1.4 Time series

The time series presented in this chapter are discussed and compared with the results obtained from *WADAM*. The experimental results are post-processed with analysis procedures presented in Chapter 4.5.

Waves

The time series of waves with different steepness for test series *4012003* without a model present in the tank are shown in figure 5.11, for a regular wave with full scale wave period $T = 8s$ and $T = 8.2s$. The filtered waves are represented by the green lines in the same plot. As expected, the steepest waves with $H/\lambda = 1/30$ show some second order effects. The positive peaks are more peaked, and the through are more flat.

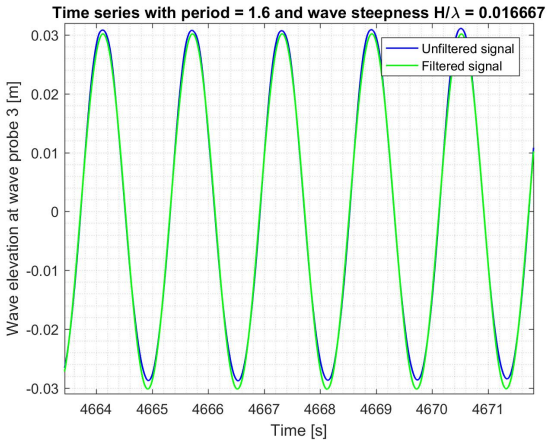

(a) Waves with $T = 8s$, $H/\lambda = 1/60$

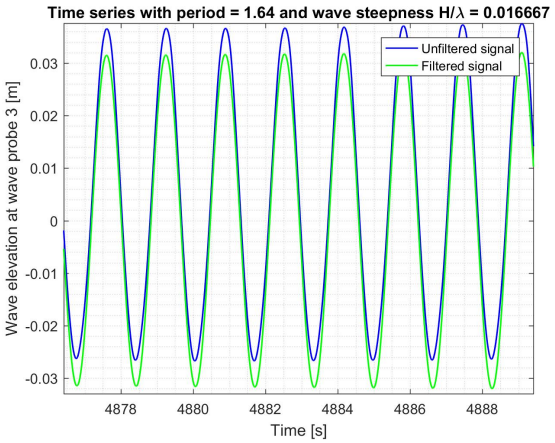

(b) Waves with $T = 8.2s$, $H/\lambda = 1/60$

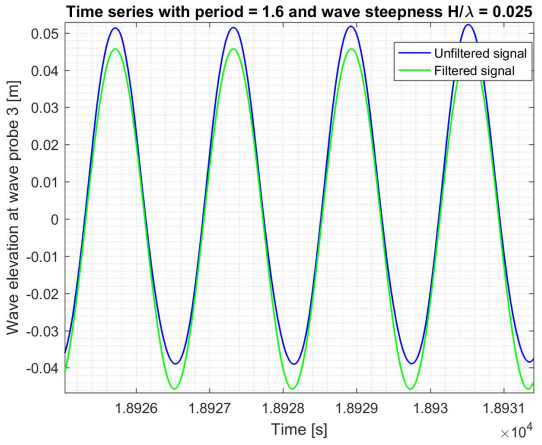

(c) Waves with $T = 8s$, $H/\lambda = 1/40$

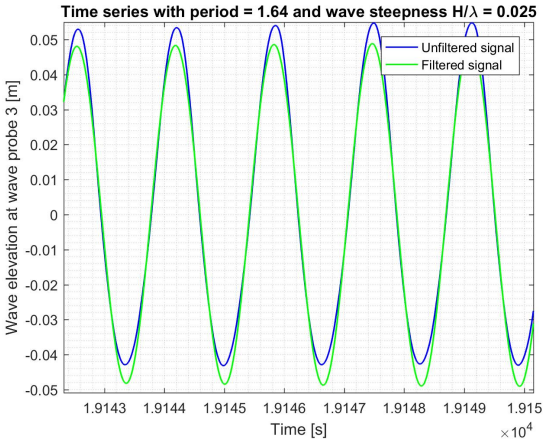

(d) Waves with $T = 8.2s$, $H/\lambda = 1/40$

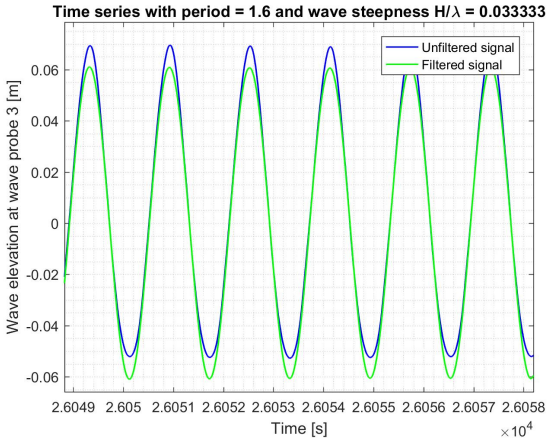

(e) Waves with $T = 8s$, $H/\lambda = 1/30$

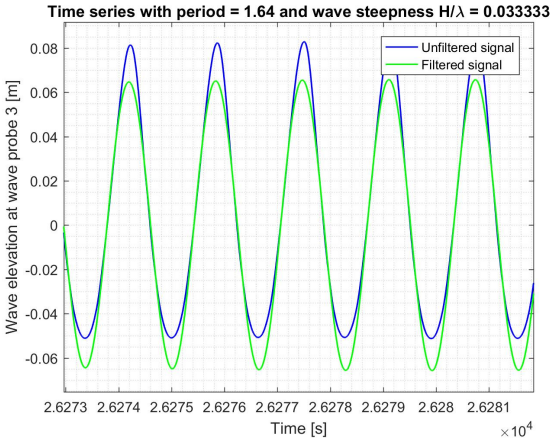

(f) Waves with $T = 8.2s$, $H/\lambda = 1/30$

Figure 5.11: Measured time series of wave elevation in wave probe 3 for test series *4012003*

Time series for all wave steepness with same wave period $T = 8s$ ($T = 1.6s$ in model scale) are shown in figure 5.12. The filtered wave elevations are plotted in the same figure as dotted lines. As expected, the wave peaks are increasing with increased wave steepness because the wave number is constant for the same period. With a constant wave number for the same period, the wave length will increase for higher wave steepness.

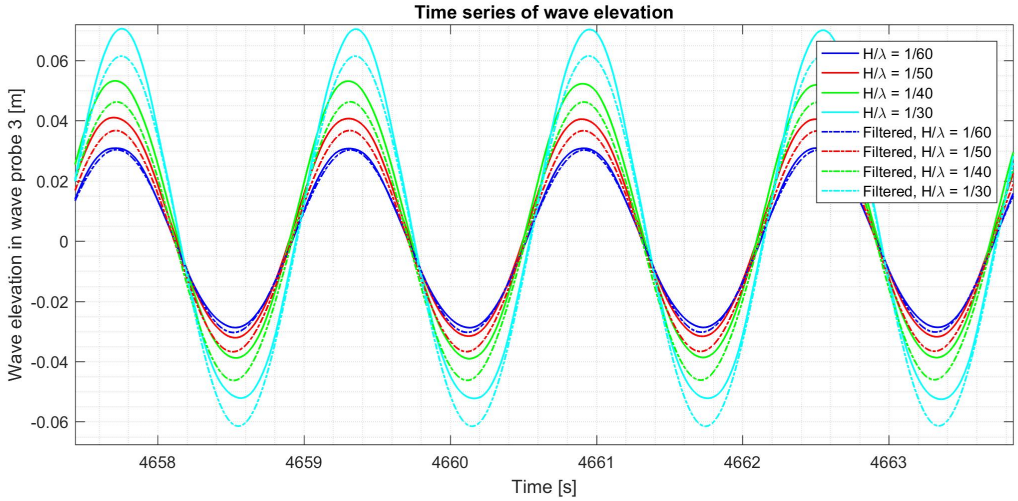

Figure 5.12: Time series of waves with wave period $T = 8s$ (model scale $T = 1.6s$) for different wave steepness in test series *4012003*. Dotted lines represent the filtered time series

Motions

The time series of the motions for the barge may be simulated by using the RAO calculated from the experiments and *WADAM*. This can be done by inserting the incoming wave amplitude with the corresponding wave frequency in the wave elevation equation for the sinusoidal waves, $\eta_{ij} = \eta_a \sin(\omega t)$. The time series of the pitch motion with full scale wave period $T = 7s$ are shown in figure 5.13. It is shown that the pitch amplitude from the numerical results are larger than the experimental results.

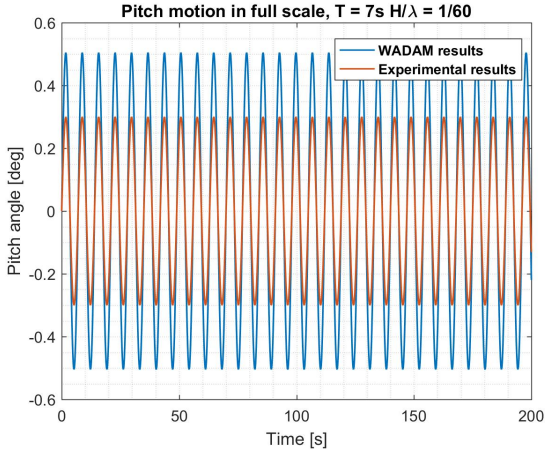

Figure 5.13: Time series obtained by using RAO from the experiments and *WADAM* for wave period $T = 7s$, $H/\lambda = 1/60$ for test series *4012003*

Motions of the barge may also be calculated by using the added mass, potential damping

and the excitation force which are calculated from *WADAM*, and solve the differential motion equations. This can be done by using the build-in solver in *MATLAB*, *ode15s*. This solver can solve first order ordinary differentiation equations, thus the method mentioned in Chapter 2.4 can be implemented.

The time series simulated by using the hydrodynamic coefficients obtained from *WADAM* have been compared with the measured time series *4012003* from the experiments. The simulations have the wave periods in full scale because the hydrodynamic coefficients from *WADAM* are dependent on wave frequencies. Hence, the results from the experiments are scaled to full scale.

The results are shown in figures below for wave steepness $H/\lambda = 1/60$. The numerical simulations are obtained by solving the differential equation with the hydrodynamic coefficients obtained from *WADAM* for a wave with period $T = 7s$ and $T = 9s$. It can be seen that the transient part are present in the simulated results.

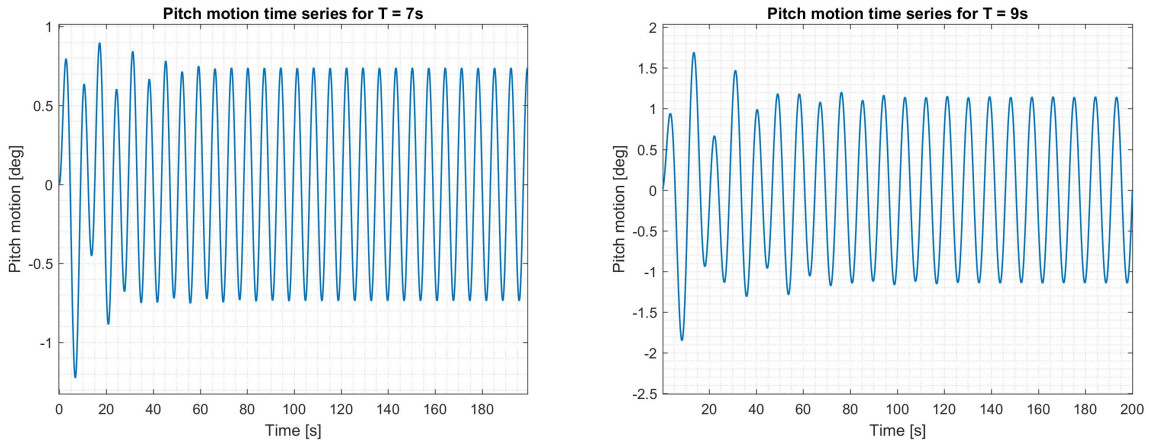

(a) $T = 7s$ (b) $T = 9s$

Figure 5.14: Time series in pitch with $H/\lambda = 1/60$ simulated in *MATLAB* in full scale with hydrodynamic coefficients from *WADAM*

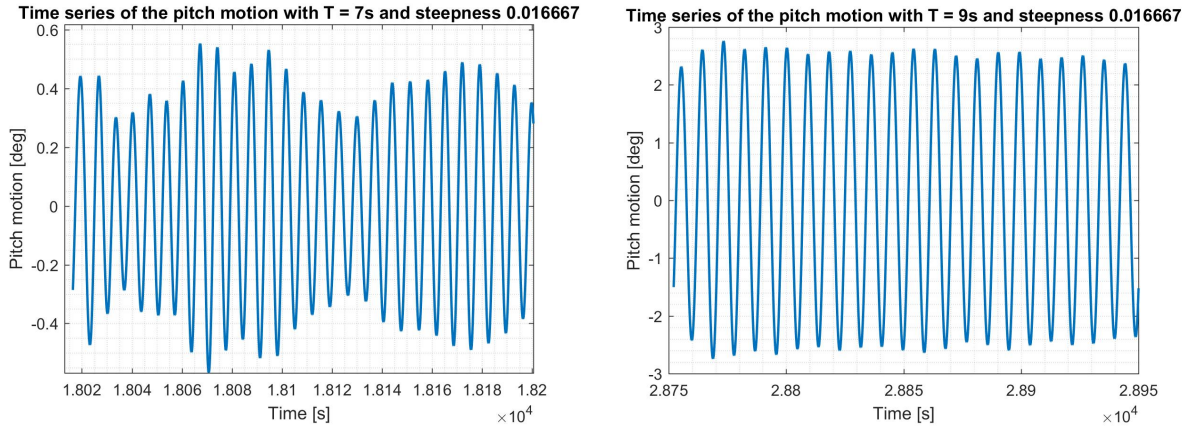

(a) Wave period $T = 7s$ (b) Wave period $T = 9s$

Figure 5.15: Pitch motions from the experiments for full scale wave period $T = 7s$ and $T = 9s$ and steepness 1/60 from test series *4012003*

As shown in the figure 5.15a, the amplitude from the measured data are varying. This is due to the disturbance of the waves and the parametric instabilities. It can be seen that the numerical simulations give a pitch amplitude approximately 0.7 degrees, which

is larger than the measured data. From another time series with $T = 9s$, it can be seen that the pitch motions are more stable, and the experimental results show a larger pitch amplitude than the numerical simulated results. This difference can be seen in the RAOs in figure 5.9. This can possibly be due to the tank reflections or coupled effects. The rest of the time series simulated from *MATLAB* can be found in Appendix B.6.

The time series for pitch and surge motions are shown in figure 5.16. The pitch motion at $T = 6s$ (model scale wave period $T = 1.2s$) has not a constant amplitude. This is possibly due to the parametric instabilities that occur during the half of the pitch natural frequency. It is shown that approximately at the natural frequency of the pitch motion $T = 12s$ ($T = 2.4s$ in model scale), the pitch motion has a constant amplitude. By comparing the time series of surge motion, it can be shown that the surge motion is coupled with pitch motion.

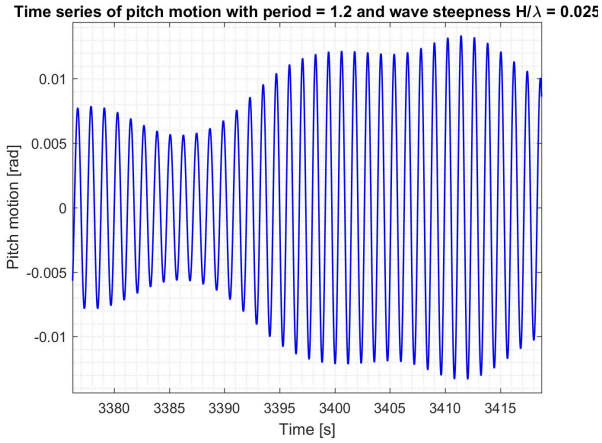

(a) Pitch motion with $T = 6s$, $H/\lambda = 1/40$

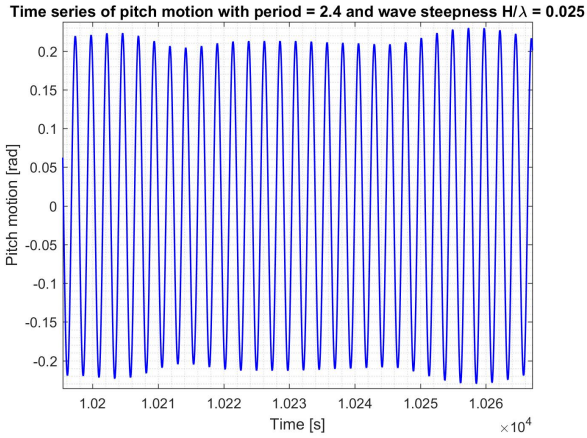

(b) Pitch motion with $T = 12s$, $H/\lambda = 1/40$

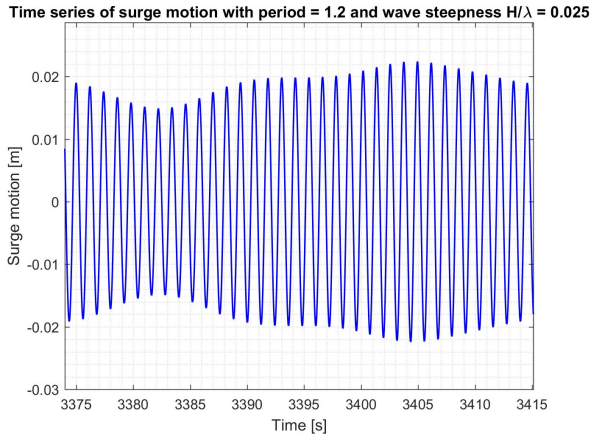

(c) Surge motion with $T = 6s$, $H/\lambda = 1/40$

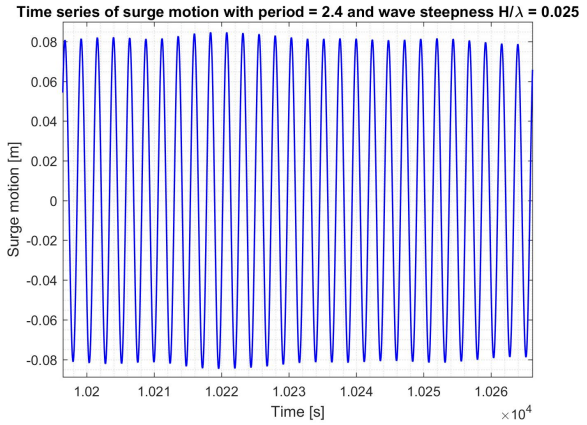

(d) Surge motion with $T = 12s$, $H/\lambda = 1/40$

Figure 5.16: Pitch and surge motion time series from the experiments

5.2 Parametric pitch

From the time series presented in previous chapters, it is shown that the pith motion is unstable when the incoming wave has a period of $T = 6s$ ($T = 1.2s$ in model scale), approximately half of the natural frequency of the pitch in model scale. The RAO for the motions can be obtained by data that are filtered with 0.5ω from a band pass filter. The results are plotted in figure 5.17 where the green lines are filtered with half of the frequencies of the incoming waves. It can be seen that the heave motion is not affect much by this effect.

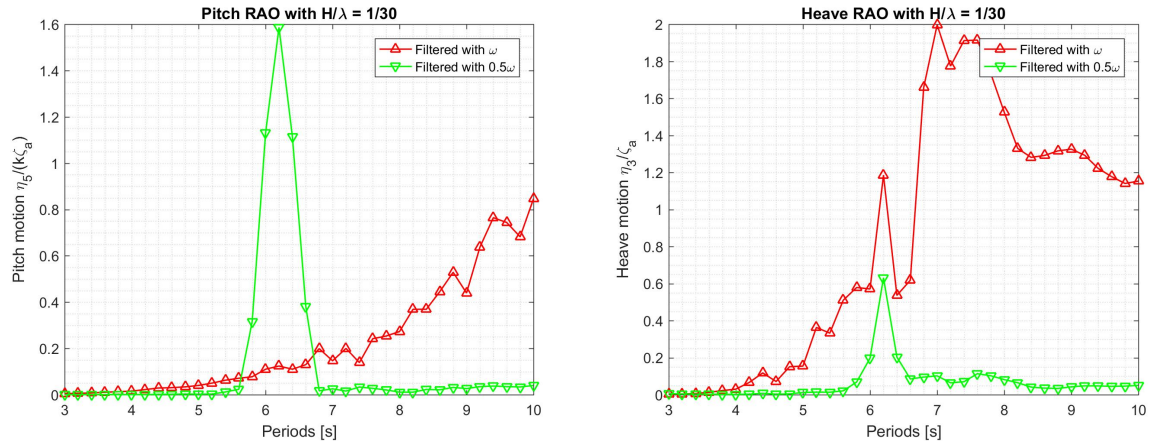

Figure 5.17: RAO in pitch (left) and heave (right) for test series *4012003* in full scale wave periods. Results are filtered with band pass filter with concentration at ω and 0.5ω

As the pitch RAO in figure 5.17 shows, the RAO obtained by filtering the measured accelerations with 0.5ω show a peak at $T = 6s$ in full scale. This corresponds to the time series presented in previous sections, showing that the pitch motion is unstable with varying amplitudes. This instability occurs close to the heave natural period, which is about $T = 7s$ in full scale. From Mathieu instability, it shows the unstable area for 0.5ω is larger than for ω. This correspond well to the measured results, as the instability is present for other periods at $T = 6.2s$ and $T = 6.4s$. The RAOs in Appendix B.3 for the results filtered with 0.5ω show that peak has different width for different wave steepness.

This instability can possibly be a result of the sloshing modes inside the tank. From the *MATLAB* script written by professor Trygve Kristiansen, *linwave.m*, the sloshing period is estimated to be approximately around $T = 6.2s$, which is the period when the parametric instability occur. The trigger of the instability can also be a consequence of the asymmetric forces during the heave motion. This is illustrated in figure 5.18. The vortex shedding from the sharp corners of the structure can be another possibility to trigger the instability.

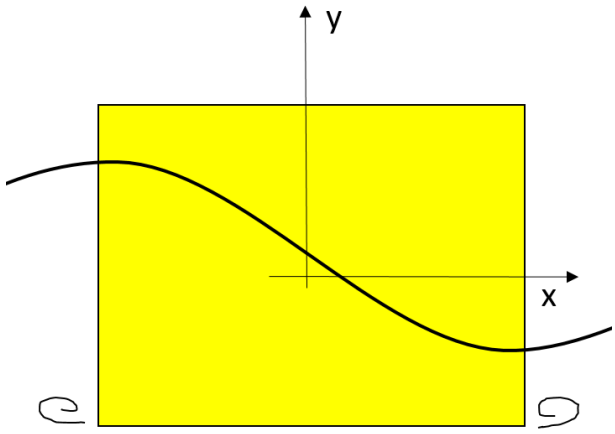

Figure 5.18: Heave excitation force that can trigger parametric instabilities, in addition to vortex shedding from the sharp edges of the structure

5.3 Slamming forces

The force sensor that measures the impact force has its own natural frequency. Oscillations from this system can possibly affect the measured results. In order to check this, a sensitivity test of the low-pass filtering has been performed. From the plate decay test, the results give the dominating peaks that are located approximately at $265Hz$, which means that the natural frequency for the sensor is at this region. It is expected that the power spectrum from the time series of the slamming forces should give a peak at a frequency lower than this because of the added mass. This is due to that the decay test is performed in air.

The results of the sensitivity test are shown in figure 5.19, where the PSD of the cut off frequency are shown in a green window. The filtered time series are plotted against the original signal in figure 5.20.

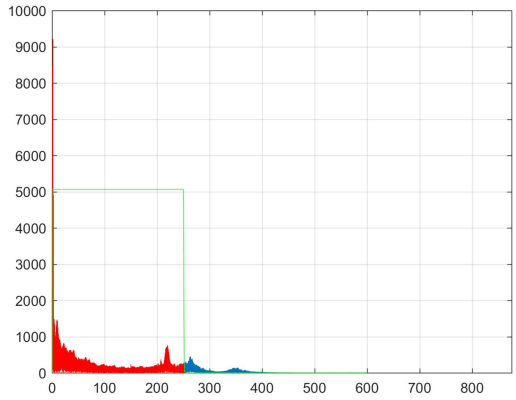

(a) PSD of the time series filtered between frequencies $0.1Hz$ and $250Hz$

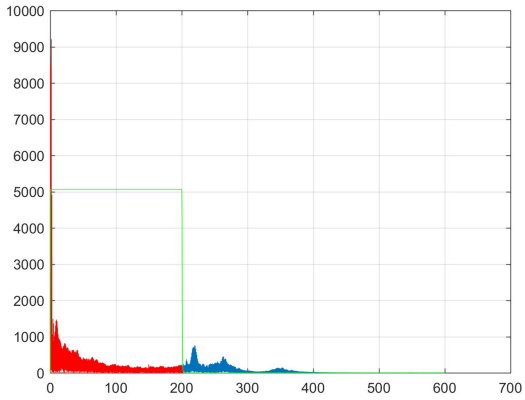

(b) PSD of the time series filtered with frequencies between $0.1Hz$ and $200Hz$

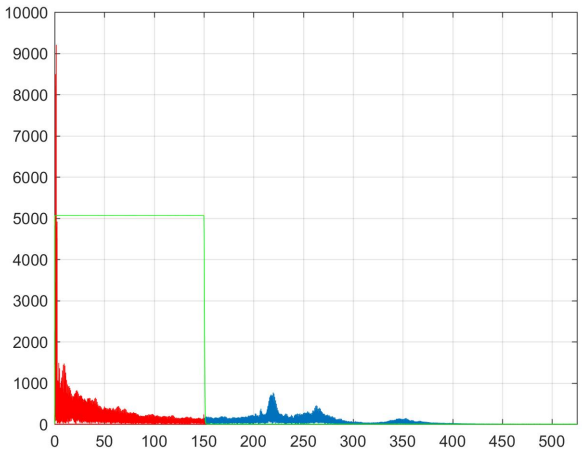

(c) PSD of the time series filtered with frequencies between $0.1Hz$ and $150Hz$

Figure 5.19: Time serie of the slamming forces filtered with different values in the low pass filter. PSD for different cut-off frequencies

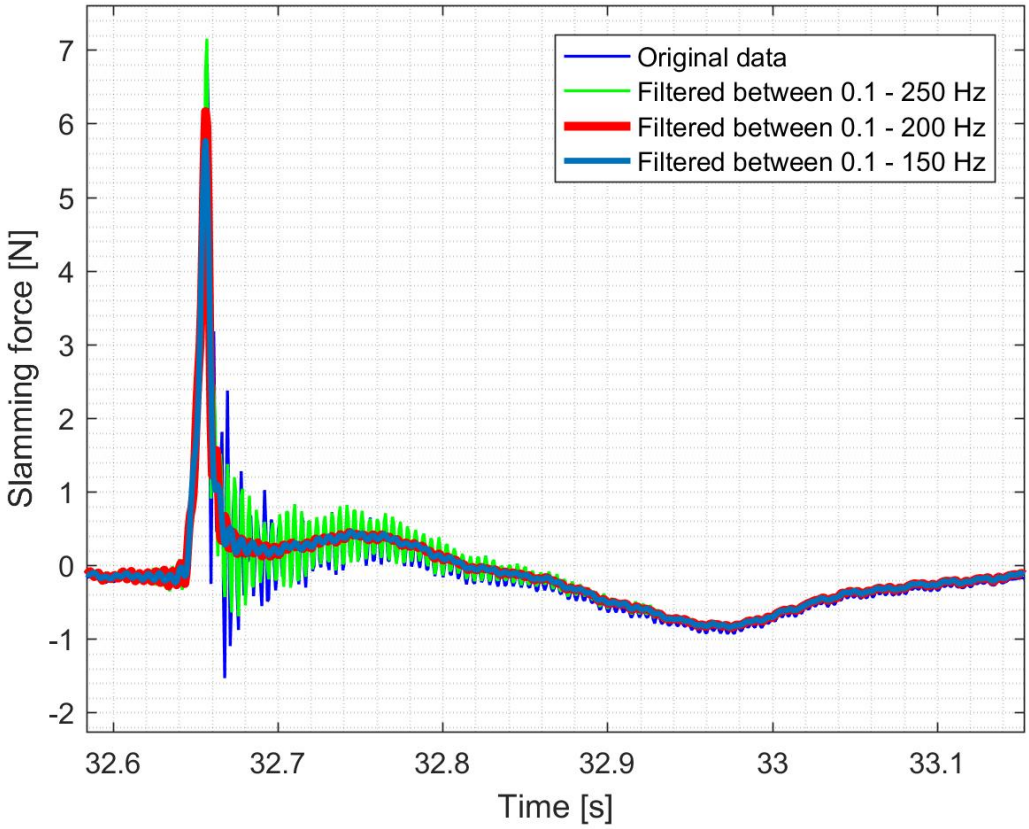

Figure 5.20: Time series of the slamming forces where different filtered data are plotted

The time series in figure 5.20 show that the filtering affects the maximum peak and the oscillations after the peak. The filtered data with the cut-off frequency at $200Hz$ and $150Hz$ show approximately the same results. Whereas the filtered data with a cut-off frequency at $250Hz$ show similar trend to the original signal. This is because the peak at approximately $220Hz$ in the spectrum is taken into account. This peak might be the responses from the sensor, and not from the structure. Thus, the time series of the slamming forces should be filtered with a low-pass filter in frequency range $0.1Hz$ to $200Hz$.

The contribution of the sensor mass can alternatively be estimated by using the mass of the system that can be determined by the local acceleration. The measured forces are the sum of the hydrodynamic forces, slamming forces, and the forces due to the local acceleration. The local acceleration can be determined from the time series. When there are no slamming events, the sensor will measure a time series due to the local acceleration. This can be seen in figure 5.21, where there are small oscillations. The mass of the sensor can be determined by using the time series of the measured force divided by the local accelerations, and subtract the mass of the plate. The estimated mass of the sensor is $0.088kg$, which is not much from than the exact value of the sensor which is $0.082.5kg$.

The actual slamming force can be obtained by subtracting the force due to the sensor mass multiplied with the local acceleration from the measured time series. This method is used for the test series that have sampling frequency of $200Hz$. The reason is that the low pass filtering mentioned earlier will not work in this case. However, this force is not dominating as the contribution is small.

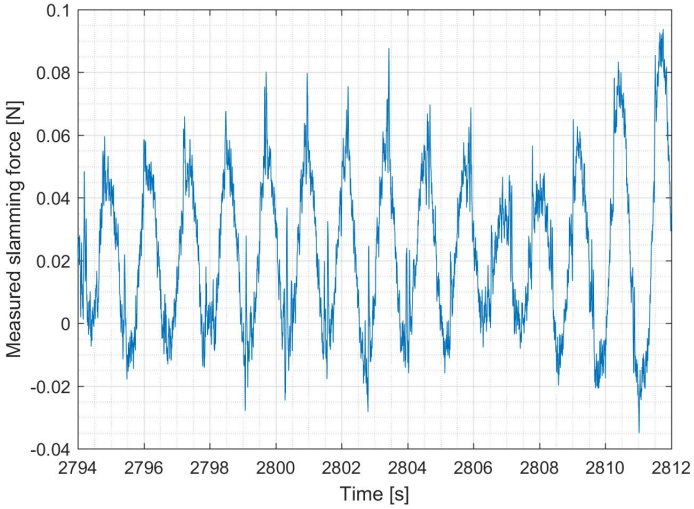

Figure 5.21: Time series of the measured slamming force when no slamming events occur

The impulse from a slamming force time series is analyzed. This is done by integrating the area under the force as the impulse is the integral of force over a time interval. The analyzed time series are taken from test series *80000* with a full scale wave period $T = 6s$ and a wave steepness $H/\lambda = 1/26$. The slamming force time series with the corresponding impulse is shown in figure 5.22.

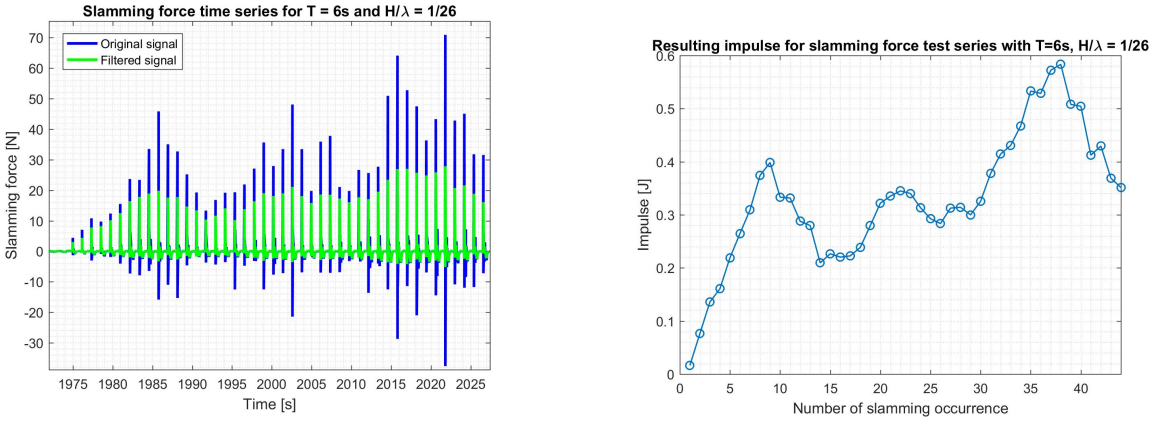

(a) Slamming force time series where the green line is the filtered data

(b) Corresponding impulse plotted against the number of peaks from the time series

Figure 5.22: Slamming force time series for test series *80000* with $T = 6s$ and $H/\lambda = 1/26$ and the corresponding impulse

The impulse plot from figure 5.22b shows that the impulse are varying consistently with the slamming peaks from the time series. The values of the impulse are small which can imply that the duration of the impact is short. This means that for a high impact force, the structure has not enough time to react.

5.3.1 Implementing Wagner solution

The impact problem of the platform can be analyzed in an analogy to the water entry problem of a wedge structure by assuming symmetry and rigid body during the impact. By

using the method introduced in Chapter 4.5.6, the slamming forces from the experiments can be compared with the numerical solutions from Wagner model. Investigations of the local wave profile from a regular wave with model scale wave period $T = 1.4s$ (full scale $T = 7s$) is shown in figure 5.23.

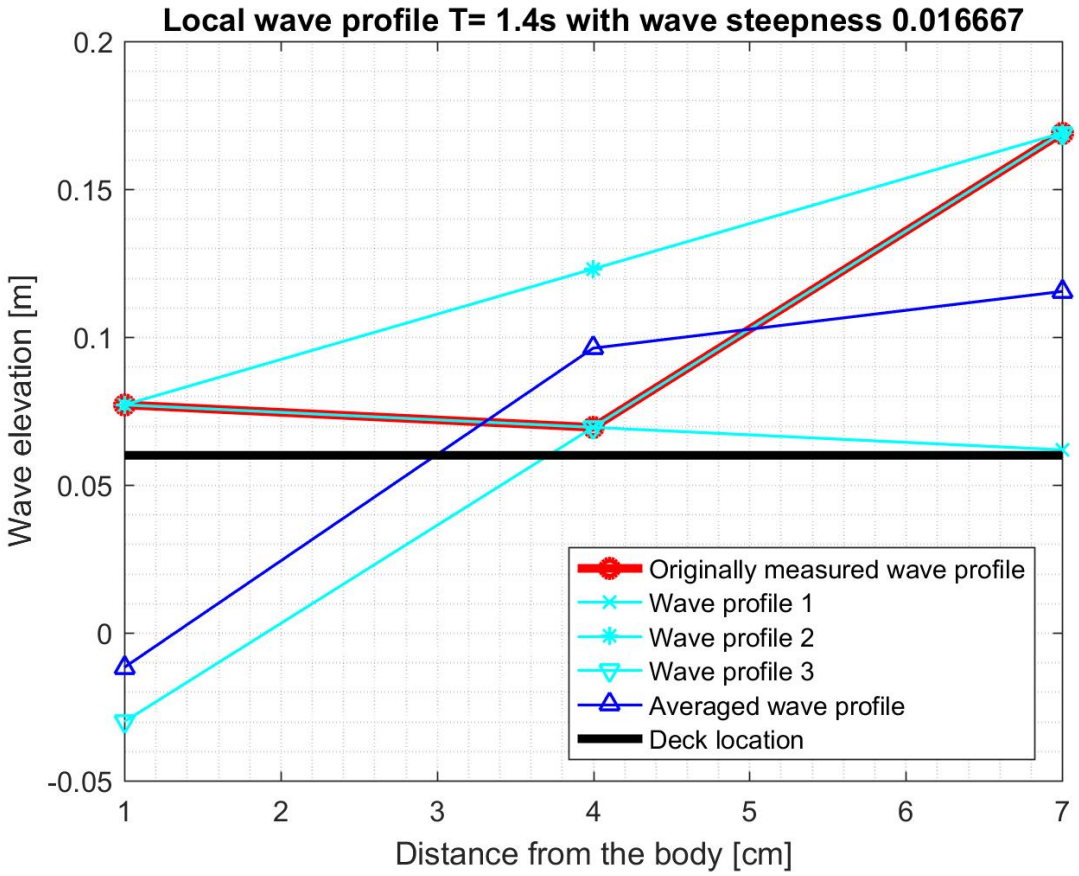

Figure 5.23: Wave profile from test series *4012003* with different methods at mode scaled wave period $T = 1.4s$ ($T = 7s$ in full scale) with wave steepness $H/\lambda = 1/60$

The originally measured wave profile at the deck area is extrapolated in order to obtain a deadrise angle for the wedge theory. The estimated angle of each wave profile are listed in table 5.6.

Table 5.6: Estimation of deadrise angle from test series *4012003* with wave period $T = 1.4s$ and steepness 1/60 with corresponding factor from the Wagner solution

	Wave profile 1	**Wave profile 2**
Description	Extrapolated between WP1cm and WP4cm	Extrapolated between WP1cm and WP7cm
Estimated angle [deg]	14.22	56.87
Factor from Wagner theory	6.1	3.8
	Wave profile 3	**Averaged profile**
Description	Extrapolated between WP4cm and WP7cm	Average of all wave profiles
Estimated angle [deg]	73.23	70.36
Factor from Wagner theory	2.1	2.1

The local vertical velocity during the motion is estimated to be $0.7259 m/s$. This value is obtained by differentiate the measured time series from the three wave probes that are attached to the body with respect to time. By using figure 2.7 in Chapter 2.8.1, the vertical force can be found for the different wave profiles. The slamming force varies linearly with the time. A comparison of the experimental result and the theory is shown in figure 5.24. It can be seen that the experimental result lies between the smallest and largest values of the theoretically estimated results.

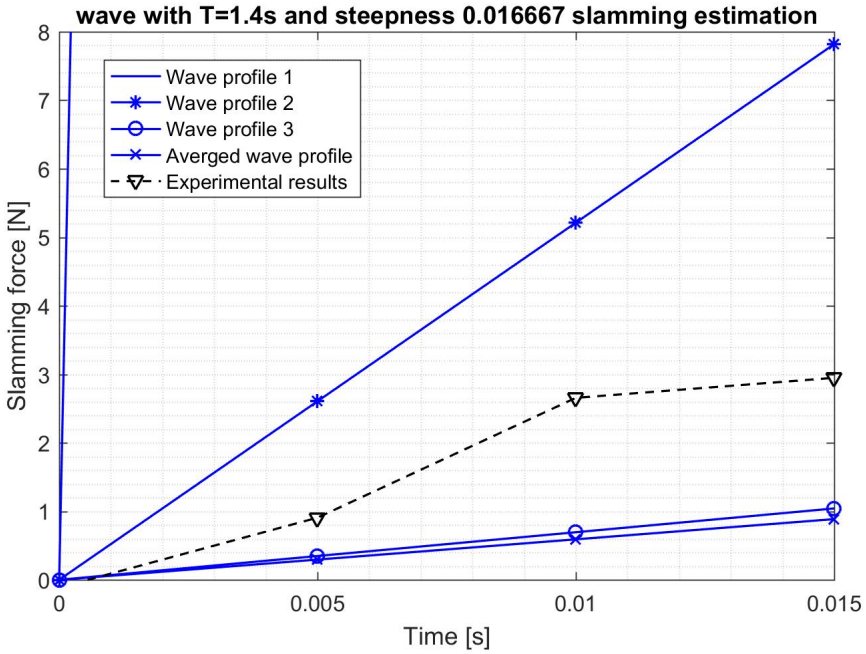

Figure 5.24: Estimated slamming forces from wedge theory by using the four wave profiles

By analyzing more slamming peaks, the results are observed to lie within the estimated ones. Time series of the corresponding four slamming peaks are compared with the estimated results. This is shown in figure 5.25.

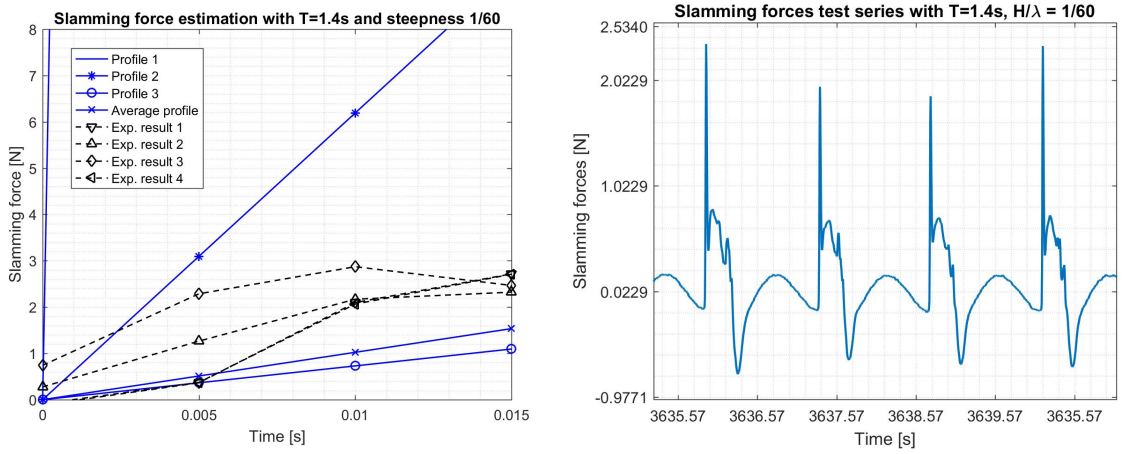

(a) Slamming Estimation of the forces

(b) Slamming force time series used in the estimation

Figure 5.25: Estimated slamming force compared with the slamming force measured from the time series from test series *4012003* with wave period $T = 1.4s$ with wave steepness $H/\lambda = 1/60$ in model scale

Due to large uncertainties to the deadrise angle, which is estimated from the wave profiles from the corresponding time series, it is expected that the estimated slamming forces would not correspond well with the experimental results. However, the experimental results are within the solutions by using the angles estimated from wave profile 2 and wave profile 3. This implies that the exact deadrise angle in the time series of a regular wave with period $T = 1.4s$ and steepness 1/40, will approximately be between 57 and 74 degrees.

The Wagner model is very sensitive to the deadrise angle and the impact surface. Time series with a different wave period has been analyzed. It is mentioned earlier about the parametric instability occurs about $T = 6.2s$ in full scale, and the time series of the slamming forces during this wave period in model scale, $T = 1.24s$, are shown in figure 5.26. The resulting wave profiles are different. This leads to different estimations of the slamming forces which is shown in figure 5.27a.

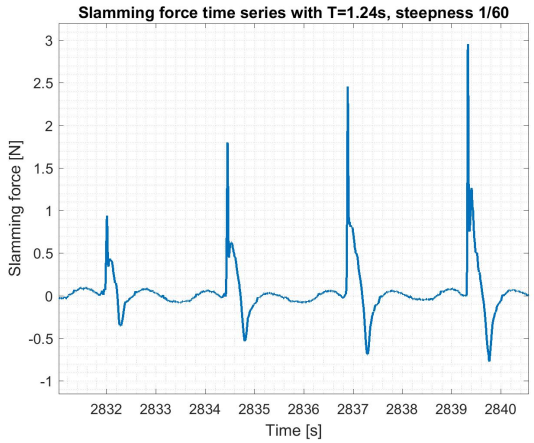

Figure 5.26: Slamming force time series with wave period $T = 1.24s$ in model scale and steepness 1/60 from test series 4012003

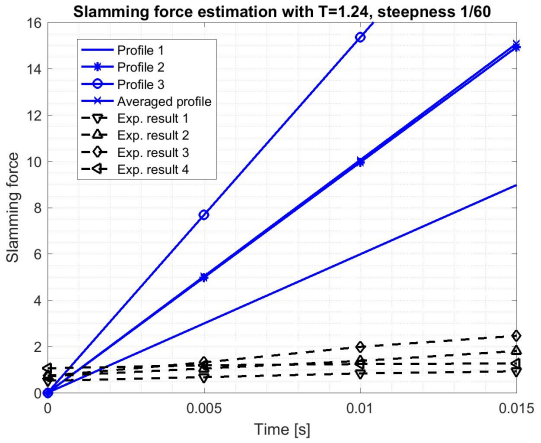

(a) Slamming Estimation of the forces

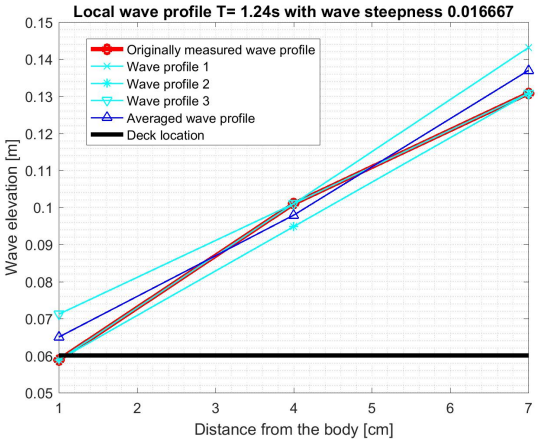

(b) Wave profiles estimated from a time series with wave period $T = 1.24s$ and steepness 1/60

Figure 5.27: Estimated slamming force compared with the slamming force measured from test series *4012003* with model scale wave period $T = 1.24s$ and $H/\lambda = 1/60$

The local relative velocity for the regular wave with period $T = 1.24s$ is estimated to be $0.7118m/s$, and the estimated angle between the water and the body are listed in table

5.7. As the results show, the estimated angles within 50 degrees in this case overestimate the slamming forces. Hence, the accuracy of the deadrise angle and the wave length are essential for the estimation of the slamming forces by using Wagner model.

Table 5.7: Estimated deadrise angle in degrees for the wave profiles with time series for a period $T = 1.24s$ and steepness 1/60 for test series *4012003*

Wave profile 1	**Wave profile 2**	**Wave profile 3**	**Averaged profile**
54.67	50.29	44.813	50.186

5.3.2 The slamming coefficient

The slamming coefficient is plotted against the wave periods. Formula 2.32 from Chapter 2.8.1 is used, and the vertical force is the mean maximum force in the slamming force time series from each wave period with a wave steepness. This is shown in figure 5.28.

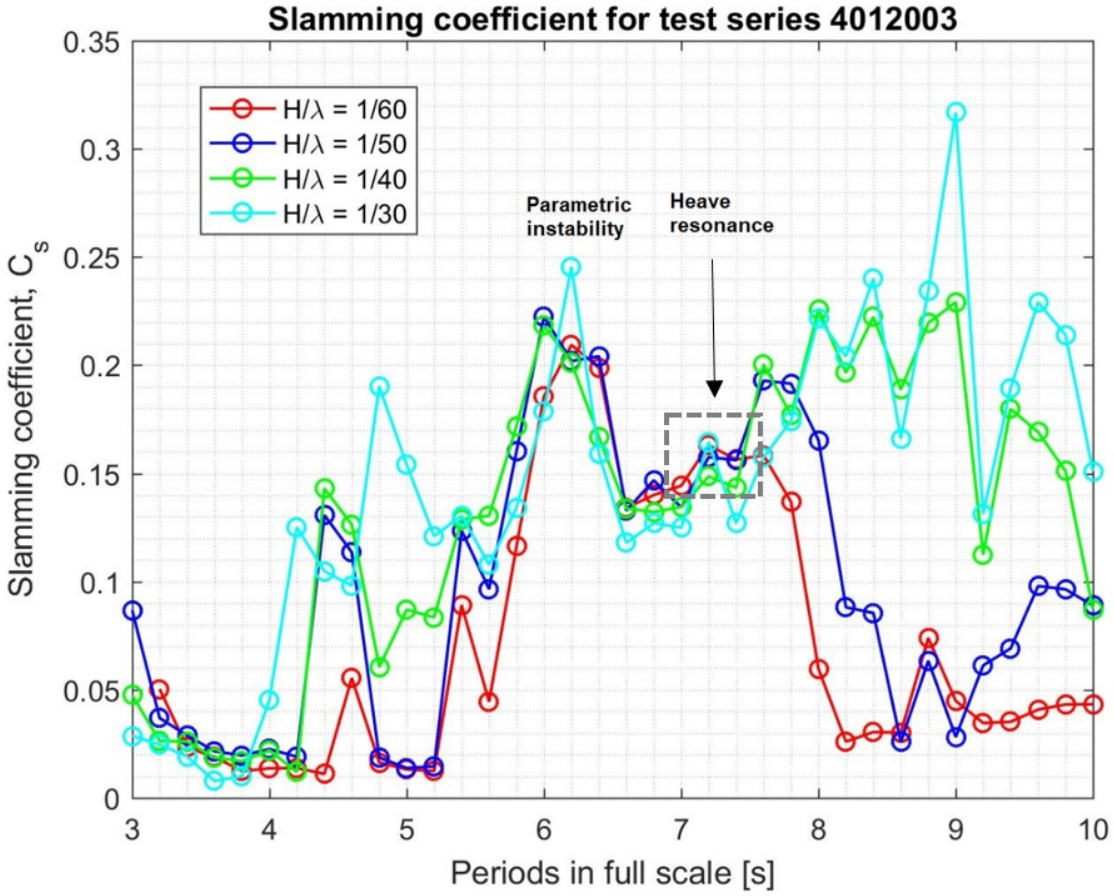

Figure 5.28: Slamming coefficient from test series *4012003* for the mean maximum slamming force in the time series

It can be seen that the slamming coefficient is largest at wave period $T = 6s$ to $T = 9s$ in full scale. The peak at $T = 6s$ is due to the parametric instability. At $T = 7s$, it is

close to the heave resonance that creates large heave motions. At $T = 4s$, it is shown a peak that appears in the slamming coefficient plot. This is when the waves are higher than the height of the deck. It is the same as for the higher periods where the slamming coefficient is not zero even if there is no impact at all.

5.3.3 Comparison with Perforated plate

The slamming force time series of the perforated plate are compared with the solid plate. The perforated plate is tested with same waves as test series *80000* and *90000* with a sampling frequency of $1200Hz$. Time series of the measured slamming forces are shown in figure 5.29 for an incoming regular wave with full scale wave period $T = 7s$ and wave steepness of 1/30.

The comparison shows that the maximum slamming force is much smaller for the perforated plate than the solid plate. This is due to the difference of added mass of the two plates. The slamming force is a consequence of the rate of change of the added mass as explained in Chapter 2.8.2. As the dry mass is different for the perforated plate, the added mass during the impact will be different.

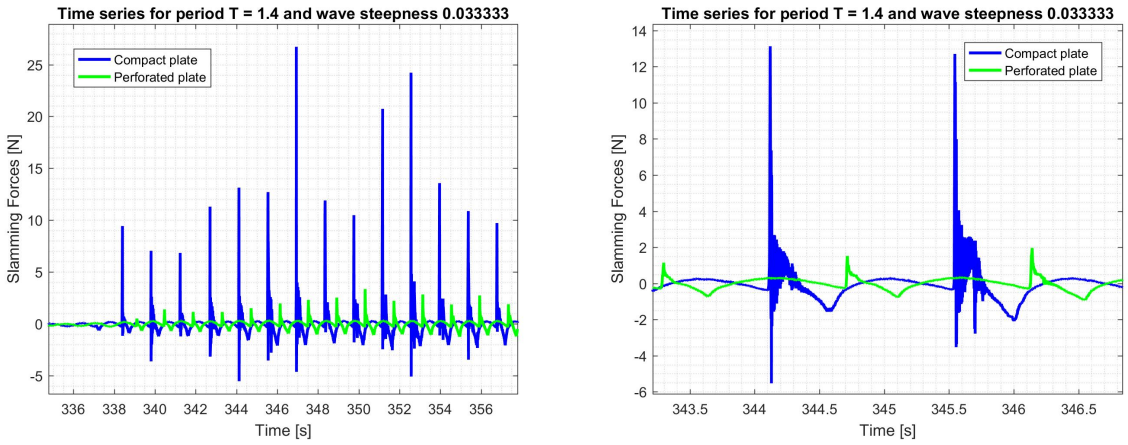

Figure 5.29: Time series of slamming force for perforated and solid plate. Blue lines: Slamming forces measured from solid plate. Green lines: Slamming forces measured from perforated plate

With the perforated plate, the water will flow between the small openings. For the solid plate, the water particles are forced to move along the plate during the impact which give larger acceleration. This effect, alongside with the effect of the water that flows around the plate edges, will contribute to a rotational flow.

From [An and Faltinsen, 2013], it is discovered that for a perforated plate with a single opening in the middle of the plate, the added mass and drag coefficient of the plate are dependent on KC number which is the Keulegan Carpenter number. The KC number is defined in [Keulegan and Carpenter, 1958] as a number that describes the relationship of the drag and inertia forces for objects in oscillatory fluid flow. [Tao and Dray, 2008] have performed a test with a circular solid and perforated disk which is submerged in water. The results show that the heave added mass and damping coefficients are nearly linearly dependent of KC number. Furthermore, if the perforation ratio of the plate is large, the value of the drag coefficient will become large and the added mass will decrease.

A distribution of the maximum slamming force is plotted for both perforated and solid plate. It shows that the maximum impact force is much lower for the perforated plate. This means that the perforated plate will be more suitable with respect to the structure responses.

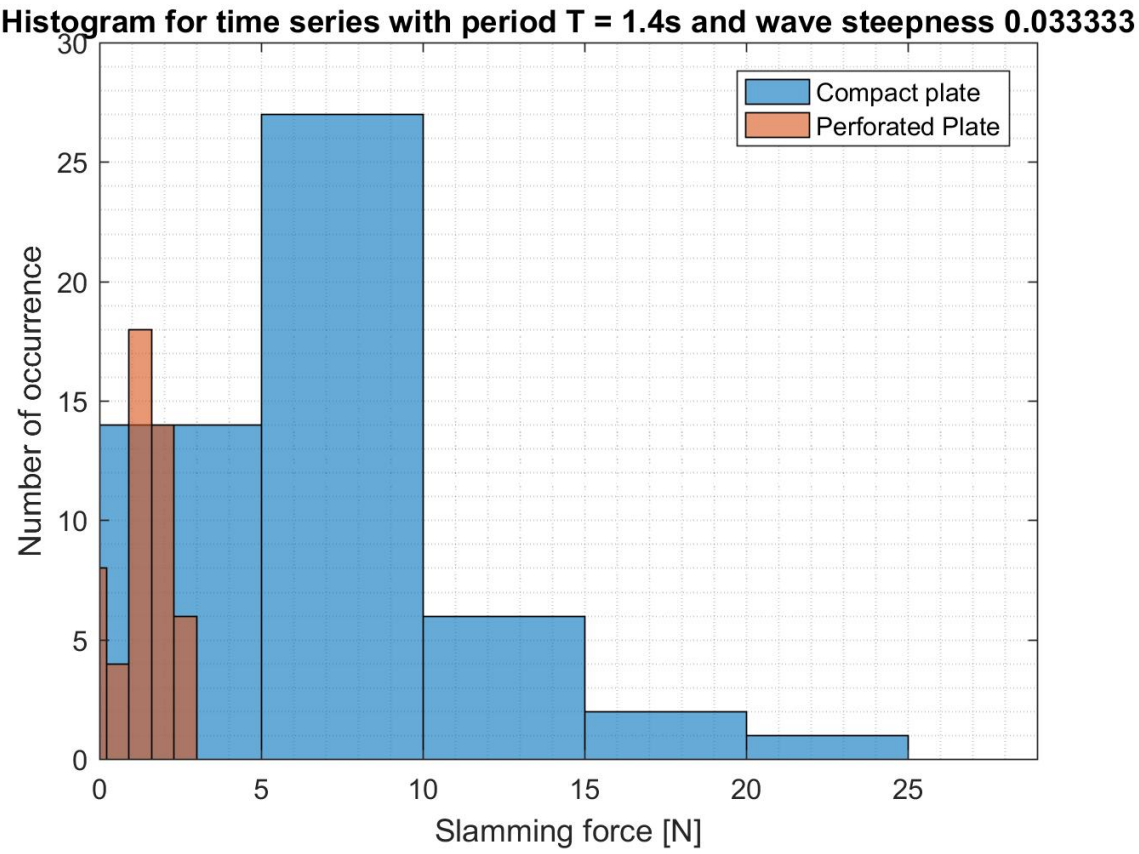

Figure 5.30: Histogram of the slamming force time series in test series *80000* with wave period $T = 7s$ in full scale and $H/\lambda = 1/30$

5.4 Experimental errors

It is observed after the experiments that there is water inside the model. The total weight of the water is $1235g$ during tests in *January*, and $335g$ in *April*. This is taken into consideration by running the numerical simulations with new gravitation center and added the scaled weight to the mass model. However, the water inside the body might give other effects which can affect the measured responses.

The decay tests show some differences for tests in *January* and *April*. This can possibly be that the loading condition in the two laboratory works are slightly different.

Tank leakage occurs during all experiment tests. Deviations on all wave probes are found before and after the experiments. This can possibly be due to incorrect calibration. With a changing water level, the zero reference point will be difficult to determine.

6 Further work and conclusions

6.1 Conclusions

Global motions for an aquaculture barge are studied both using numerical and experimental models. A numerical model is made in full scale in *WADAM* as a panel model, where the roll damping is estimated. Other additional matrices are added in order to imitate the physical model used during the experiments. The global motions are solved numerically by using linear wave theory, and the wall effects from the experiments are imitated by using mirroring techniques.

The numerical model is analyzed with finite and infinite water depth. The numerical results show that the added mass and damping are different for different water depths.The results from the finite water analysis are in good agreement with the experimental results. The experiments are carried out twice with total 9 test series in the small towing tank at the center of Marine Technology, *"Lilletanken"*. The physical model has 1:25 scale, and the small platform is made by aluminum. The model is moored with four springs, where the forces on each mooring line are measured. The tests consist of only regular waves with varying wave period and steepness.

The RAOs obtained from the experiments show good agreement with the numerical results. It is observed that large responses in heave occur for waves with full scale wave period of $T = 7s$. This is the natural period in heave, which lies close to the period for the parametric instability. The parametric roll in beam sea occurs at the half value of natural period of roll, which is in full scale $T = 6.02s$. This instability can possibly be a consequence of the asymmetric heave excitation forces from the waves, the wall reflection effect, and the vortex shedding at the sharp edges of the barge.

The largest slamming forces occur at the largest heave motions. This is about $T = 7.2s$ and $T = 7.6s$ in full scale. The side deck is periodically submerged in the water, and the water exit force is observed as the negative suction force in the time series. It is observed that the slamming force is dependent on the wave steepness, the global motions, the wave amplitude and the relative local velocity. The slamming force is observed to be largest at the steepest waves, and the high impact force has very short time duration.

Wagner model does not correspond well with the experimental results. Due to large uncertainties of the wave profile, the deadrise angle cannot be accurately estimated. A few tests with a perforated plate which has the same dimensions as the solid plate are conducted with same test series. It is observed that the perforated plate has smaller slamming force. This is due to the water that flow through the small openings during the impact which cause less acceleration to the water particles.

The experimental work is time consuming, and experiences are required for a faultless laboratory exercise. To plan and design an experiment requires guidance and advice from experienced people. The post-processing of the measured data from the laboratory exercises is important, and the data should be filtered consistently to make sure that the useful data are not filtered out. To be able to understand and interpret the measured data is important in order to relate the theory and physical events.

6.2 Further work

It is shown that the slamming loads are periodic with waves, but with different peaks on each cycle. This can be a fatigue related problem, and a fatigue analysis can be performed. A model for the fatigue trend of the side deck can be established. If necessary, the slamming loads can be analyzed by using advanced computational fluid dynamic programs. As shown from the time series of the slamming forces, the duration of the negative forces is longer than that of positive impact forces. Investigations of the water exit force can be carried out in future work.

It is recommended to run more tests with same test set up, but with irregular waves. This gives the possibility to investigate the responses of the model in a realistic environment.

Bibliography

[ABS, 2004] (2004). *Assessment of Parametric Roll Resonance in the Design of Container Carriers*.

[DNV, 2011] (2011). *Recommended Practice DNV-RP-H103, Modelling and Analysis of Marine Operations*. DNV.

[WAD, 2015] (2015). *WADAM user manual*.

[An and Faltinsen, 2013] An, S. and Faltinsen, O. M. (2013). An experimental and numerical study of heave added mass and damping of horizontally submerged and perforated rectangular plates. *Journal of Fluids and Structures*, 39:87–101.

[CENGEL, 2013] CENGEL (2013). *Fluid Mechanics*. McGraw Hill.

[Chabaud, 2015] Chabaud, V. (2015). Experimental methods in marine hydrodynamics. Lecture notes.

[Dhavalikar and Negi, 2009] Dhavalikar, S. S. and Negi, A. (2009). Estimation of roll damping for transportation barges. In *OMAE2009*.

[Dingemans, 1996] Dingemans (1996). *Water Wave Propagation Over Uneven Bottoms*. World Scientific Publishing.

[Faltinsen, 1993] Faltinsen, O. (1993). *Sea Loads on Ships and Offshore Structures (Cambridge Ocean Technology Series)*. Cambridge University Press.

[Faltinsen and Michelsen, 1974] Faltinsen, O. and Michelsen, F. (1974). Motions of large structures in waves at zero froude number.

[Faltinsen, 2012] Faltinsen, O. M. (2012). *Hydrodynamics of High-Speed Marine Vehicles*. CAMBRIDGE UNIV PR.

[Faltinsen et al., 2003] Faltinsen, O. M., Landrini, M., and Greco, M. (2003). Slamming in marine applications. *Journal of Engineering Mathematics*, 48:187–217.

[Faltinsen and Timokha, 2009] Faltinsen, O. M. and Timokha, A. N. (2009). *Sloshing*. Cambridge University Press.

[Howison et al., 2002] Howison, S. D., Ockendon, J. R., and Oliver, J. M. (2002). Deep- and shallow-water slamming at small and zero deadrise angles. *Journal of Engineering Mathematics*.

[J.Kirkegaard et al., 2011] J.Kirkegaard, Wolters, G., J.Sutherland, Soulsby, R., L:Frostick, McLelland, S., Mercer, T., and Gerritsen, H. (2011). *Users guide to Physical Modelling and Experimentation*. CRC Press.

[Karman, 1929] Karman, T. V. (1929). The impact on seaplane flaots during landing. *National Advisory Comittee for Aeronautics*, page Technical Notes.

[Keulegan and Carpenter, 1958] Keulegan, G. H. and Carpenter, L. H. (1958). Forces on cylinders and plates in an oscillating fluid. *Journal of Research of the National Bureau of Standards*, 60(5).

[Kim et al., 2015] Kim, J.-H., Kim, Y., Yuck, R.-H., and Lee, D.-Y. (2015). Comparison of slamming and whipping loads by fully coupled hydroelastic analysis and experimental measurement. *Journal of Fluid and Structures Volume 52*.

[Korobkin and Iafrati, 2017] Korobkin, A. A. and Iafrati, A. (2017). Early stage of floating plate impact.

[Kristiansen et al., 2018] Kristiansen, D., Endresen, P. C., Lader, P., Su, B., Volent, Z., and Aksnes, V. (2018). Sluttrapport sjoflo. https://www.sintef.no/prosjekter/sjoflo/.

[Lekang, 2017] Lekang, O. I. (2017). Overview of fishery/capture and aquaculture. Aquatic Food Primary Production: Fishery and Aquaculture.

[Miskovic et al., 2008] Miskovic, I., Eskinja, Z., and Horvat, K. (2008). Wavemaker control system for irregular developed sea waves generation. In *Conference on Control and Automation*.

[Moran, 1965] Moran, J. P. (1965). On the hydrodynamic theory of water-exit and -entry. Technical report, Fluid Dynamics Branch Office of Naval Research.

[Mukhlas, 2017] Mukhlas, M. (2017). Roll damping investigation of two-dimensional ship section with bilge boxes. Master's thesis, Norwegian University of Science and Technology.

[Nielsen and Berg, 2007] Nielsen, F. G. and Berg, T. E. (2007). Experimental determination of hydrodynamic coefficients. Lecture notes.

[Pettersen, 2007] Pettersen, B. (2007). *Kompendium i TMR4247 Marin teknikk 3 - Hydrodynamikk*. Kompendieforlaget.

[Sheikh, 2008] Sheikh, I. A. (2008). Parametric roll instability. Master's thesis, University of Oslo.

[Smith et al., 1997] Smith, N. J., Stansby, P. K., and Wright, J. R. (1997). The slam force on a flat plate in free flight due to impact on a wave crest. *Journal of Fluids and Structures (1998)*, 12:183–196.

[Steen, 2014] Steen, S. (2014). *Experimental Methods in Marine Hydrodynamics*. Department of Marine technology.

[Steen, 2017] Steen, S. (2017). Tmr7 experimental methods in marine hydrodynamics. Course site of TMR7.

[Steinsvik, 2017] Steinsvik (2017). Fôrflater. http://www.steinsvik.no/en/products/e/seaculture/barges

[Tao and Dray, 2008] Tao, L. and Dray, D. (2008). Hydrodynamic performance of solid and porous heave plates. *Ocean Engineering*, 35:1006–1014.

[Vugts, 1968] Vugts, J. H. (1968). The hydrodynamic coefficients for swaying, heaving and rolling cylinders in a free surface.

[Zhao et al., 2016] Zhao, W., Efthymiou, M., McPhail, F., and Wille, S. (2016). Nonlinear roll damping of barge with and without liquid cargo in spherical tanks. *Journal of Ocean Engineering and Science*.

Appendix

A Additional theory

A.1 Reynolds scaling

Another scaling method is the equality of the Reynolds number as expressed in equation 1. This is called Reynolds scaling, and it implies that the flow around the structure will be scaled correctly. Reynold scaling applies to the cases where the viscous forces are important. For slamming analysis, viscous effect is second dominating effect. Hence, Reynold scaling should be considered.

$$Re = \frac{\rho U L}{\mu} \tag{1}$$

According to [Steen, 2014], it is impossible to satisfy Froude scaling and Reynolds scaling at the same time. This means, by choosing Froude scaling, the viscous forces will not be correctly scaled. It is further explained in [Faltinsen and Timokha, 2009], that there exist no fluid in model scale that can satisfy the scaling factor expressed in equation 2.

$$L_m/L_s = (\nu_m/\nu_s)^{2/3} \tag{2}$$

However, it is shown that a modified Reynolds number is possible by combining the Reynolds and Froude number as in formula 3.

$$\overline{Re} = \frac{L^{3/2} g^{1/2}}{\nu} \tag{3}$$

A.2 Boundary value problem

This section is based on Chapter 2 in *Sea Loads on Ships and Offshore Structures* by [Faltinsen, 1993], and Chapter 1 in *Hydrodynamikk* by [Pettersen, 2007]. Consider a body in a control surface with incident waves as presented in figure 1.

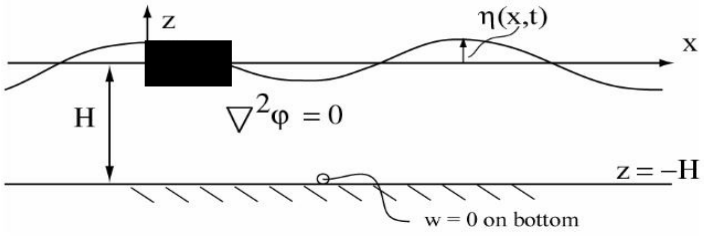

Figure 1: A body in two dimensional waves

From the physics' point of view, if there is a flow that passes through a well defined control volume, the continuity equation must be satisfied. This assumption is valid as long as the space in the control volume is significantly larger than the distance between the molecules inside it according to [CENGEL, 2013]. Mathematically, the continuity is expressed as in equation 4.

$$\frac{\partial u}{\partial x} + \frac{\partial v}{\partial y} + \frac{\partial w}{\partial z} = 0 \tag{4}$$

If the flow is incompressible, irrotational and inviscid, the potential theory can be used. The velocities of the fluid domain can expressed in terms of a velocity potential, ϕ, and the total velocity can be expressed as in equation 5.

$$\mathbf{V} = \nabla\phi = \frac{\partial \phi}{\partial x}\mathbf{i} + \frac{\partial \phi}{\partial y}\mathbf{j} + \frac{\partial \phi}{\partial z}\mathbf{k} = u\mathbf{i} + v\mathbf{j} + w\mathbf{k} \tag{5}$$

Vectors **i**, **j** and **k** are the unit vectors in x, y and z-directions in a Cartesian coordinate system respectively. Due to the assumptions that the flow is incompressible and irrotational, the equation of continuity can further be expressed as in equation 6, which is the Laplace equation.

$$\nabla^2\phi = 0 \tag{6}$$

Equation 6 must be satisfied at all time within the defined fluid domain with an exception of air-water interface. From figure 1, the vertical velocity at the sea bed must be zero for a finite water depth.

Dynamic free surface condition

On the free surface, the Bernoulli equation must be satisfied which is shown in figure 2 for two arbitrary points on the free surface. The Bernoulli equation will be expressed as in formula 7.

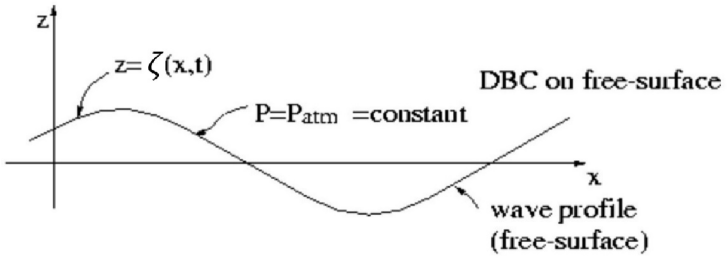

Figure 2: Dynamic free surface condition requirement of constant pressure on the free surface

$$\frac{p}{\rho} + \frac{1}{2}U_1^2 + g\zeta_1 + \frac{\partial \phi_1}{\partial t} = \frac{p}{\rho} + \frac{1}{2}U^2 + g\zeta + \frac{\partial \phi}{\partial t} = Constant \tag{7}$$

In linear wave theory, the velocity U and U_1 are assumed small compared with the other parameters in the formula, therefore the quadratic term of U are neglected. Waves are usually assumed to be harmonic. Thus, $g\zeta_1$ will disappear because of the phase shift. The expression on the left hand side will be zero, and the Bernoulli equation will be simplified as expressed in equation 8.

$$g\zeta + (\frac{\partial \phi}{\partial t})_{z=\zeta} = 0 \tag{8}$$

This formula will give the wave elevation profile, ζ, in terms of the time derivative of the velocity potential.

Kinematic boundary conditions

According to [Pettersen, 2007], the water particles at the free surface will stay on the surface when the waves are small. This indicates that the fluid particles at the surface have the same vertical motion of the wave profile. Figure 3 illustrates the velocity component of the water particle on the surface. This can be mathematically expressed as in equation 9.

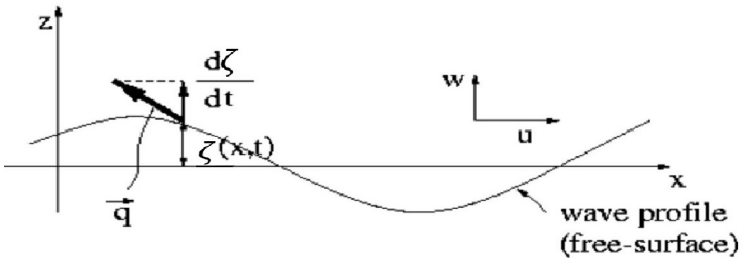

Figure 3: Velocity at the free surface and for the water particles

$$\frac{\partial \zeta}{\partial t} = \frac{\partial \phi}{\partial z} \tag{9}$$

By using equation 8 obtained from the dynamic free surface condition, and taking the derivative of the wave elevation profile, ζ, the kinematic free surface condition can be rewritten as equation 10. Assuming small wave elevation, the free surface condition is satisfied on the mean free surface at $z = 0$.

$$\frac{\partial^2 \phi}{\partial t^2} + g\frac{\partial \phi}{\partial z} = 0 \tag{10}$$

If the velocity potential oscillates harmonically with an angular frequency, ω, equation 10 can be rewritten as following:

$$-\omega^2 \phi + g\frac{\partial \phi}{\partial z} = 0 \tag{11}$$

If a finite water depth is assumed, the boundary condition for an impermeable sea can be applied. Equation 11 will give a solution of the velocity potential of incident waves as expressed in formula 12 for finite water depth.

$$\phi = \frac{g\zeta}{\omega} \frac{\cosh k(z+h)}{\cosh kh} \cos(\omega t - kx) \tag{12}$$

Where h is the water depth, and k is the wave number that depends on the wave angular frequency. The dispersion relation is shown in equation 13 for constant water depth.

$$\frac{\omega^2}{g} = k \tanh(kh) \tag{13}$$

If infinite water depth is assumed, h will approach to infinity, and $tanh(kh)$ will approach to 1. The dispersion relation with the corresponding velocity potential will be expressed in equation 14 for deep water condition.

$$\phi = \frac{g\zeta}{\omega} e^{kz} \cos(\omega t - kx) \qquad \frac{\omega^2}{g} = k \tag{14}$$

On the body surface, it is required that the normal velocity is equal to the differentiation of the velocity potential. This is generalized as in equation 15.

$$\frac{\partial \phi}{\partial n} = \boldsymbol{V} \cdot \boldsymbol{n} \tag{15}$$

Where $\boldsymbol{V}$ is any type of velocity the body moves with, and $\partial/\partial n$ denotes the differentiation along the normal direction of the body surface, where the positive normal direction is defined into the fluid domain. This condition implies that there is no fluid that enters or leaves the body surface.

A.3 Regular wave theory

Linear wave theory gives the linearized mathematical formulation of gravity induced waves. This is achieved by using the free surface condition together with Laplace equation and the sea bottom condition.

The wave number, k, can be expressed as a function of the wave length, λ. This is shown in equation 16.

$$k = \frac{2\pi}{\lambda} \tag{16}$$

The restrictions for linear analysis for propagating waves is stated in [Dingemans, 1996], that the wave steepness has to be small for deep water waves. As for shallow water waves, the restrictions is that the wave amplitude has to be small compared to the water depth. With this, it can be expected that the linear wave theory will differ for physical waves with higher steepness.

Phase and Group velocity

As mentioned in section A.2, the dispersion relation for deep water and shallow water are different. This will lead to different expressions for phase velocity and group velocity of the waves that travel in deep and shallow water.

If some interference of the two sinusoidal waves occurs, and the two waves have slightly different wave lengths but same amplitude and the propagation direction, a wave group can be defined with the group velocity. The group velocity are generally expressed as in equation 17.

$$c_g = \frac{d\omega}{dk} \tag{17}$$

The group velocity is different depending on which dispersion relationship of the ω and k from the wave. Table 1 gives an overview of three cases for a linear wave with a wave number $k = 2\pi/\lambda$ and the angular frequency as $\omega = 2\pi/T$. The formulas has been taken from [Dingemans, 1996] and [Faltinsen, 1993]. It should be noted that for intermediate depth, the wave length is the solution of the implicit equation by solving λ for a specific period, T.

Table 1: Linear theory frequency dispersion of gravity waves

Quantity	deep water ($h \geq 0.5\lambda$)	shallow water ($h \leq 0.05\lambda$)	Intermediate depth (all λ and h)
Dispersion relation	$\omega^2/g = k$	$\omega^2 = k^2 gh$	$\omega^2 = gk\tanh(kh)$
Phase velocity	$c_p = \frac{g}{2\pi} \cdot T$	$c_p = \sqrt{gh}$	$c_p = \sqrt{\frac{g}{k}\tanh(kh)}$
Group velocity	$c_g = \frac{g}{4\pi} \cdot T$	$c_g = \sqrt{gh}$	$c_g = \frac{1}{2}c_p(1 + \frac{2kh}{\sinh(2kh)})$
Wave length	$\frac{g}{2\pi} \cdot T^2$	$T \cdot \sqrt{gh}$	$(\frac{2\pi}{T})^2 = \frac{2\pi g}{\lambda}\tanh(\frac{2\pi h}{\lambda})$

A.4 Analytic slamming theory

Slamming on a cylinder

According to [Faltinsen, 1993], the free surface condition is $\phi = 0$ when $z = 0$. This comes from the kinematic condition expressed in equation 10 in A.2 with the assumption of the fluid accelerations are much larger than the gravitational acceleration. The pressure is assumed to be constant and equal to atmospheric pressure. In order to simplify the problem further, the cylinder is replaced by an equivalent flat plate. The boundary condition can approximately be described as in equation 18.

$$\frac{\partial\phi}{\partial z} = -V \quad on \quad z = 0 \tag{18}$$

This boundary value problem can be solved. In [Faltinsen, 1993] the solution is obtained as the velocity potential on the body, expressed as in formula 19.

$$\phi = -V(c^2 - x^2)^{\frac{1}{2}} \quad |x| \leq c(t) \tag{19}$$

Here, V is the constant velocity, x is the x-coordinate on the body, and c is the wetted body area expressed as in formula 20 related to the Von Karma method. The wetted body area is illustrated in figure 4 for a cylinder.

$$c^2(t) = 2VtR - V^2t^2 \tag{20}$$

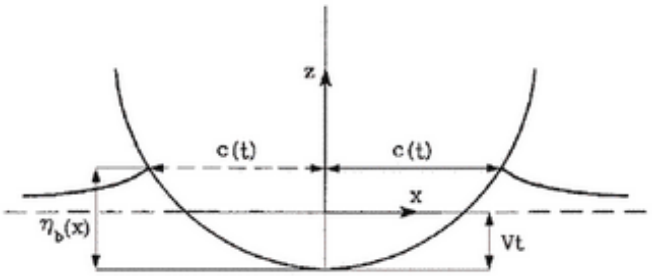

Figure 4: Definition of the wetted body area

In this case, the body is a circular cylinder with a characteristic length R as the cylinder radius. When the velocity potential is obtained, the pressure and the force can be calculated. However, as mentioned, the slamming occurs over a small time duration. This means that the change of time will be larger than the change in space. This indicates that the time derivative will be dominating in the pressure term. The hydrodynamic pressure will approximately be expressed as following:

$$p = -\rho\frac{\partial\phi}{\partial t} = \rho V\frac{c}{(c^2 - x^2)^{\frac{1}{2}}}\frac{dc}{dt} \tag{21}$$

The force can be obtained by integrating along the body surface, which is expressed in formula 22.

$$F_3 = \int_{-c}^{c} pdx = \rho Vc\int_{-c}^{c}\frac{dx}{(c^2 - x^2)^{\frac{1}{2}}} = V\frac{d}{dt}(\rho\frac{\pi}{2}c^2) \tag{22}$$

By using equation 22 for slamming force, and inserting the expression for wetted body area, the slamming coefficient can be determined as formula 23.

$$C_s = \frac{F_3}{\frac{1}{2}\rho V^2 2R} \tag{23}$$

The slamming coefficient is used to compare the experimental results with the analytic calculations. It has been proved in many experiments in [Faltinsen, 1993] that the experimental C_s is larger than the calculated one. Wagner (1932) presented his method, which suggests that the reason for C_s is larger during the experiments is that the estimated wetted body in Von Karman method is too small. His work concludes that the wetted body area for a circular cylinder should be defined as in equation 24.

$$c = 2\sqrt{VtR} \tag{24}$$

Solution of Wagner model

The solution of the boundary value problem in Wagner model can be found in complex representation. In [Faltinsen and Timokha, 2009], the complex velocity potential is expressed as in equation 25.

$$W = \phi + i\psi = iVz - iV(z^2 - c^2)^{1/2} \tag{25}$$

Where ϕ is the velocity potential and ψ is the stream line function. The complex velocity is the partial derivative with respect to z, and the expression becomes $\partial W/\partial z = iV - iV\frac{z}{(z^2-c^2)^{1/2}}$.

In order to check if the boundary conditions are satisfied, the polar coordinates can be used related to the complex number analysis. By introducing $z - c = r_1 \exp(i\theta_1)$ and $z + c = r_2 \exp(i\theta_2)$ the expression of the partial part from the compelex velocity becomes:

$$(z^2 - c^2)^{1/2} = \sqrt{r_1 r_2} \exp[i\frac{1}{2}(\theta_1 + \theta_2)] \tag{26}$$

When $\theta_1 = \pi$ and $\theta_2 = 0$, the $|x| \leq c$ and $y = 0^-$ which gives $(z^2 - c^2)^{1/2} = i(c^2 - x^2)^{1/2}$ with $y = 0^-$ corresponding to the underside of the body. When $x \geq c$ and $y = 0$, both θ_1 and θ_2 are zero. This leads to an expression as expressed in formula 27.

$$(z^2 - c^2)^{1/2} = (x^2 - c^2)^{1/2} \qquad \text{for} \qquad x \geq c \qquad y = 0 \tag{27}$$

Furthermore, $x \leq -c$ and $y = 0^{\pm}$ means that $\theta_1 = \theta_2 = \pm\pi$. This gives to equation 28.

$$(z^2 - c^2)^{1/2} = -(x^2 - c^2)^{1/2} \qquad \text{for} \qquad x \leq -c \qquad y = 0 \tag{28}$$

With expression 27 and 28, the solution of the boundary problem gives a velocity potenial $\phi = 0$ for $|x| \geq c$ on $y = 0$. This gives a complex velocity as following:

$$\frac{\partial W}{\partial z} = u - iv = iV + Vx(c^2 - x^2)^{-1/2} \qquad \textit{for} \qquad |x| \leq c \qquad \text{on} \qquad y = 0^- \tag{29}$$

From the imaginary part of v as $v = \partial\phi/\partial y$, the boundary condition $\phi_y = -V$ will be satisfied. The complex velocity potential can be rewritten as $W = iVx - V(c^2 - x^2)^{1/2}$ when $|x| \leq c(t)$ and $y = 0^-$. This gives the velocity potential on the body as equation 30.

$$\phi = -V(c^2 - x^2)^{1/2} \qquad \text{for} \qquad |x| \leq c(t) \tag{30}$$

In Chapter 8.3.1 from *Hydrodynamics of High-Speed Marine Vehicles* by *O.M. Faltinsen* [Faltinsen, 2012], the hydrodynamic pressure is expressed as $p - p_a = -\rho\partial\phi/\partial t$. It is stated that there is nothing in the derivations that prevents the velocity V from being dependent on time. This gives a pressure difference as expressed in equation 31.

$$p - p_a = \rho V \frac{c}{(c^2 - x^2)^{1/2}} \frac{dc}{dt} + \rho \frac{dV}{dt}(c^2 - x^2)^{1/2} \tag{31}$$

The first therm in the equation is the slamming pressure as it is associated with the rate of change of the wetted surface which is approximately $2dc/dt$. The second part is the added mass pressure. However, the slamming pressure will be infinite at the edges when $x = \pm c$, which is nonphysical.

The two dimensional vertical force acting on the body can be expressed as in formula 32.

$$F_3 = \int_{-c}^{c} p dx = \rho V c \frac{dc}{dt} \int_{-c}^{c} \frac{dx}{\sqrt{x^2 - x^2}} + \rho \frac{dV}{dt} \int_{-c}^{c} (c^2 - x^2)^{1/2} dx = \rho \phi V c \frac{dc}{dt} + \rho \frac{\pi}{2} c^2 \frac{dV}{dt} \tag{32}$$

The last therm $\rho \pi c^2/2$ is the two dimensional added mass in heave direction for the plate as shown in the boundary value problem in figure 2.6. This is due to the linearization of the problem, by assuming that $dc/dt = 0$ and that the velocity V is positive downwards. The damping is not present due to the free surface condition $\phi = 0$ where no wave can be generated. In order to generate waves, surface tension or gravity must be included.

The added mass of the plate is half of the added mass in heave of the plate in infinite fluid. This is because velocity potential is antisymmetric about x-axis. After the hydrodynamic force on the plate in infinite fluid is found, the integration is on both sides of the plate. During an impact, the pressure can be integrated on the lower side in order to get the correct forces. It follows that the heave added mass is half of the added mass of the plate in infinite fluid.

The slamming problem is considered in two dimensions. Then by using Wagner's method, the wetted surface can be predicted from the intersection of the body surface and the free surface. Due to the condition of $\phi = 0$ on the free surface, the horizontal velocity is zero on the surface. The vertical velocity can be expressed with the complex velocity and equations 27 and 28 which give following result:

$$\frac{\partial \phi}{\partial z} = \frac{V|x|}{\sqrt{x^2 - c^2(t)}} - v \qquad \text{on} \qquad z = 0 \qquad |x| \leq c(t) \tag{33}$$

The relative vertical velocities between the fluid particle on the free surface of the body must be known. This can be expressed as in equation 34.

$$w_r = \frac{\partial \phi}{\partial z} + V \tag{34}$$

The predicted vertical distance of the fluid particles that moved along the body surface can be expressed as in formula 35.

$$\eta_b(x) = \int_0^t \frac{V|x|}{\sqrt{x^2 - c^2(t)}} dt \tag{35}$$

In [Faltinsen, 2012], the vertical distance $\eta_b(x)$ is a known function. Thus equation 35 can determine the wetted length, $c(t)$. By changing the integration variable from t to c, equation 35 can be rewritten as:

$$\eta_b(x) = \int_0^x \frac{x\mu(c)dc}{\sqrt{x^2 - c^2}} \qquad \text{with} \qquad \mu(c)dc = Vdt \tag{36}$$

Where $\mu(c)$ is unknown. Therefore the integral in 36 can be used to determine $\mu(c)$ which can afterwards be used to find the wetted length. [Faltinsen, 2012] suggested an approximation for expression of $\mu(c)$ as expressed in formula 37 with two unknown constants A_0 and A_1.

$$\mu(c) \approx A_0 + A_1 c \tag{37}$$

When integrating equation 35 by using expression 37 for $\mu(c)$ the vertical distance $\eta_b(x)$ can be rewritten as following:

$$\eta_b(x) = A_0 \frac{\pi}{2} x + A_1 x^2 \tag{38}$$

If the vertical distance in equation 38 is given as a second-order polynomial, the unknown coefficients from formula 37 can be determined. This leads to an expression of $\mu(c)$ which further can be used to determined the wetted length c as a function of time. For a case with a symmetric impact of a wedge with a deadrise angle β, the vertical distance is dependent on the angle as $\eta_b(x) = |x| \tan\beta$. If a constant vertical velocity is considered, the wetted length is expressed as in equation 39.

$$c(t) = \frac{\pi V t}{2 \tan\beta} \tag{39}$$

If a time varying velocity is considered with a body shaped described as $\eta_b(x) = Ax + Bx^2$, equation 40 along with equation 36 must be solved in order to obtain the wetted length.

$$(\frac{2A}{\pi} c + \frac{B}{2} c^2) = \int_0^t V dt \tag{40}$$

By assuming that velocity is changing linearly during the impact, $V(t) = V_0 + V_1 t$, the wetted length is expressed as in formula 41 with a condition that the wetted length is a positive and real value.

$$c(t) = -\frac{2A}{\pi B} + \frac{\sqrt{(2A/\pi)^2 + 2BV_0 t + BV_1 t^2}}{B} \tag{41}$$

It should be noted that the Wagner method is not valid for water exit analysis. This is due to the free surface condition $\phi = 0$. It is explained in [Faltinsen, 2012] that during the water exit analysis, the fluid acceleration is no longer dominant relative to the gravitational acceleration. If the water exit is considered, then von Karman's solution for this problem can be used. This requires a numerical method.

A.5 Piston wave maker

The waves that were used during the experiments are generated by a piston wave maker. According to [Miskovic et al., 2008], there is a general procedure for producing the desired waveform. From the report, it is expressed by the Biesel function as described in equation 42.

$$\eta(f) = 0 + ic_0 x(f) \qquad \text{with} \qquad c_0 = \frac{2(\cosh(2kh) - 1)}{\sinh(2kh) + 2kh} \tag{42}$$

$\eta(f)$ and $x(f)$ are the surface elevation and paddle motion in frequency domain respectively, and c_0 is the Biesel transfer function for a piston wave maker.

B Experimental results

B.1 Decay test

January tests

The results of the decay test conducted in *January, 2018* are presented in this section. The model is attached with one wave probe on the deck, and the side deck is mounted with a force sensor.

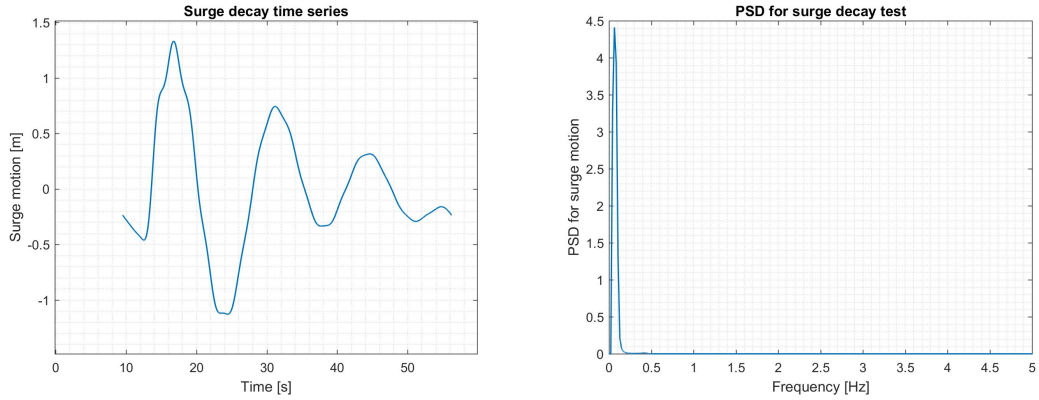

Surge decay test results measured by two accelerometers. Left: Surge motion time series. Right: PSD of the time series, peak at $0.0642Hz$

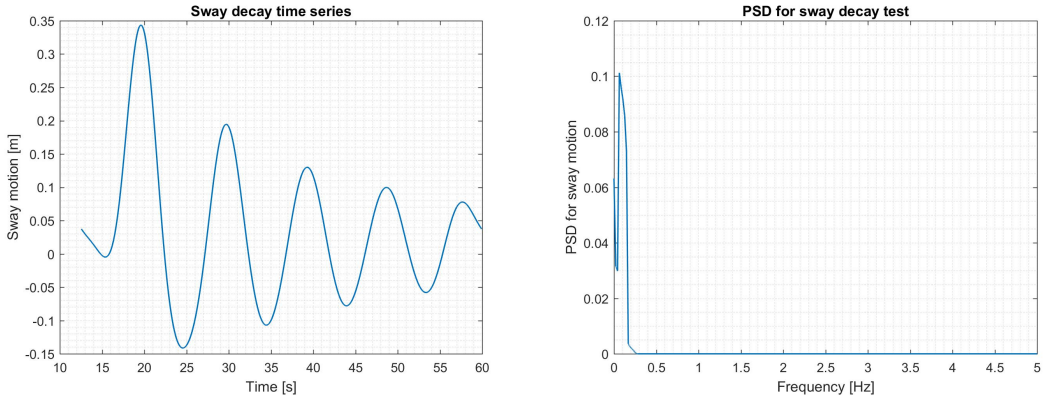

Sway decay test results measured by the springs attached to the model. Left: Sway motion time series. Right: PSD of the time series, peak at $0.0634Hz$

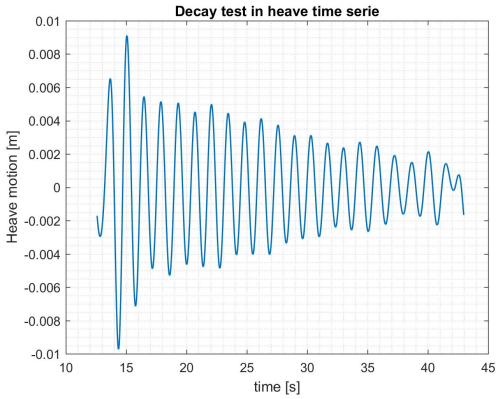

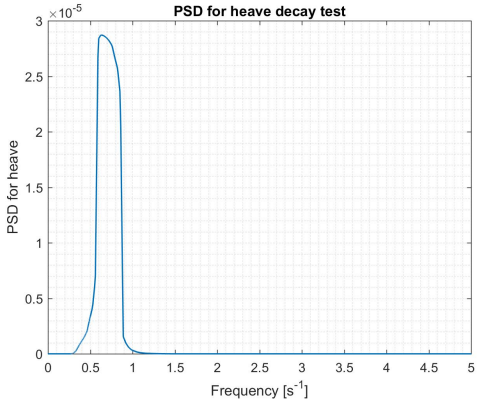

Heave decay test results measured by the accelerometers. Left: Heave motion time series. Right: PSD of the time series, peak at $0.63Hz$

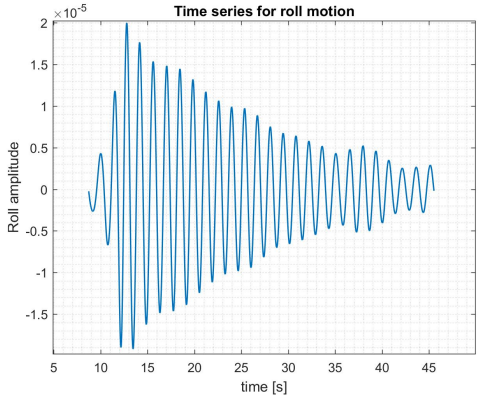

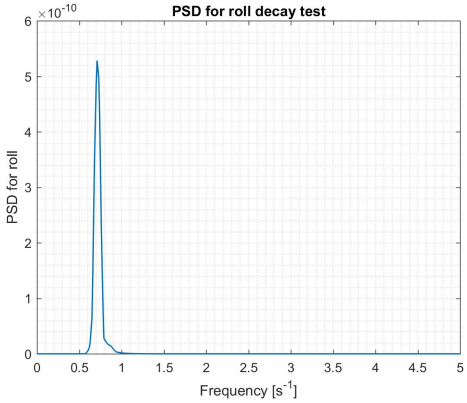

Roll decay test results measured by the accelerometers. Left: roll motion time series. Right: PSD of the time series, peak at $0.71Hz$

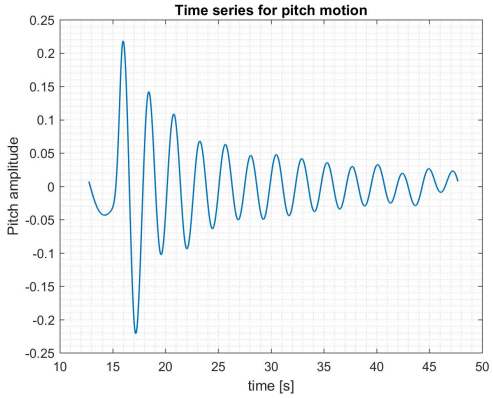

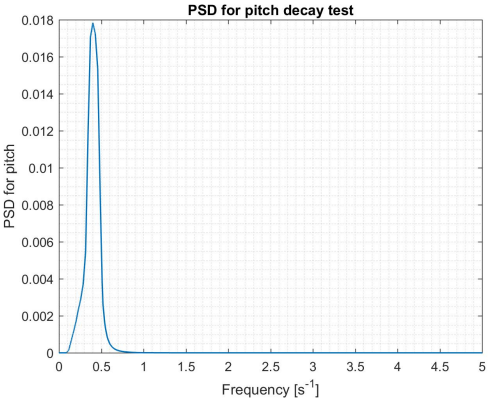

Pitch decay test results measured by the accelerometers. Left: Pitch time series. Right: PSD of the pitch time series, peak at $0.4006Hz$

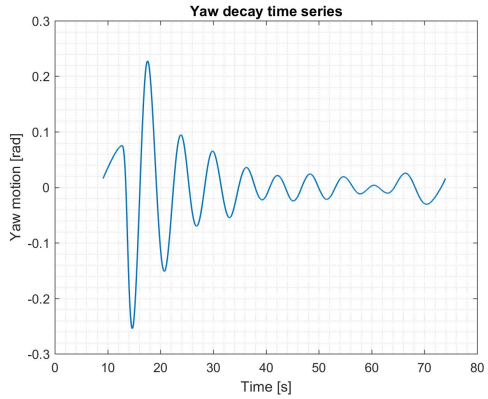

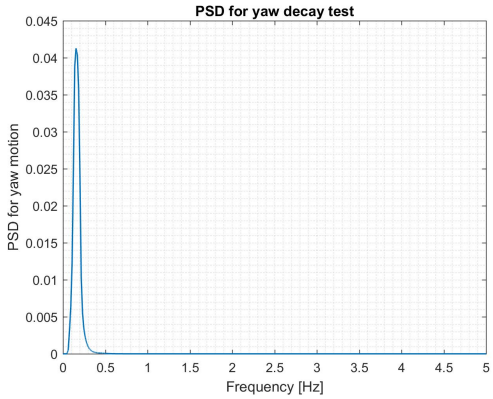

Yaw decay test results measured by the accelerometers. Left: Yaw time series. Right: PSD of the yaw time series, peak at $0.1542Hz$

***April* tests**

Results from the decay test conducted *April, 2018* at *Lilletanken* are presented in this section. The model is mounted with one wave probe, and deck is attached to the model with a force sensor.

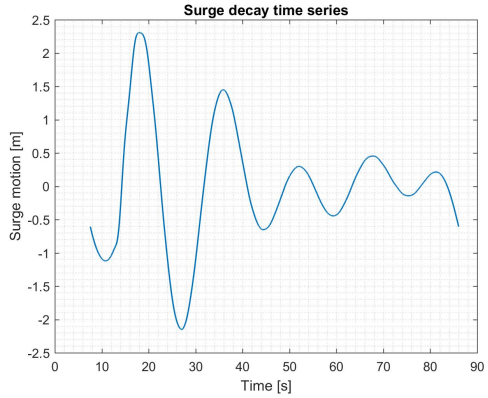

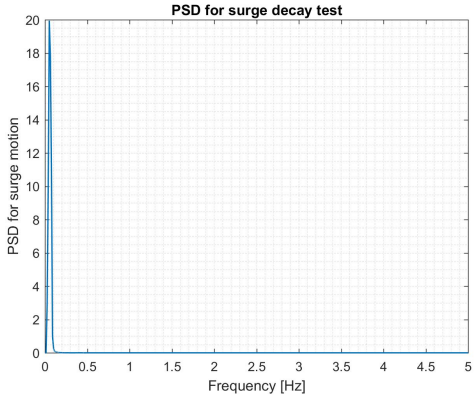

Surge decay test results. Left: Surge motion time series. Right: PSD of the time series, peak at $0.051Hz$

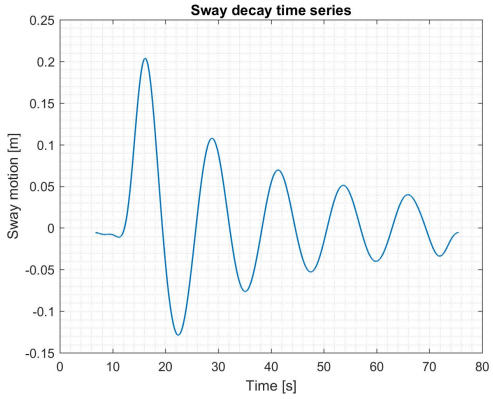

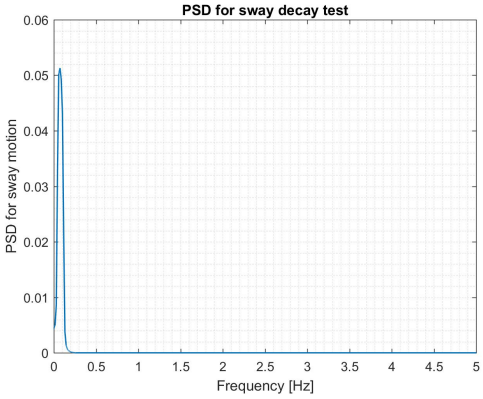

Sway decay test results. Left: Sway motion time series. Right: PSD of the time series, peak at $0.0727Hz$

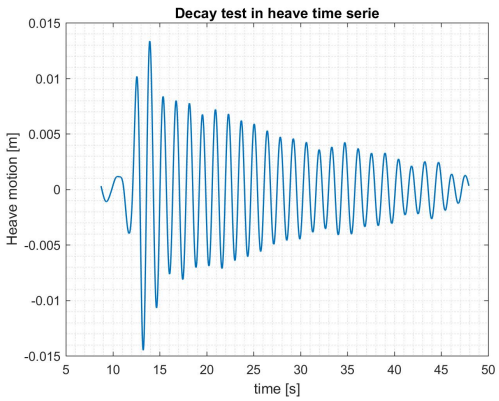

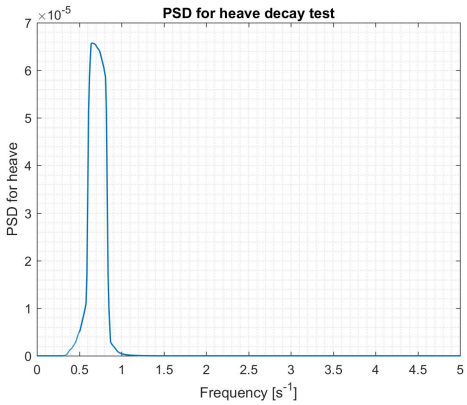

Heave decay test results. Left: Heave motion time series. Right: PSD of the time series, peak at $0.66Hz$

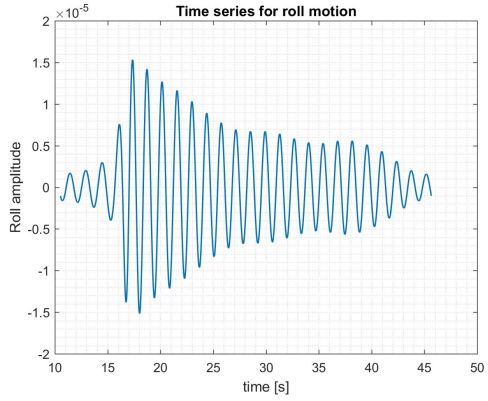

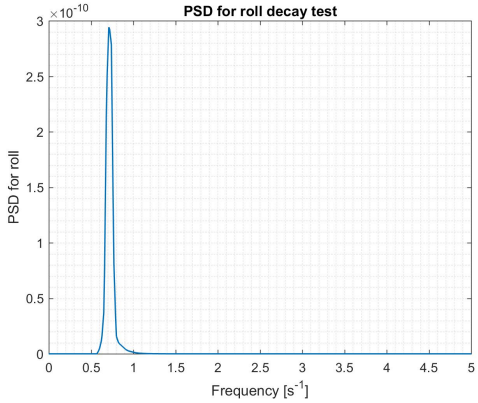

Roll decay test results. Left: Roll motion time series. Right: PSD of the roll motion time series, peak at $0.71Hz$

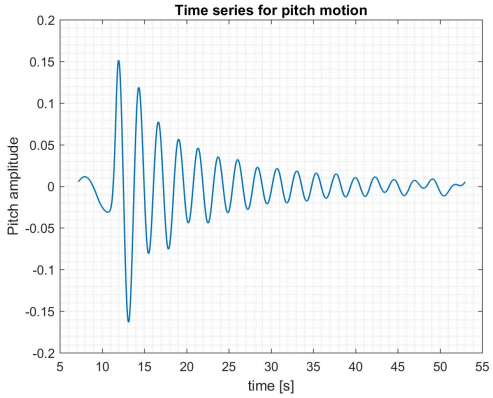

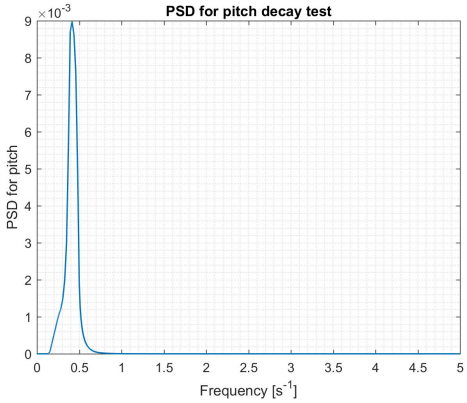

Pitch decay test results. Left: Pitch motion time series. Right: PSD of the time series, peak at $0.4159Hz$

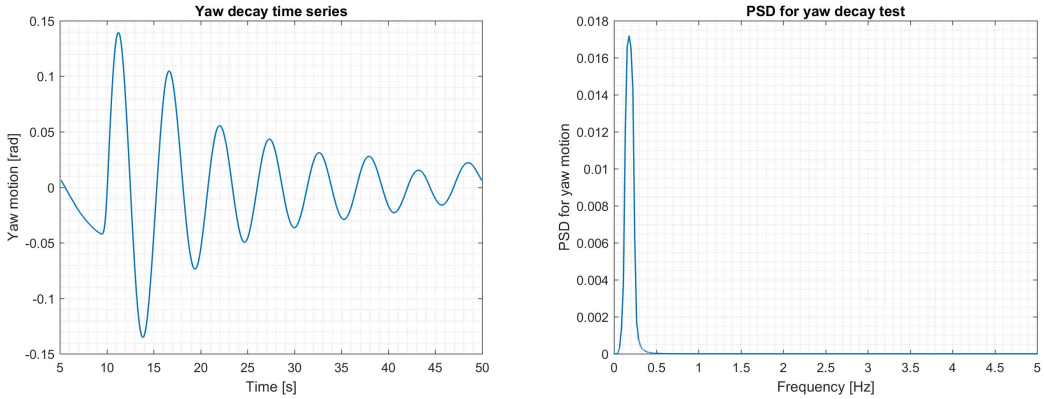

Yaw decay test results. Left: Yaw motion time series. Right: PSD of the time series, peak at $0.1786Hz$

The results of the decay test where the model is mounted with three wave probes, and the platform is not attached.

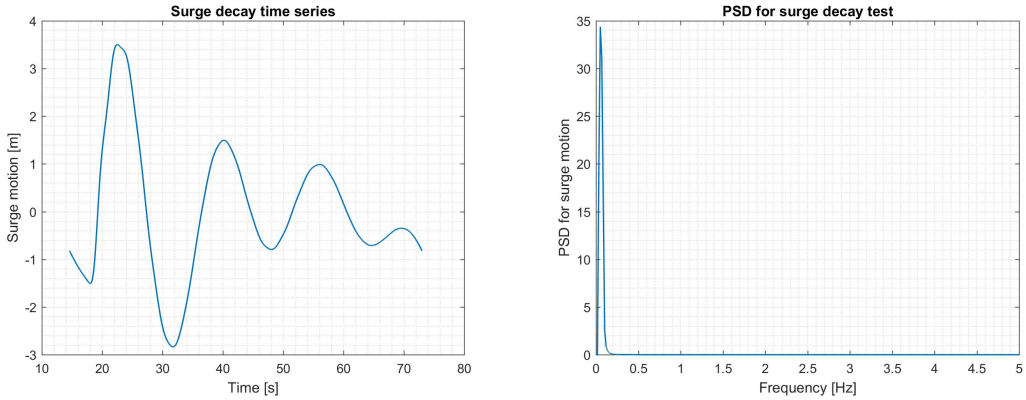

Surge decay test results. Left: surge motion time series. Right: PSD of the time series, peak at $0.0514Hz$

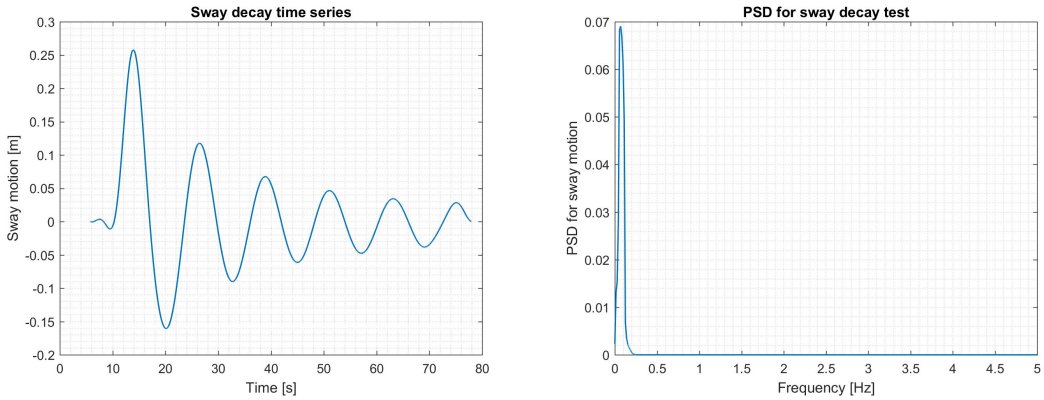

sway decay test results. Left: sway motion time series. Right: PSD of the time series, peak at $0.06906Hz$

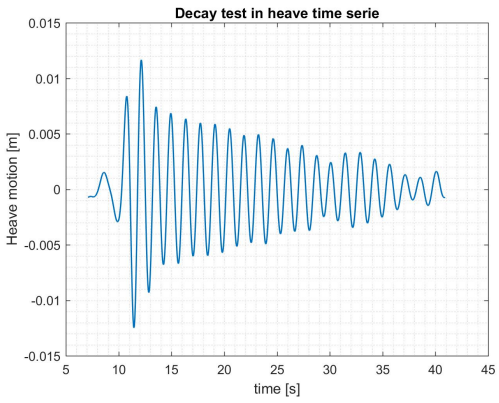

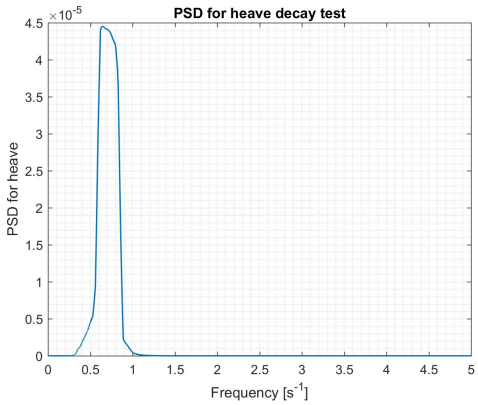

Heave decay test results. Left: Heave motion time series. Right: PSD of the time series, peak at $0.65Hz$

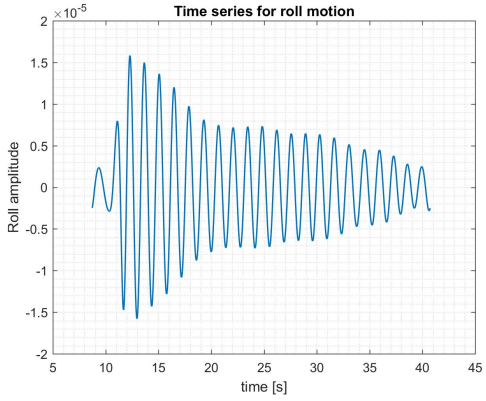

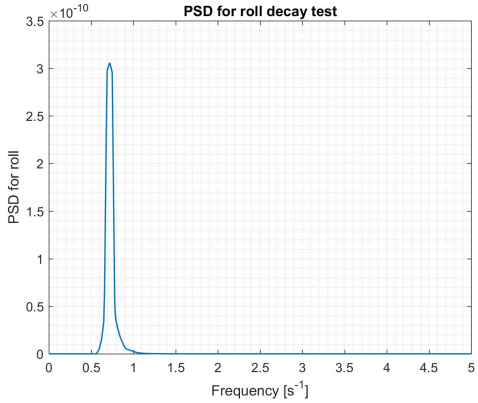

Roll decay test results. Left: Roll motion time series. Right: PSD of the time series, peak at $0.72Hz$

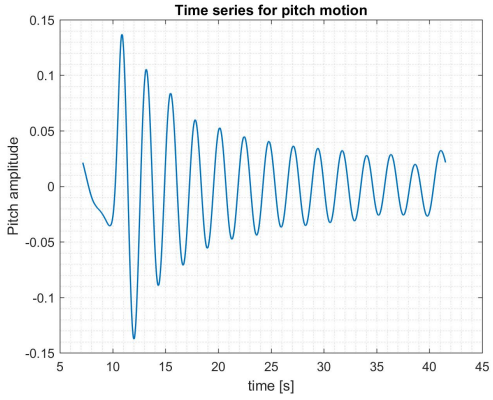

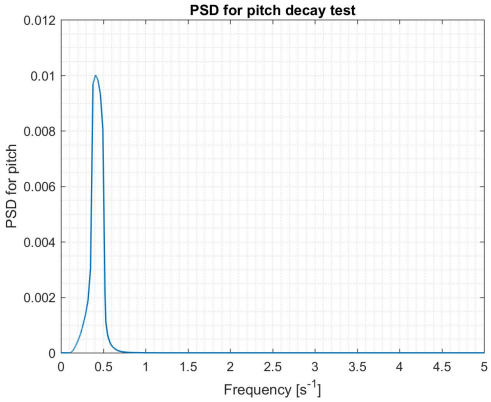

Pitch decay test results. Left: Pitch motion time series. Right: PSD of the time series, peak at $0.4284Hz$

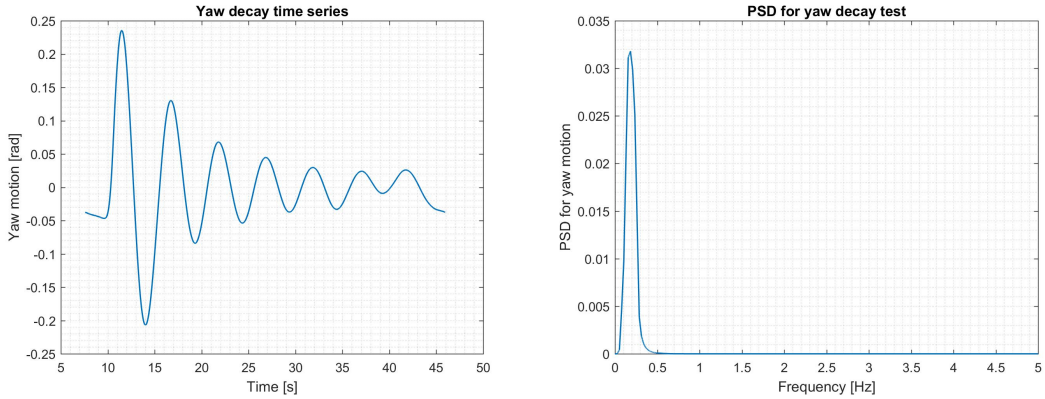

Yaw decay test results. Left: Yaw motion time series. Right: PSD of the time series, peak at $0.1825Hz$

B.2 Pluck test of the plate

Solid plate

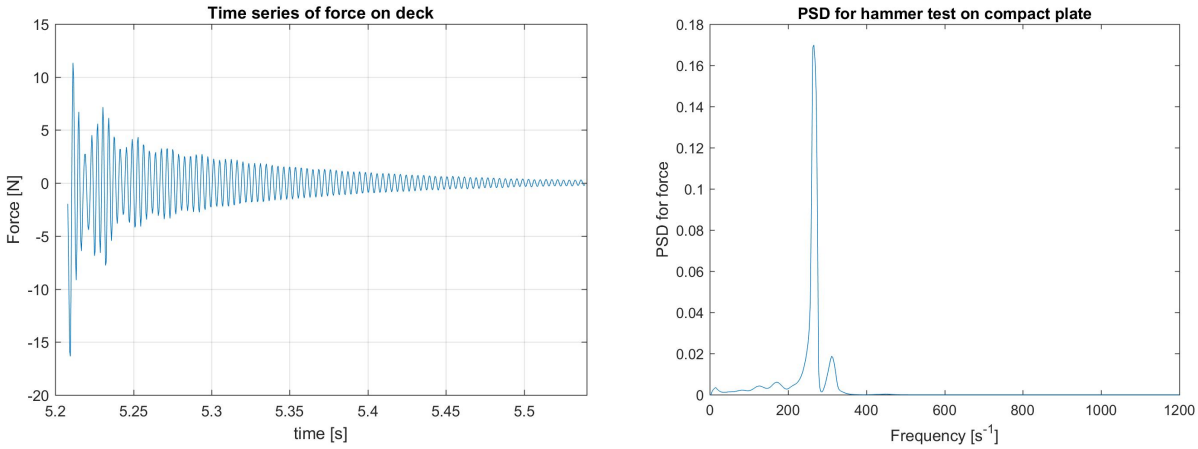

Decay test of the deck. The decay test results for test no. 2. Left: Time series. Right: The PSD of the measured time series of the force

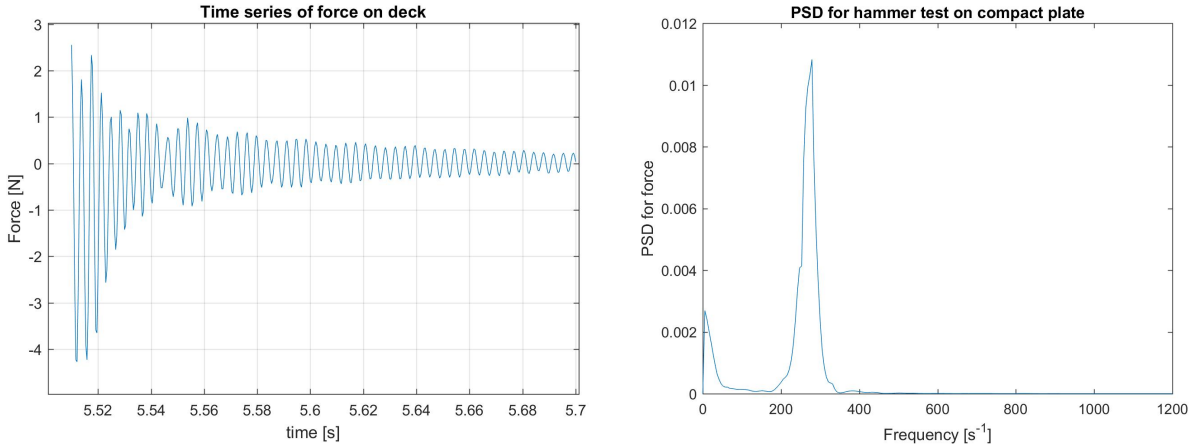

Decay test of the deck. The decay test results for test no. 3. Left: Time series. Right: The PSD of the measured time series of the force

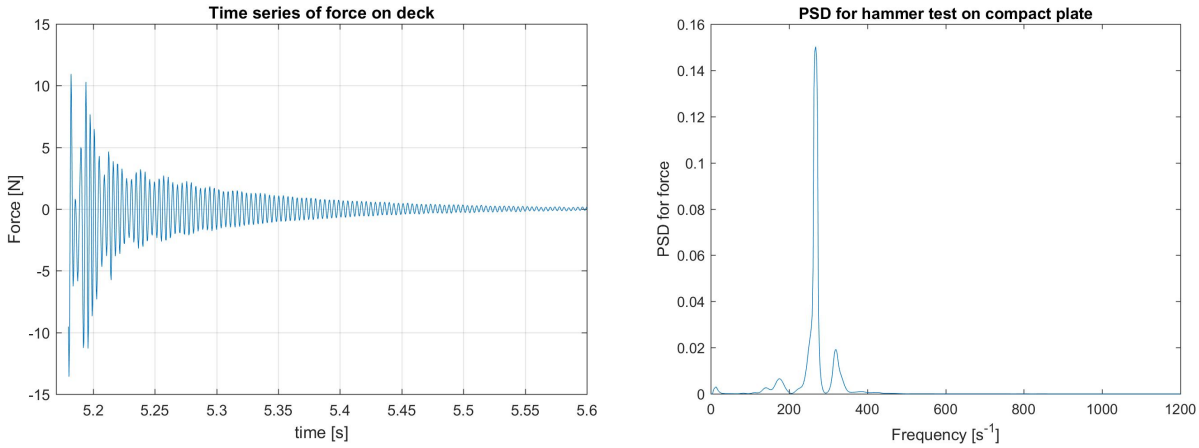

Decay test of the deck. The decay test results for test no. 4. Left: Time series. Right: The PSD of the measured time series of the force

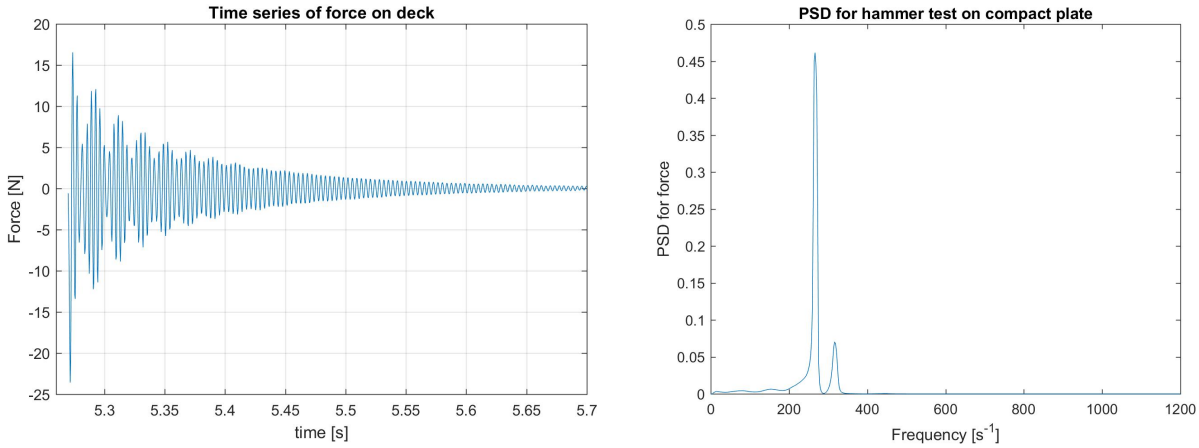

Decay test of the deck. The decay test results for test no. 5. Left: Time series. Right: The PSD of the measured time series of the force

perforated plate

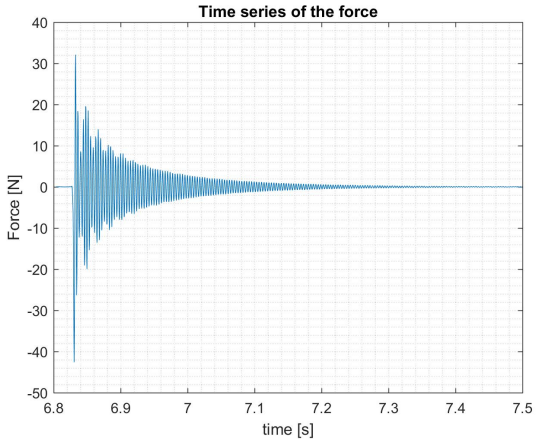

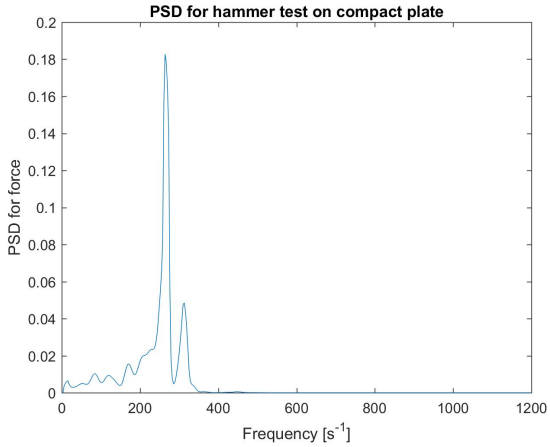

Decay test of the perforated plate. Test results for test no. 1. Left: Time series. Right: The PSD of the measured time series of the force

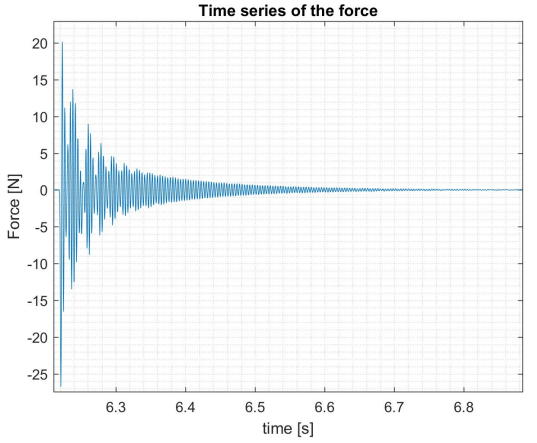

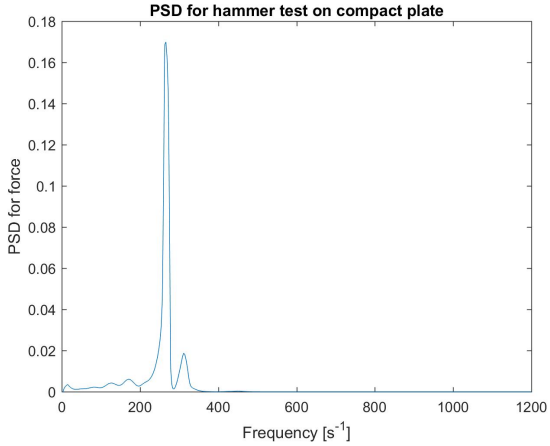

Decay test of the perforated plate. Test results for test no. 2. Left: Time series. Right: The PSD of the measured time series of the force

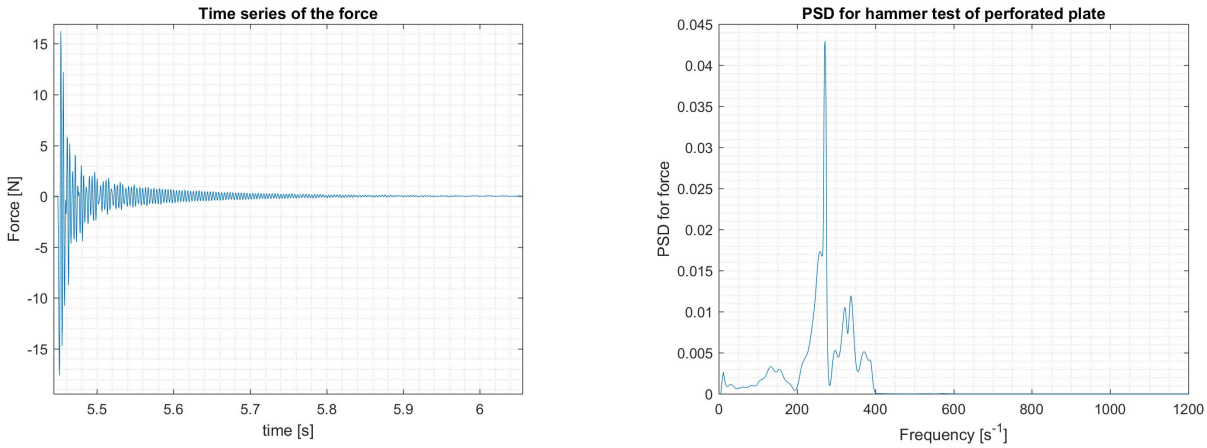

Decay test of the perforated plate. Test results for test no. 3. Left: Time series. Right: The PSD of the measured time series of the force

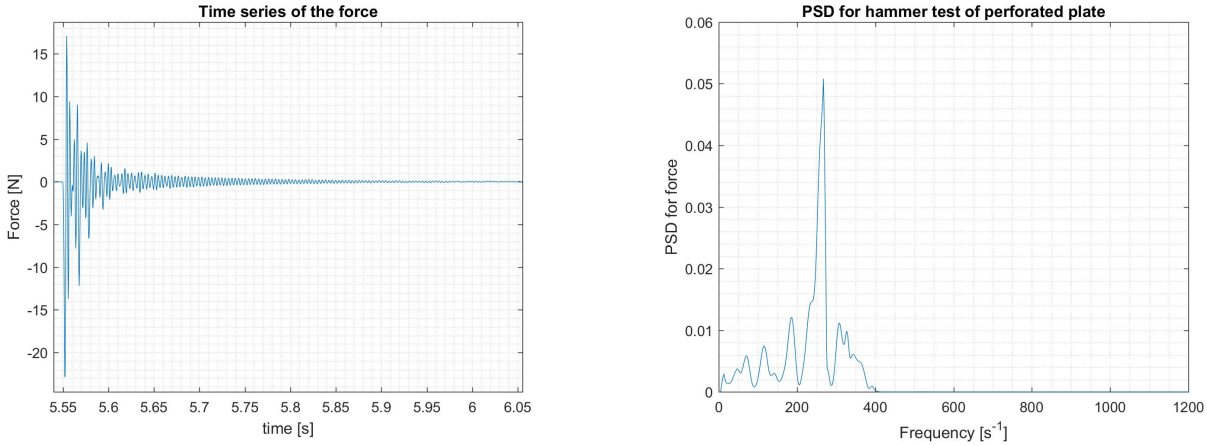

Decay test of the perforated plate. Test results for test no. 4. Left: Time series. Right: The PSD of the measured time series of the force

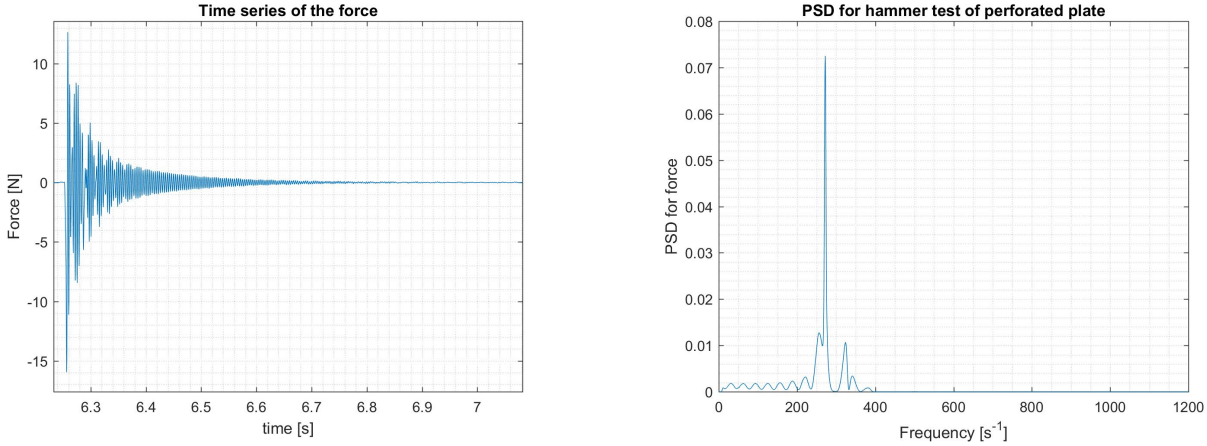

Decay test of the perforated plate. Test results for test no. 5. Left: Time series. Right: The PSD of the measured time series of the forcee

B.3 RAO

Response Amplitude Operator obtained from the experiments are plotted with the calculated RAO from *WADAM*

January tests: Test series 200

Test results from the test series *200* conducted *January, 2018* at *Lilletanken* are presented in this section.

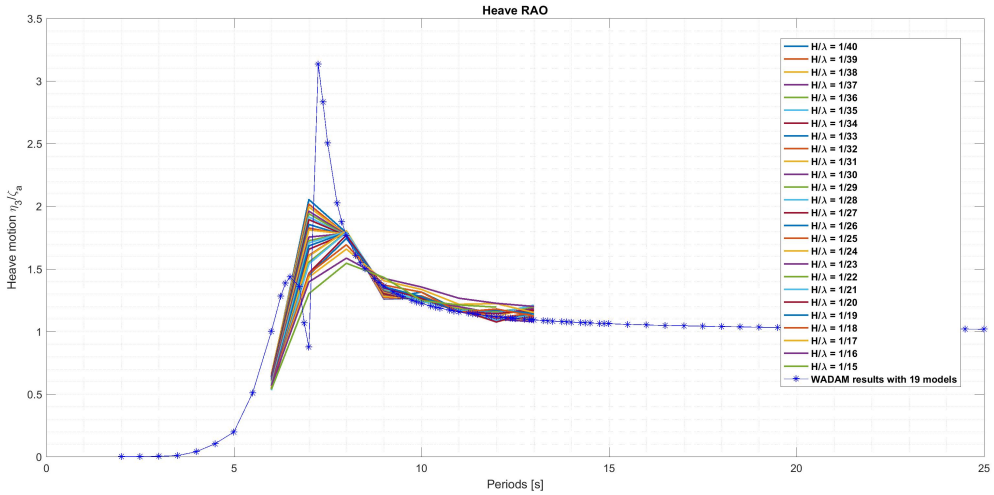

Heave RAO from test series *200* which is compared with results calculated from *WADAM* with 19 mirroring images

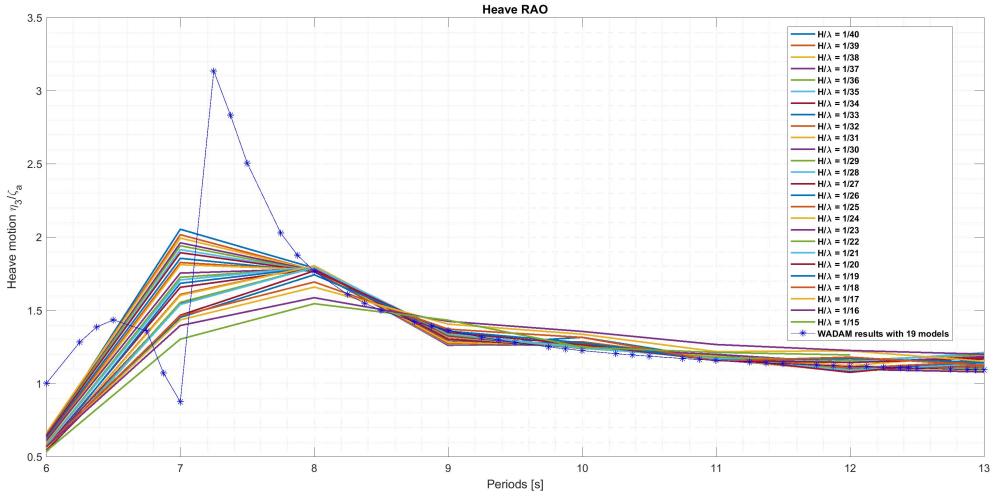

A region which is zoomed in from period $T = 6s$ to $T = 13s$ of heave RAO from test series *200* with results from *WADAM* calculated with 19 bodies for all steepness

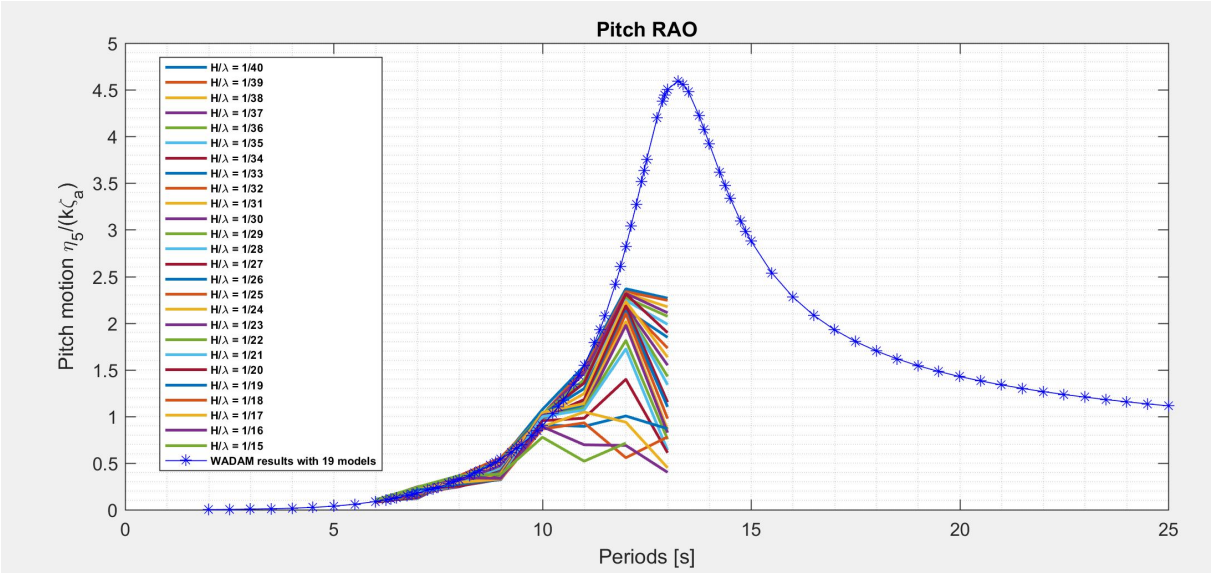

Pitch RAO from test series *200* which is compared with results calculated from *WADAM* with 19 mirroring images

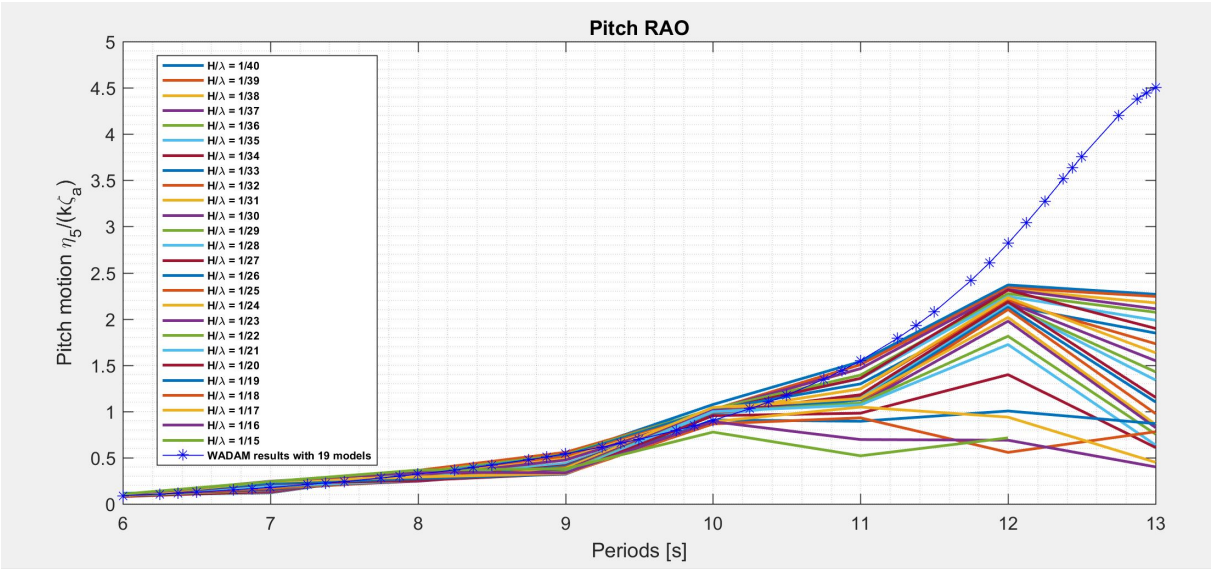

A region which is zoomed in from period $T = 6s$ to $T = 13s$ of pitch RAO for all steepness from test series *200* with results from *WADAM* calculated with 19 bodies

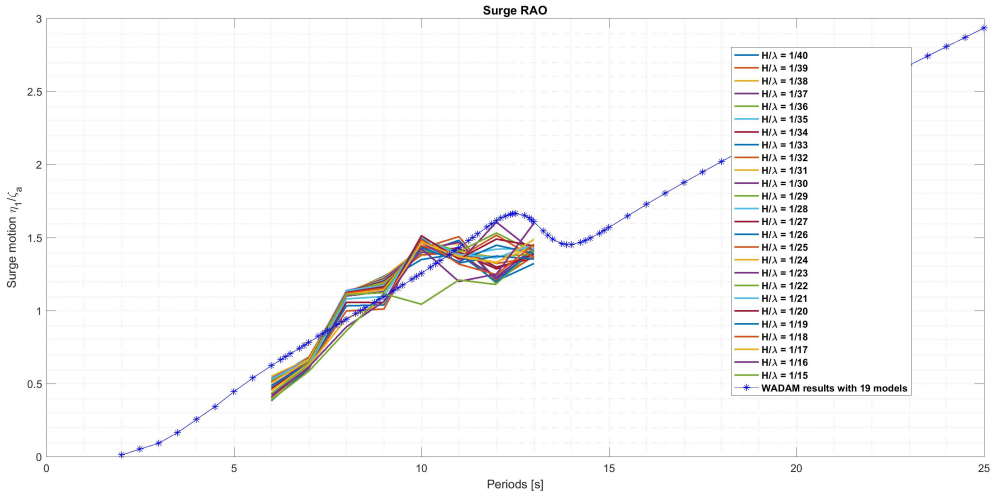

Surge RAO from test series *200* which is compared with the results calculated from *WADAM* with 19 mirroring images

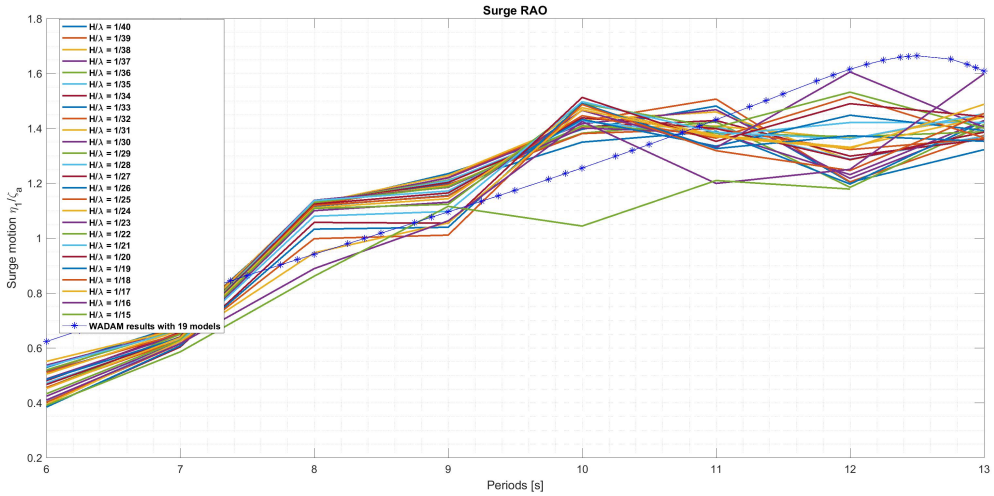

A region which is zoomed in from period $T = 6s$ to $T = 13s$ of surge RAO from test series *200* with results from *WADAM* calculated with 19 bodies

January tests: **Test series 7000**

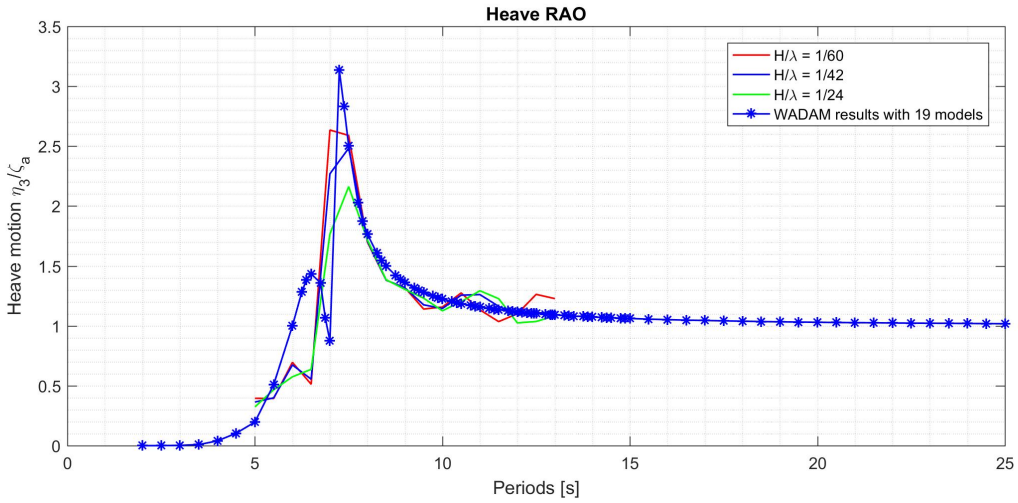

Heave RAO from the test series *7000* with wave steepness of $H/\lambda = 1/60, 1/42, 1/24$ that are compared with results calculated from *WADAM* with 19 mirroring bodies

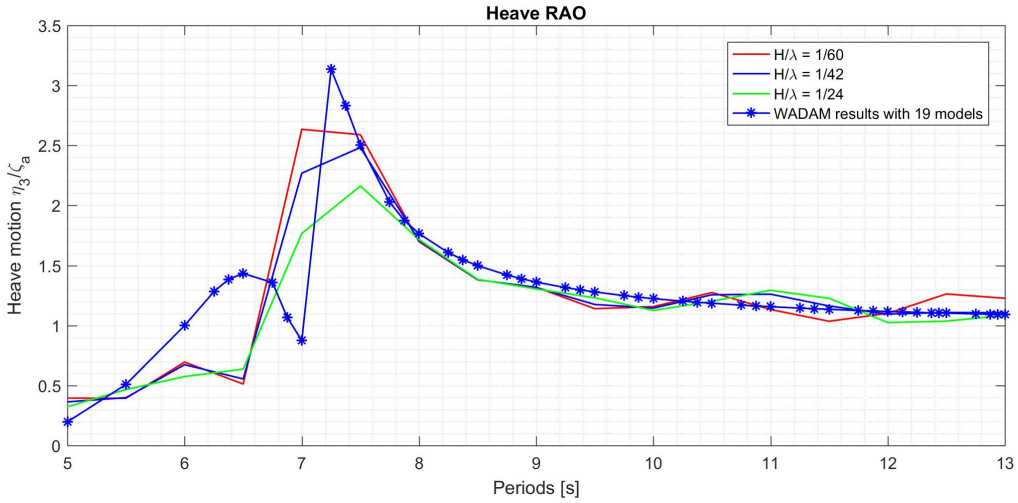

A zoomed in region from period $I = 5s$ to $T = 13s$ of heave RAO obtained from test series *7000* compared with *WADAM* results with 19 mirroring images.

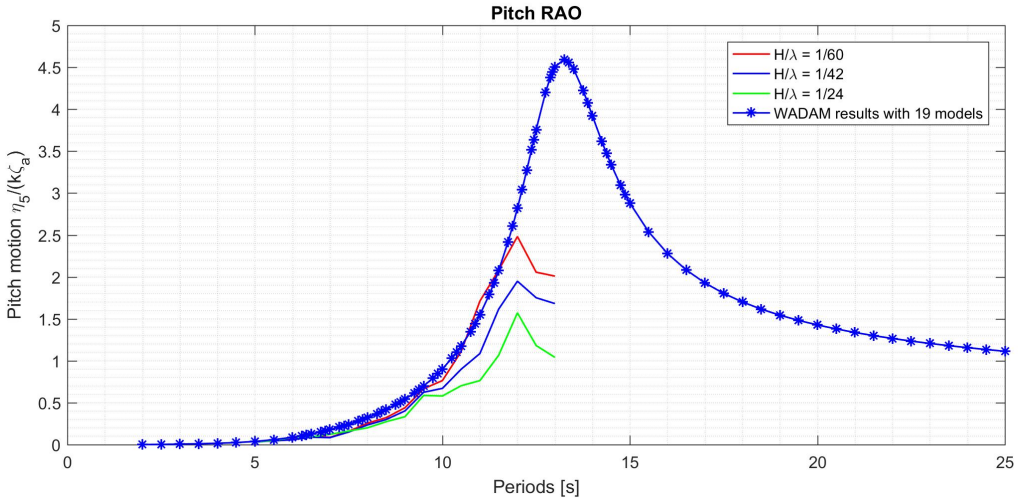

Pitch RAO from the test series *7000* with wave steepness of $H/\lambda = 1/60, 1/42, 1/24$ that are compared with results calculated from *WADAM* with 19 mirroring bodies

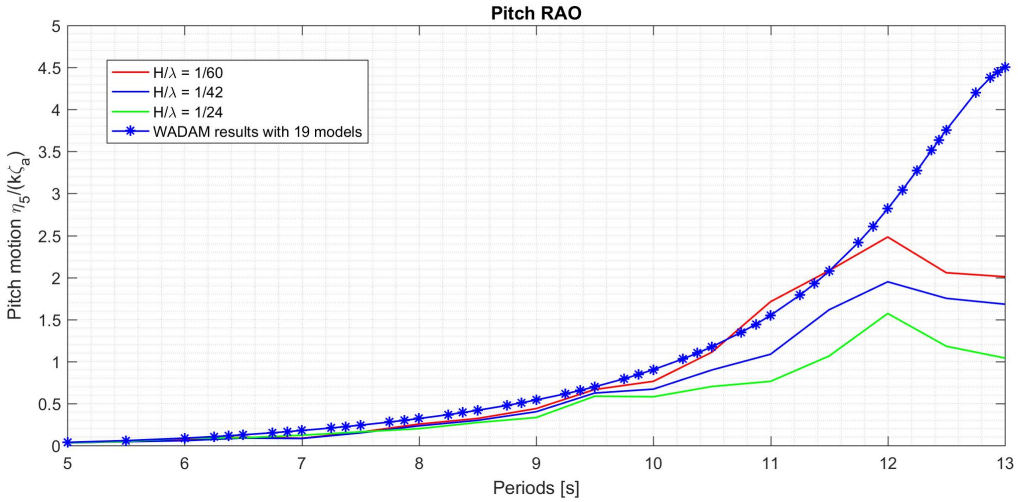

A zoomed in region from period $I = 5s$ to $T = 13s$ of pitch RAO obtained from test series *7000* compared with *WADAM* results with 19 mirroring images.

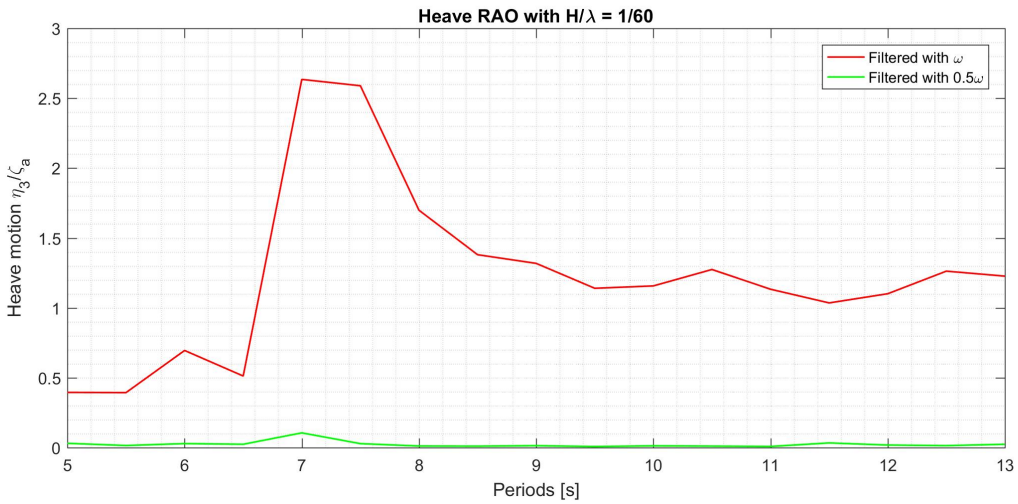

Illustration of the parametric instability with heave RAO obetained by filtering the measured data with a band pass filter. The high and low frequency are concentrated around $\omega, 0.5\omega$ where ω is the frequency of the incoming waves. The plot is for a wave with steepness of $H/\lambda = 1/60$.

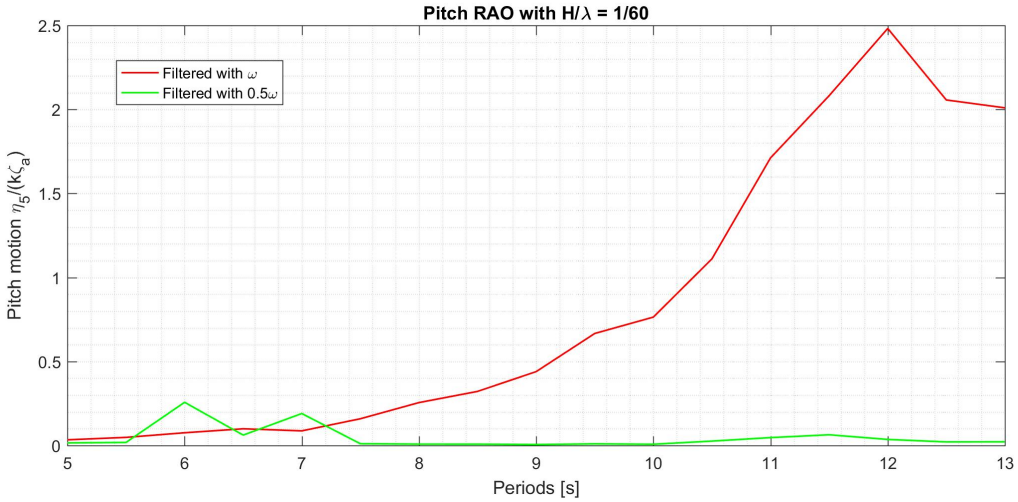

Pitch RAO obetained by filtering the measured data with a band pass filter with high and low frequency concentrated around $\omega, 0.5\omega$ where ω is the frequency of the incoming waves. The plot is from a wave with a wave steepness of $H/\lambda = 1/60$. Two peaks located at $T = 6s$ and $T = 7s$

January tests: **Merged test series of 80000 and 90000 with sample frequency 1200Hz**

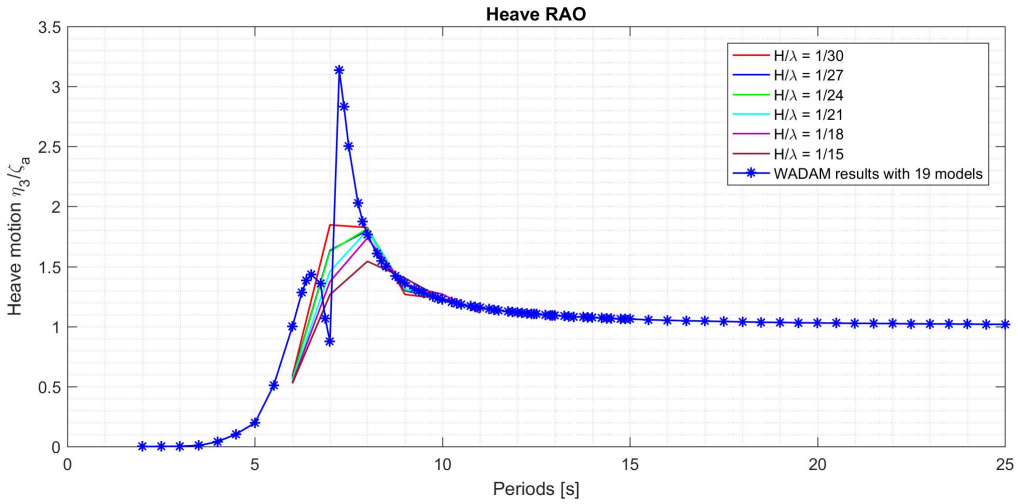

Heave RAO from the merged test series with wave steepness of $H/\lambda = 1/30, 1/27, 1/24, 1/21, 1/18, 1/15$ compared with results calculated from $WADAM$ with 19 mirroring bodies

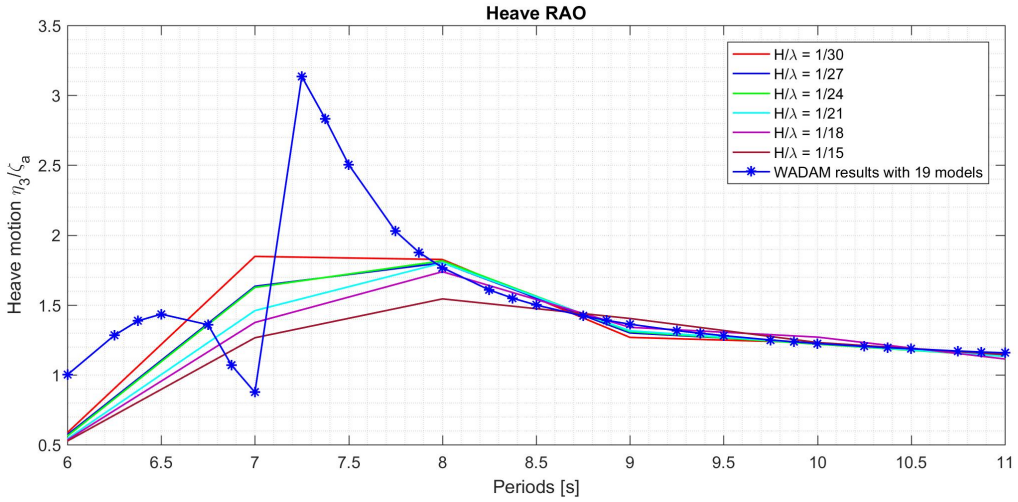

A zoomed in region with period from $T = 6s$ to $T = 11s$ from heave RAO compared with $WADAM$ results calculated from 19 mirroring bodies

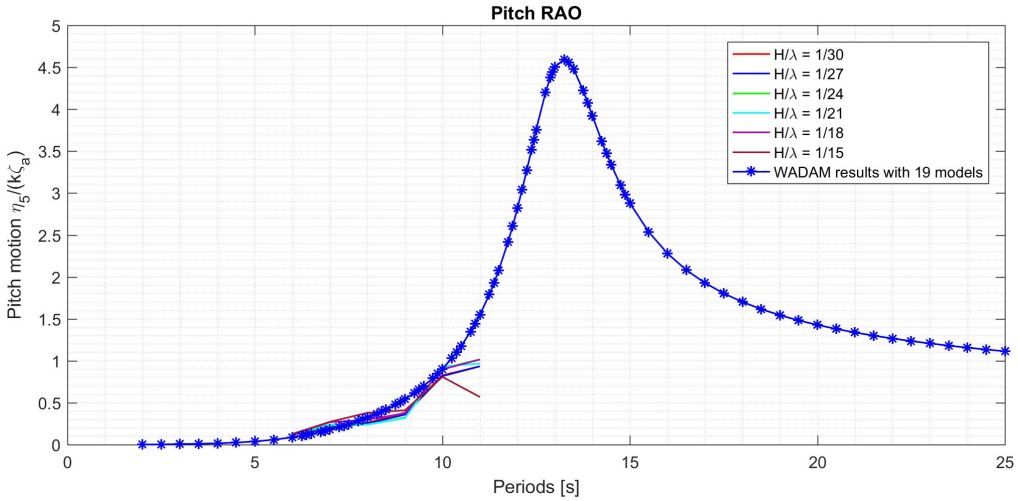

Pitch RAO from the merged test series with wave steepness of $H/\lambda = 1/30, 1/27, 1/24, 1/21, 1/18, 1/15$ compared with results calculated from *WADAM* with 19 mirroring bodies

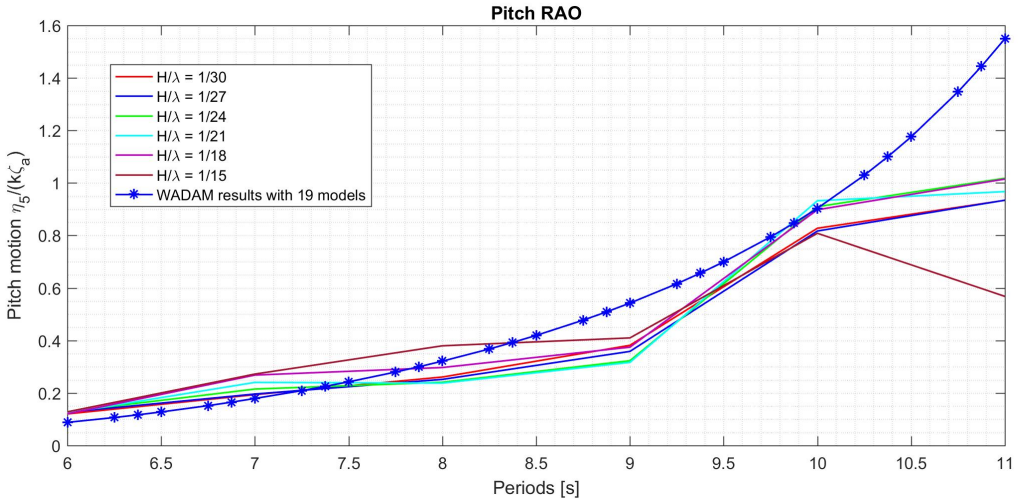

A zoomed in region with period from $T = 6s$ to $T = 11s$ from pitch RAO compared with *WADAM* results calculated from 19 mirroring bodies

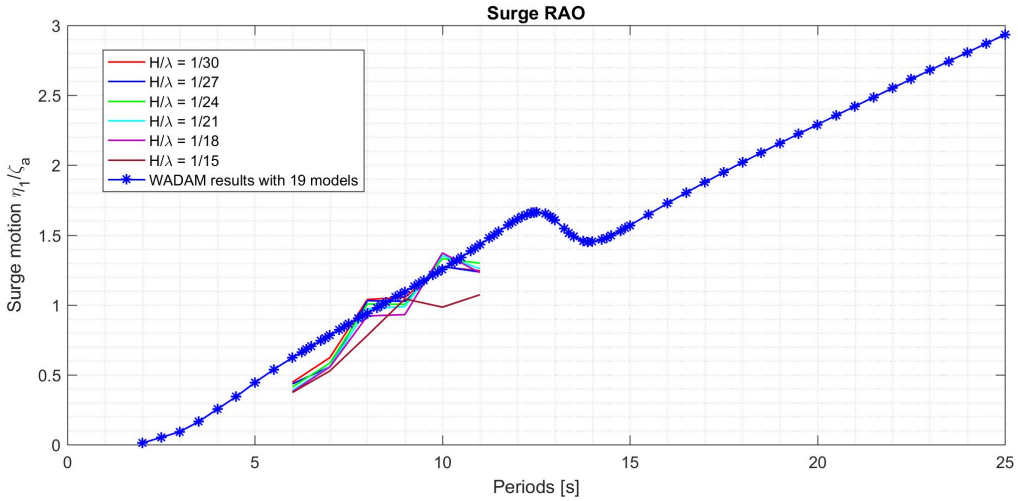

surge RAO from the merged test series with wave steepness of $H/\lambda = 1/30, 1/27, 1/24, 1/21, 1/18, 1/15$ compared with results calculated from *WADAM* with 19 mirroring bodies

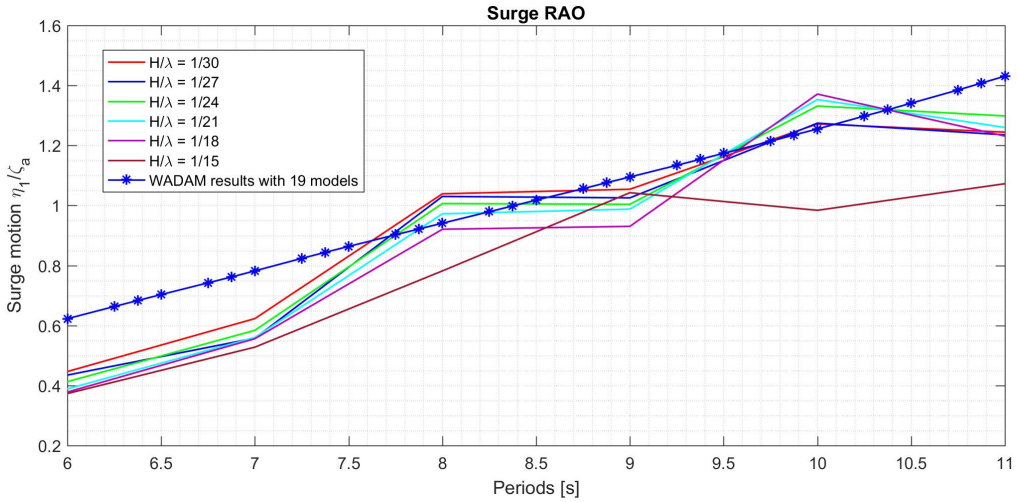

A zoomed in region with period from $T = 6s$ to $T = 11s$ from surge RAO compared with *WADAM* results calculated from 19 mirroring bodies

April tests: **Test series 401003**

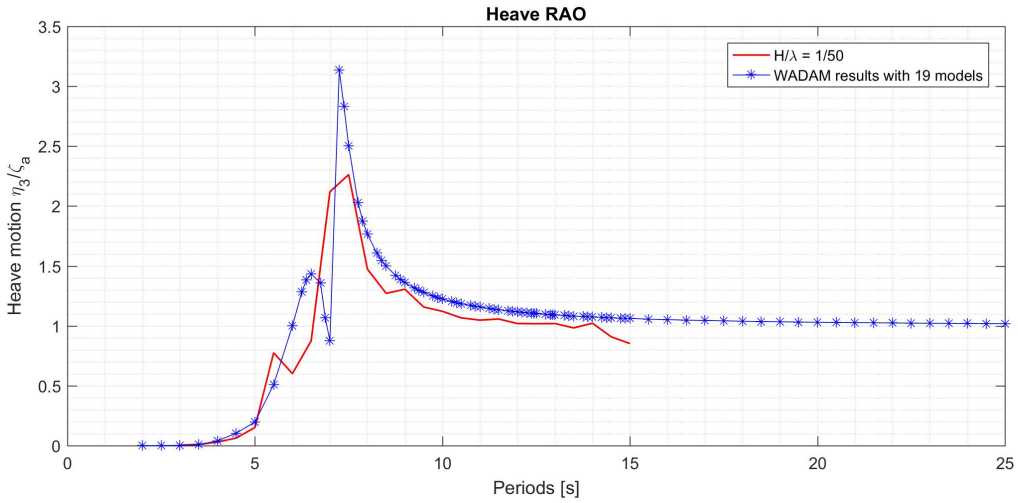

Heave RAO from test series *401003* with wave steepness $H/\lambda = 1/50$ compared with results calculated from 19 mirroring bodies in *WADAM*

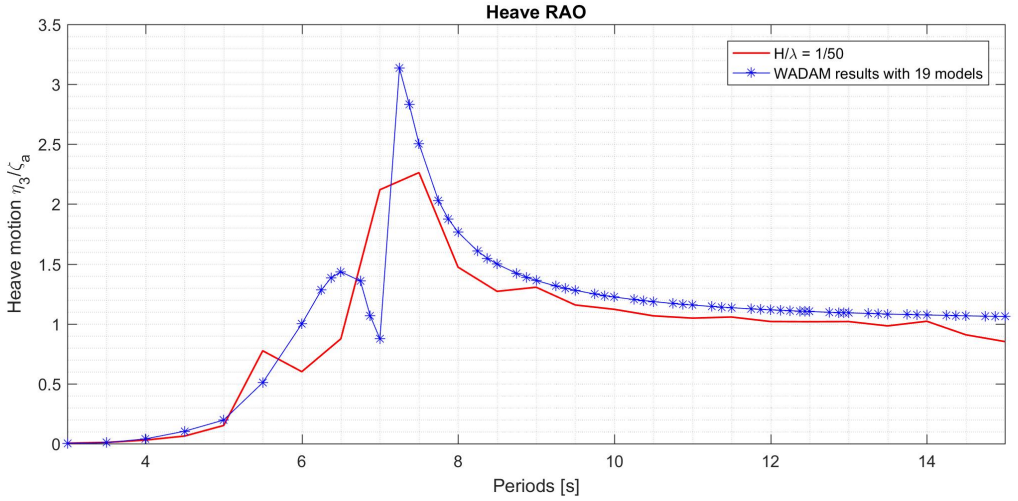

A zoomed in region from period $T = 3s$ to $T = 15s$ of the heave RAO from test series *401003* compared with results from *WADAM*

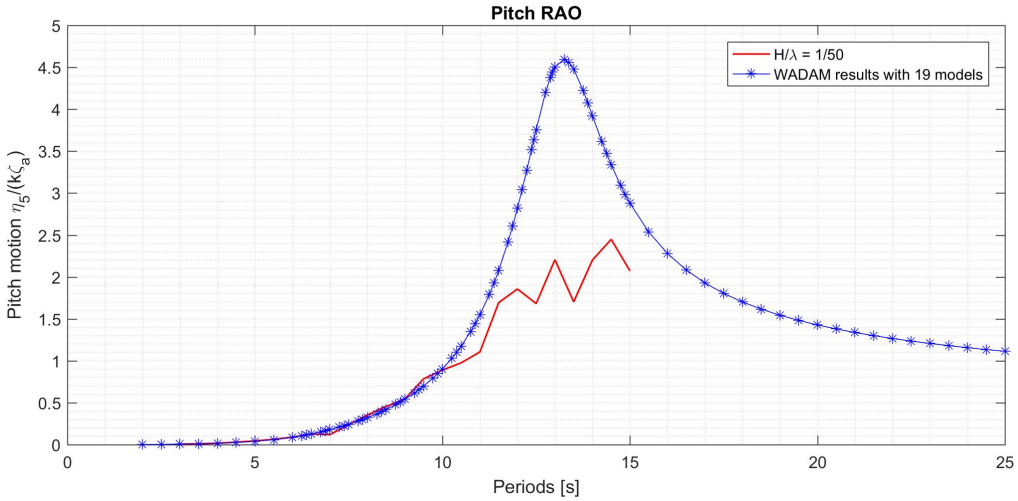

Pitch RAO from test series *401003* with wave steepness $H/\lambda = 1/50$ compared with results calculated from 19 mirroring bodies in *WADAM*

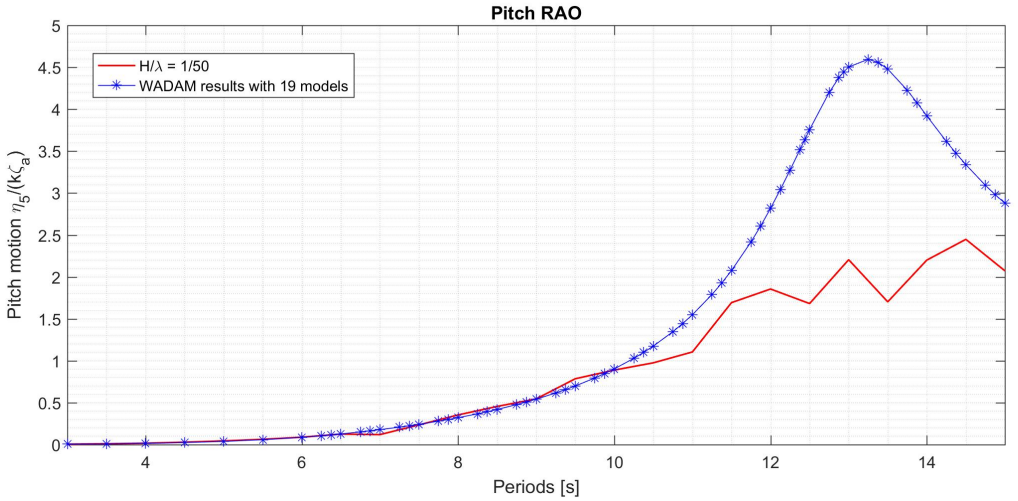

A zoomed in region from period $T = 3s$ to $T = 15s$ of pitch RAO from test series *401003* compared with results from *WADAM*

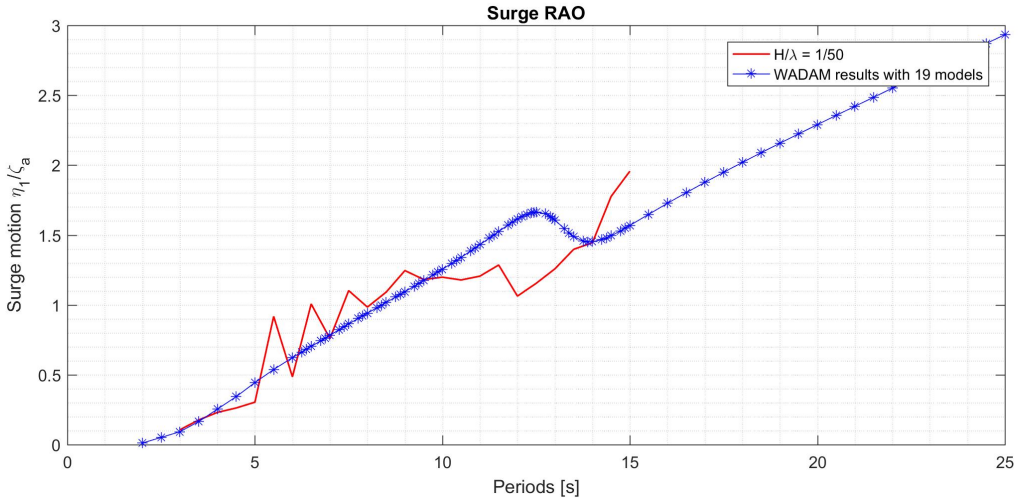

Surge RAO from test series *401003* with wave steepness $H/\lambda = 1/50$ compared with results calculated from 19 mirroring bodies in *WADAM*

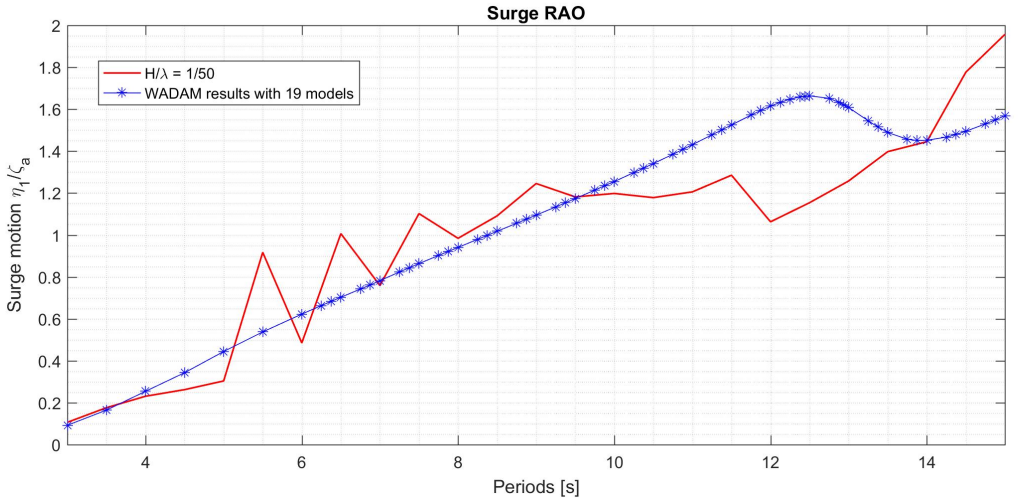

A zoomed in region from period $T = 3s$ to $T = 15s$ of surge RAO from test series *401003* compared with results from *WADAM*

April tests: **Test series 4090011**

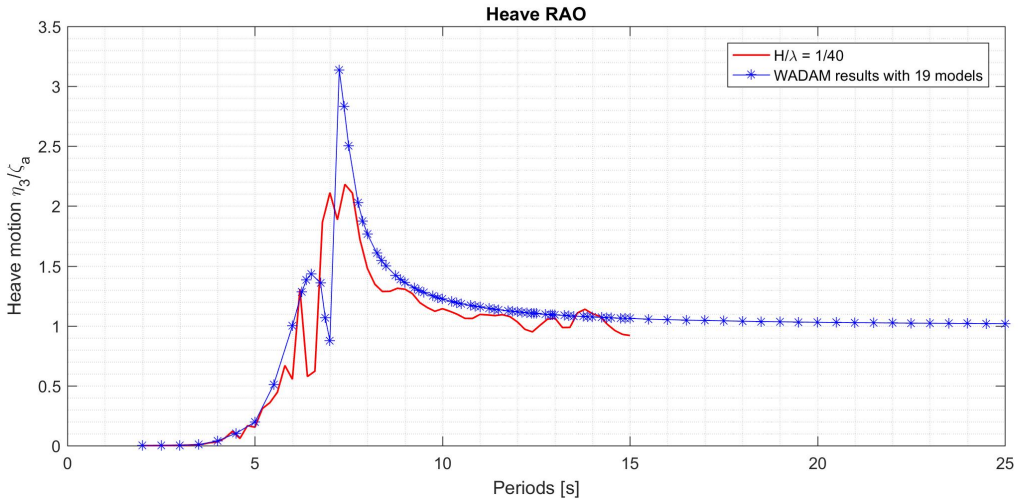

Heave RAO from test series *4090011* with wave steepness $H/\lambda = 1/40$ compared with *WADAM* results of 19 mirroring models

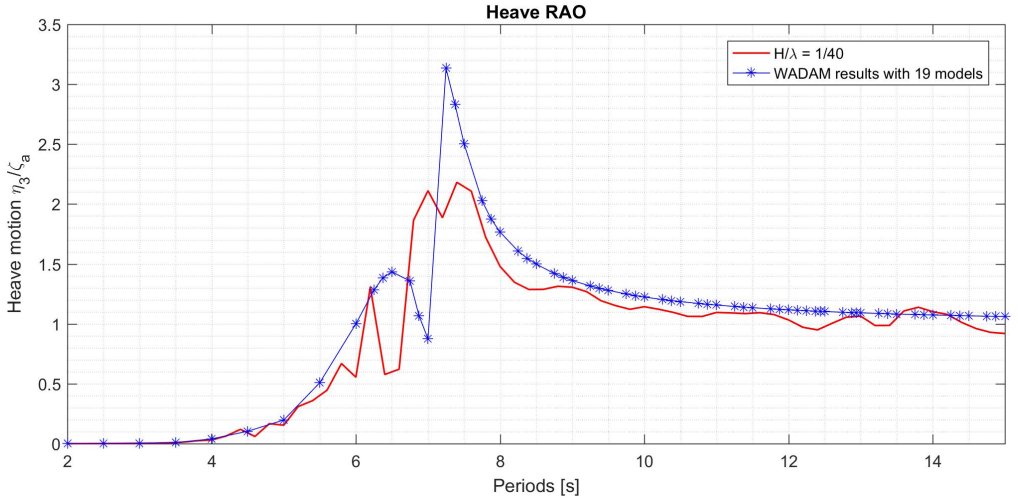

Zoomed in region from period $T = 2s$ to $T = 15s$ of heave RAO from test series *4090011* with wave steepness $H/\lambda = 1/40$ compared with *WADAM* results

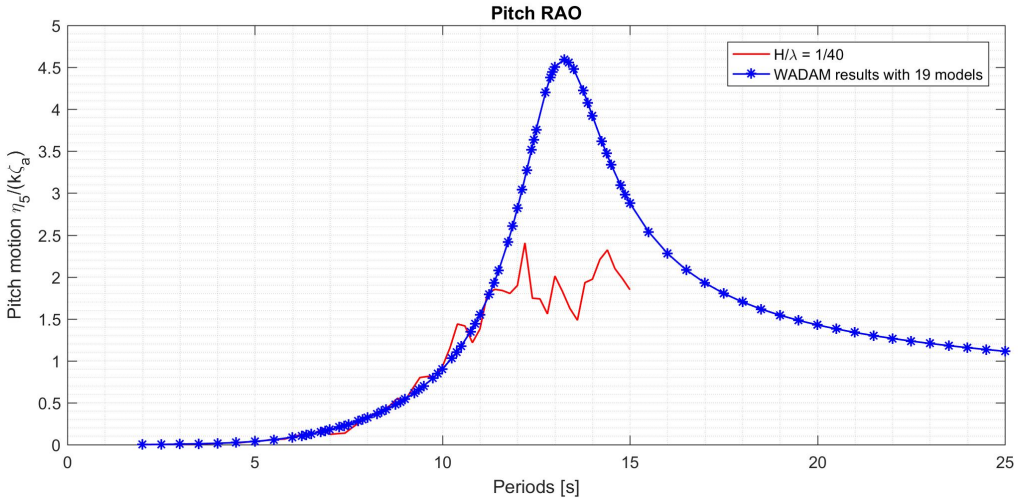

Pitch RAO from test series *4090011* with wave steepness $H/\lambda = 1/40$ compared with *WADAM* results of 19 mirroring models

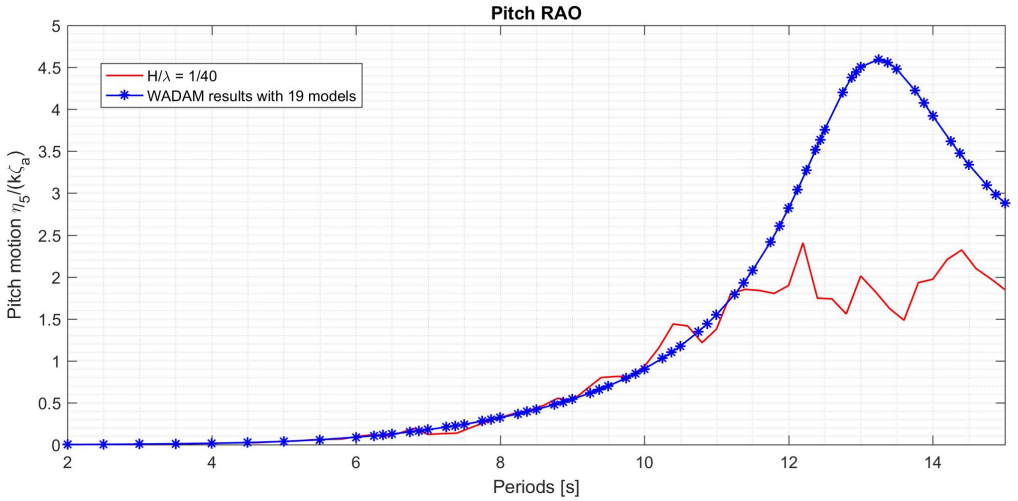

Zoomed in region from period $T = 2s$ to $T = 15s$ of pitch RAO from test series *4090011* with wave steepness $H/\lambda = 1/40$ compared with *WADAM* results

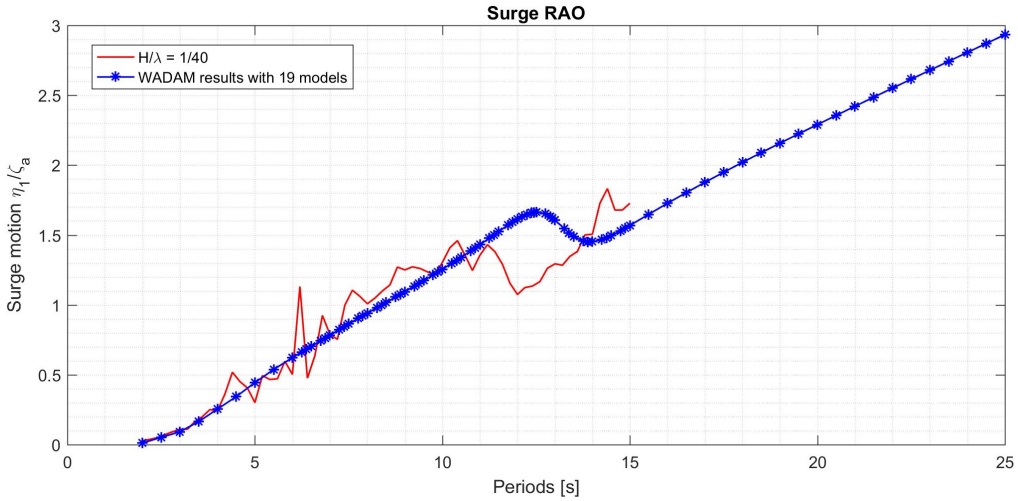

Surge RAO from test series *4090011* with wave steepness $H/\lambda = 1/40$ compared with *WADAM* results of 19 mirroring models

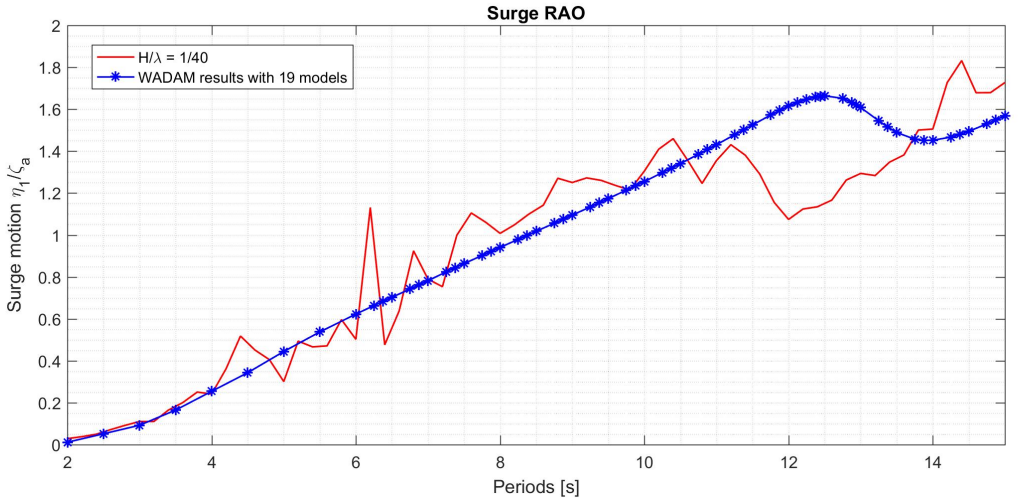

Zoomed in region from period $T = 2s$ to $T = 15s$ of surge RAO from test series *4090011* with wave steepness $H/\lambda = 1/40$ compared with *WADAM* results

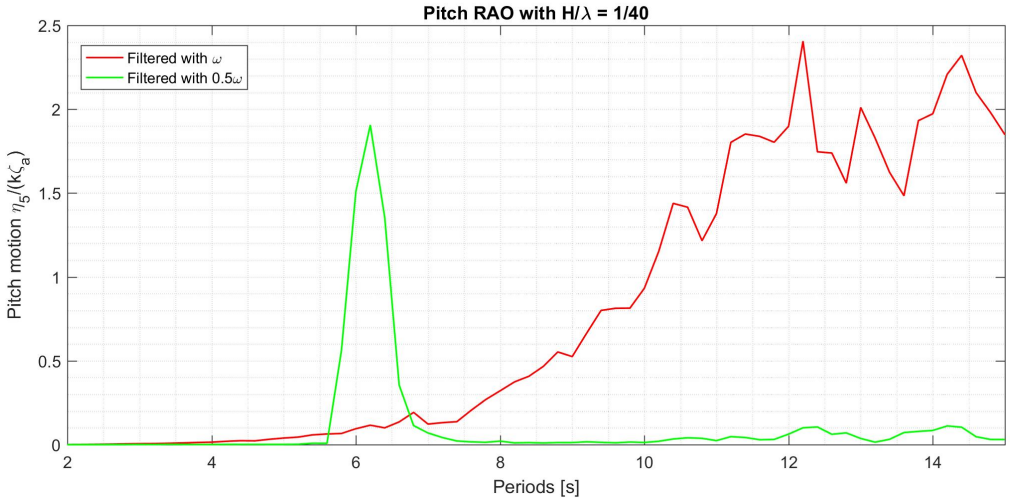

Illustration of parametric instability by plotting pitch RAO obtained from test series *4090011* by filter the data concentrated at ω and 0.5ω of the signal, where ω is the frequency of the incoming waves. Peak in green line at $T = 6.2s$

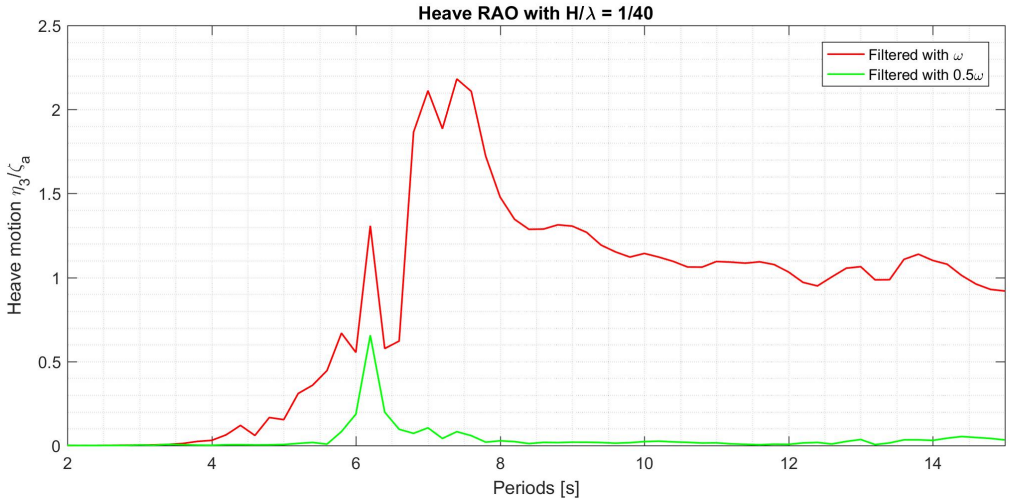

Heave RAO obtained from by using band pass filtering of ω and 0.5ω of the signal, where the ω is the frequency of the incoming waves

April tests: **Test series 4012002**

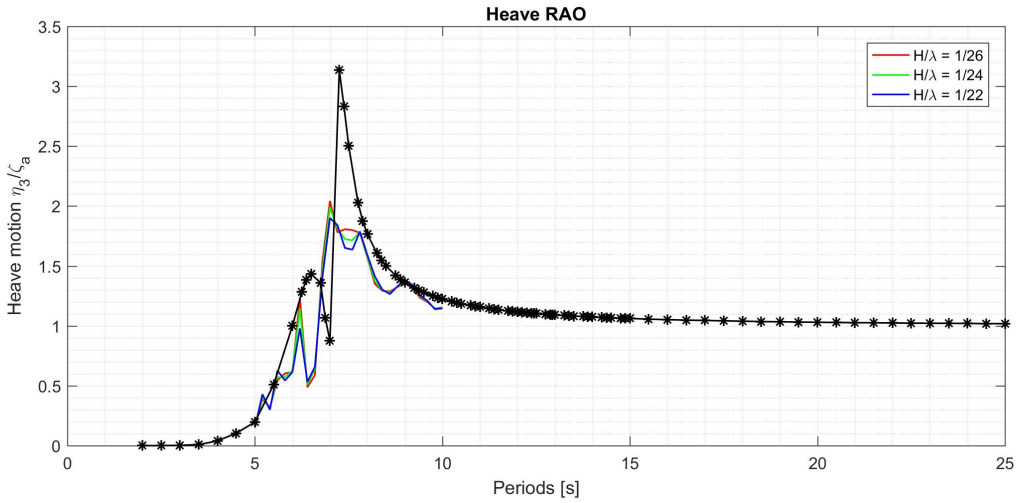

Heave RAO from test series *4012002* with wave steepness $H/\lambda = 1/26, 1/24, 1/22$ compared with *WADAM* results of 19 mirroring models

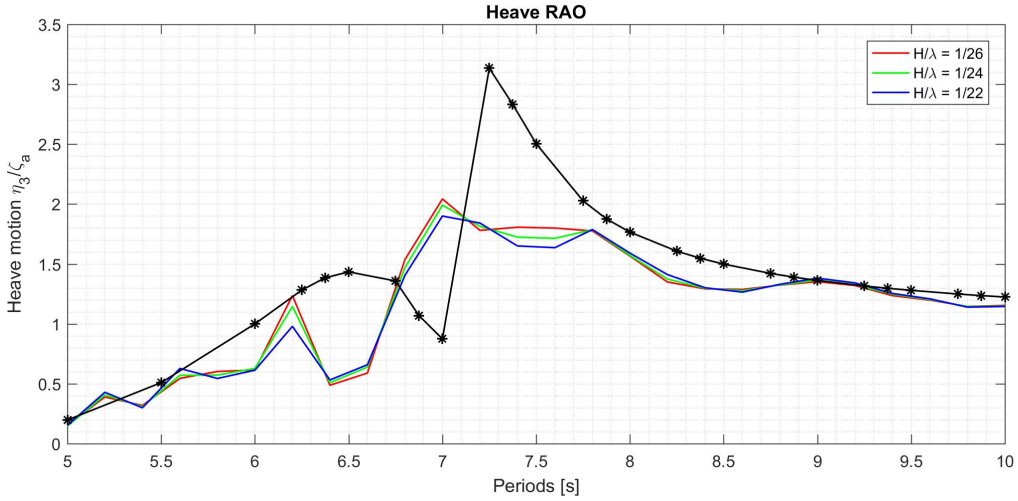

Zoomed in region from period $T = 2s$ to $T = 15s$ of heave RAO from test series *4012002* compared with *WADAM* results

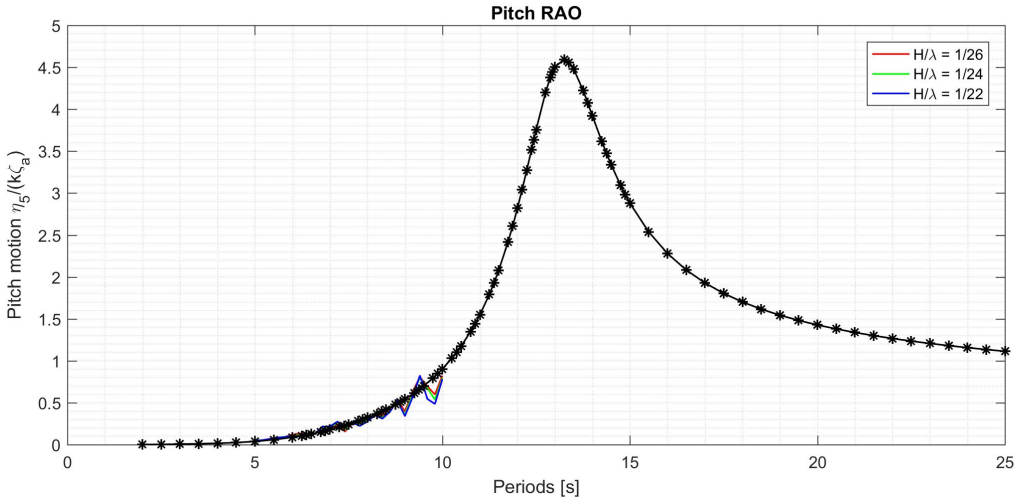

Pitch RAO from test series *4012002* with wave steepness $H/\lambda = 1/26, 1/24, 1/22$ compared with *WADAM* results of 19 mirroring models

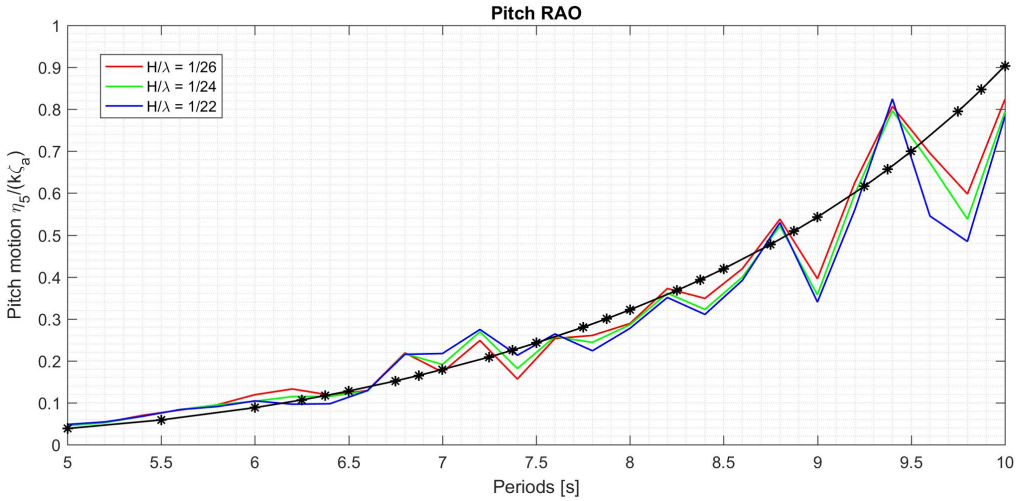

Zoomed in region from period $T = 2s$ to $T = 15s$ of pitch RAO from test series *4012002* compared with *WADAM* results

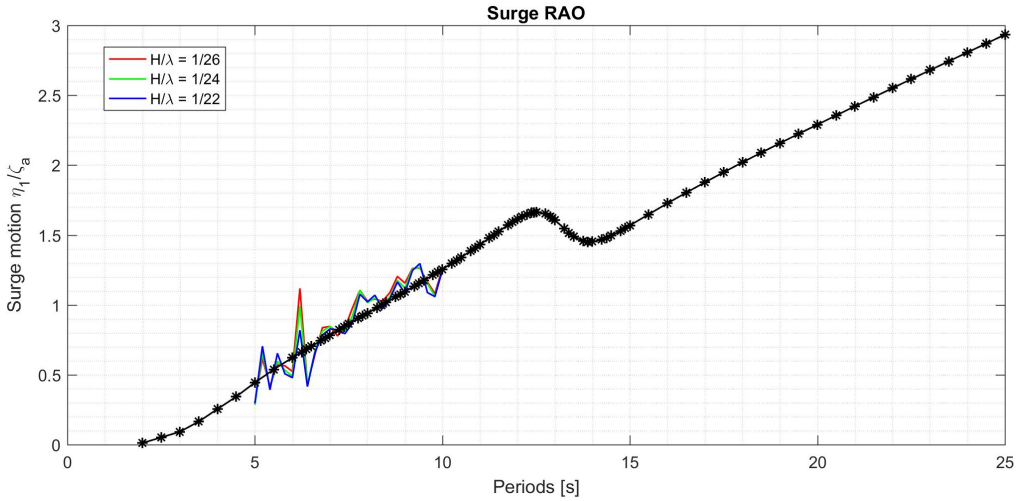

Surge RAO from test series *4012002* with wave steepness $H/\lambda = 1/26, 1/24, 1/22$ compared with *WADAM* results of 19 mirroring models

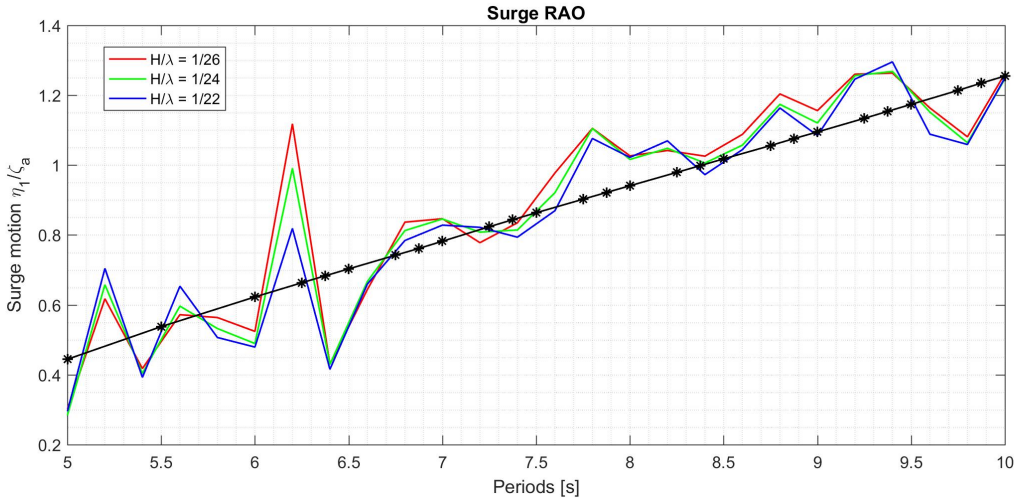

Zoomed in region from period $T = 2s$ to $T = 15s$ of surge RAO from test series *4012002* compared with *WADAM* results

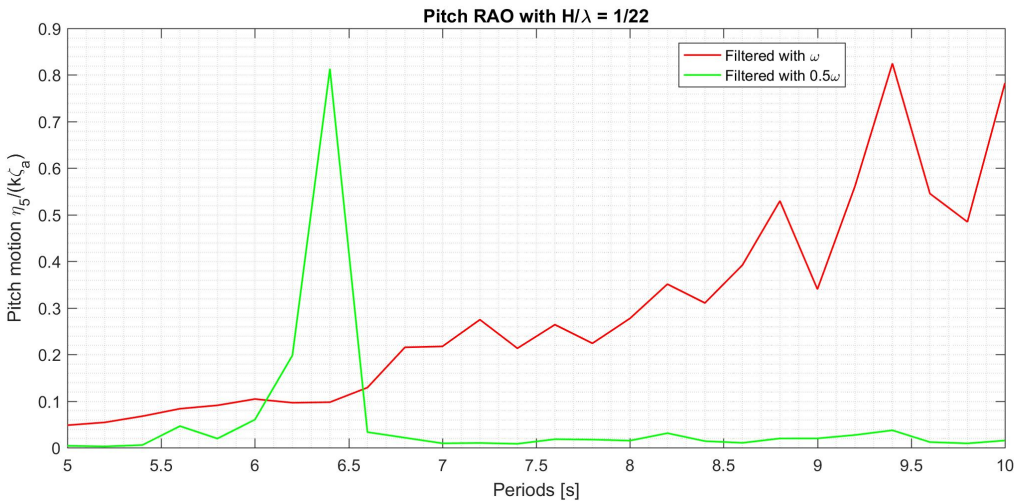

Pitch RAO obtained by using band pass filtering of ω and 0.5ω of the signal, where the ω is the frequency of the incoming waves. This plot is for waves with wave $H/\lambda = 1/22$. Peak at the green line at $T = 5.6s$ and $T = 6.4s$

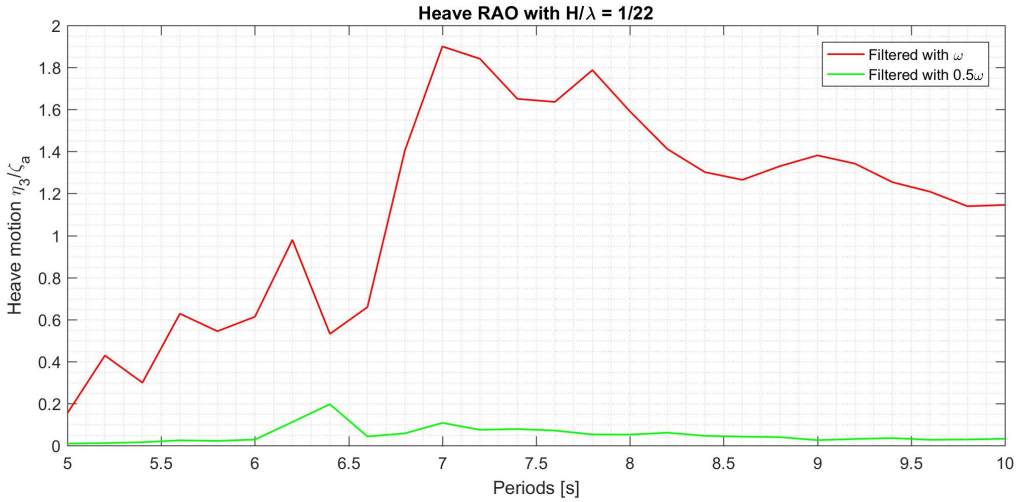

Heave RAO obtained from test series *4012002* by using band pass filtering of ω and 0.5ω of the signal. This plot is for waves with wave steepness $H/\lambda = 1/22$

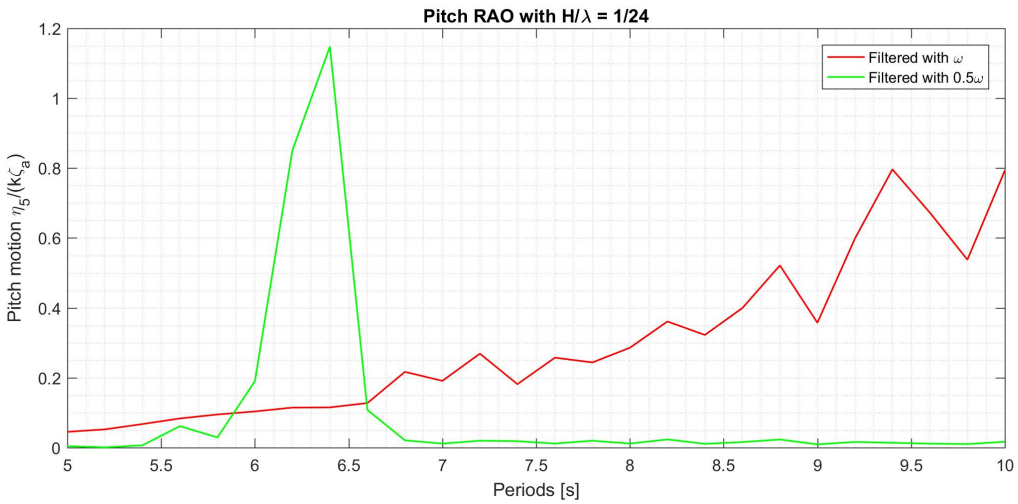

Pitch RAO obtained by using band pass filtering of ω and 0.5ω of the signal, where the ω is the frequency of the incoming waves. Peak at the green line at $T = 5.6s$ and $T = 6.4s$. This plot is for waves with wave steepness $H/\lambda = 1/24$

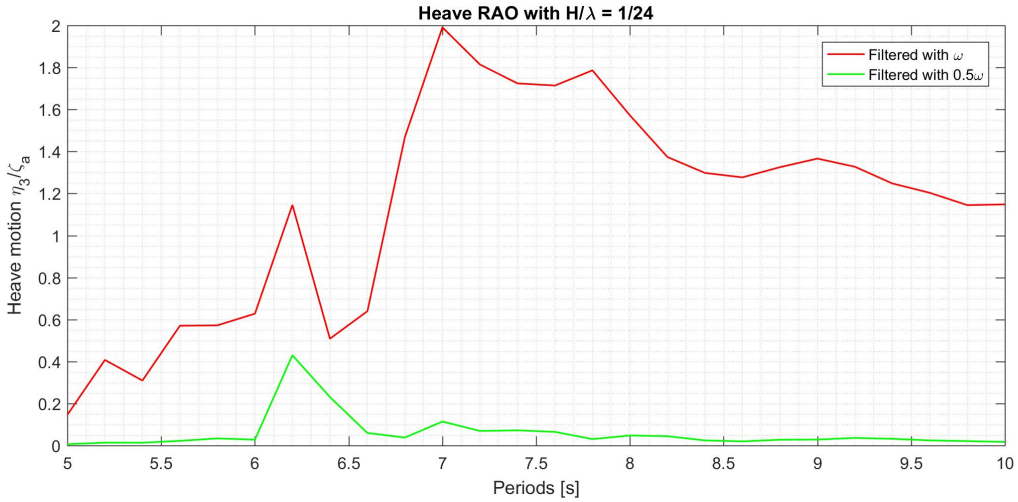

Heave RAO obtained from test series *4012002* by using band pass filtering of ω and 0.5ω of the signal. This plot is for waves with wave steepness $H/\lambda = 1/24$

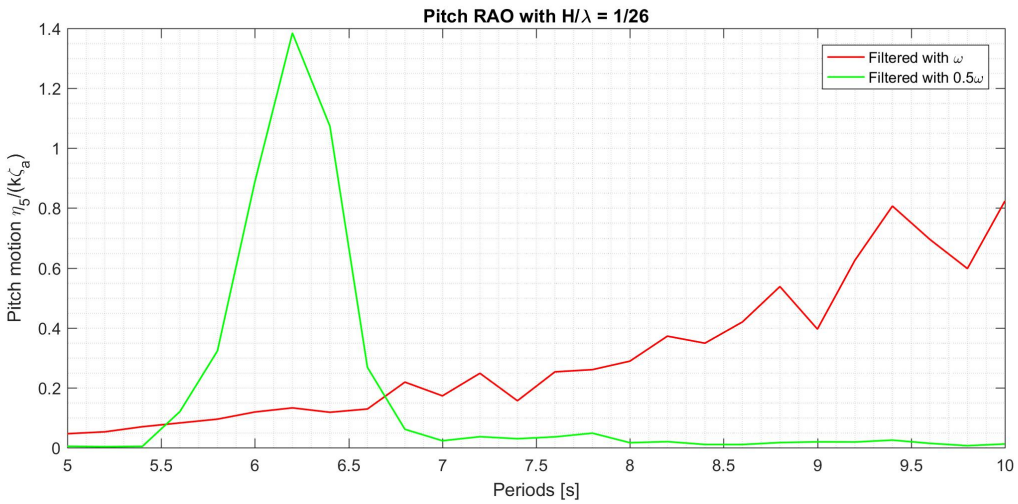

Pitch RAO obtained by using band pass filtering of ω and 0.5ω of the signal, where the ω is the frequency of the incoming waves. Peak at the green line at $T = 6.25s$. This plot is for waves with wave steepness $H/\lambda = 1/26$

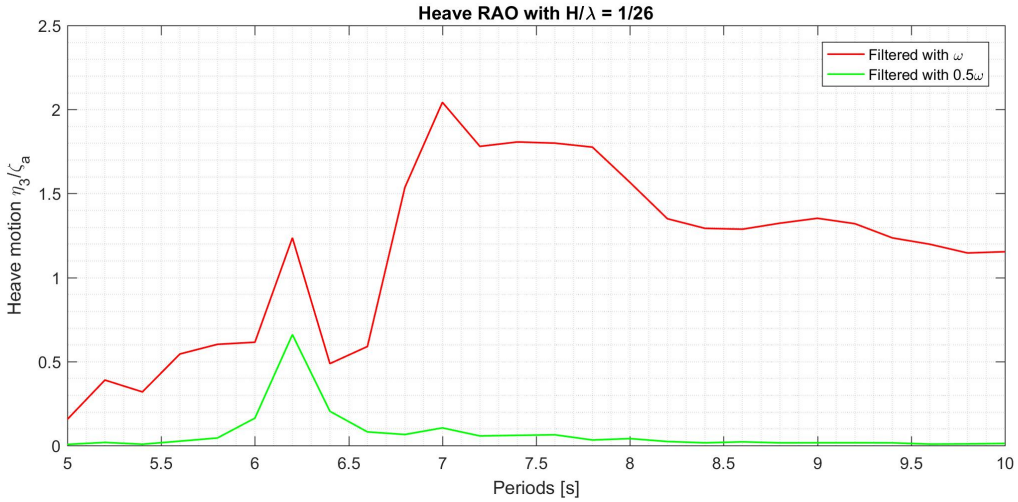

Heave RAO obtained from test series *4012002* by using band pass filtering of ω and 0.5ω of the signal. This plot is for waves with wave steepness $H/\lambda = 1/26$

April tests: **Test series 4012003**

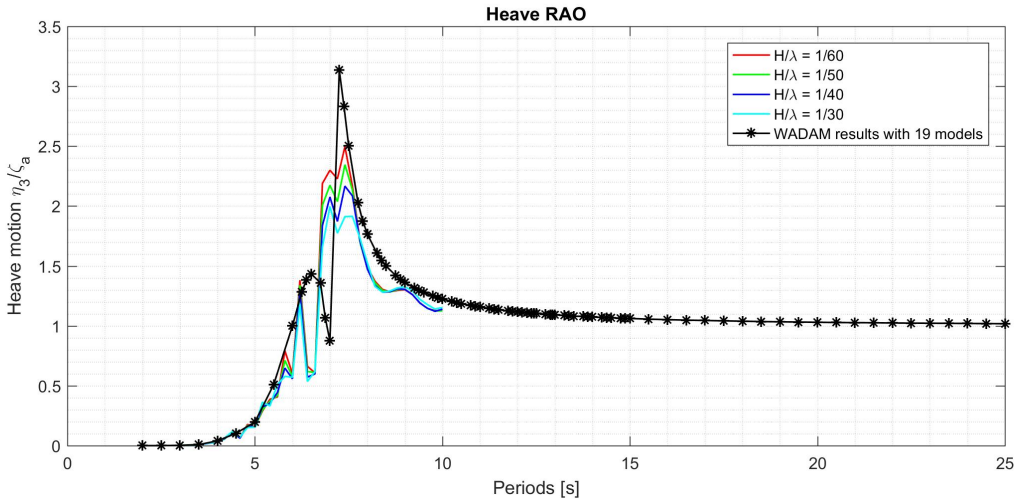

Heave RAO from test series *4012003* with wave steepness $H/\lambda = 1/60, 1/50, 1/40, 1/30$ compared with *WADAM* results of 19 mirroring models

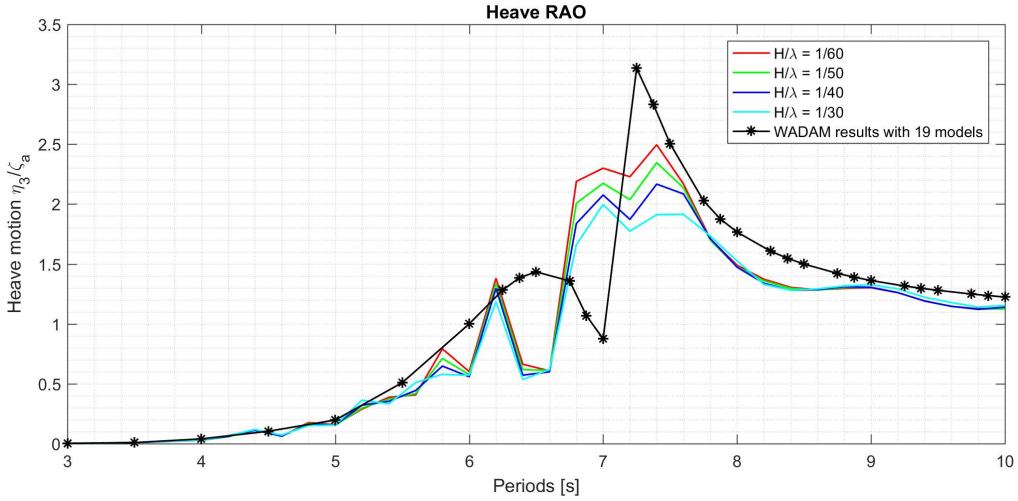

Zoomed in region from period $T = 3s$ to $T = 10s$ of heave RAO from test series *4012003* compared with *WADAM* results

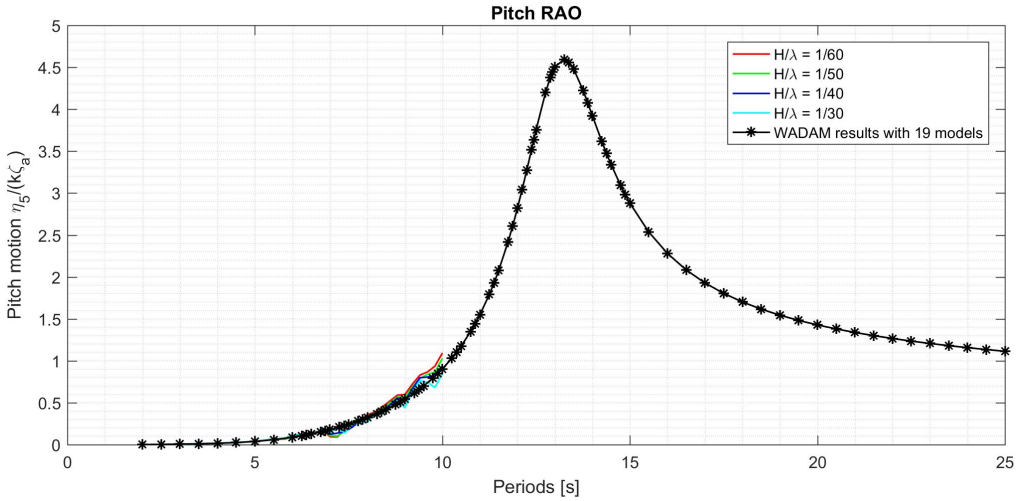

Pitch RAO from test series *4012003* with wave steepness $H/\lambda = 1/60, 1/50, 1/40, 1/30$ compared with *WADAM* results of 19 mirroring models

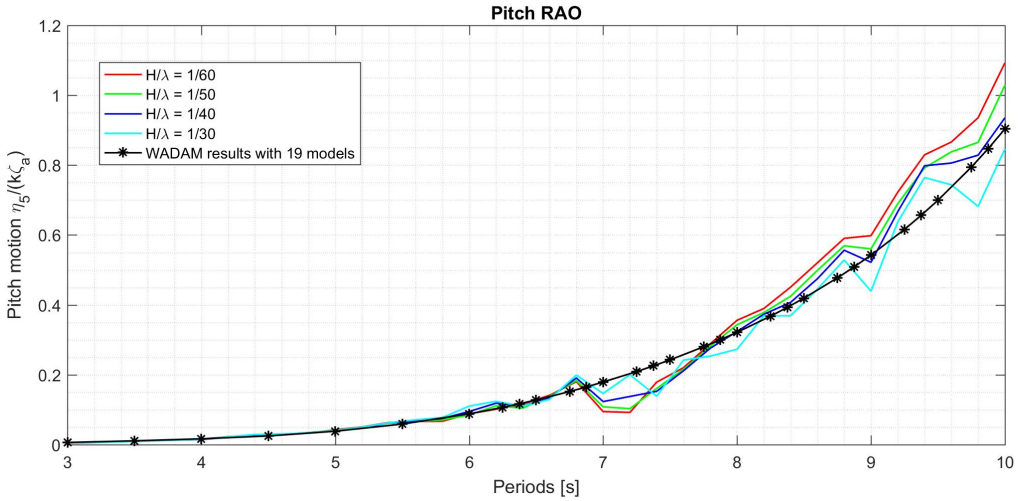

Zoomed in region from period $T = 3s$ to $T = 10s$ of pitch RAO from test series *4012003* compared with *WADAM* results

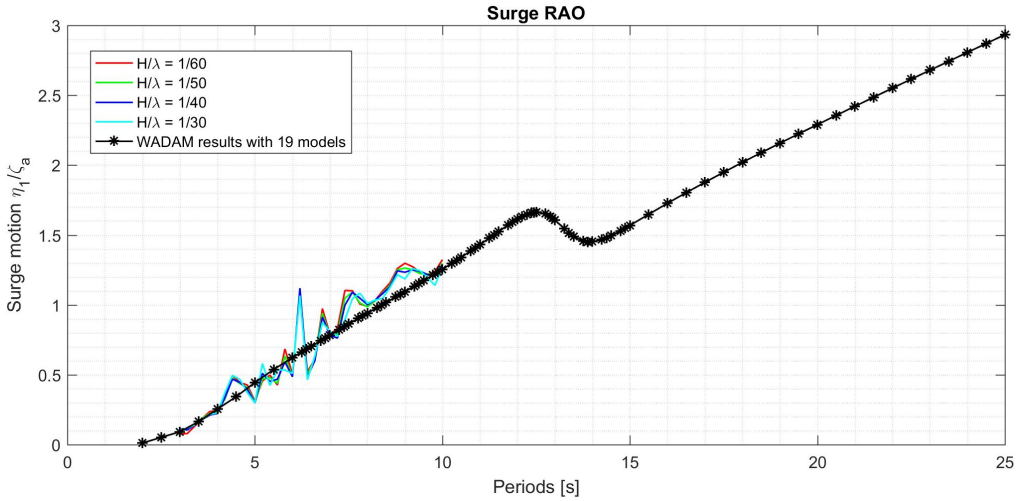

Surge RAO from test series *4012003* with wave steepness $H/\lambda = 1/60, 1/50, 1/40, 1/30$ compared with *WADAM* results of 19 mirroring models

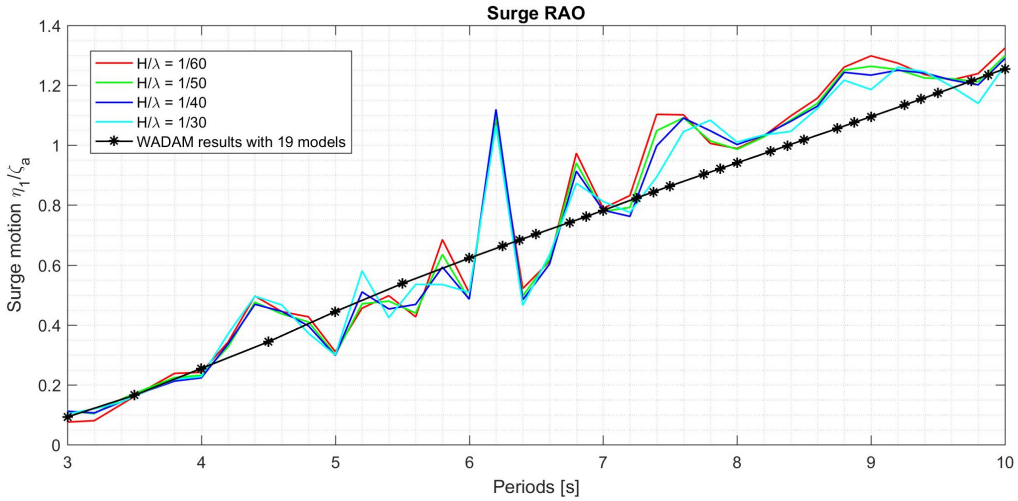

Zoomed in region from period $T = 3s$ to $T = 10s$ of surge RAO from test series *4012003* compared with *WADAM* results

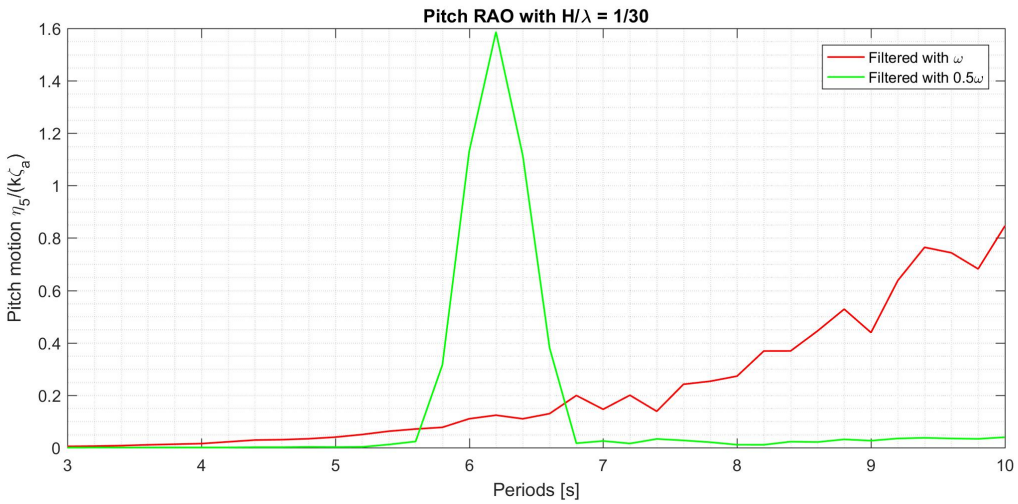

Pitch RAO obtained by using band pass filtering of ω and 0.5ω of the signal, where the ω is the frequency of the incoming waves. Peak at the green line at $T = 6.2s$. This plot is for waves with wave steepness $H/\lambda = 1/30$

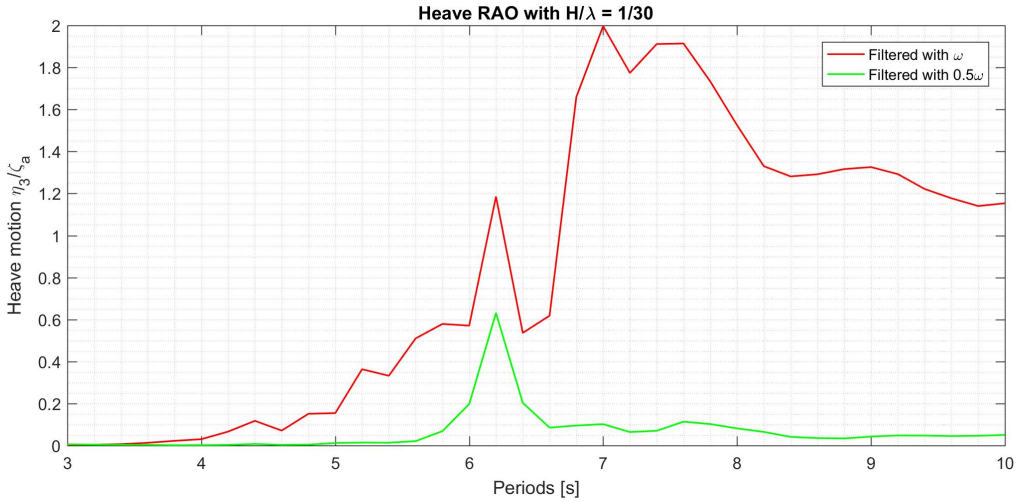

Heave RAO obtained from test series by using band pass filtering of ω and 0.5ω of the signal. This plot is for waves with wave steepness $H/\lambda = 1/30$

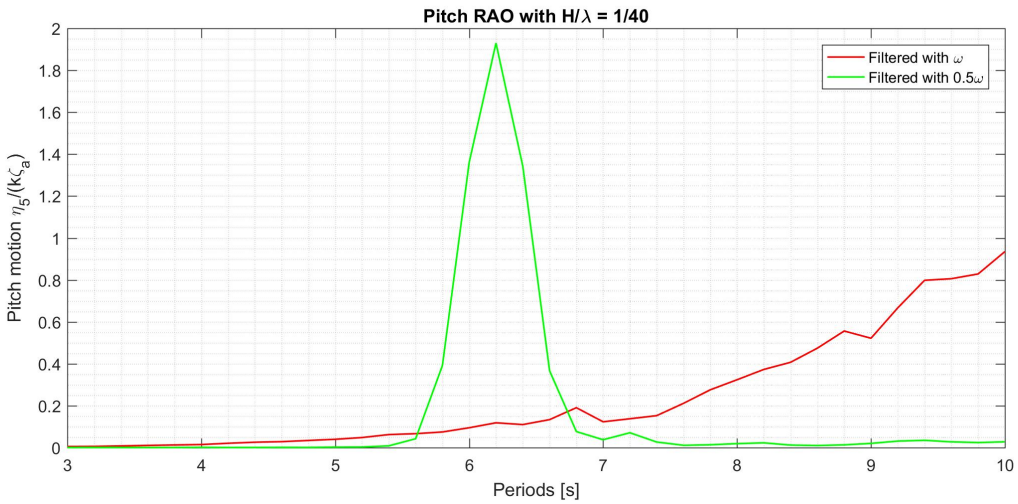

Pitch RAO obtained by using band pass filtering of ω and 0.5ω of the signal, where the ω is the frequency of the incoming waves. Peak at the green line at $T = 6.2s$. This plot is for waves with wave steepness $H/\lambda = 1/40$

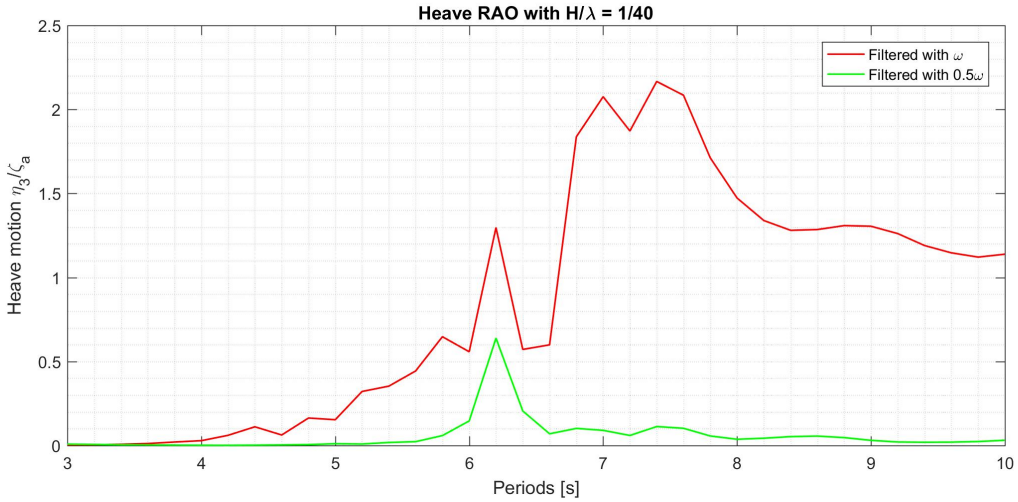

Heave RAO obtained from test series by using band pass filtering of ω and 0.5ω of the signal. This plot is for waves with wave steepness $H/\lambda = 1/40$

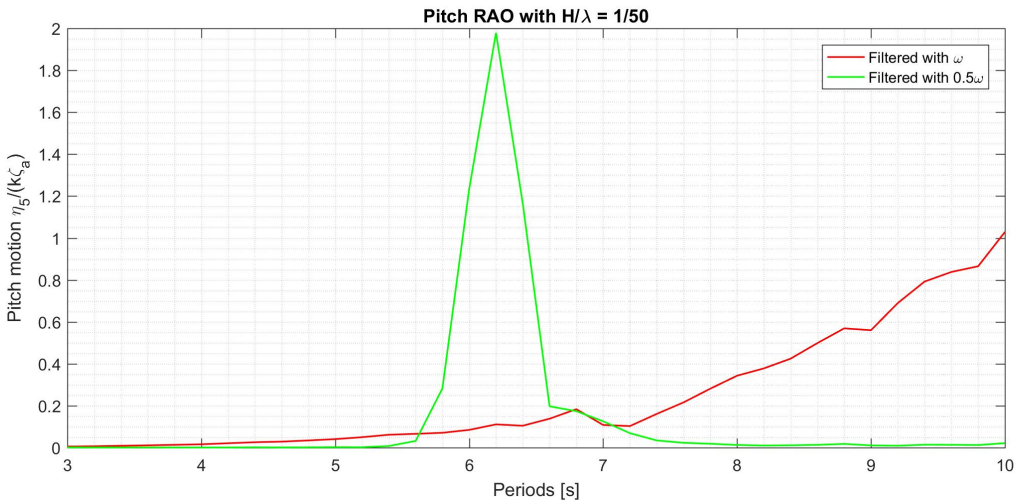

Pitch RAO obtained by using band pass filtering of ω and 0.5ω of the signal, where the ω is the frequency of the incoming waves. Peak at the green line at $T = 6.2s$. This plot is for waves with wave steepness $H/\lambda = 1/50$

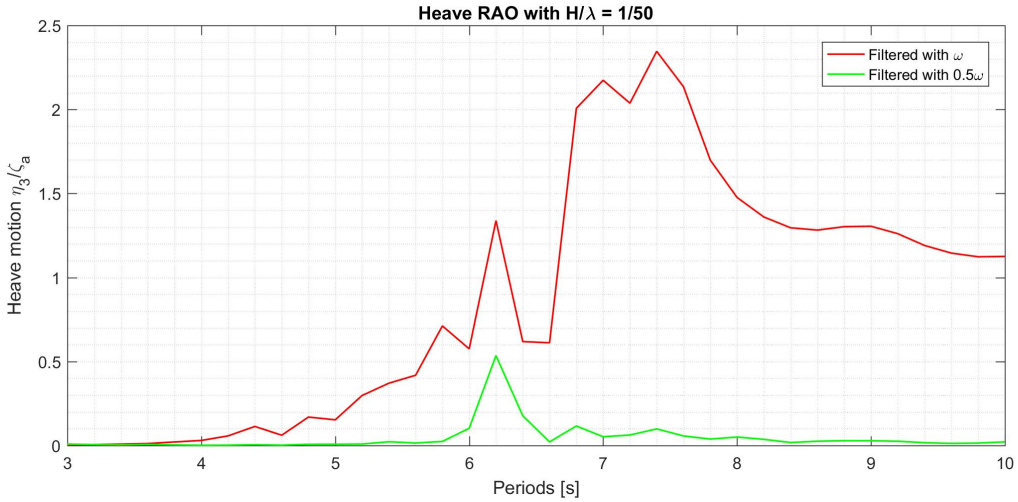

Heave RAO obtained from test series by using band pass filtering of ω and 0.5ω of the signal. This plot is for waves with wave steepness $H/\lambda = 1/50$

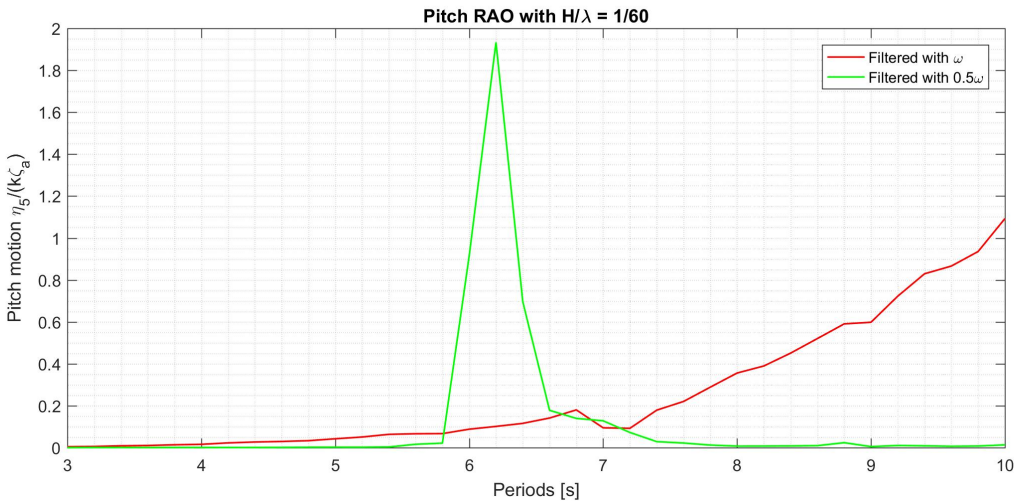

Pitch RAO obtained by using band pass filtering of ω and 0.5ω of the signal, where the ω is the frequency of the incoming waves. Peak at the green line at $T = 6.2s$. This plot is for waves with wave steepness $H/\lambda = 1/60$

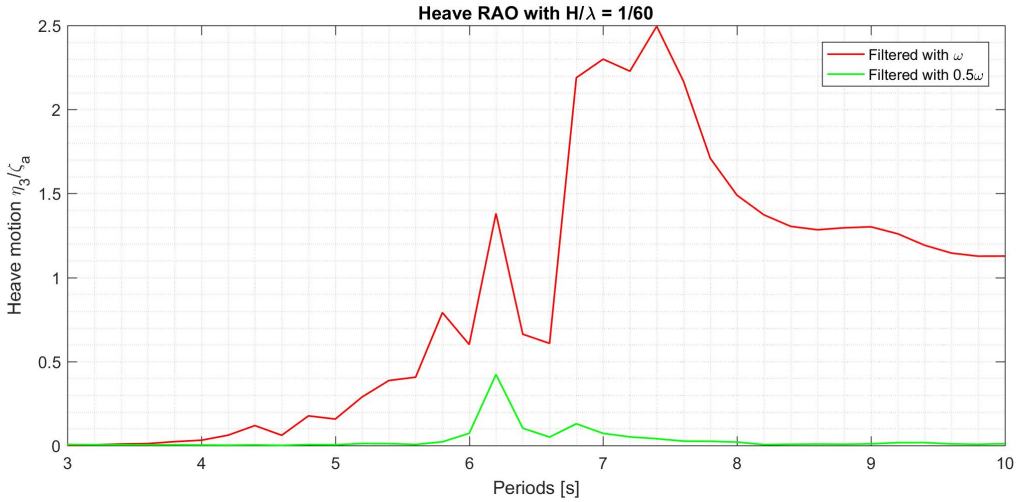

Heave RAO obtained from test series by using band pass filtering of ω and 0.5ω of the signal. This plot is for waves with wave steepness $H/\lambda = 1/60$

B.4 Comparison of the waves

The comparison of the linear wave theory and the measured waves. The results of the wave measurement when the towing tank is subjected with four wave probes. For all plots, dots represent the measured wave height, and solid blue line represent the theoretically estimated wave height for intermediate water depth.

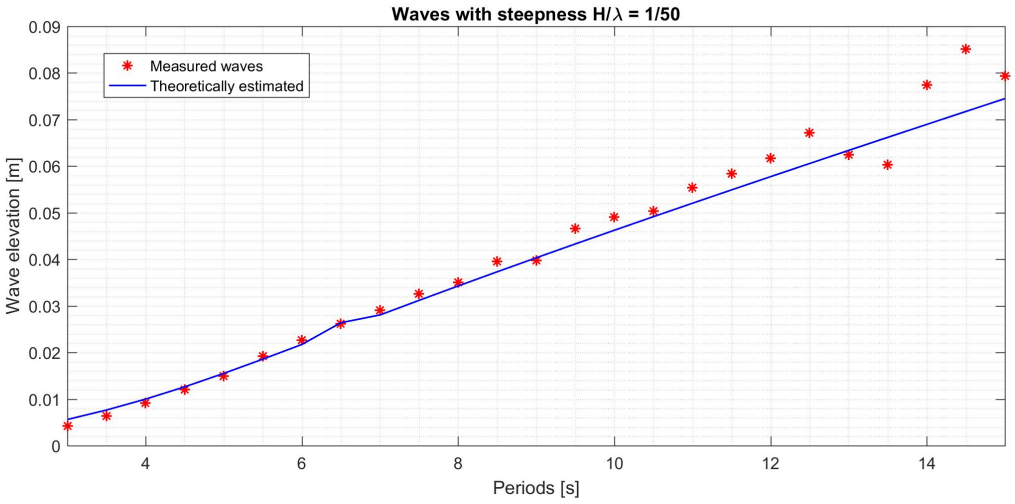

Comparison of the measured waves and the theoretically estimated wave height from the linear wave theory. The waves are tested with test series *401003*, with wave steepness $H/\lambda = 1/50$

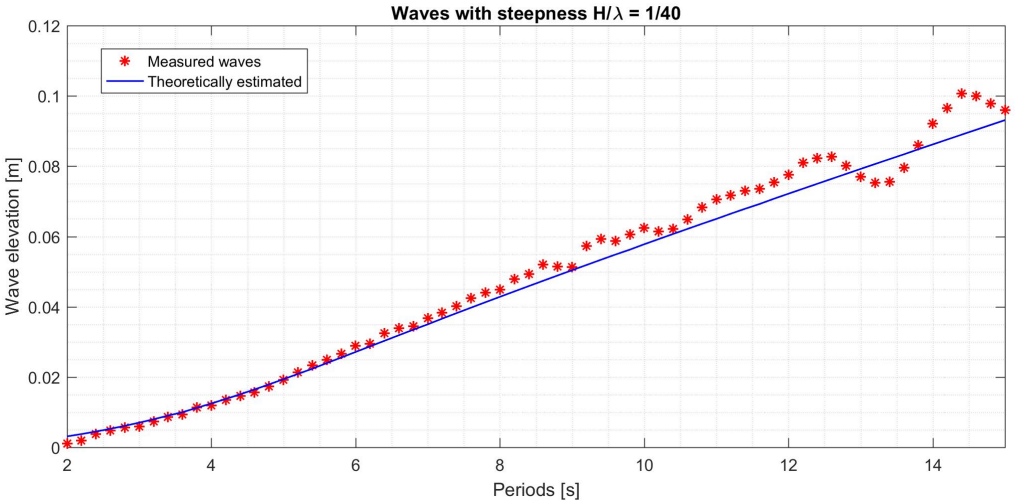

Comparison of the measured waves and the theoretically estimated wave height from the linear wave theory from test series *4090011*, with wave steepness $H/\lambda = 1/40$

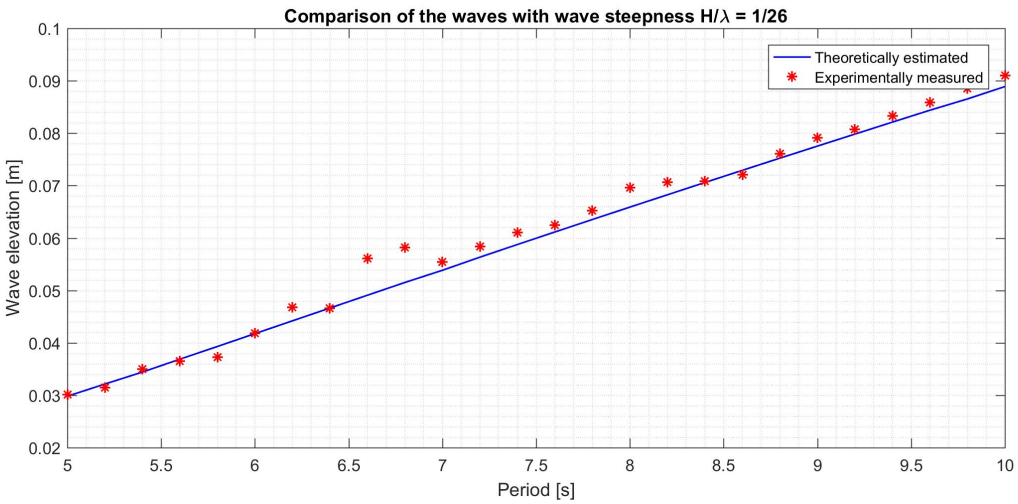

Comparison of the measured waves and the theoretically estimated wave height from the linear wave theory from test series *4012002* with wave steepness $H/\lambda = 1/26$

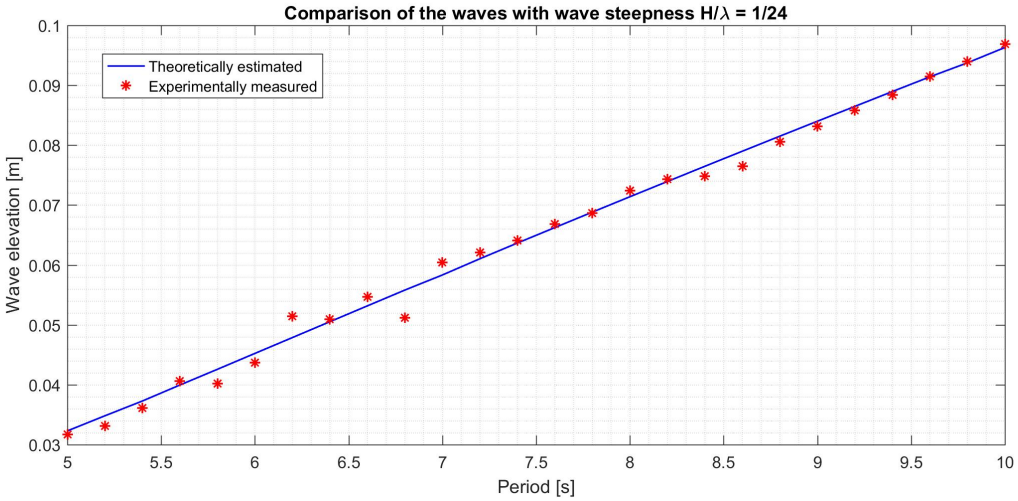

Comparison of the measured waves and the theoretically estimated wave height from the linear wave theory from test series *4012002* with wave steepness $H/\lambda = 1/24$

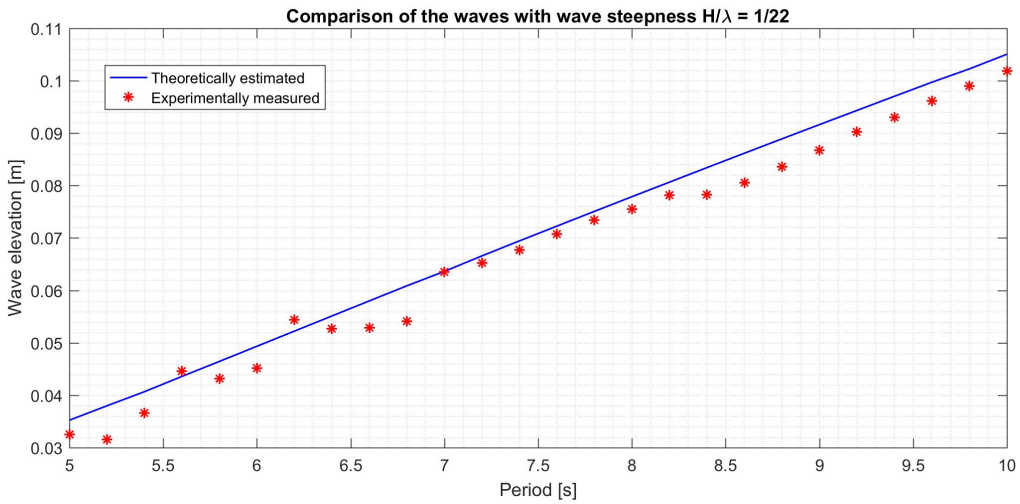

Comparison of the measured waves and the theoretically estimated wave height from the linear wave theory from test series *4012002* with wave steepness $H/\lambda = 1/22$

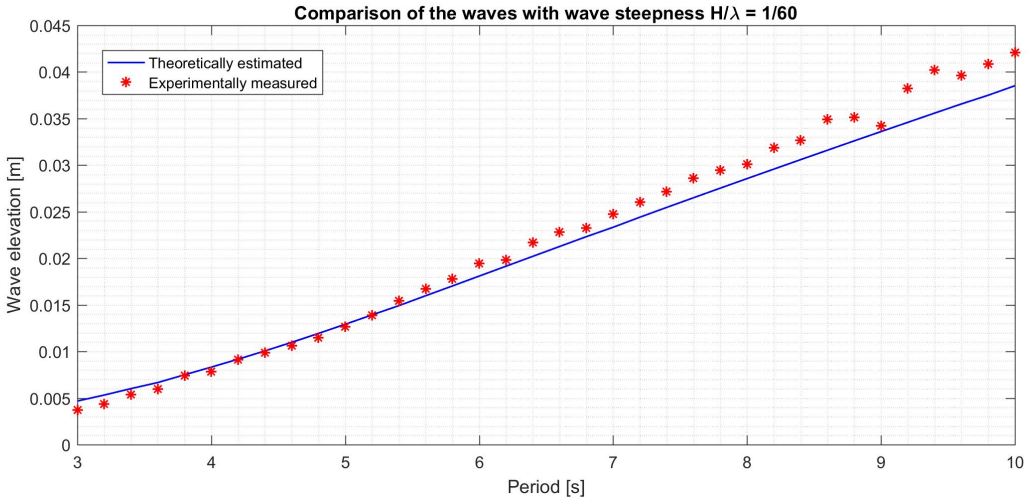

Comparison of the measured waves and the theoretically estimated wave height from the linear wave theory from test series *4012003* with wave steepness $H/\lambda = 1/60$

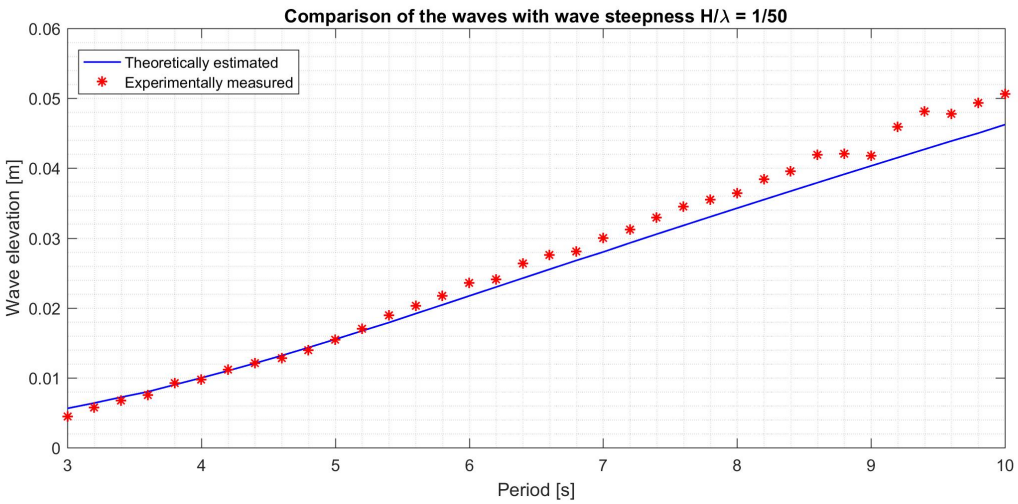

Comparison of the measured waves and the theoretically estimated wave height from the linear wave theory from test series *4012003* with wave steepness $H/\lambda = 1/50$

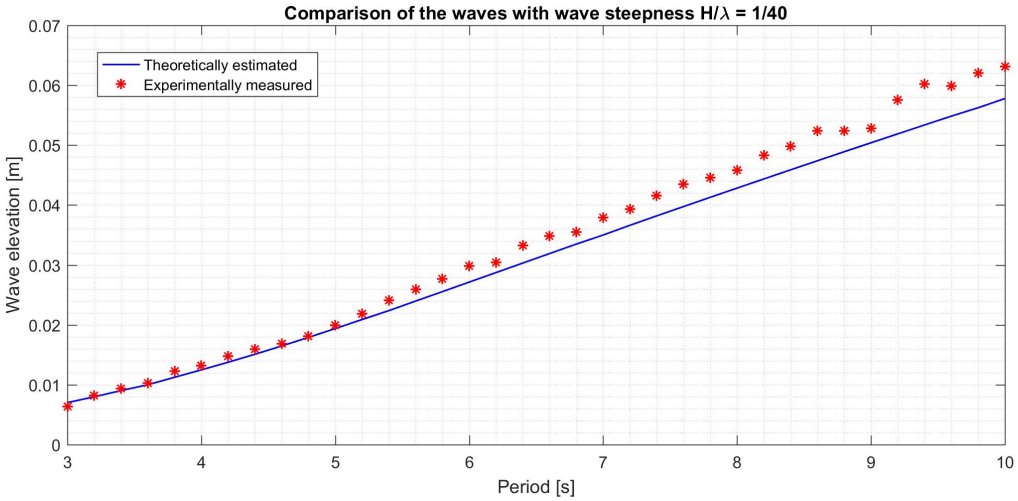

Comparison of the measured waves and the theoretically estimated wave height from the linear wave theory from test series *4012003* with wave steepness $H/\lambda = 1/40$

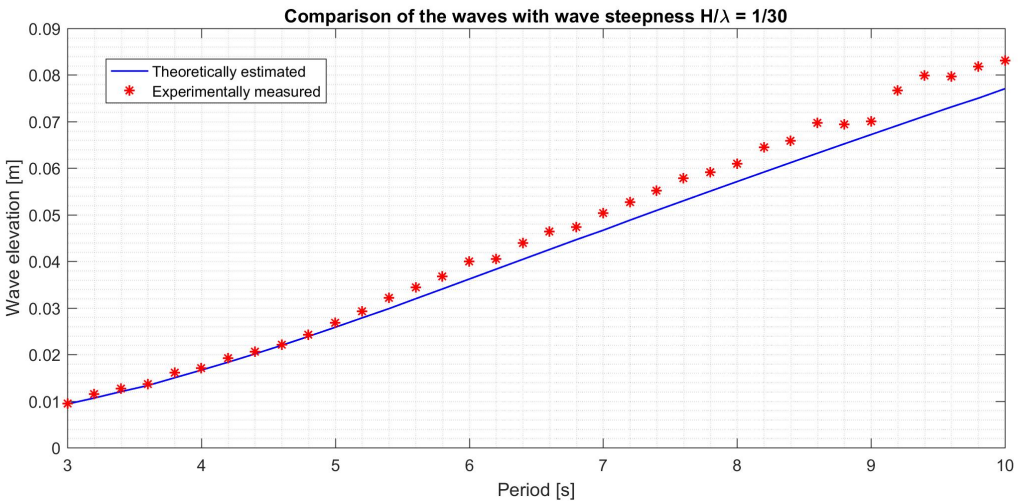

Comparison of the measured waves and the theoretically estimated wave height from the linear wave theory from test series *4012003* with wave steepness $H/\lambda = 1/30$

B.5 Wave profile of the run-up area

Wave profiles estimated from the three wave probes, *WP1cm, WP4cm* and *WP7cm* before the platform from experiments conducted in *April, 2018*. The wave profiles estimated for periods listed in the table below for the corresponding test series.

Test series	Periods in full scale where wave profiles are estimated	Wave steepness that are considered
401003	T = 3, 4, 5, 6, 7, 8, 9, 10, 11, 12, 13, 14, 15	$H/\lambda = 1/50$
4090011	T = 2, 3, 4, 5, 6, 7, 8, 9, 10, 11, 12, 13, 14, 15	$H/\lambda = 1/40$
4012002	T = 5, 6, 7, 8, 9, 10	$H/\lambda = 1/26, 1/22$
4012003	T = 3, 4, 5, 6, 7, 8, 9, 10	$H/\lambda = 1/60, 1/50$

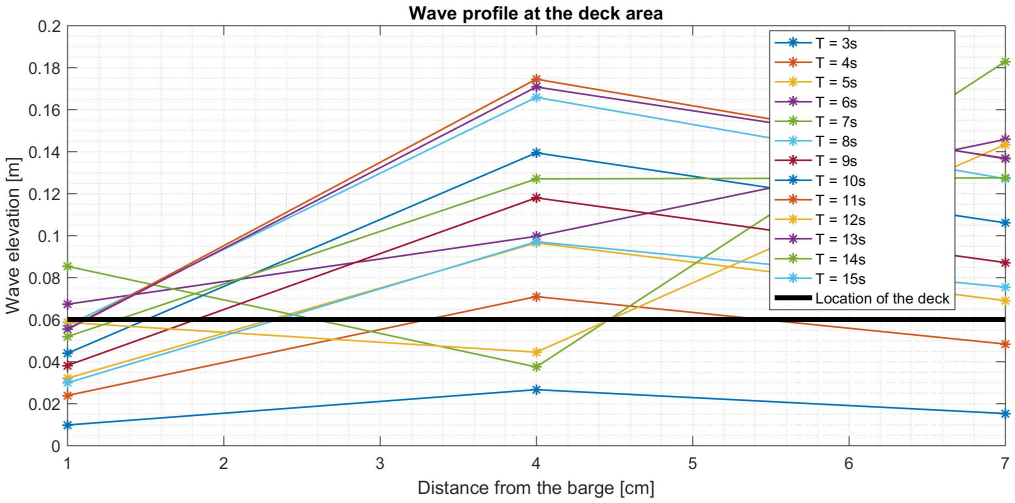

Wave profile of the run-up area before the deck tested with test series *401003*. Plotted with waves periods from $T = 3$ to $T = 15s$ with a step size of $1s$ and wave steepness of $H/\lambda = 1/50$. The location of the deck is marked as a black line

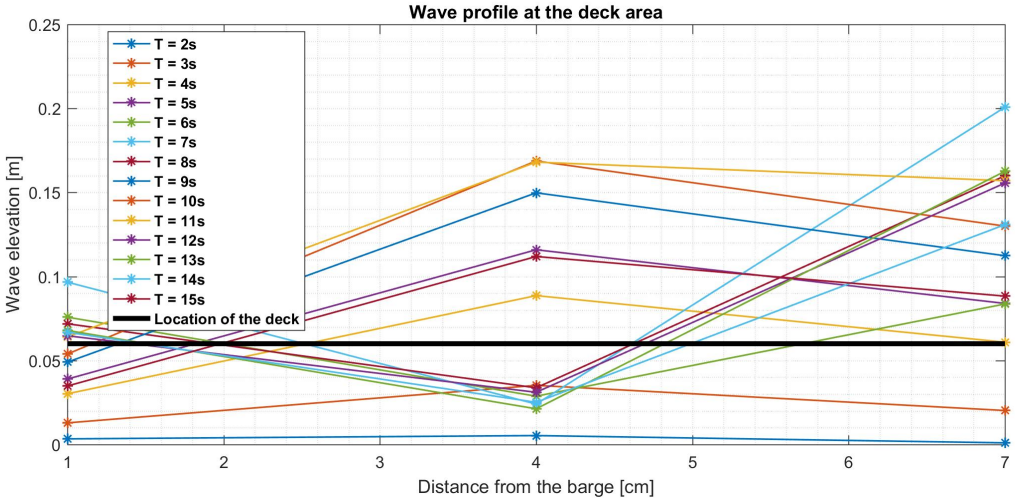

Wave profile of the run-up area before the deck tested with test series *4090011*. Plotted with waves periods from $T = 2$ to $T = 15s$ with a step size of $1s$ and wave steepness of $H/\lambda = 1/40$. The location of the deck is marked as a black line

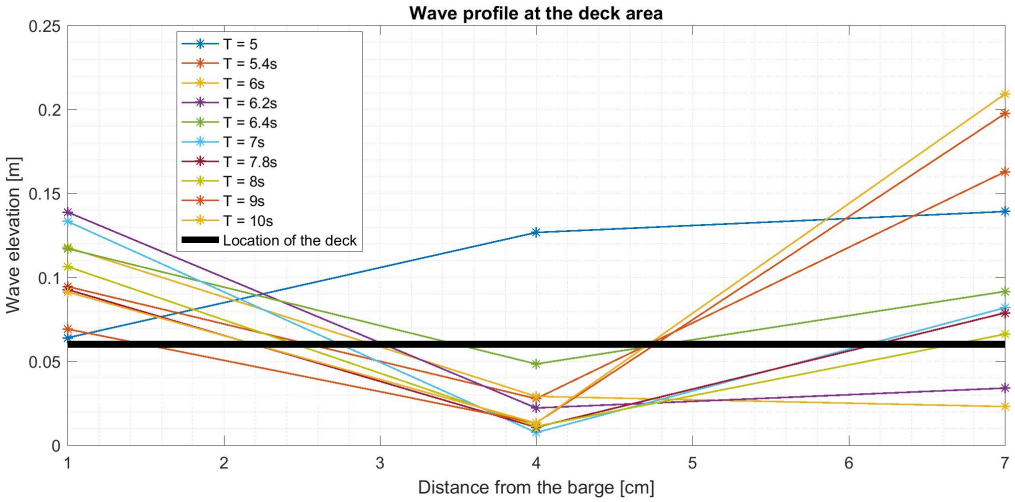

Wave profile of the run-up area before the deck tested with test series *4012002*. Plotted with waves of periods from $T = 5$ to $T = 10s$ with a step size of $1s$ with wave steepness of $H/\lambda = 1/26$. The location of the deck is marked as a black line

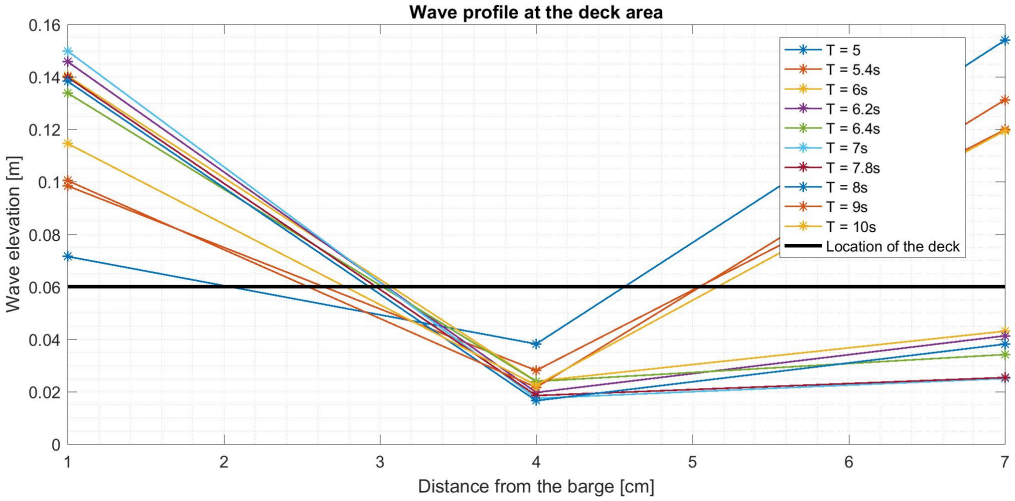

Wave profile of the run-up area before the deck tested with test series *4012002*. Plotted with waves of periods from $T = 5$ to $T = 10s$ with a step size of $1s$ with wave steepness of $H/\lambda = 1/22$. The location of the deck is marked as a black line

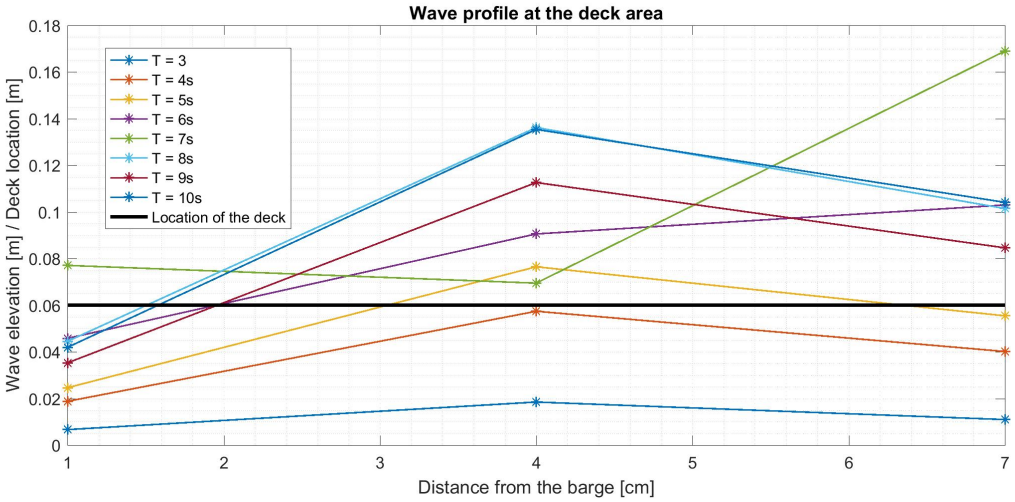

Wave profile of the run-up area before the deck tested with test series *4012003*. Plotted with waves of periods from $T = 3$ to $T = 10s$ with a step size of $1s$ with wave steepness of $H/\lambda = 1/60$. The location of the deck is marked as a black line

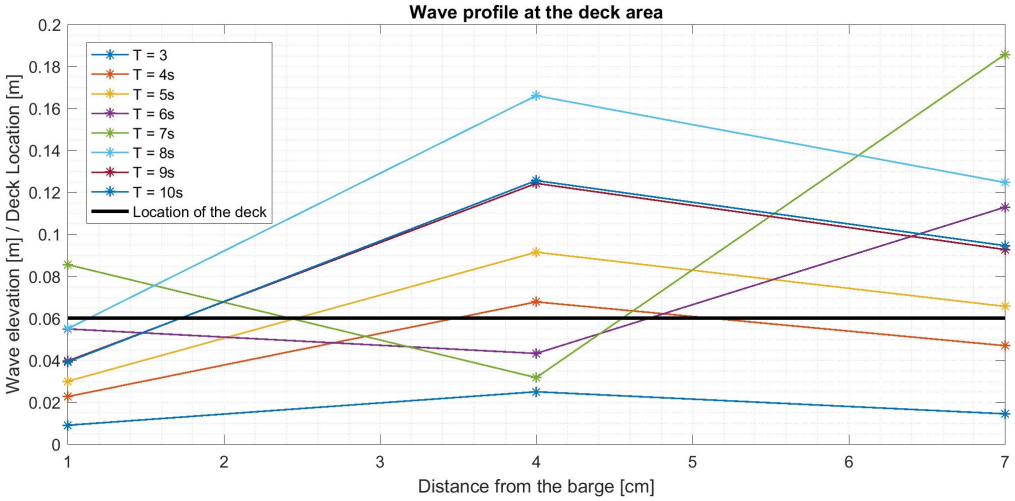

Wave profile of the run-up area before the deck tested with test series *4012003*. Plotted with waves of periods from $T = 3$ to $T = 10s$ with a step size of $1s$ with wave steepness of $H/\lambda = 1/50$. The location of the deck is marked as a black line

B.6 *MATLAB* Simulations

The *MATLAB* simulations are calculated by using the hydrodynamic coefficient from *WADAM* and the RAO from the experiments are presented. Table below gives the period and wave steepness of the pitch time series. The periods in the table are given in full scale.

Test series	Period [s]	Steepness	Wave height in full scale [m]
4012003	T = 7	H/λ = 1/60, 1/50, 1/40, 1/30	H = 1.167, 1.4, 1.75, 2.33
	T = 9	H/λ = 1/60, 1/50, 1/40, 1/30	H = 1.168, 2.016, 2.52, 3.36
Pitch RAO from the experiment	T = 7	0.1, 0.11, 0.12, 0.15 with k = 0.0898	
	T = 9	0.45, 0.525, 0.575, 0.6 with k = 0.0623	
Pitch amplitude from WADAM	T = 7	0.8651	
	T = 9	1.889	

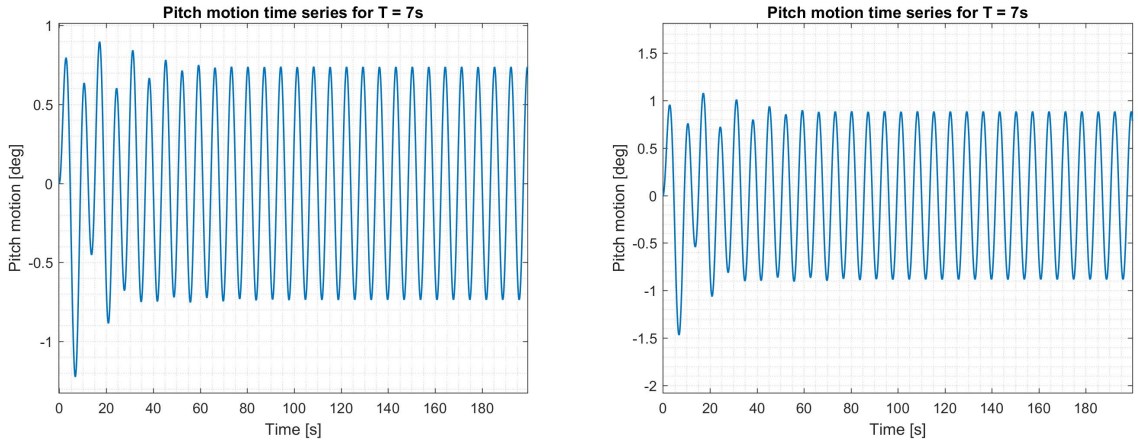

Pitch time series solved by ODE using the hydrodynamic coefficients from *WADAM*. Left: results with $H/\lambda = 1/60$. Right: results with $H/\lambda = 1/50$ with a period $T = 7s$ in full scale

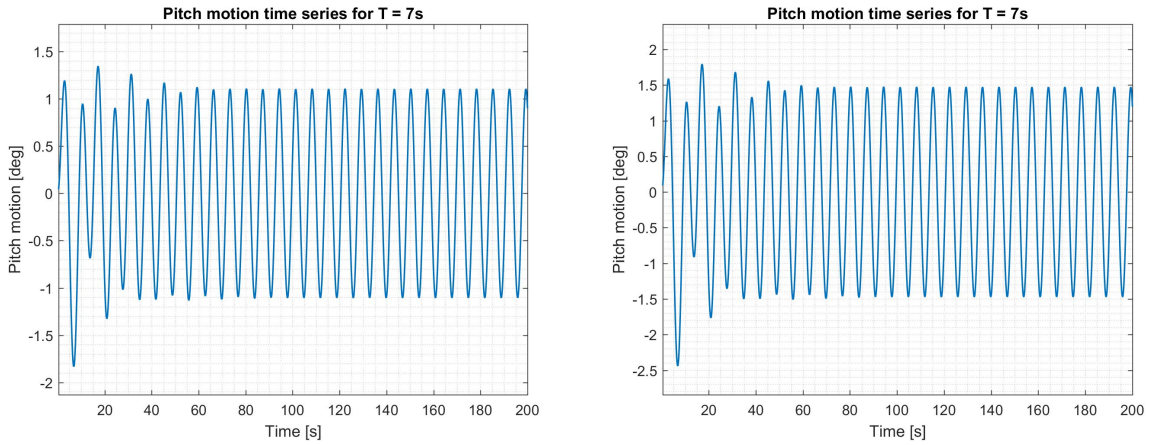

Pitch time series solved by ODE using the hydrodynamic coefficients from *WADAM*. Left: results with $H/\lambda = 1/40$. Right: results with $H/\lambda = 1/30$ with a period $T = 7s$ in full scale

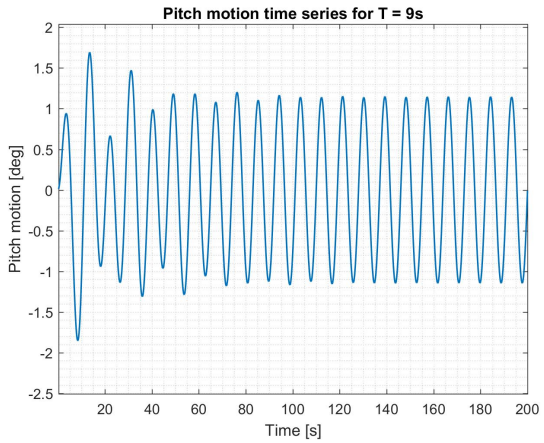

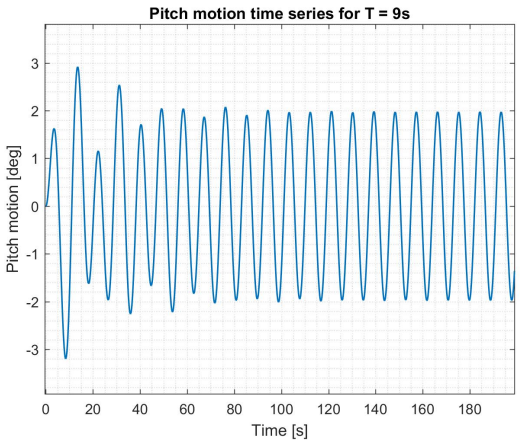

Pitch time series solved by ODE using the hydrodynamic coefficients from *WADAM*. Left: results with $H/\lambda = 1/60$. Right: results with $H/\lambda = 1/50$ with a period $T = 9s$ in full scale

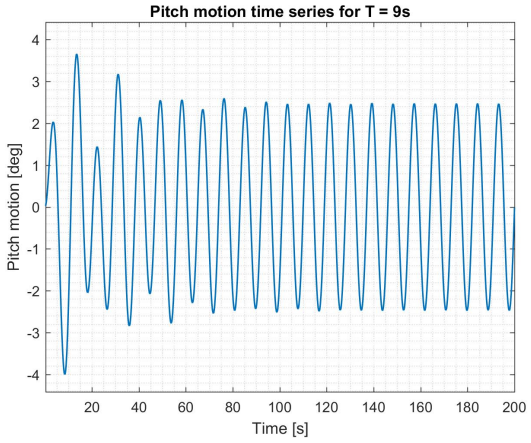

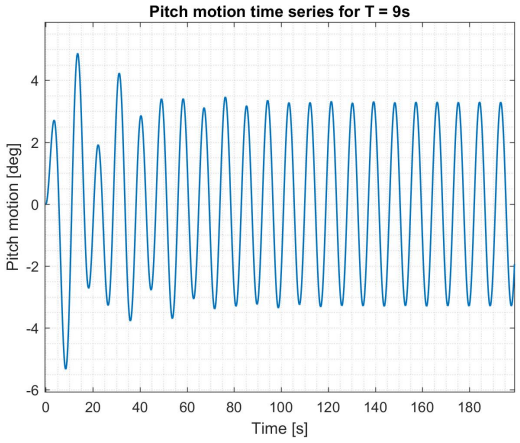

Pitch time series solved by ODE using the hydrodynamic coefficients from *WADAM*. Left: results with $H/\lambda = 1/40$. Right: results with $H/\lambda = 1/30$ with a period $T = 9s$ in full scale

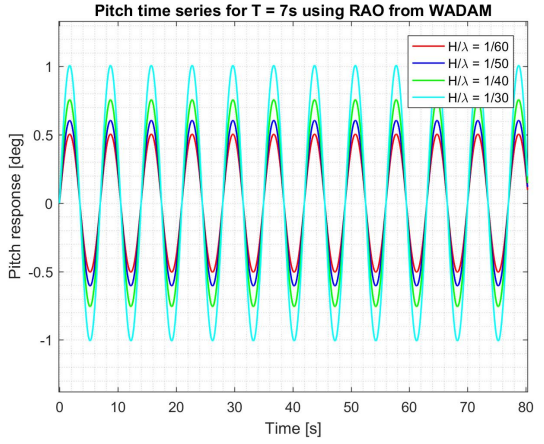

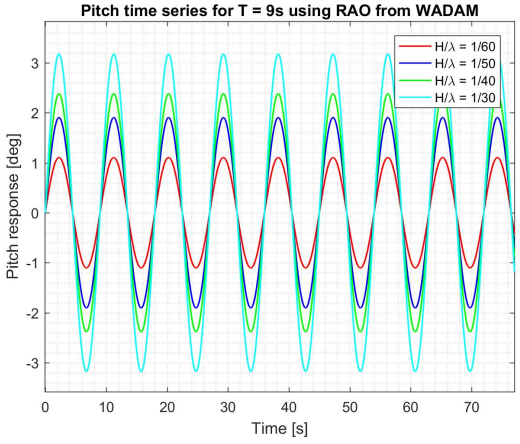

Pitch time series solved by using the pitch amplitude from RAO calculated from *WADAM* multiplied with the wave amplitude for different wave steepness. Left: Results with $T = 7s$. Right: Results with $T = 9s$

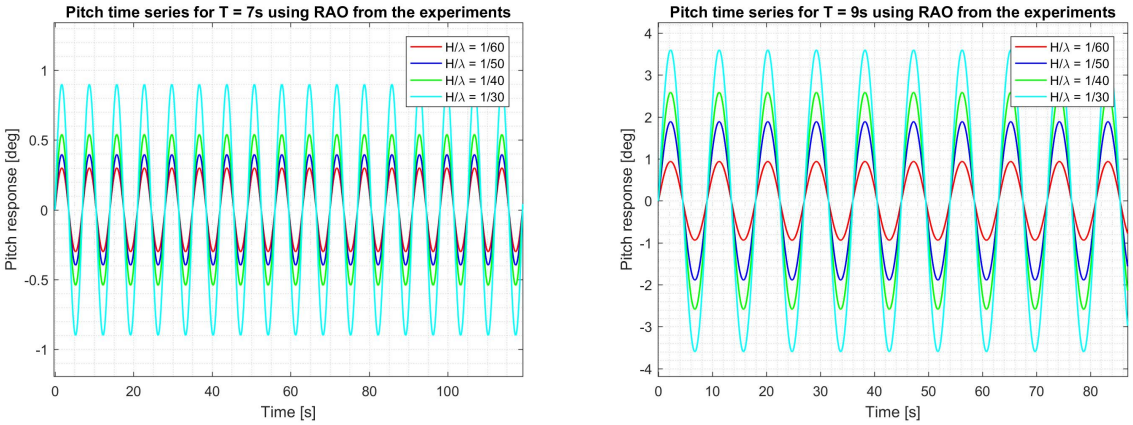

Pitch time series solved by using pitch amplitude from RAO obtained from the experiments. The pitch amplitude are multiplied with wave number, k. Left: Results with $T = 7s$. Right: Results with $T = 9s$

B.7 Time series

The time series results from the experiments during *January* and *April* are presented with the parameters according to the table below. Time series of wave elevations are only plotted for test series *80000*.

Test serie	Periods in full scale considered	Steepness considered
80000	T = 6, 7	$H/\lambda = 1/30, 1/15$
401003	T = 6, 6.5, 7, 9	$H/\lambda = 1/50$
4012002	T = 6, 6.2, 7, 9	$H/\lambda = 1/22$
4012003	T = 6, 6.2, 7, 9	$H/\lambda = 1/60, 1/40, 1/30$

Wave elevation

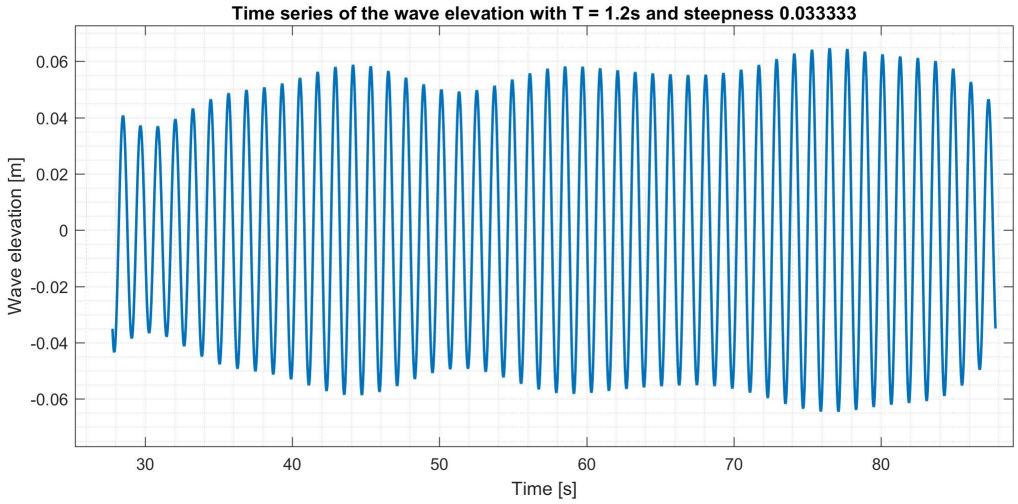

Time series of the wave elevation measured by *WP3* for a regular wave with wave steepness $H/\lambda = 1/30$ and corresponding wave period $T = 6s$ in full scale for test series *80000*

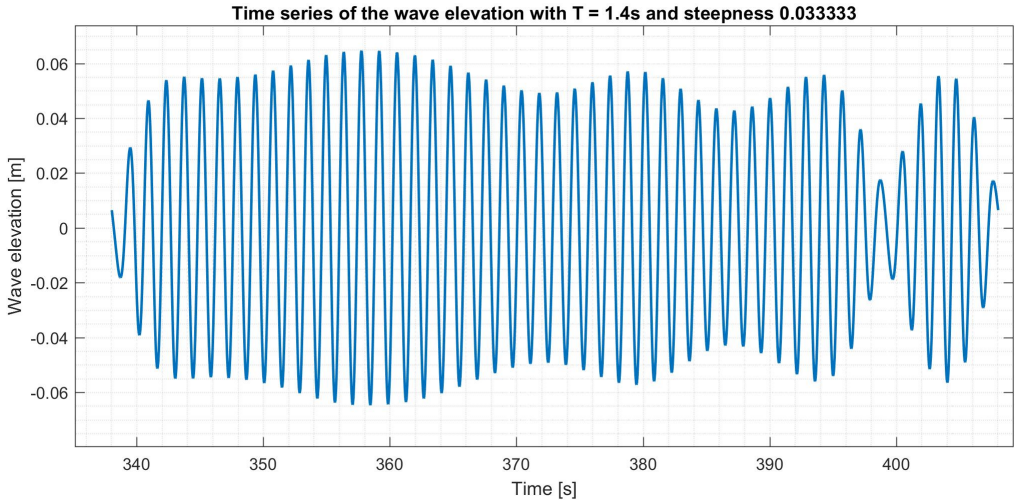

Time series of the wave elevation measured by *WP3* for a regular wave with wave steepness $H/\lambda = 1/30$ and corresponding wave period $T = 7s$ in full scale for test series *80000*

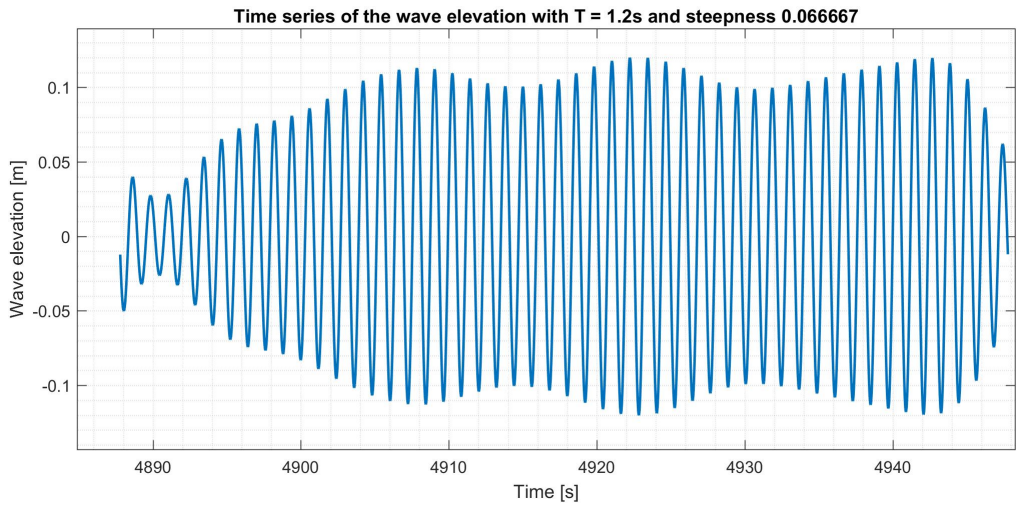

Time series of the wave elevation measured by *WP3* for a regular wave with wave steepness $H/\lambda = 1/15$ and corresponding wave period $T = 6s$ in full scale for test series *80000*

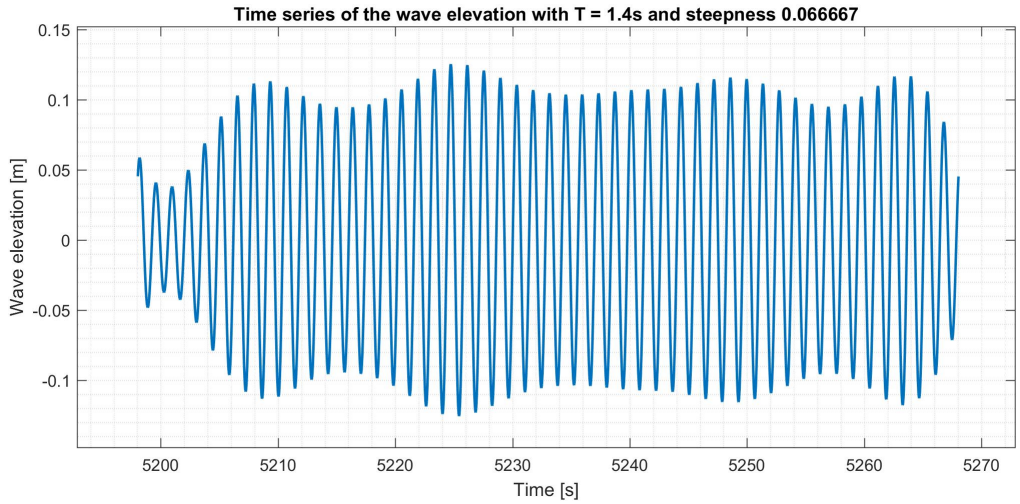

Time series of the wave elevation measured by *WP3* for a regular wave with wave steepness $H/\lambda = 1/15$ and corresponding wave period $T = 7s$ in full scale for test series *80000*

Motions

Time series of the heave motions

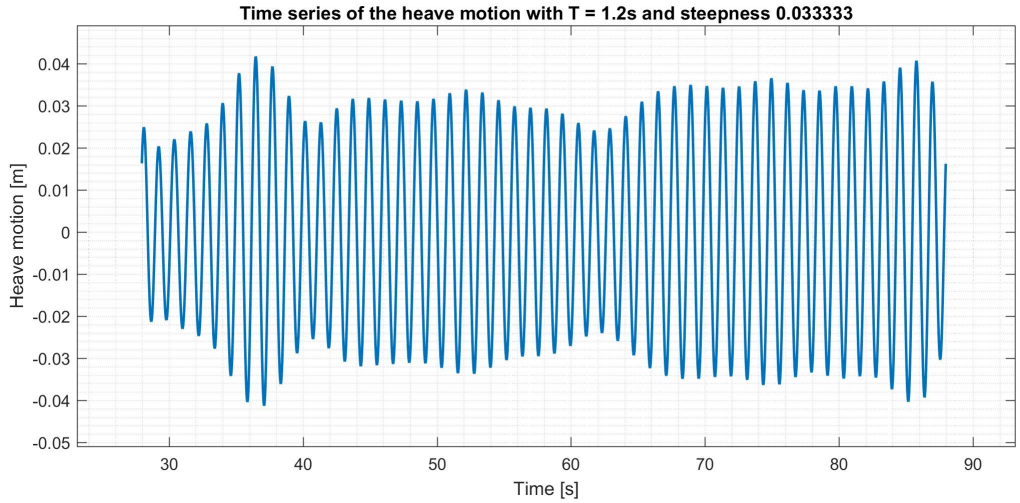

Time series of the heave motion from a regular wave with wave steepness $H/\lambda = 1/30$ and corresponding wave period $T = 6s$ in full scale for test series *80000*

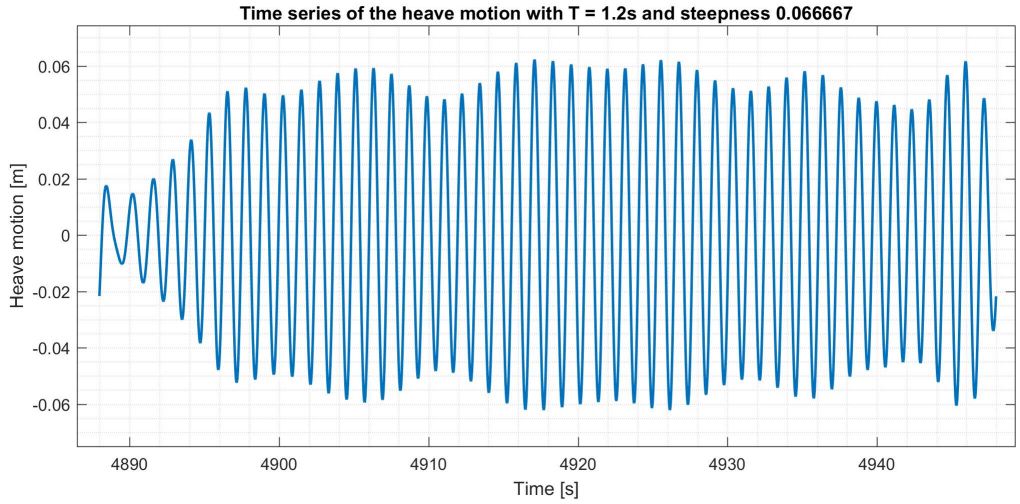

Time series of the heave motion from a regular wave with wave steepness $H/\lambda = 1/15$ and corresponding wave period $T = 6s$ in full scale for test series *80000*

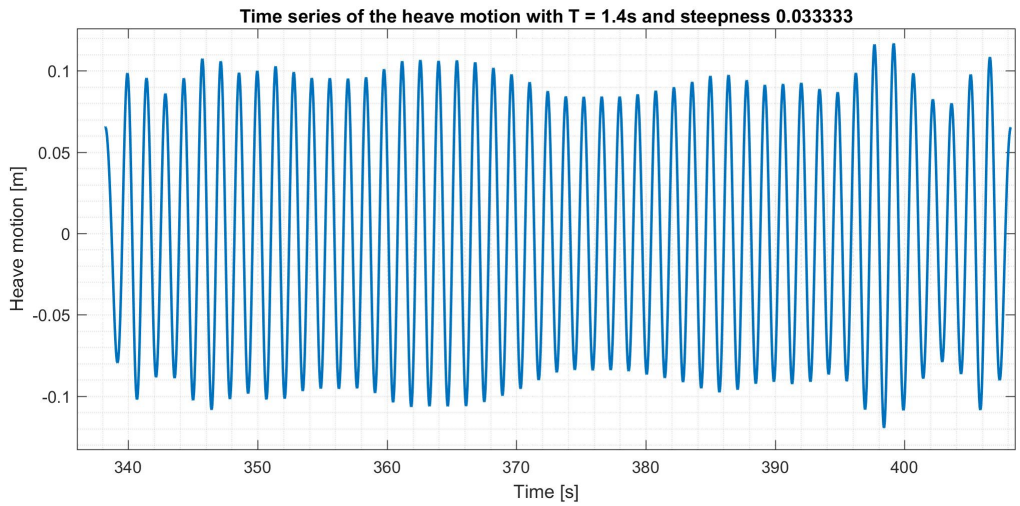

Time series of the heave motion from a regular wave with wave steepness $H/\lambda = 1/30$ and corresponding wave period $T = 7s$ in full scale for test series *80000*

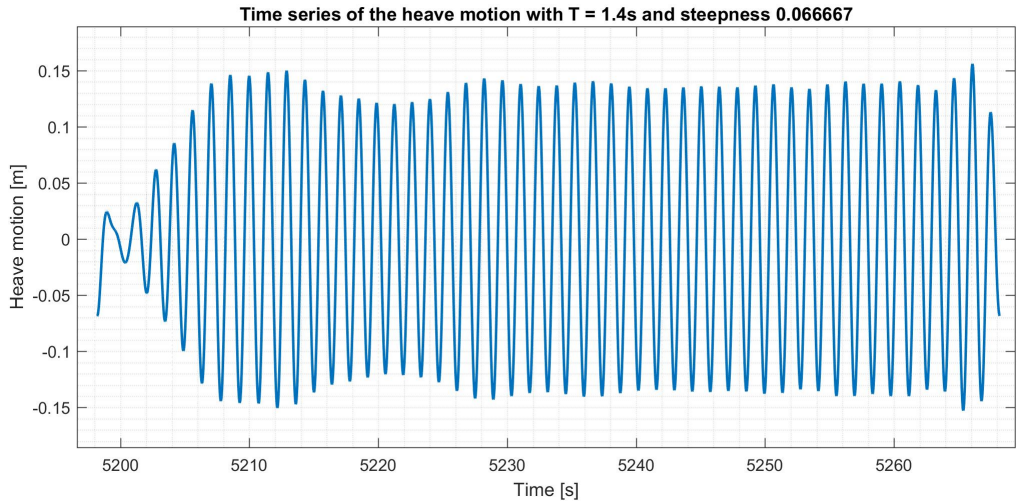

Time series of the heave motion from a regular wave with wave steepness $H/\lambda = 1/15$ and corresponding wave period $T = 7s$ in full scale for test series *80000*

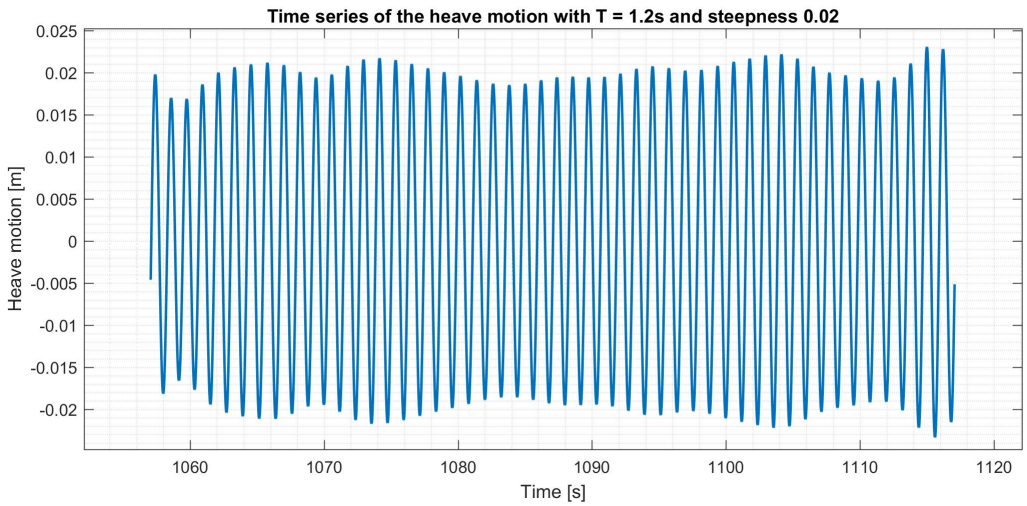

Time series of the heave motion from a regular wave with wave steepness $H/\lambda = 1/50$ and corresponding wave period $T = 6s$ in full scale for test series *401003*

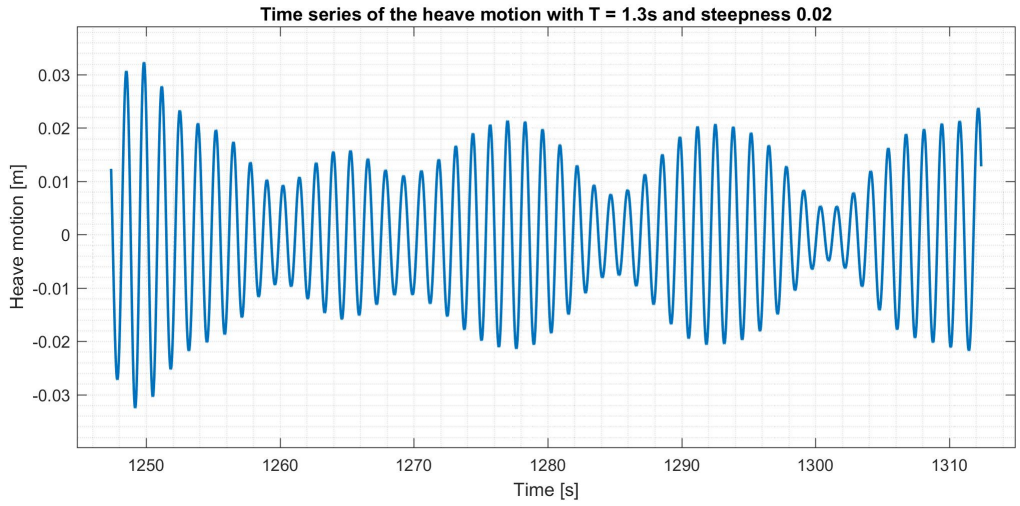

Time series of the heave motion from a regular wave with wave steepness $H/\lambda = 1/50$ and corresponding wave period $T = 6.5s$ in full scale for test series *401003*

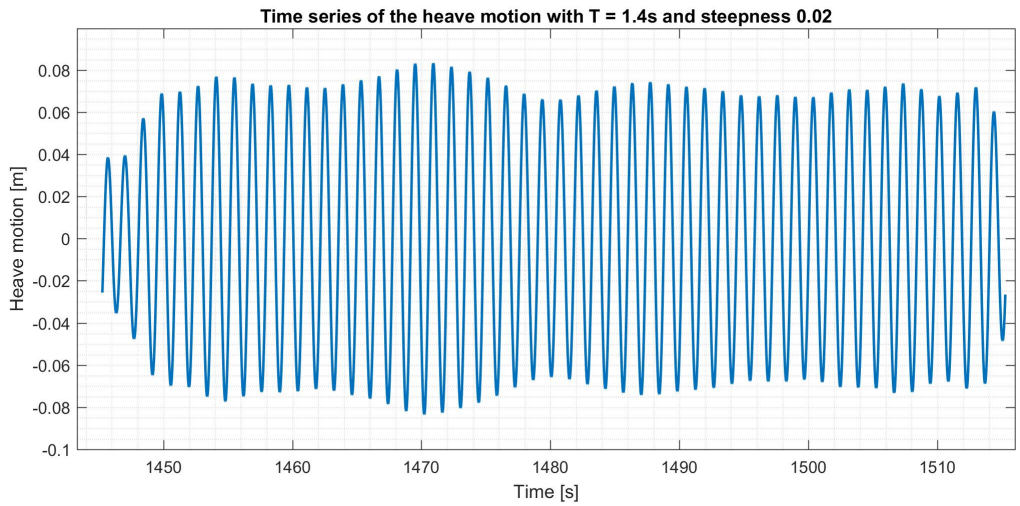

Time series of the heave motion from a regular wave with wave steepness $H/\lambda = 1/50$ and corresponding wave period $T = 7s$ in full scale for test series *401003*

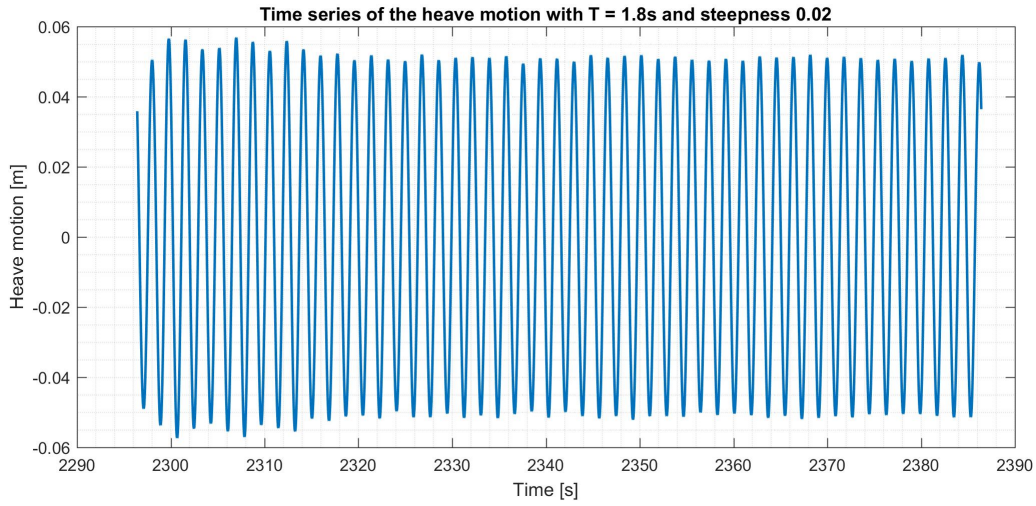

Time series of the heave motion from a regular wave with wave steepness $H/\lambda = 1/50$ and corresponding wave period $T = 9s$ in full scale for test series *401003*

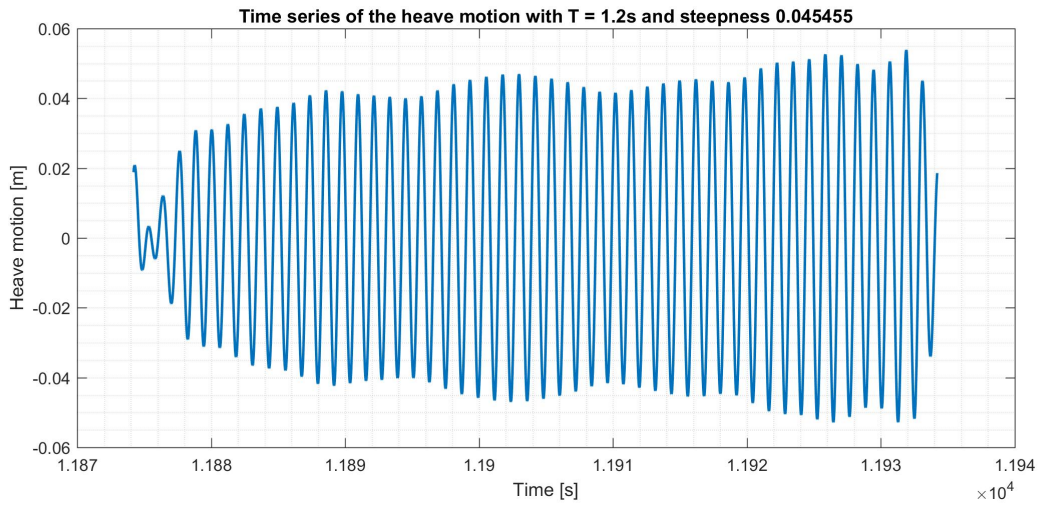

Time series of the heave motion from a regular wave with wave steepness $H/\lambda = 1/22$ and corresponding wave period $T = 6s$ in full scale for test series *4012002*

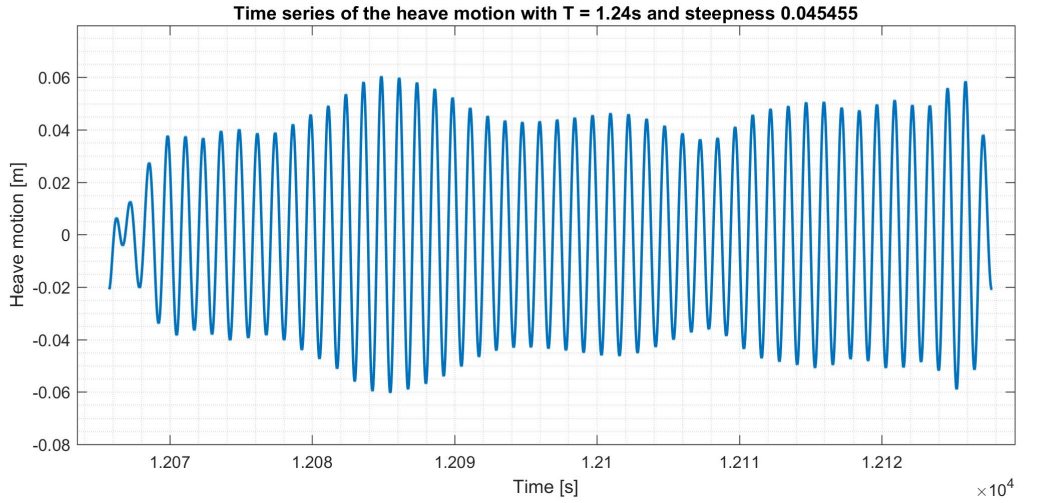

Time series of the heave motion from a regular wave with wave steepness $H/\lambda = 1/22$ and corresponding wave period $T = 6.2s$ in full scale for test series *401003*

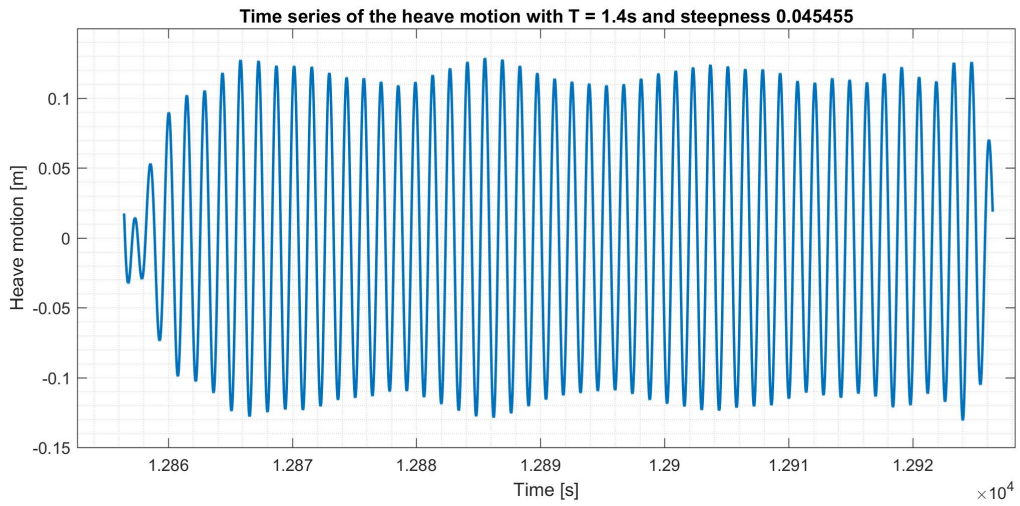

Time series of the heave motion from a regular wave with wave steepness $H/\lambda = 1/22$ and corresponding wave period $T = 7s$ in full scale for test series *4012002*

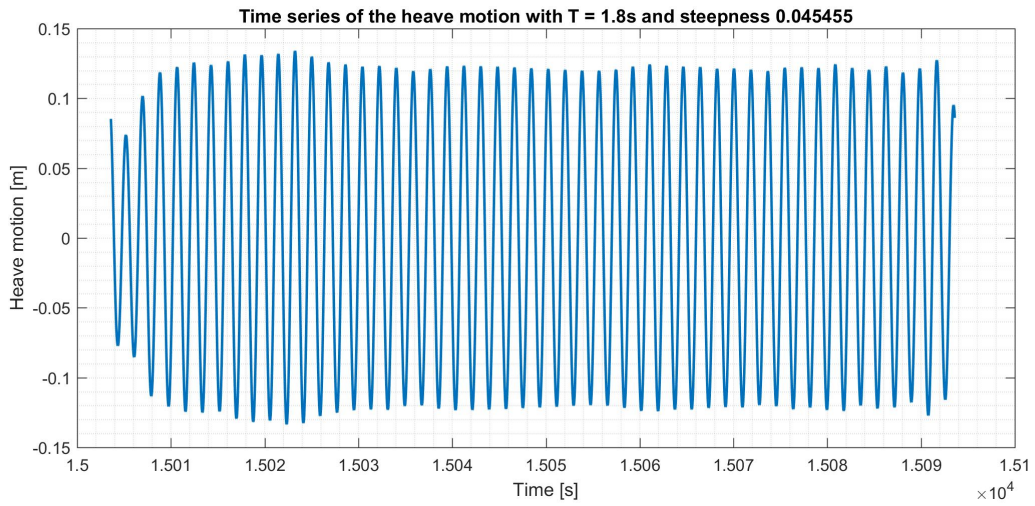

Time series of the heave motion from a regular wave with wave steepness $H/\lambda = 1/22$ and corresponding wave period $T = 9s$ in full scale for test series *4012002*

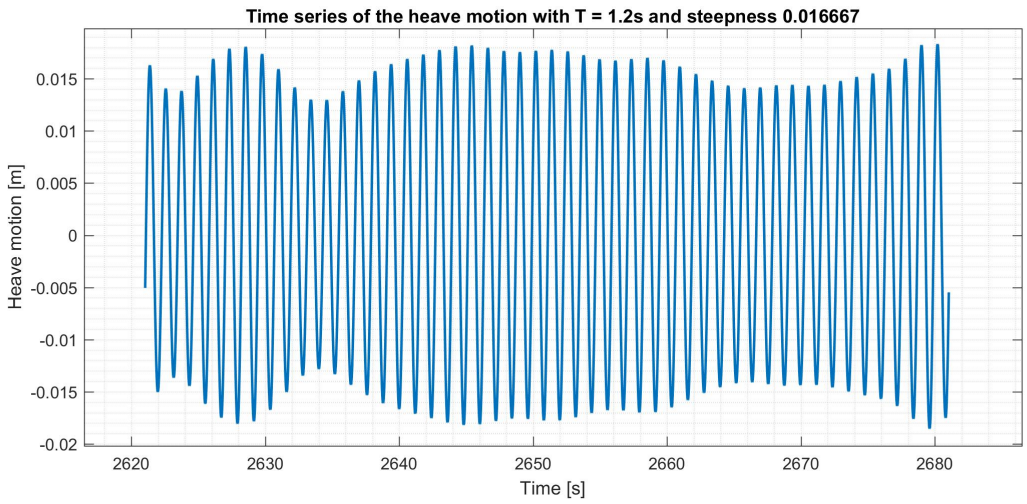

Time series of the heave motion from a regular wave with wave steepness $H/\lambda = 1/60$ and corresponding wave period $T = 6s$ in full scale for test series *4012003*

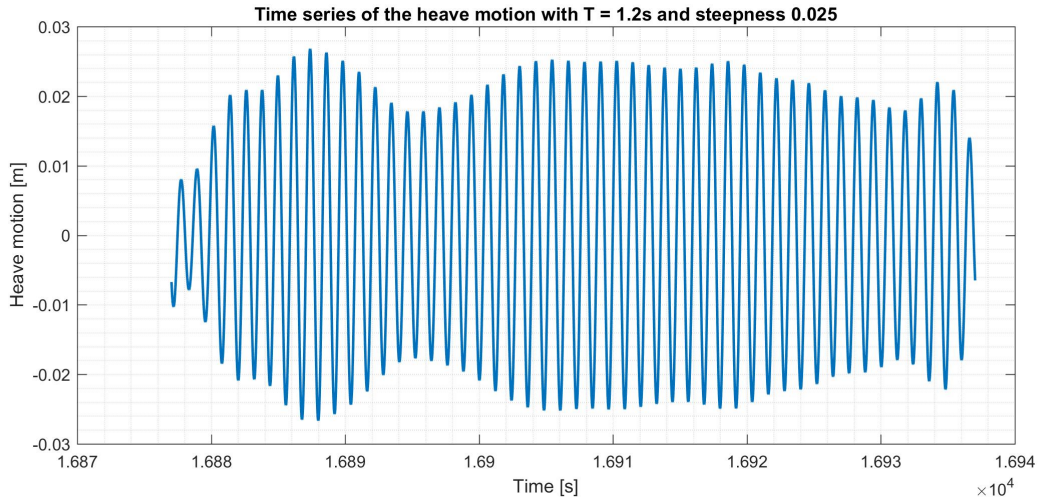

Time series of the heave motion from a regular wave with wave steepness $H/\lambda = 1/40$ and corresponding wave period $T = 6s$ in full scale for test series *4012003*

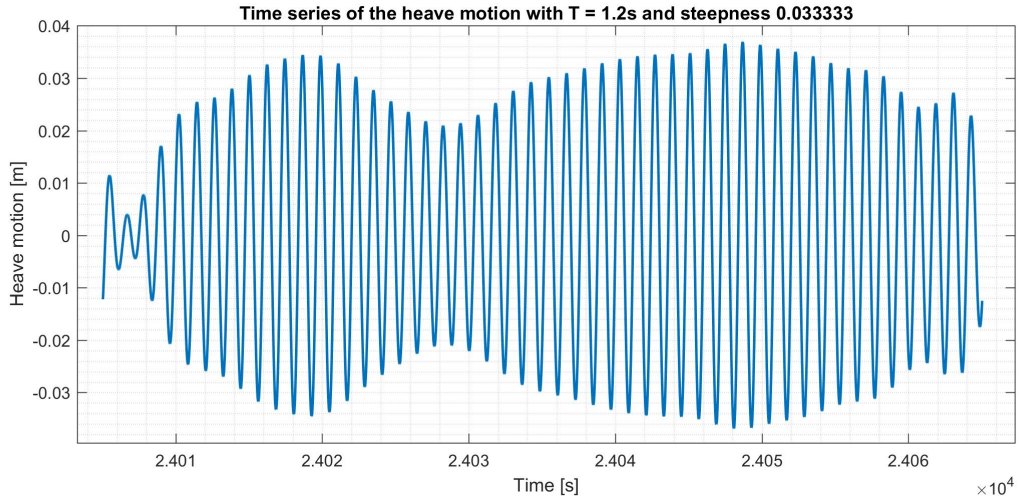

Time series of the heave motion from a regular wave with wave steepness $H/\lambda = 1/30$ and corresponding wave period $T = 6s$ in full scale for test series *4012003*

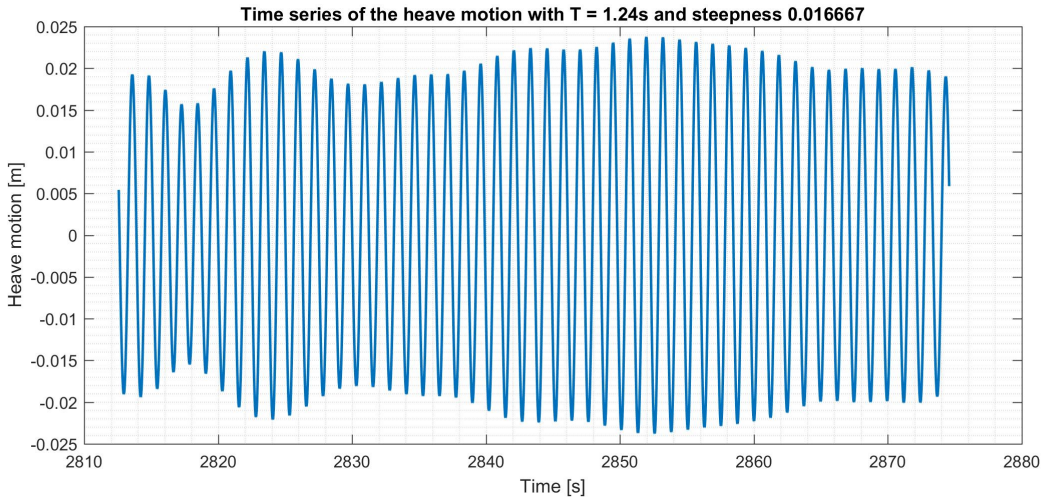

Time series of the heave motion from a regular wave with wave steepness $H/\lambda = 1/60$ and corresponding wave period $T = 6.2s$ in full scale for test series *4012003*

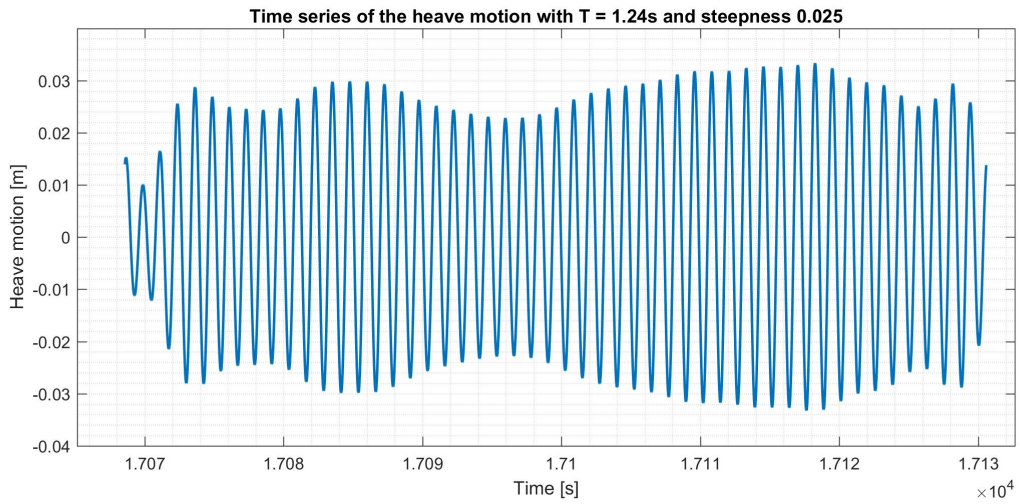

Time series of the heave motion from a regular wave with wave steepness $H/\lambda = 1/40$ and corresponding wave period $T = 6.2s$ in full scale for test series *4012003*

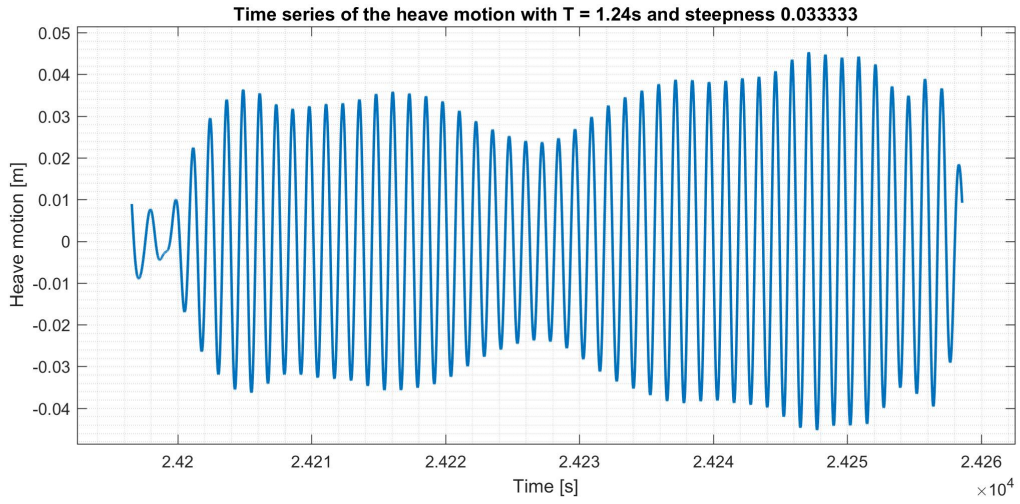

Time series of the heave motion from a regular wave with wave steepness $H/\lambda = 1/30$ and corresponding wave period $T = 6.2s$ in full scale for test series *4012003*

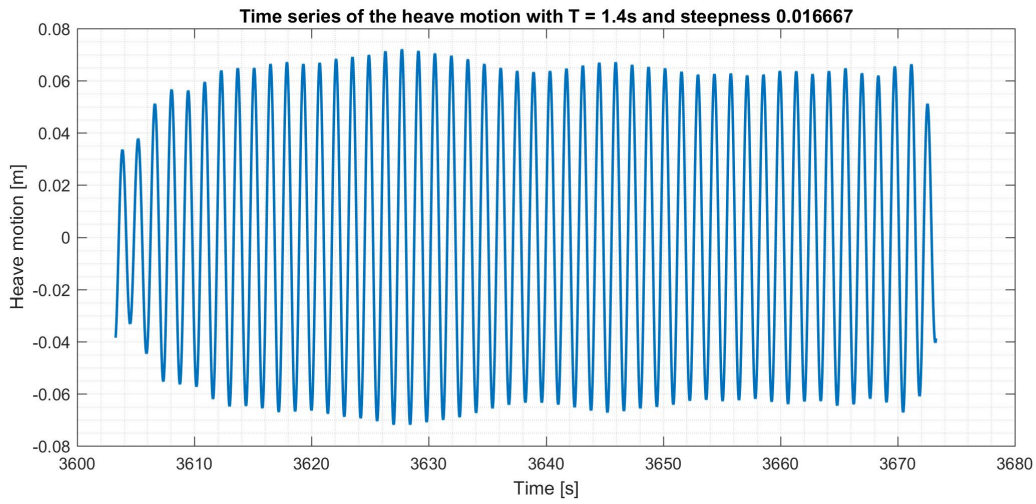

Time series of the heave motion from a regular wave with wave steepness $H/\lambda = 1/60$ and corresponding wave period $T = 7s$ in full scale for test series *4012003*

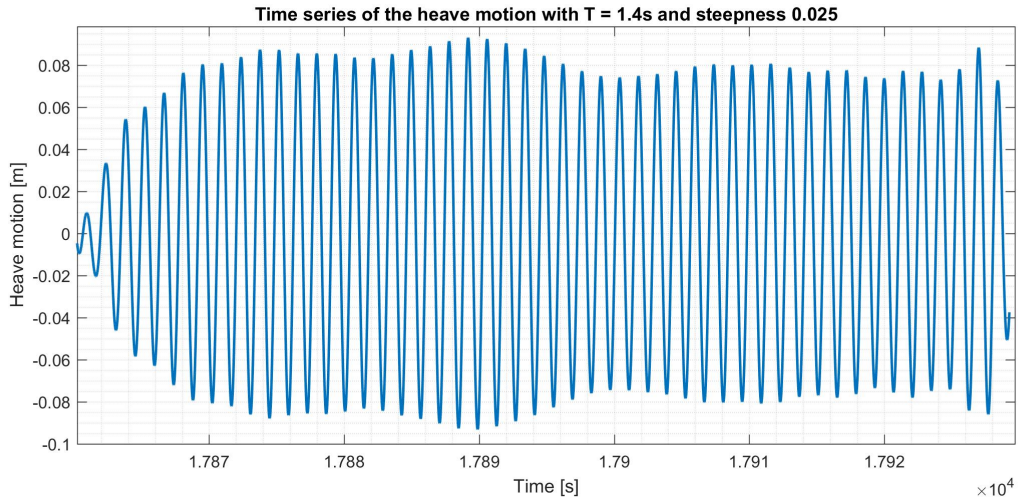

Time series of the heave motion from a regular wave with wave steepness $H/\lambda = 1/40$ and corresponding wave period $T = 7s$ in full scale for test series *4012003*

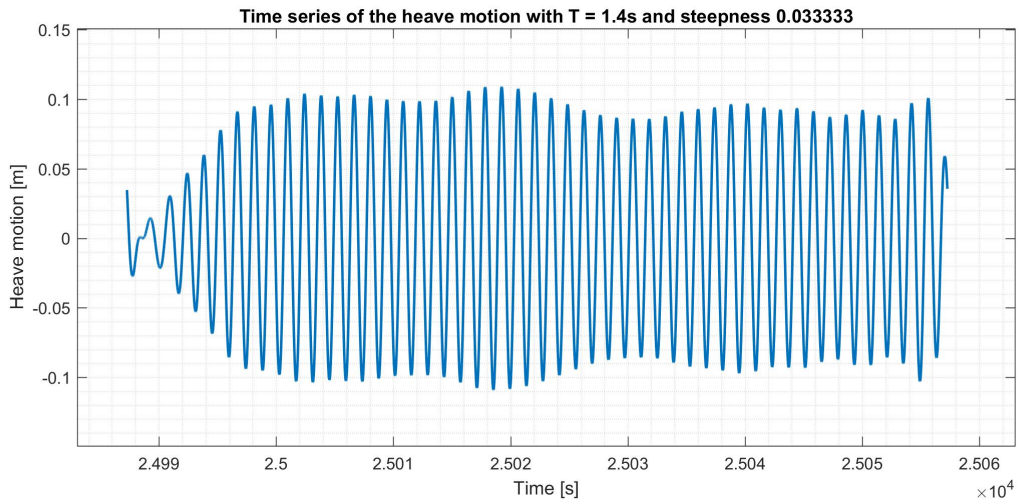

Time series of the heave motion from a regular wave with wave steepness $H/\lambda = 1/30$ and corresponding wave period $T = 7s$ in full scale for test series *4012003*

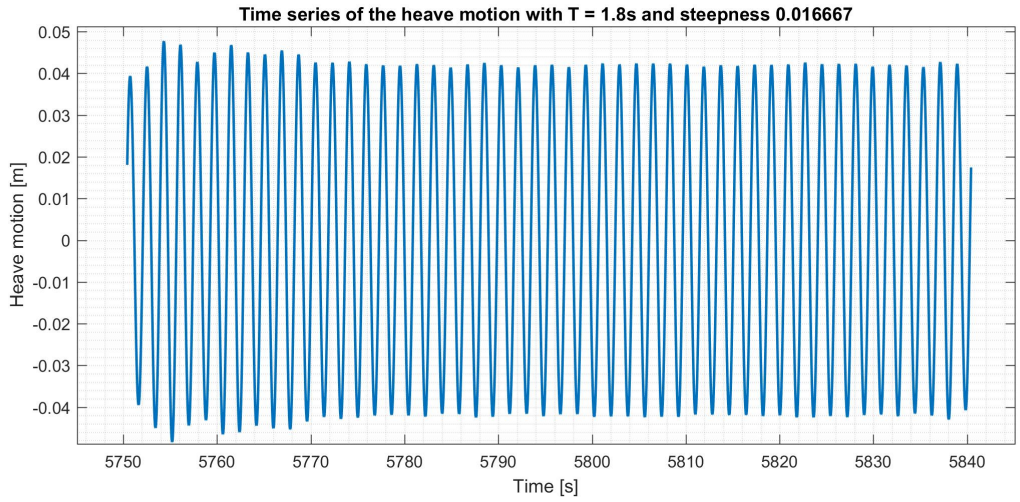

Time series of the heave motion from a regular wave with wave steepness $H/\lambda = 1/60$ and corresponding wave period $T = 9s$ in full scale for test series *4012003*

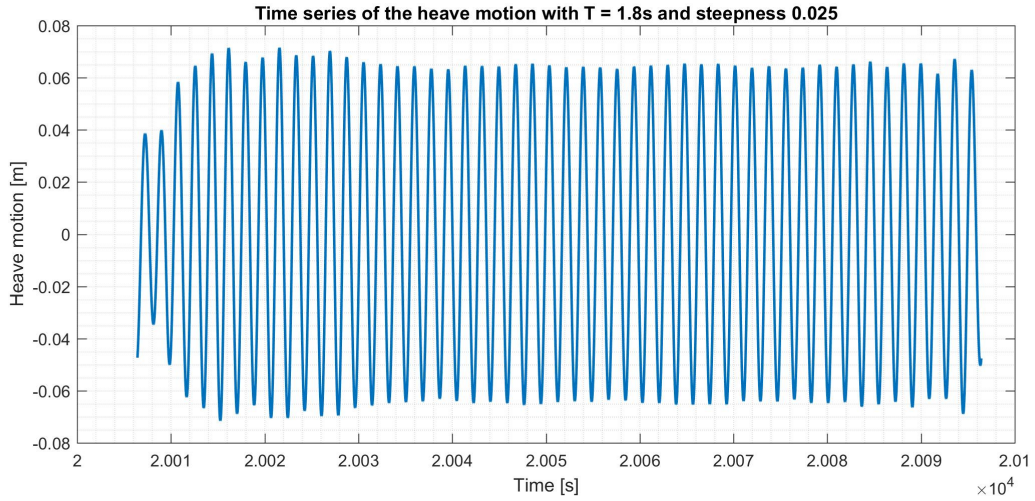

Time series of the heave motion from a regular wave with wave steepness $H/\lambda = 1/40$ and corresponding wave period $T = 9s$ in full scale for test series *4012003*

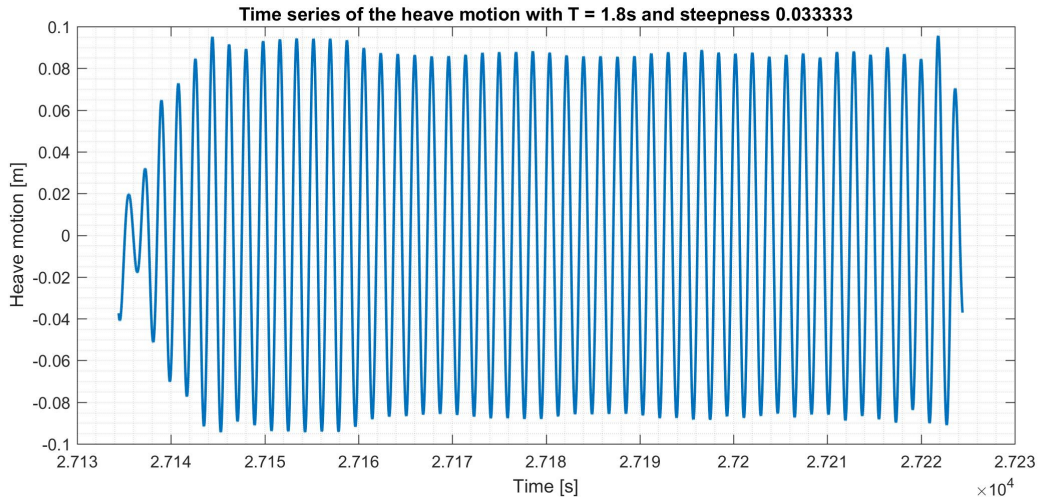

Time series of the heave motion from a regular wave with wave steepness $H/\lambda = 1/30$ and corresponding wave period $T = 9s$ in full scale for test series *4012003*

Time series of pitch motions

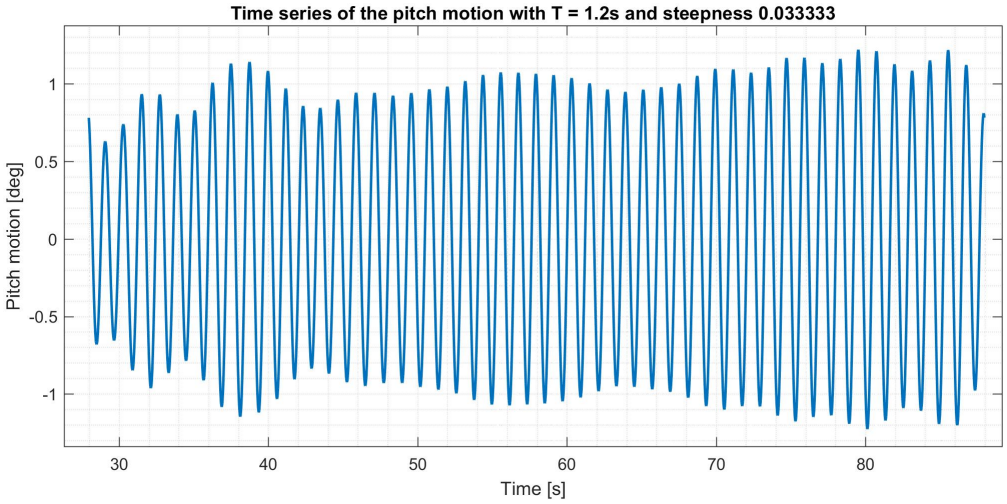

Time series of the pitch motion from a regular wave with wave steepness $H/\lambda = 1/30$ and corresponding wave period $T = 6s$ in full scale for test series *80000*

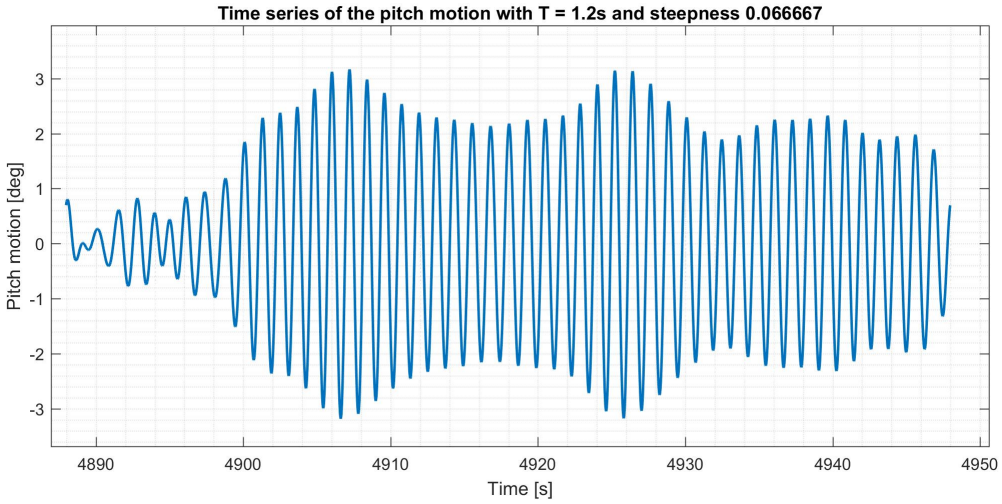

Time series of the pitch motion from a regular wave with wave steepness $H/\lambda = 1/15$ and corresponding wave period $T = 6s$ in full scale for test series *80000*

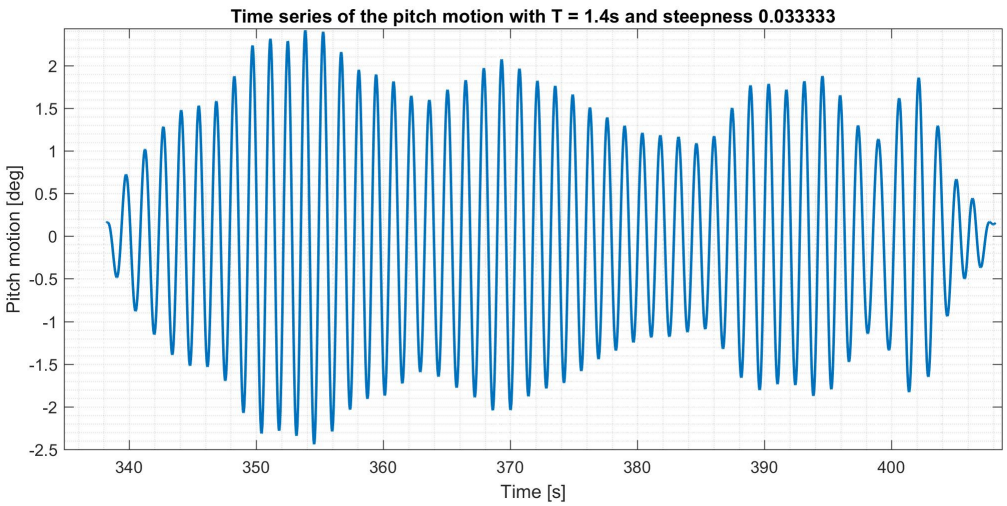

Time series of the pitch motion from a regular wave with wave steepness $H/\lambda = 1/30$ and corresponding wave period $T = 7s$ in full scale for test series *80000*

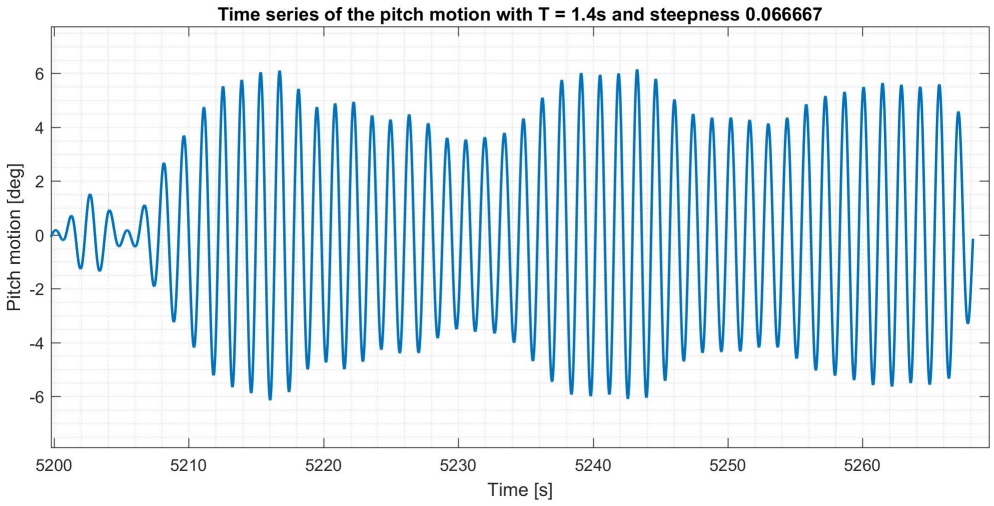

Time series of the pitch motion from a regular wave with wave steepness $H/\lambda = 1/15$ and corresponding wave period $T = 7s$ in full scale for test series *80000*

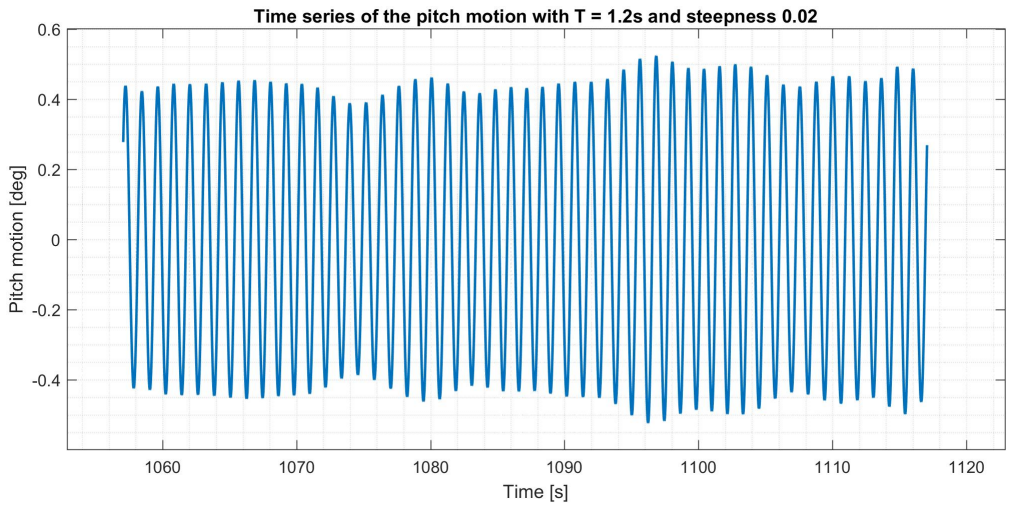

Time series of the pitch motion from a regular wave with wave steepness $H/\lambda = 1/50$ and corresponding wave period $T = 6s$ in full scale for test series *401003*

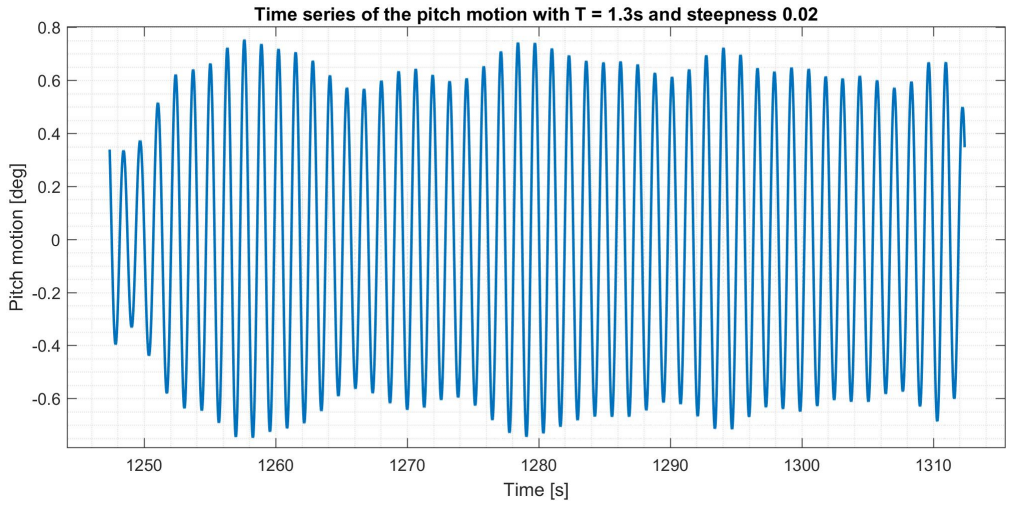

Time series of the pitch motion from a regular wave with wave steepness $H/\lambda = 1/50$ and corresponding wave period $T = 6.5s$ in full scale for test series *401003*

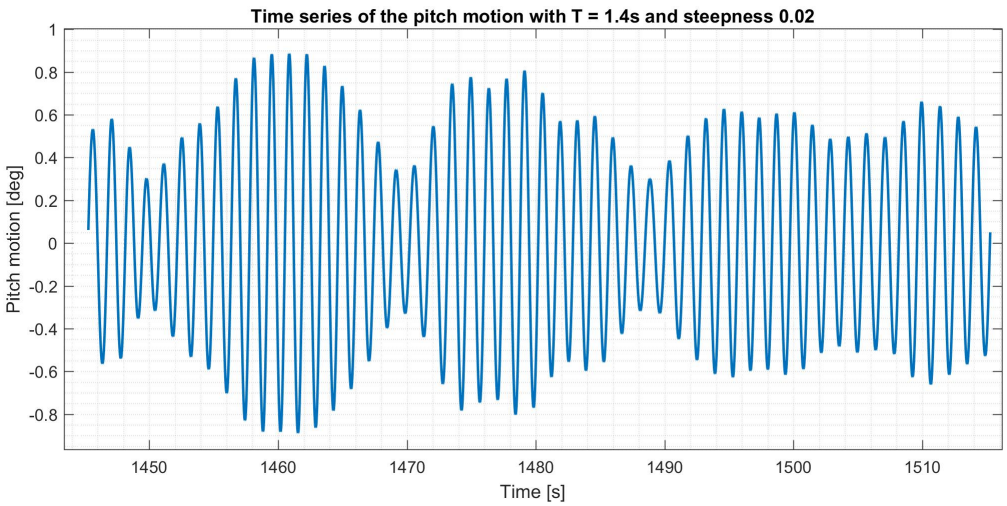

Time series of the pitch motion from a regular wave with wave steepness $H/\lambda = 1/50$ and corresponding wave period $T = 7s$ in full scale for test series *401003*

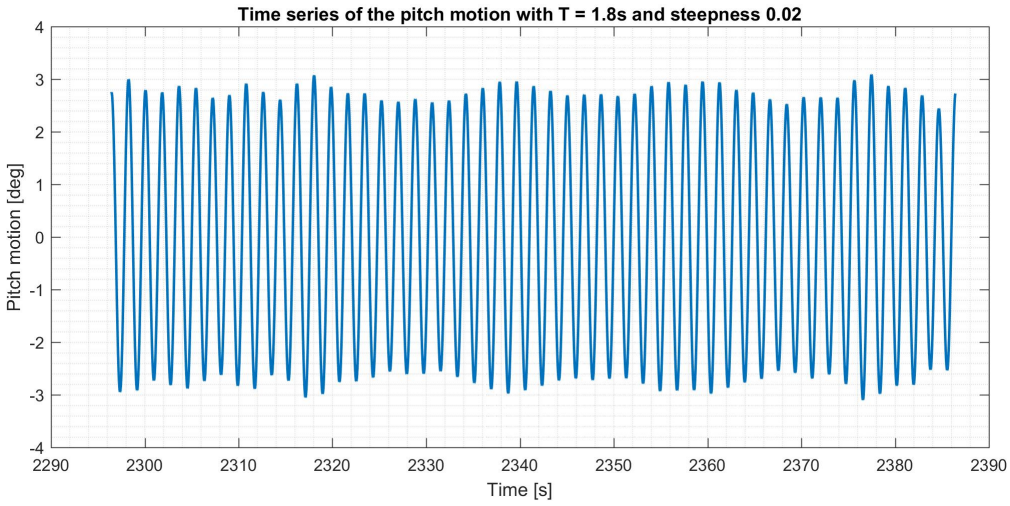

Time series of the pitch motion from a regular wave with wave steepness $H/\lambda = 1/50$ and corresponding wave period $T = 9s$ in full scale for test series *401003*

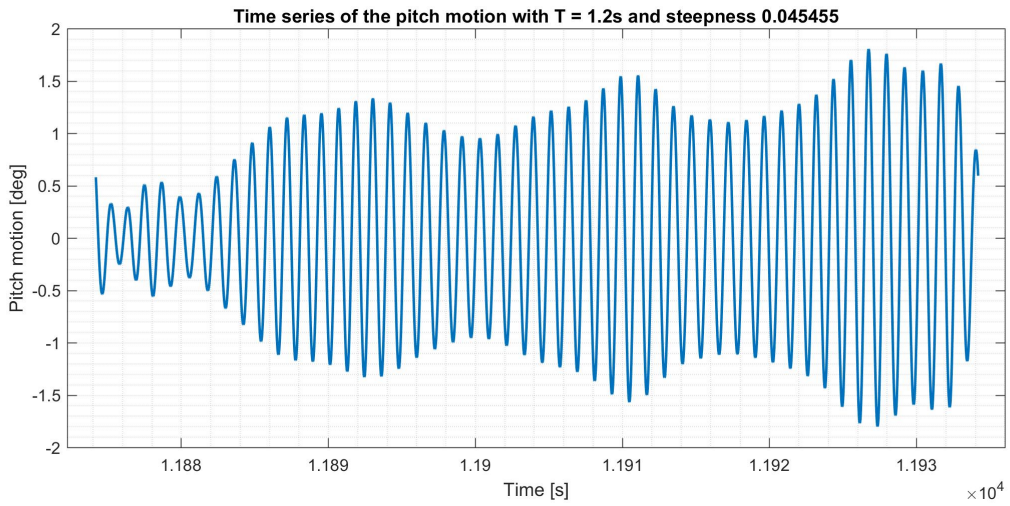

Time series of the pitch motion from a regular wave with wave steepness $H/\lambda = 1/22$ and corresponding wave period $T = 6s$ in full scale for test series *4012002*

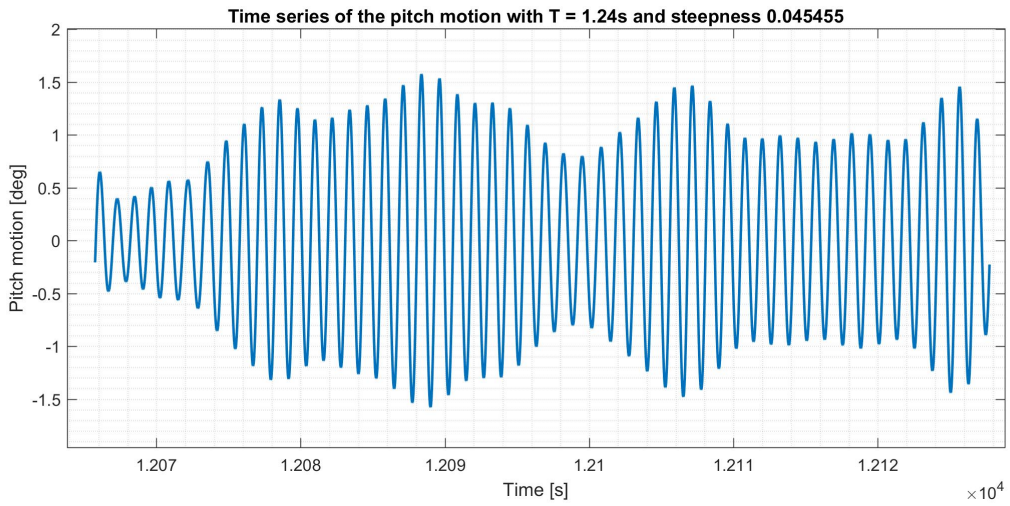

Time series of the pitch motion from a regular wave with wave steepness $H/\lambda = 1/22$ and corresponding wave period $T = 6.2s$ in full scale for test series *401003*

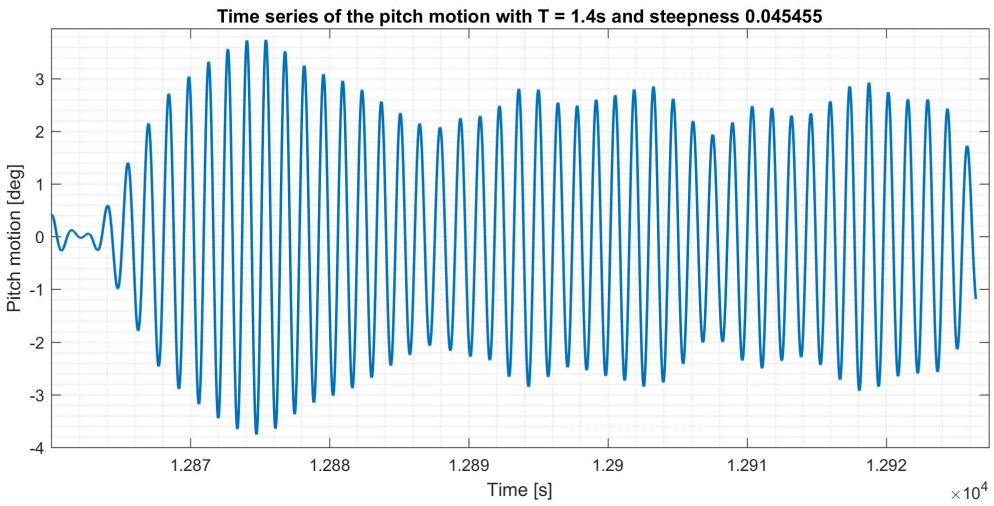

Time series of the pitch motion from a regular wave with wave steepness $H/\lambda = 1/22$ and corresponding wave period $T = 7s$ in full scale for test series *4012002*

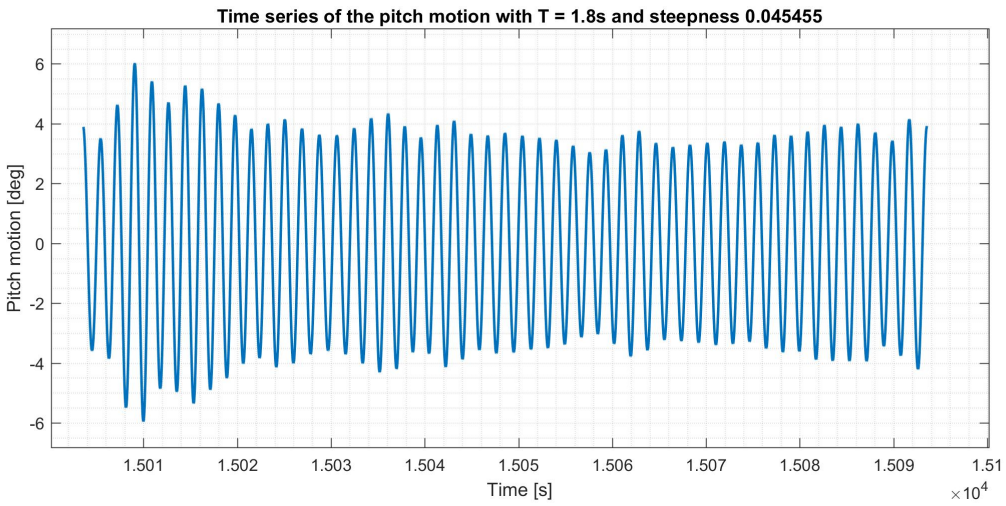

Time series of the pitch motion from a regular wave with wave steepness $H/\lambda = 1/22$ and corresponding wave period $T = 9s$ in full scale for test series *4012002*

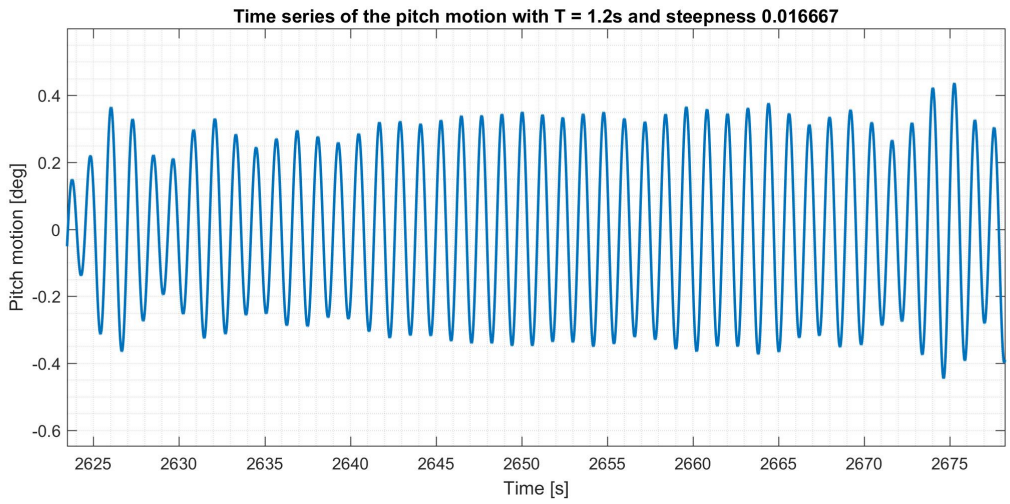

Time series of the pitch motion from a regular wave with wave steepness $H/\lambda = 1/60$ and corresponding wave period $T = 6s$ in full scale for test series *4012003*

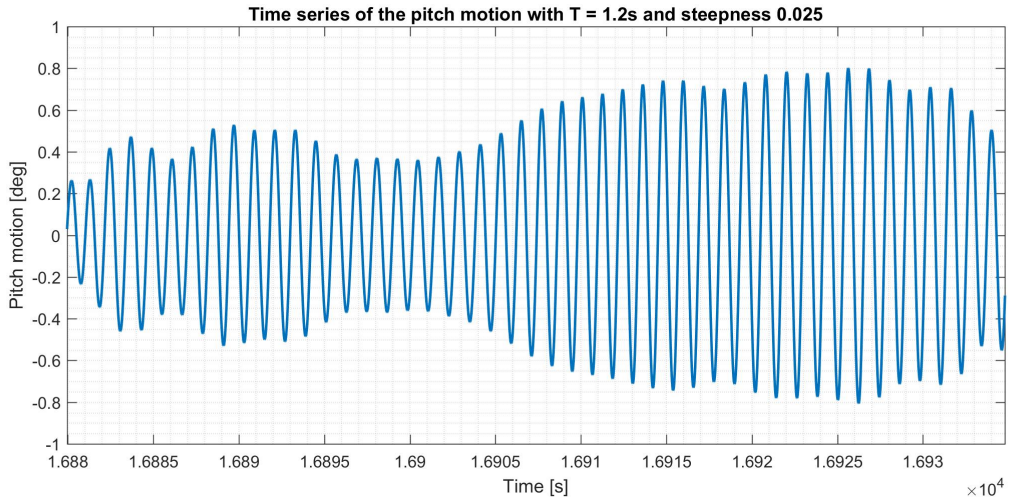

Time series of the pitch motion from a regular wave with wave steepness $H/\lambda = 1/40$ and corresponding wave period $T = 6s$ in full scale for test series *4012003*

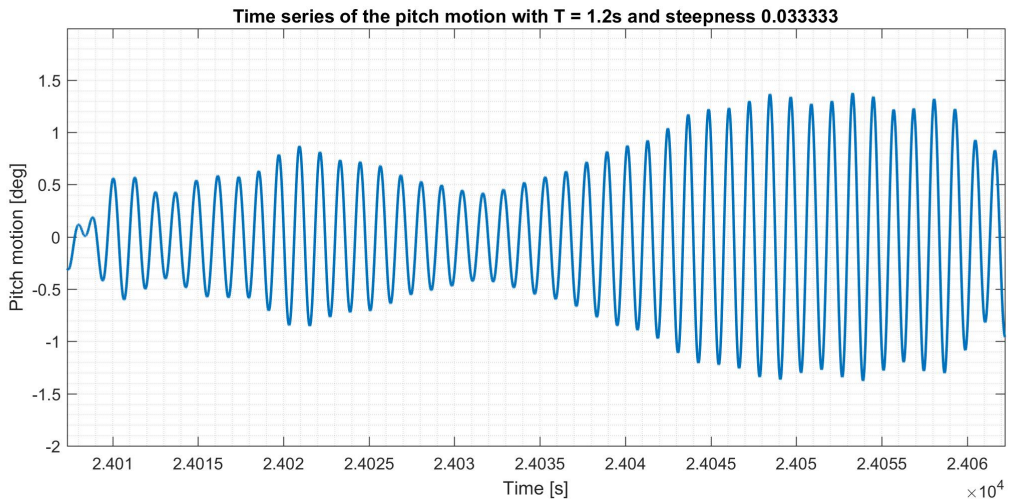

Time series of the pitch motion from a regular wave with wave steepness $H/\lambda = 1/30$ and corresponding wave period $T = 6s$ in full scale for test series *4012003*

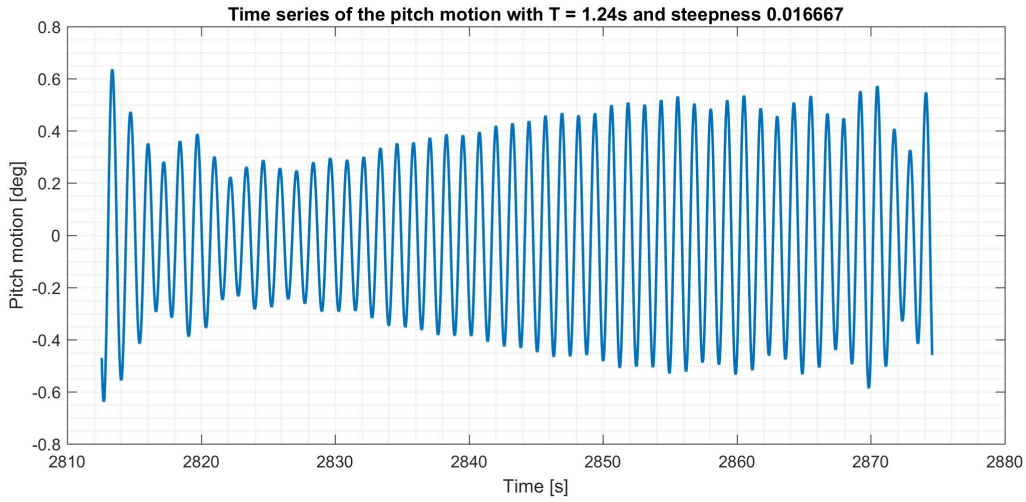

Time series of the pitch motion from a regular wave with wave steepness $H/\lambda = 1/60$ and corresponding wave period $T = 6.2s$ in full scale for test series *4012003*

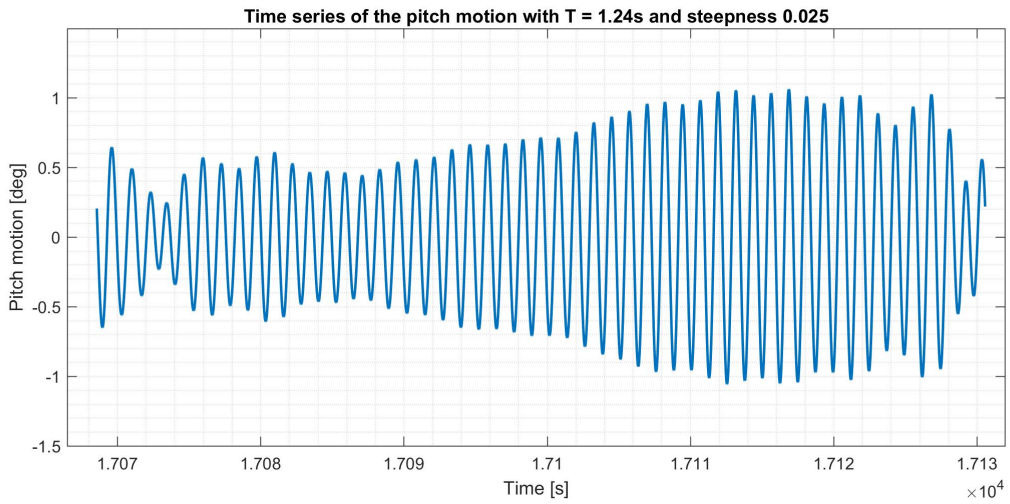

Time series of the pitch motion from a regular wave with wave steepness $H/\lambda = 1/40$ and corresponding wave period $T = 6.2s$ in full scale for test series *4012003*

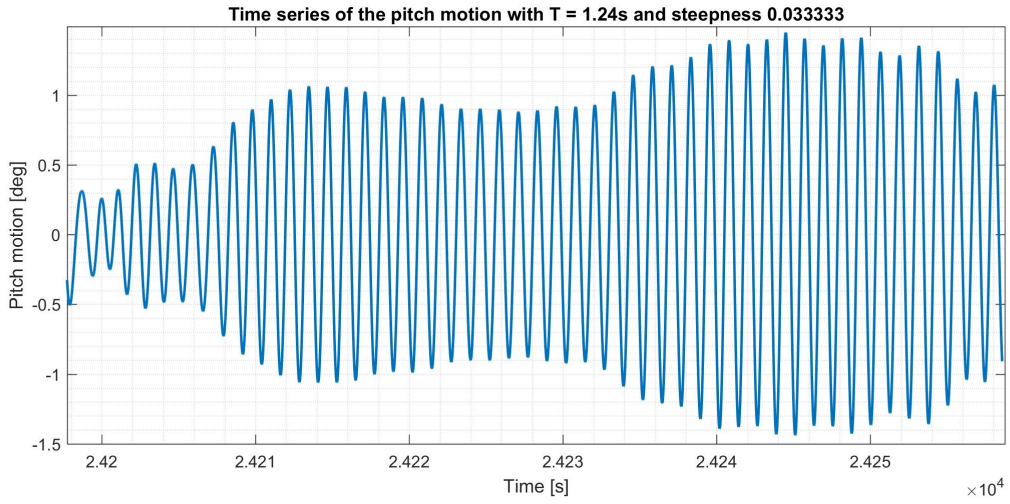

Time series of the pitch motion from a regular wave with wave steepness $H/\lambda = 1/30$ and corresponding wave period $T = 6.2s$ in full scale for test series *4012003*

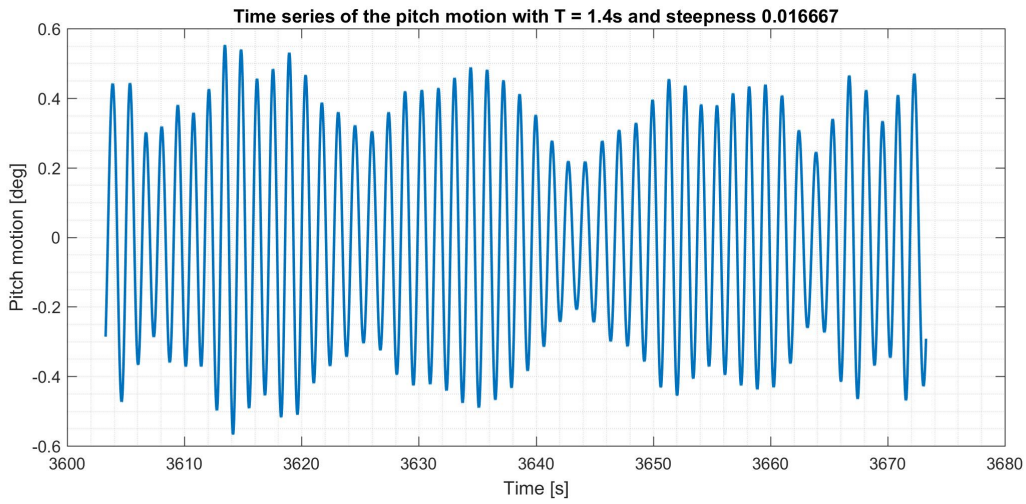

Time series of the pitch motion from a regular wave with wave steepness $H/\lambda = 1/60$ and corresponding wave period $T = 7s$ in full scale for test series *4012003*

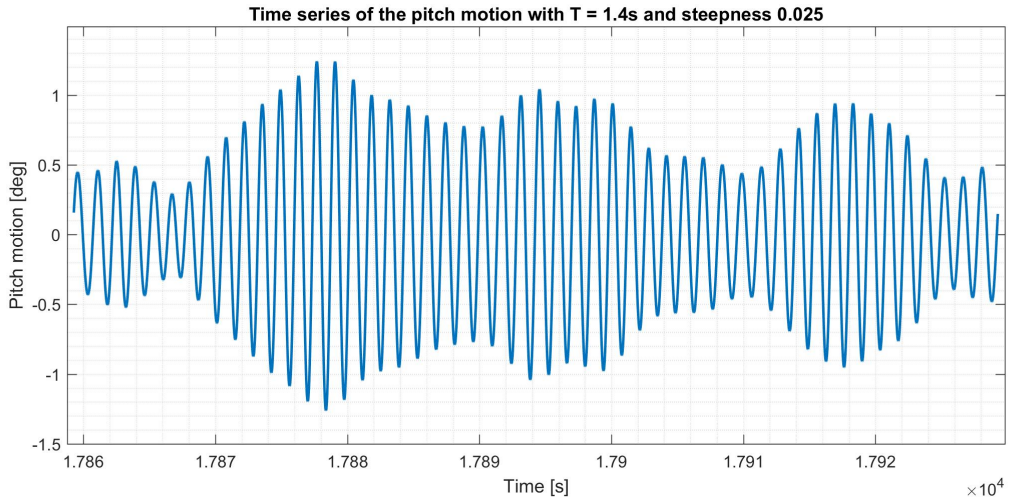

Time series of the pitch motion from a regular wave with wave steepness $H/\lambda = 1/40$ and corresponding wave period $T = 7s$ in full scale for test series *4012003*

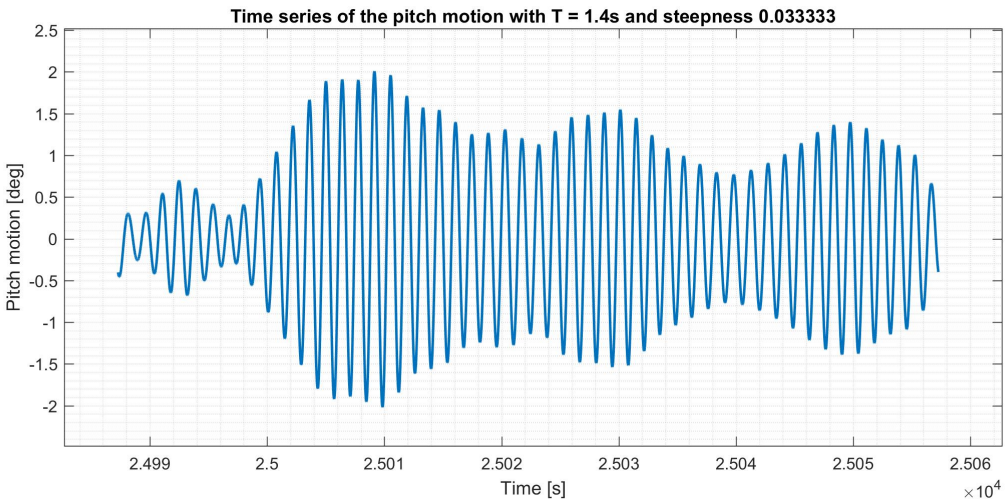

Time series of the pitch motion from a regular wave with wave steepness $H/\lambda = 1/30$ and corresponding wave period $T = 7s$ in full scale for test series *4012003*

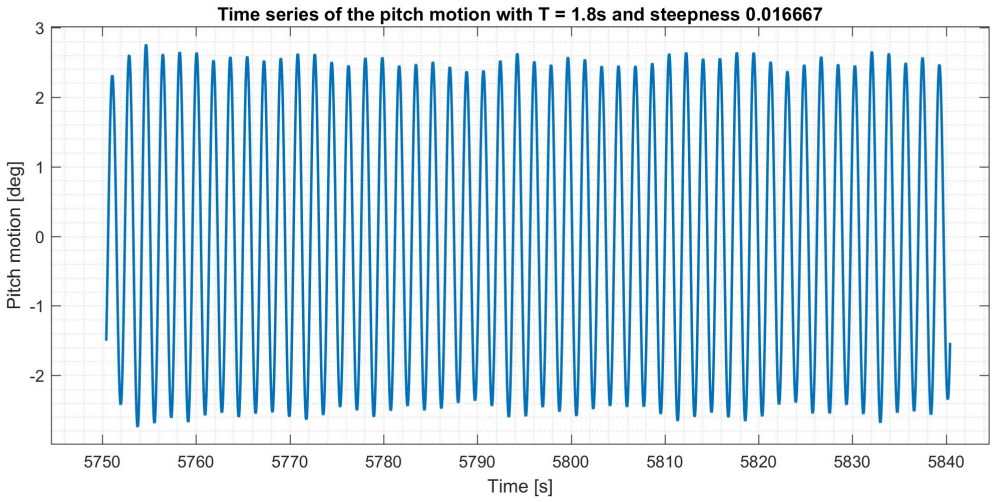

Time series of the pitch motion from a regular wave with wave steepness $H/\lambda = 1/60$ and corresponding wave period $T = 9s$ in full scale for test series *4012003*

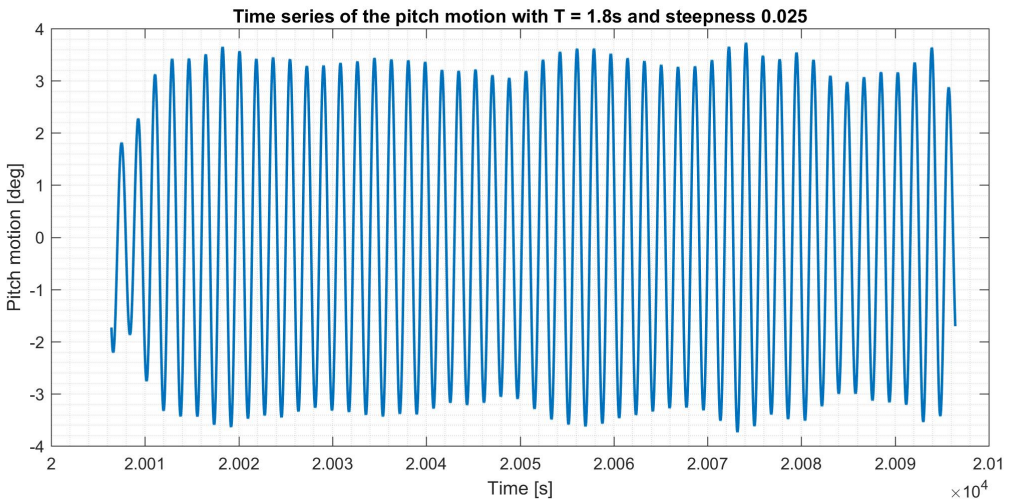

Time series of the pitch motion from a regular wave with wave steepness $H/\lambda = 1/40$ and corresponding wave period $T = 9s$ in full scale for test series *4012003*

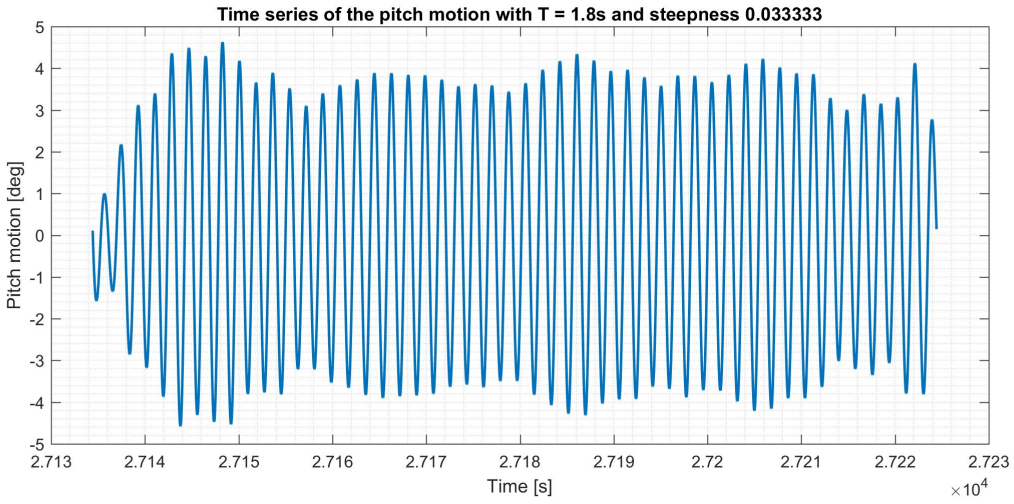

Time series of the pitch motion from a regular wave with wave steepness $H/\lambda = 1/30$ and corresponding wave period $T = 9s$ in full scale for test series *4012003*

Slamming forces

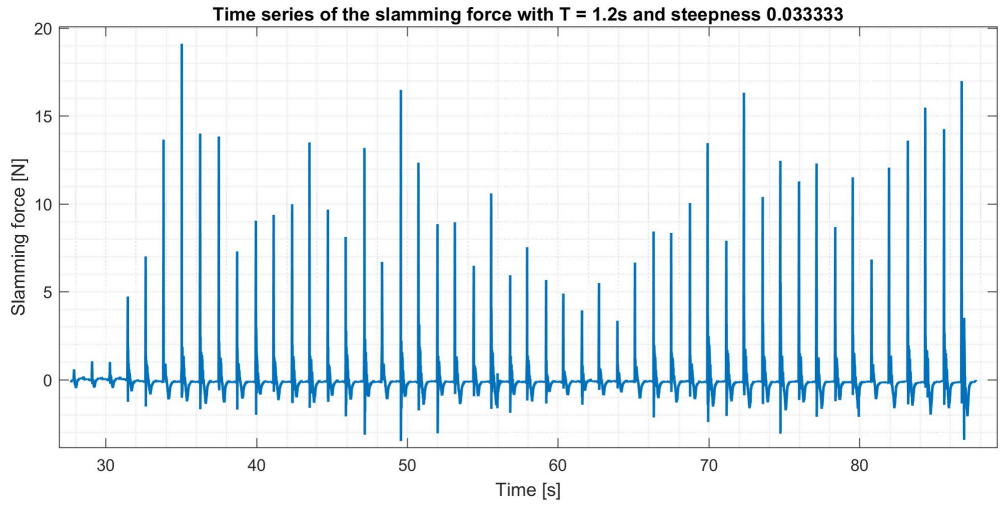

Time series of the slamming force from a regular wave with wave steepness $H/\lambda = 1/30$ and corresponding wave period $T = 6s$ in full scale for test series *80000*

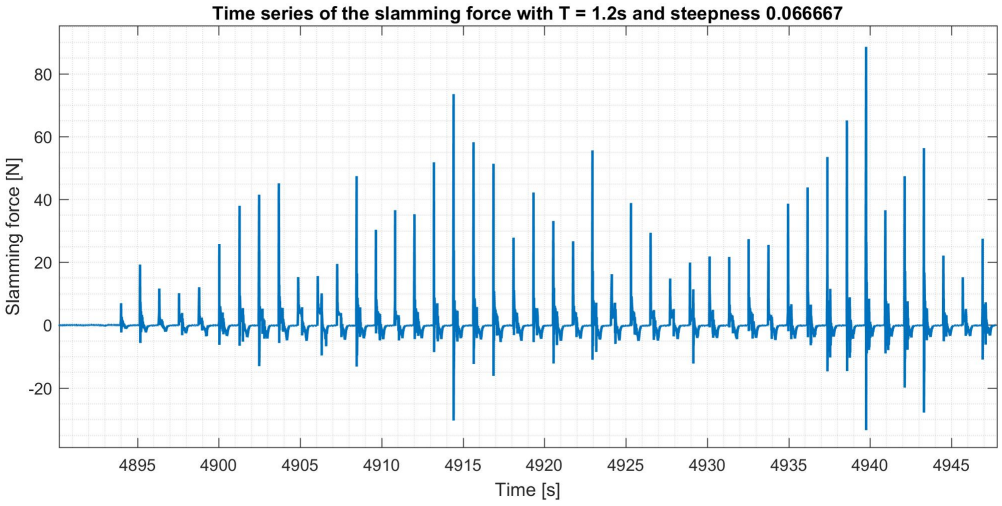

Time series of the slamming force from a regular wave with wave steepness $H/\lambda = 1/15$ and corresponding wave period $T = 6s$ in full scale for test series *80000*

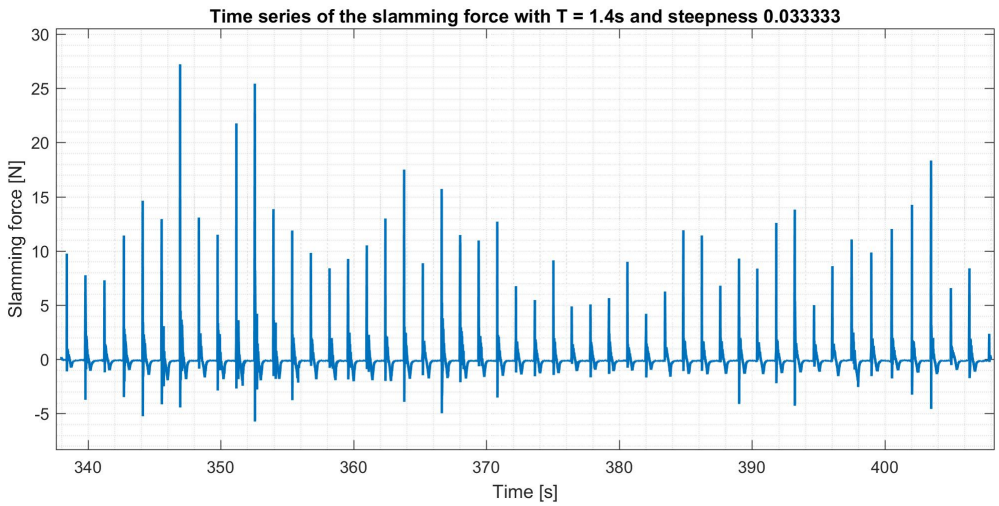

Time series of the slamming force from a regular wave with wave steepness $H/\lambda = 1/30$ and corresponding wave period $T = 7s$ in full scale for test series *80000*

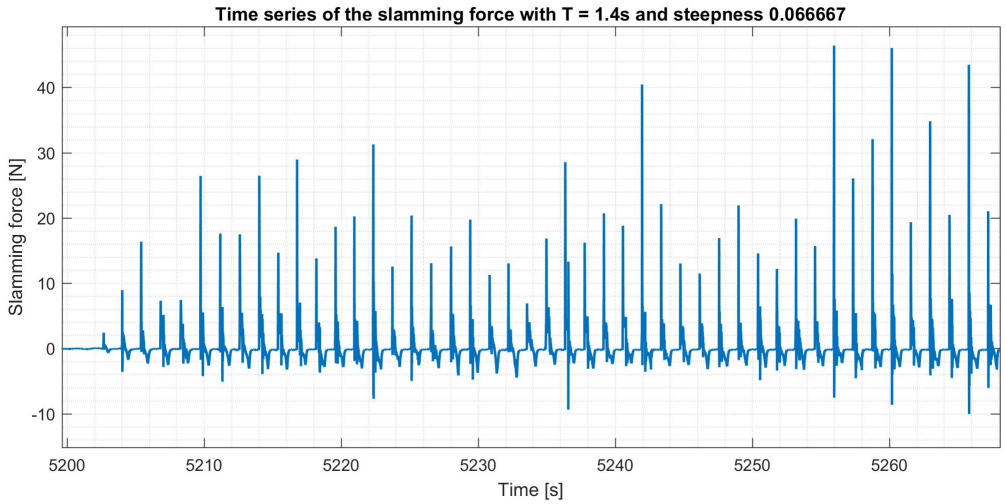

Time series of the slamming force from a regular wave with wave steepness $H/\lambda = 1/15$ and corresponding wave period $T = 7s$ in full scale for test series *80000*

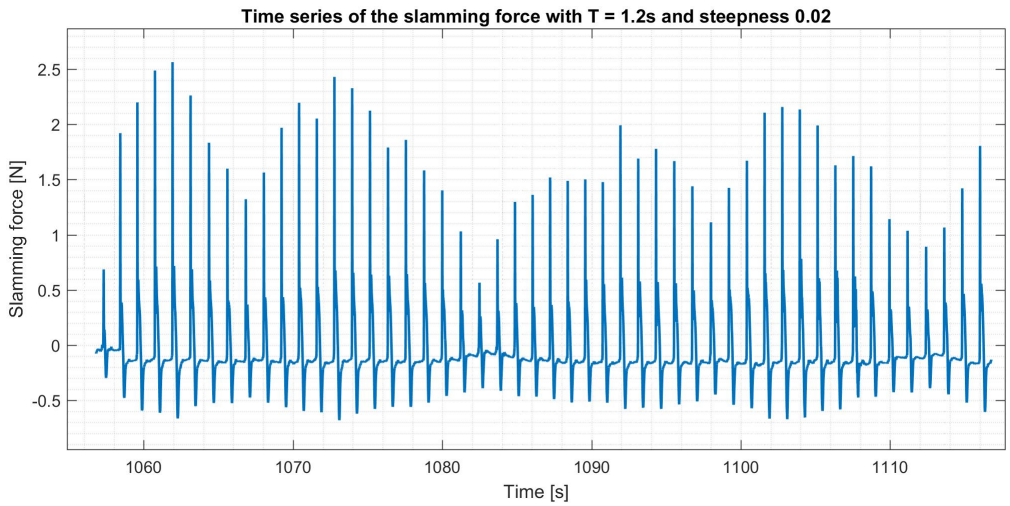

Time series of the slamming force from a regular wave with wave steepness $H/\lambda = 1/50$ and corresponding wave period $T = 6s$ in full scale for test series *401003*

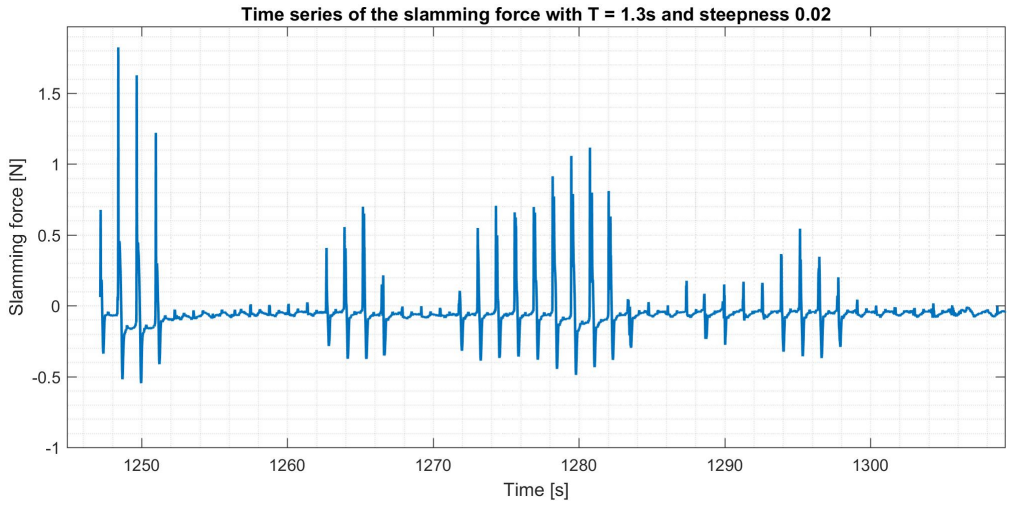

Time series of the slamming force from a regular wave with wave steepness $H/\lambda = 1/50$ and corresponding wave period $T = 6.5s$ in full scale for test series *401003*

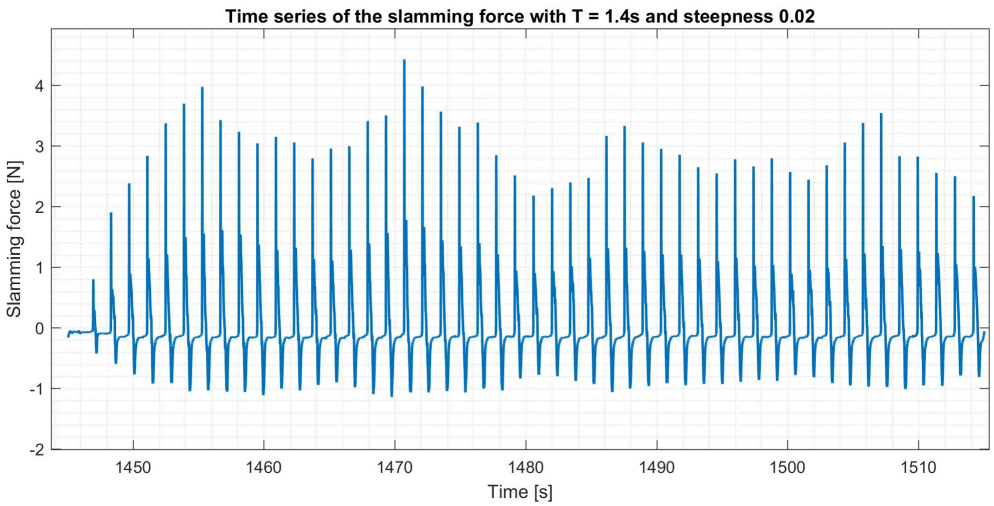

Time series of the slamming force from a regular wave with wave steepness $H/\lambda = 1/50$ and corresponding wave period $T = 7s$ in full scale for test series *401003*

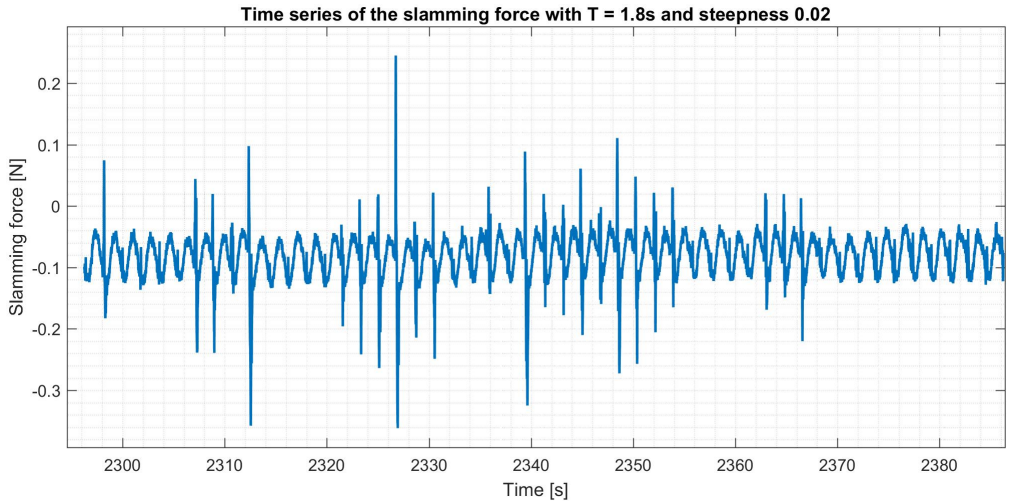

Time series of the slamming force from a regular wave with wave steepness $H/\lambda = 1/50$ and corresponding wave period $T = 9s$ in full scale for test series *401003*

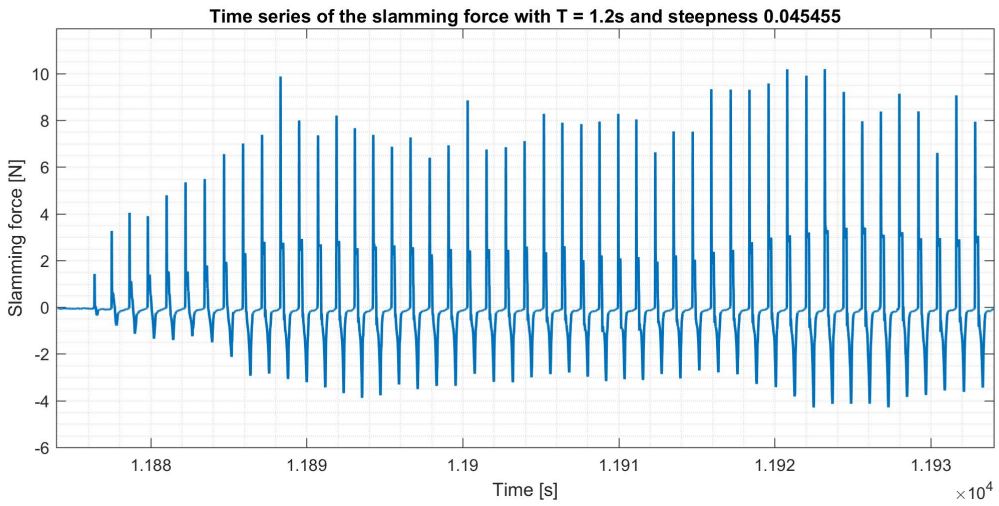

Time series of the slamming force from a regular wave with wave steepness $H/\lambda = 1/22$ and corresponding wave period $T = 6s$ in full scale for test series *4012002*

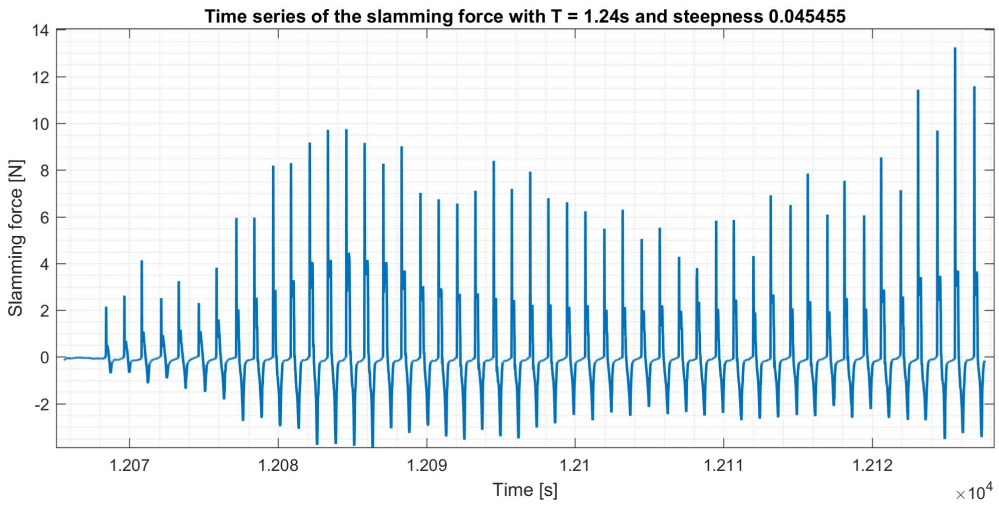

Time series of the slamming force from a regular wave with wave steepness $H/\lambda = 1/22$ and corresponding wave period $T = 6.2s$ in full scale for test series *401003*

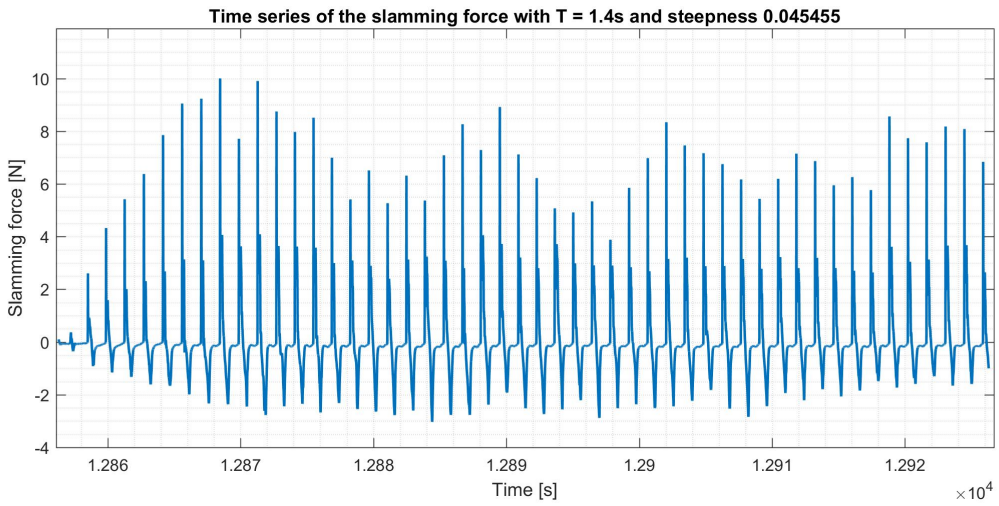

Time series of the slamming force from a regular wave with wave steepness $H/\lambda = 1/22$ and corresponding wave period $T = 7s$ in full scale for test series *4012002*

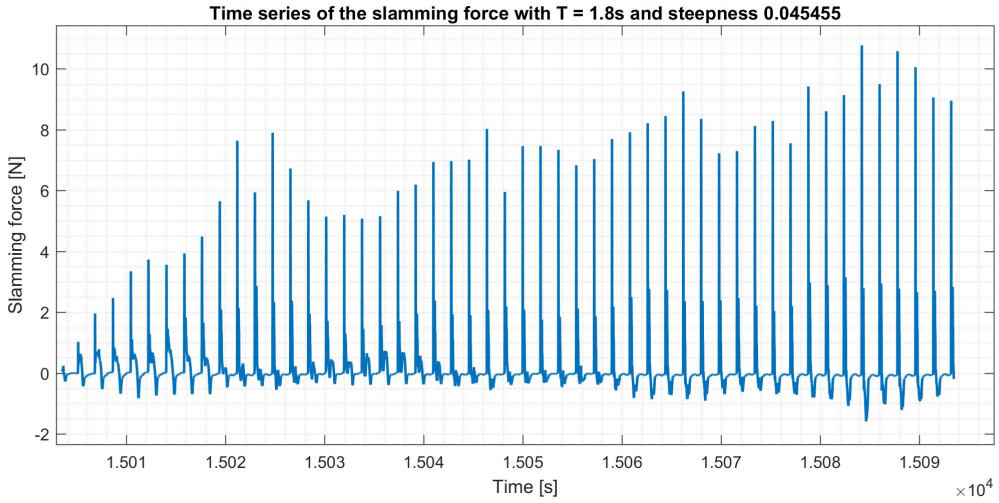

Time series of the slamming force from a regular wave with wave steepness $H/\lambda = 1/22$ and corresponding wave period $T = 9s$ in full scale for test series *4012002*

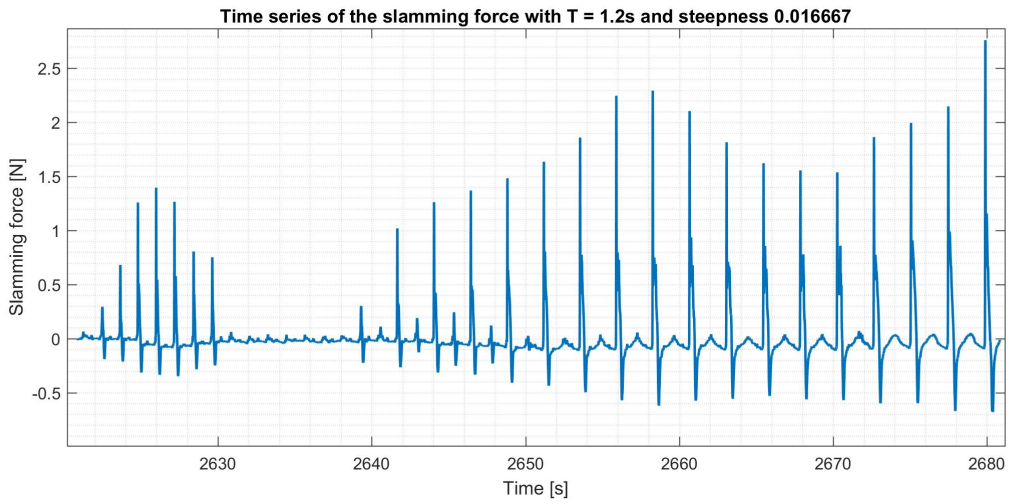

Time series of the slamming force from a regular wave with wave steepness $H/\lambda = 1/60$ and corresponding wave period $T = 6s$ in full scale for test series *4012003*

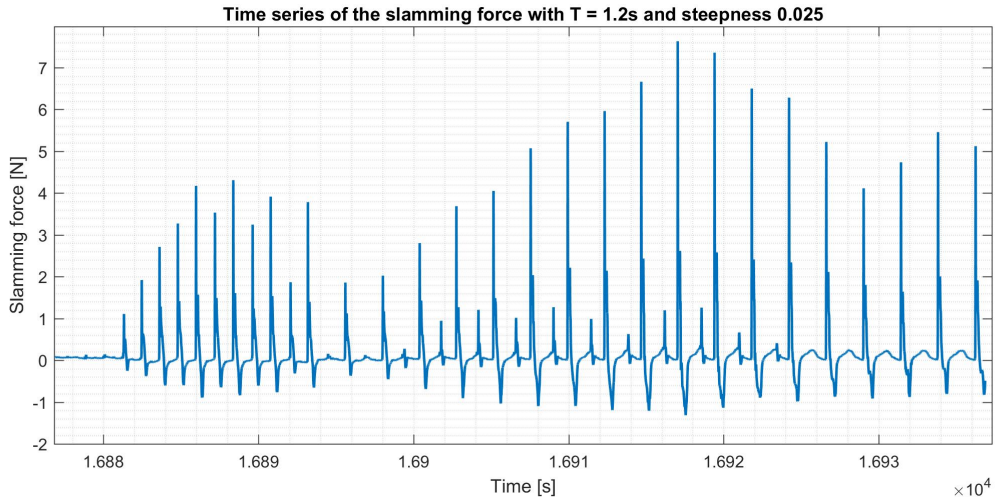

Time series of the slamming force from a regular wave with wave steepness $H/\lambda = 1/40$ and corresponding wave period $T = 6s$ in full scale for test series *4012003*

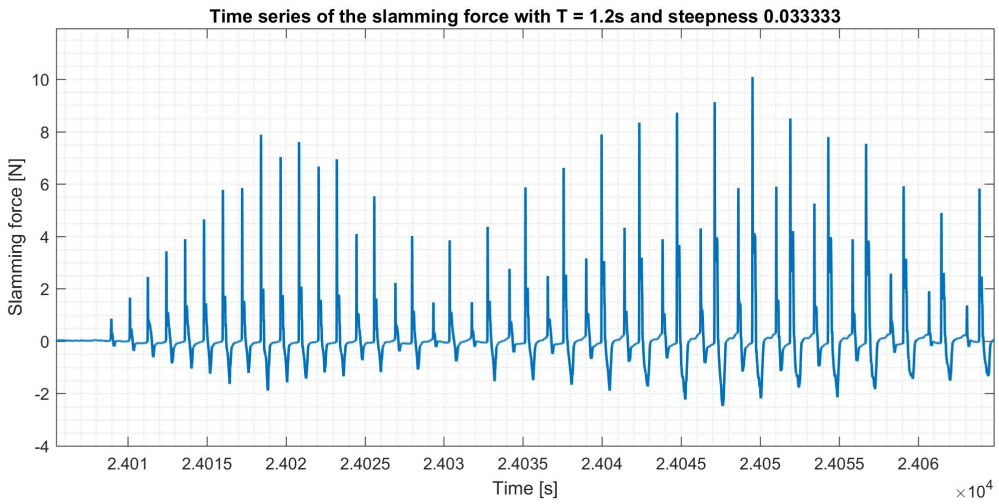

Time series of the slamming force from a regular wave with wave steepness $H/\lambda = 1/30$ and corresponding wave period $T = 6s$ in full scale for test series *4012003*

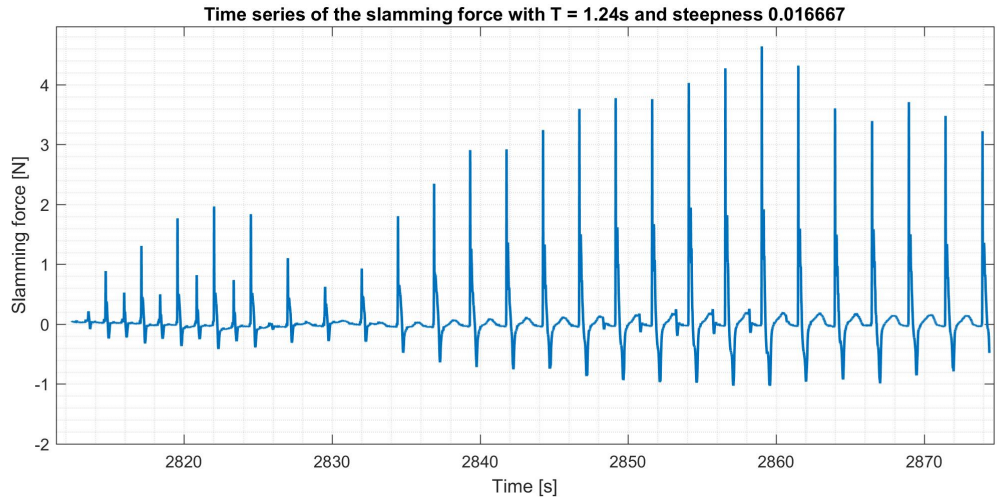

Time series of the slamming force from a regular wave with wave steepness $H/\lambda = 1/60$ and corresponding wave period $T = 6.2s$ in full scale for test series *4012003*

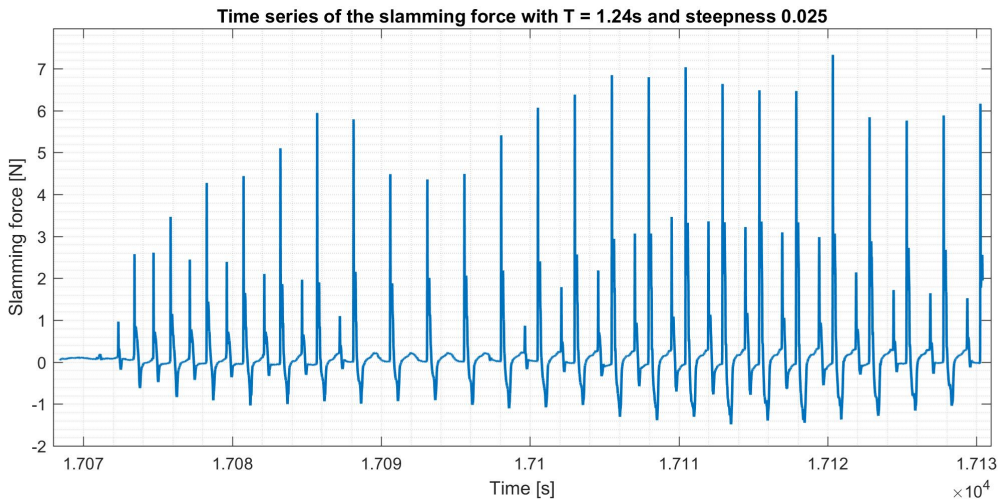

Time series of the slamming force from a regular wave with wave steepness $H/\lambda = 1/40$ and corresponding wave period $T = 6.2s$ in full scale for test series *4012003*

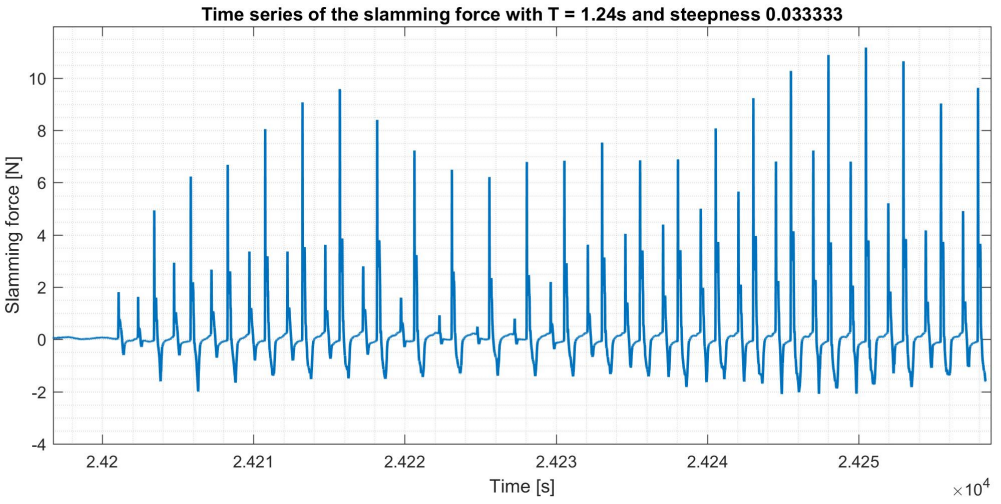

Time series of the slamming force from a regular wave with wave steepness $H/\lambda = 1/30$ and corresponding wave period $T = 6.2s$ in full scale for test series *4012003*

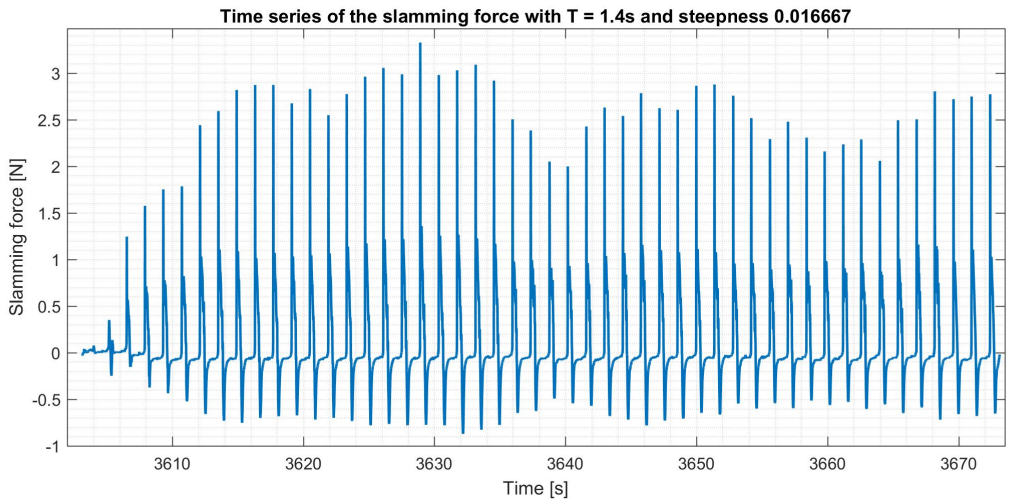

Time series of the slamming force from a regular wave with wave steepness $H/\lambda = 1/60$ and corresponding wave period $T = 7s$ in full scale for test series *4012003*

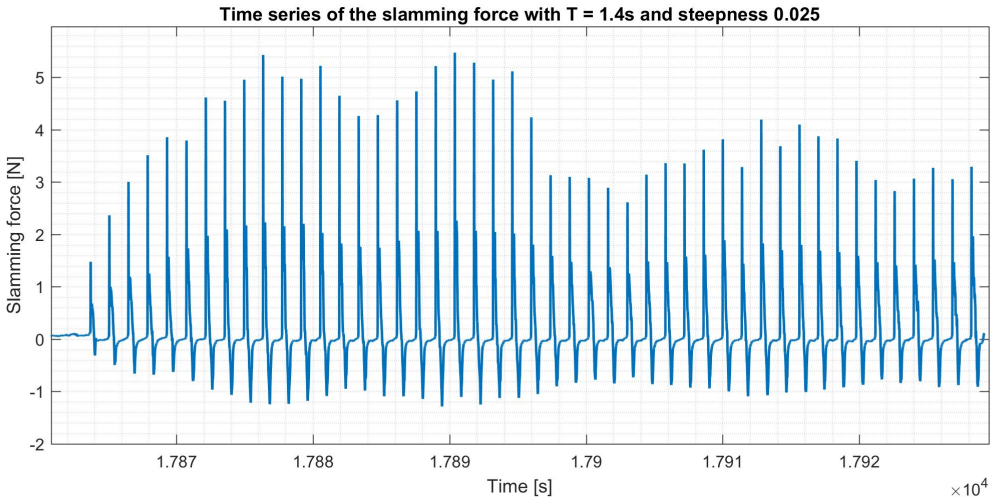

Time series of the slamming force from a regular wave with wave steepness $H/\lambda = 1/40$ and corresponding wave period $T = 7s$ in full scale for test series *4012003*

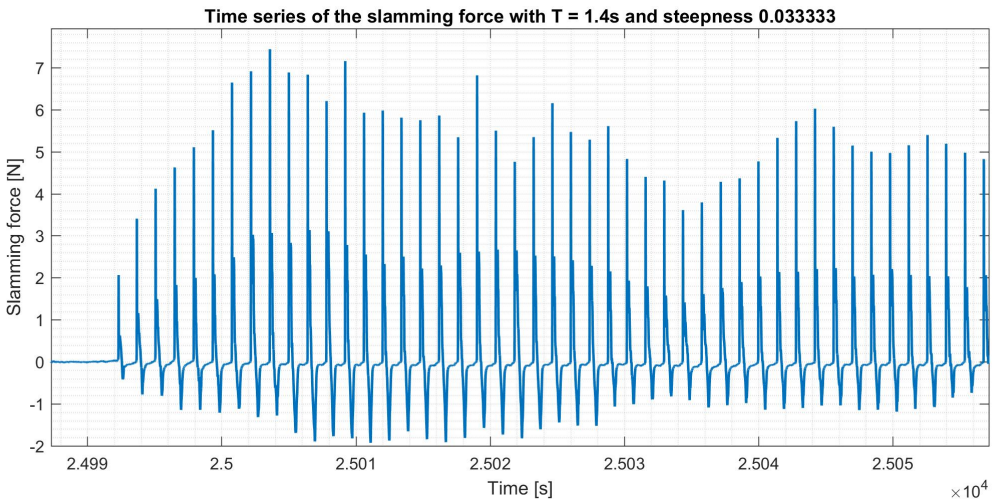

Time series of the slamming force from a regular wave with wave steepness $H/\lambda = 1/30$ and corresponding wave period $T = 7s$ in full scale for test series *4012003*

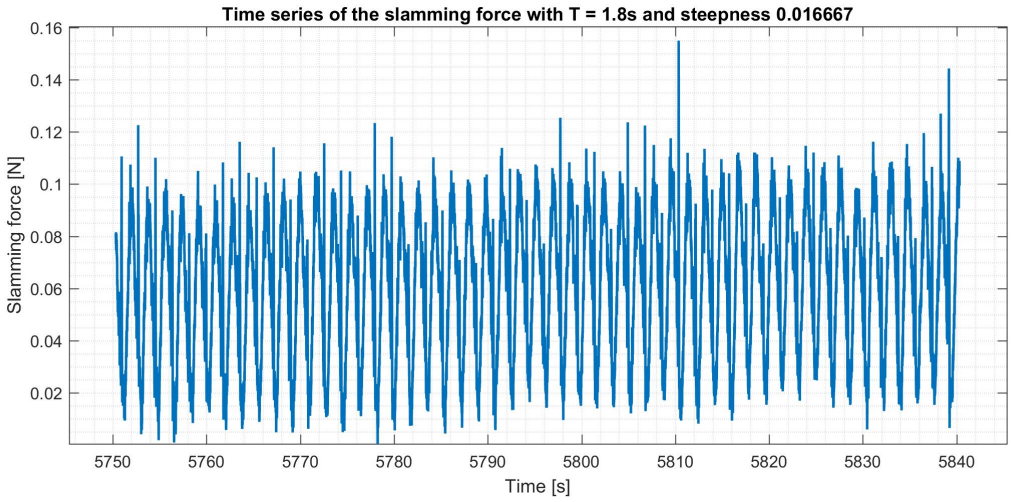

Time series of the slamming force from a regular wave with wave steepness $H/\lambda = 1/60$ and corresponding wave period $T = 9s$ in full scale for test series *4012003*

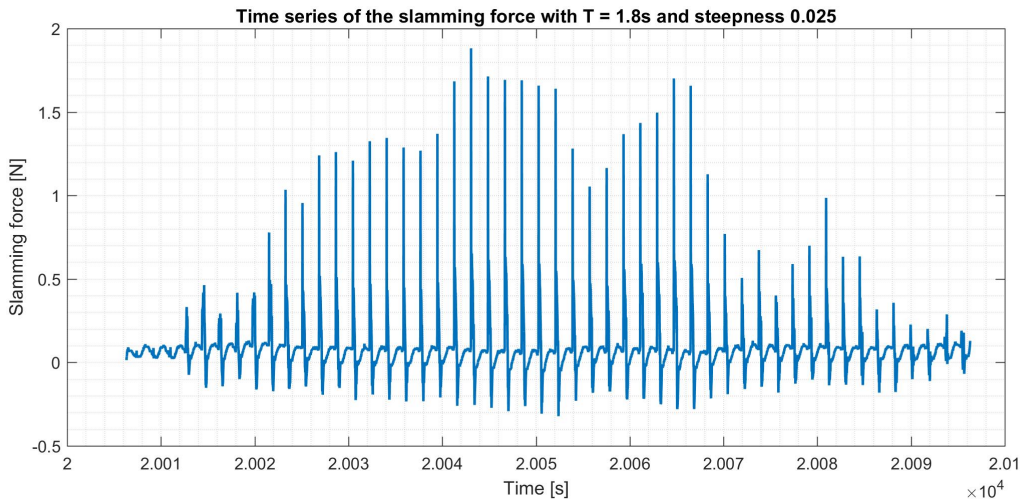

Time series of the slamming force from a regular wave with wave steepness $H/\lambda = 1/40$ and corresponding wave period $T = 9s$ in full scale for test series *4012003*

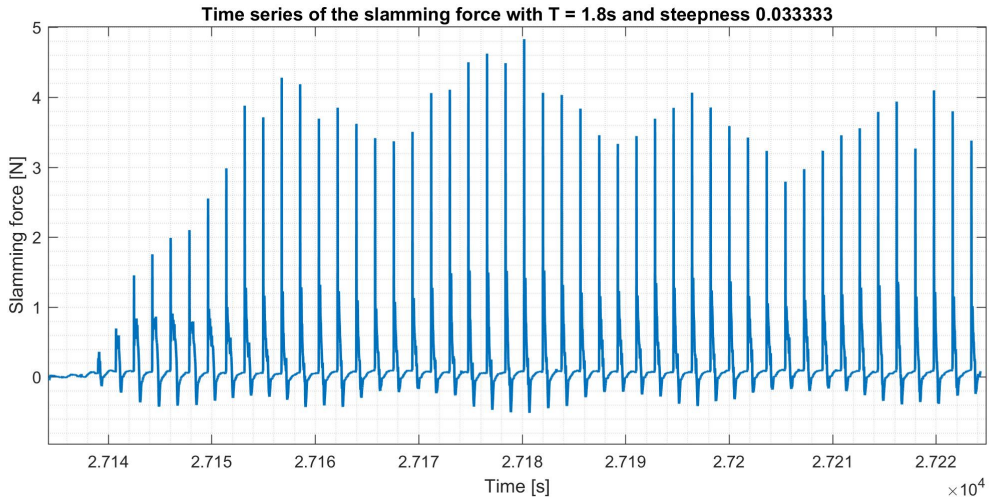

Time series of the slamming force from a regular wave with wave steepness $H/\lambda = 1/30$ and corresponding wave period $T = 9s$ in full scale for test series *4012003*

Local acceleration and measured forces

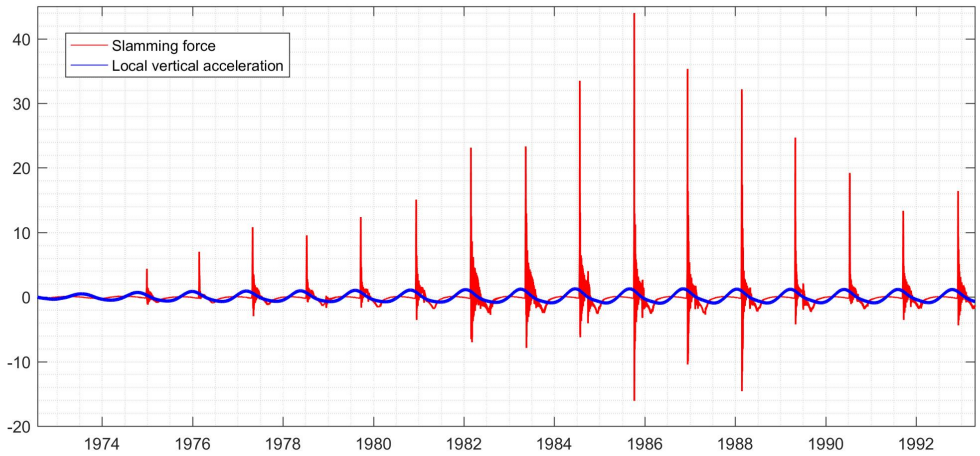

Time series of slamming forces plotted with the local vertical acceleration of the side deck. The period of the incoming wave is $T = 6s$ with a wave steepness $H/\lambda = 1/24$

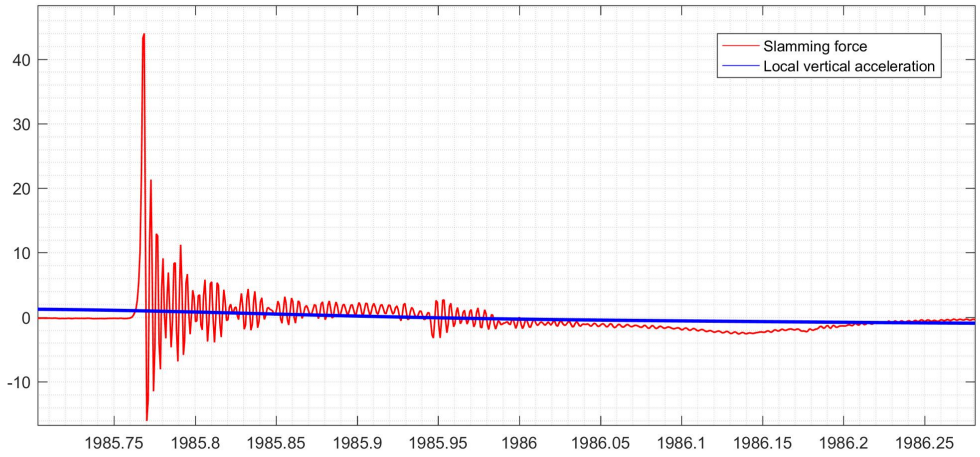

A zoomed in region of one impact cycles of the slamming force time series plotted with the local vertical acceleration of the side deck from test series *80000* with a period of $T = 6s$ and a wave steepness of $H/\lambda = 1/24$

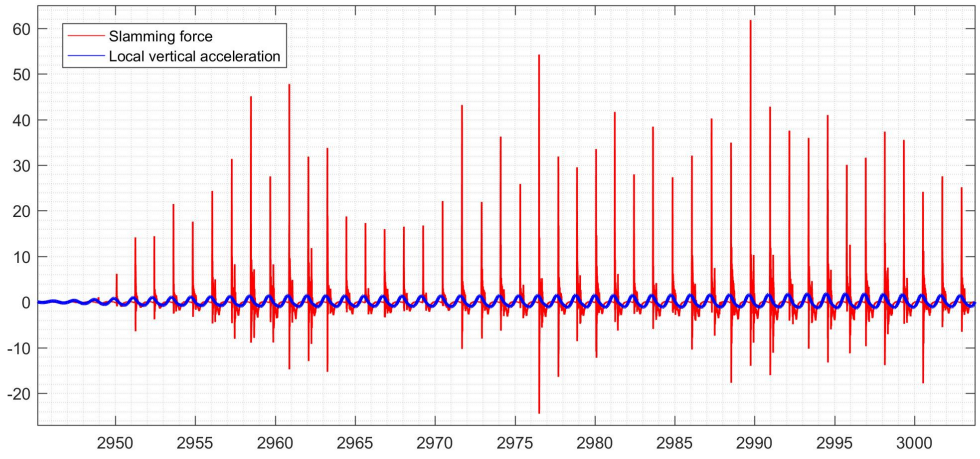

Time series of slamming forces plotted with the local vertical acceleration of the side deck. The period of the incoming wave is $T = 6s$ with a wave steepness $H/\lambda = 1/21$

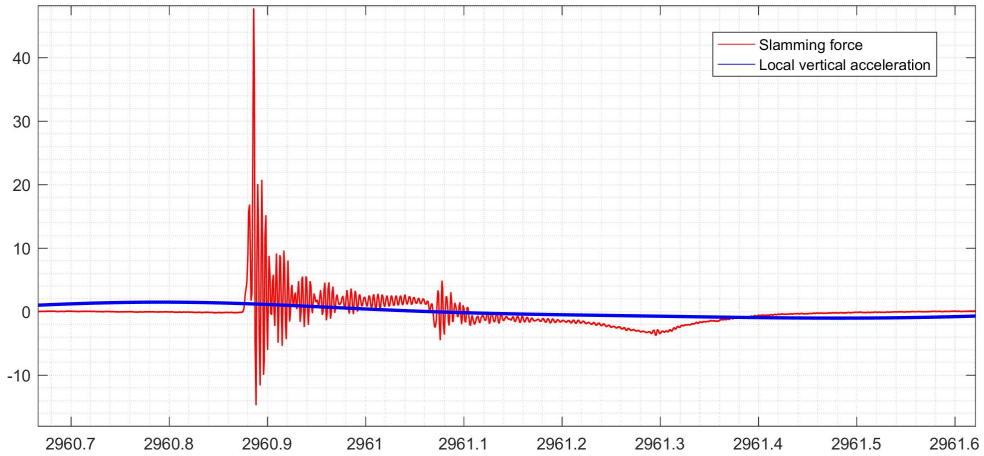

A zoomed in region of one impact cycles of the slamming force time series plotted with the local vertical acceleration of the side deck from test series *80000* with a period of $T = 6s$ and a wave steepness of $H/\lambda = 1/21$

Local velocity

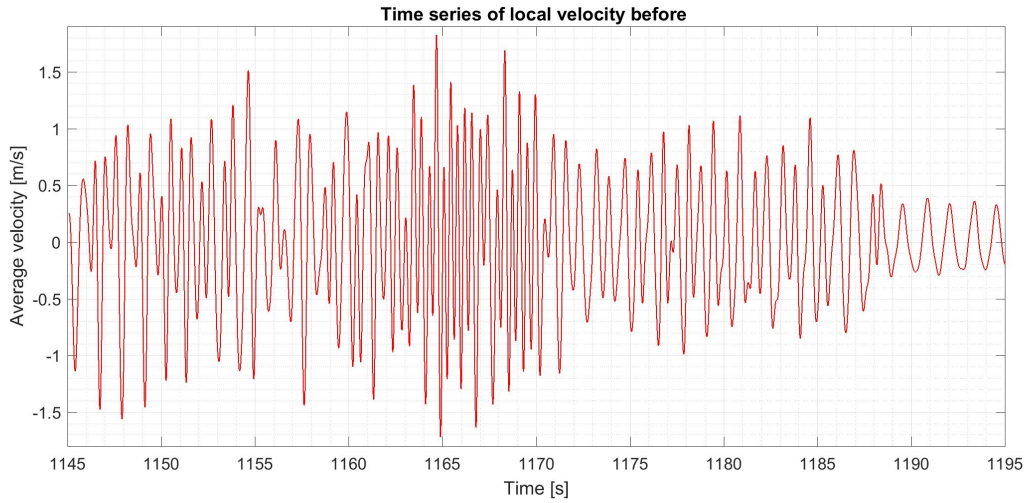

Time series of the local velocity beneath the deck, i.e at the run-up area. The velocity is obtained from the average wave elevation on the deck area and differentiated with respect to time. The results in the plot is obtained from a wave with a period of $T = 6.2s$ and a wave steepness of $H/\lambda = 1/26$

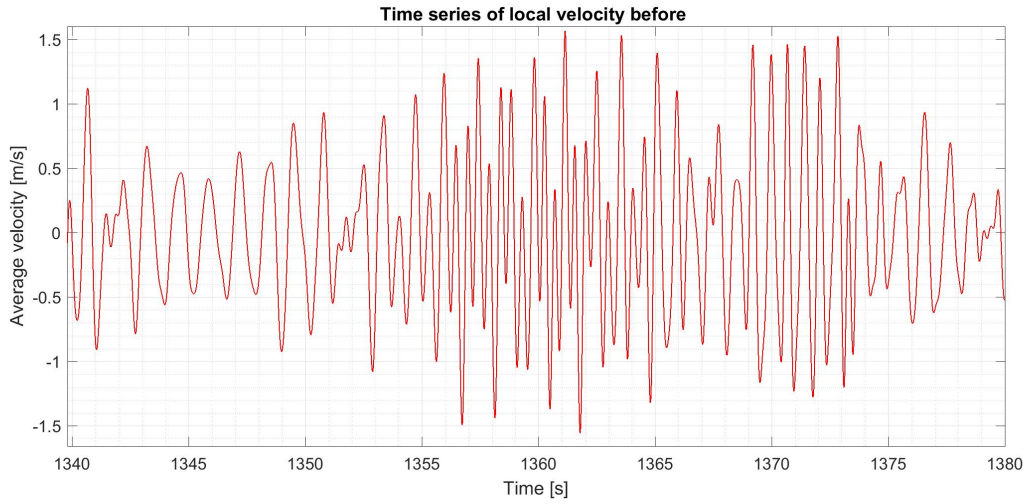

Time series of the local velocity beneath the deck, i.e at the run-up area. The velocity is obtained from the average wave elevation on the deck area and differentiated with respect to time.The results in the plot is obtained from a wave with a period of $T = 6.4s$ and a wave steepness of $H/\lambda = 1/26$

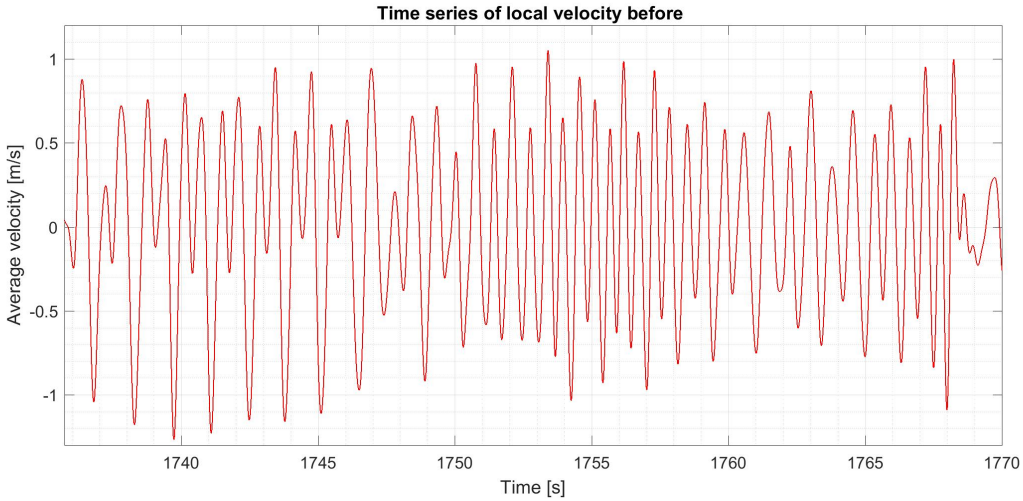

Time series of the local velocity beneath the deck, i.e at the run-up area. The velocity is obtained from the average wave elevation on the deck area and differentiated with respect to time. The results in the plot is obtained from a wave with a period of $T = 6.8$ and a wave steepness of $H/\lambda = 1/26$

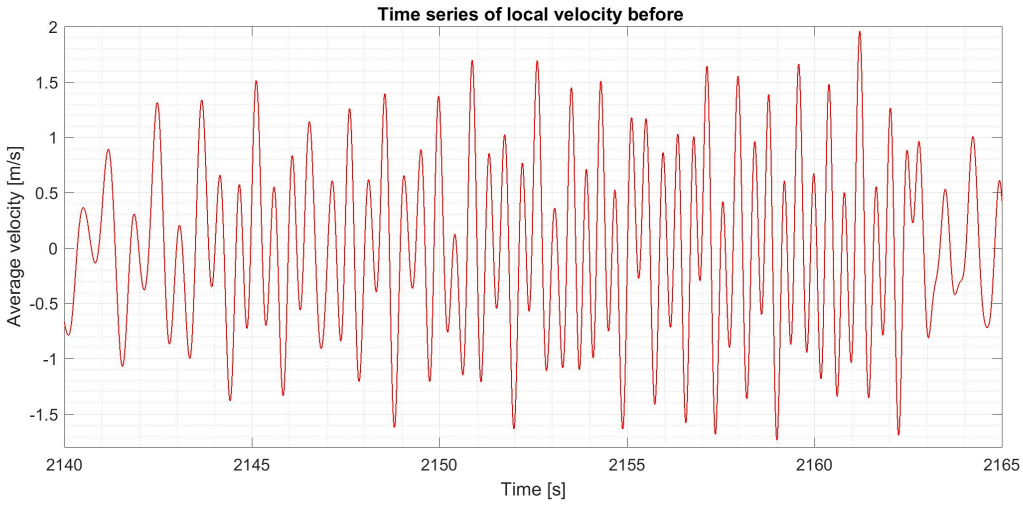

Time series of the local velocity beneath the deck, i.e at the run-up area. The velocity is obtained from the average wave elevation on the deck area and differentiated with respect to time. The results in the plot is obtained from a wave with a period of $T = 7.2s$ and a wave steepness of $H/\lambda = 1/26$

B.8 Slamming

Slamming coefficients

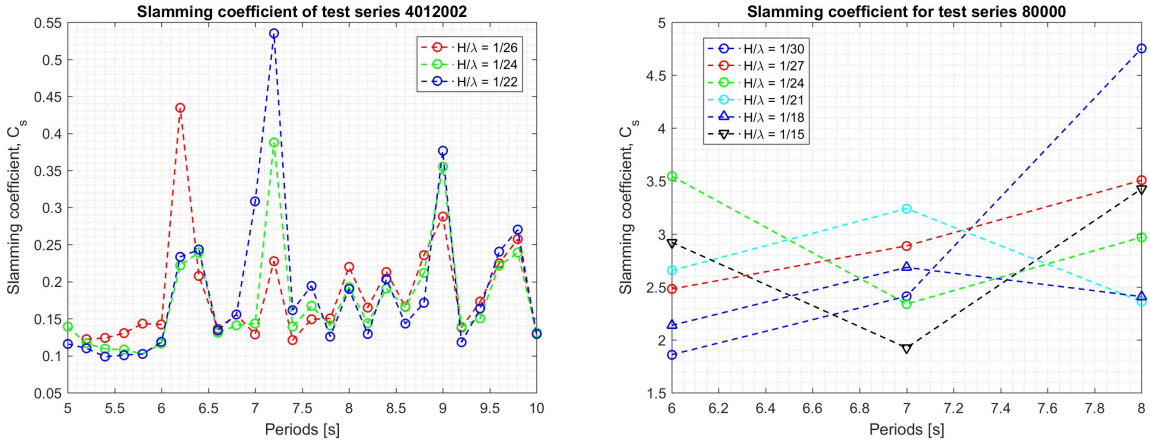

Slamming coefficient of the maximum slamming forces in the time series. Left: test series *4012002*. Right: test series *80000* from *January*

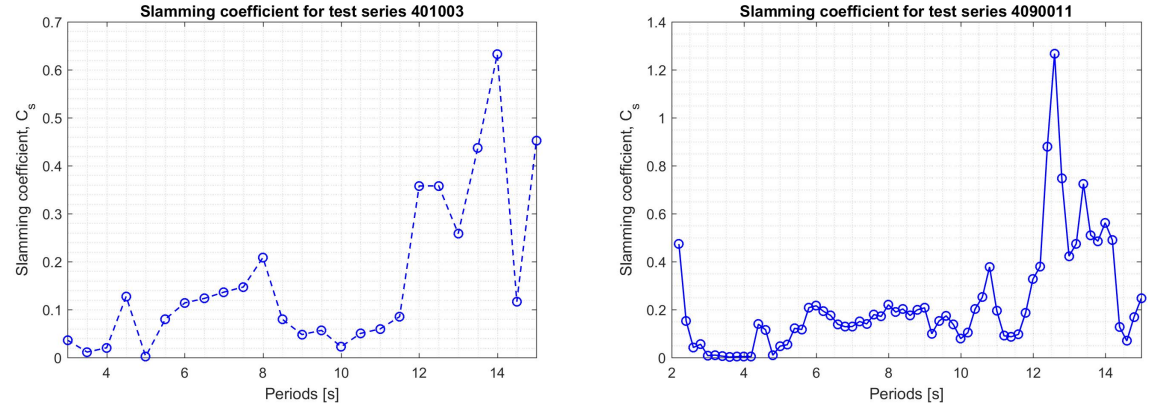

Slamming coefficient of the maximum slamming forces in the time series. Left: test series *401003*. Right: test series *4090011*

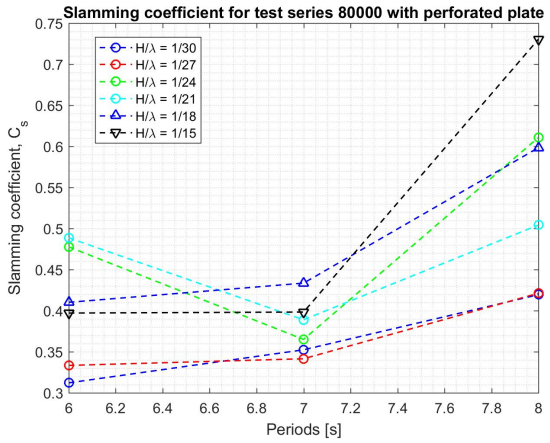

Slamming coefficient of the maximum slamming forces in the time series for the perforated plate with test series *80000* from tests in *January*

Slamming force analysis

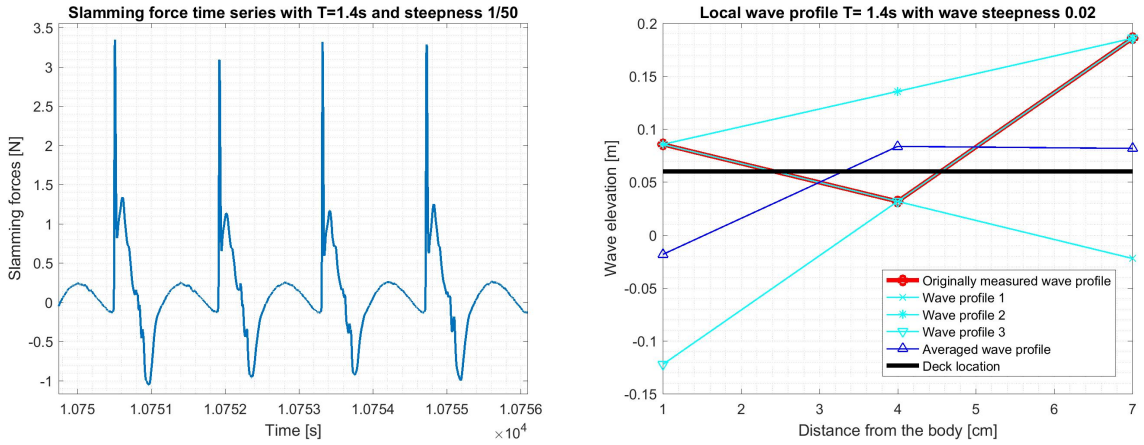

Estimation of slamming force with waves $T = 1.4s$ and steepness $1/50$. Left: Time series. Right: estimated wave profiles

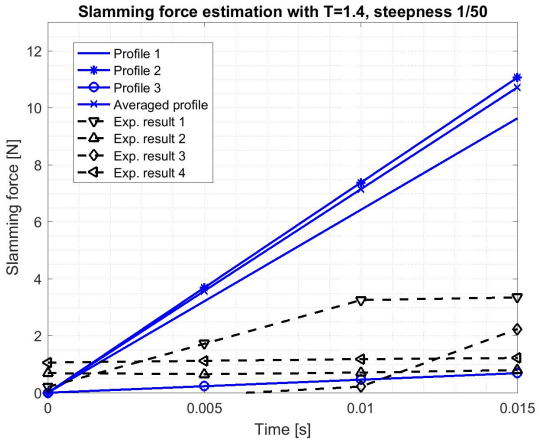

Figure 14: Estimated slamming force plotted with experimental results for time series with $T = 1.4s$ and wave steepness $1/50$

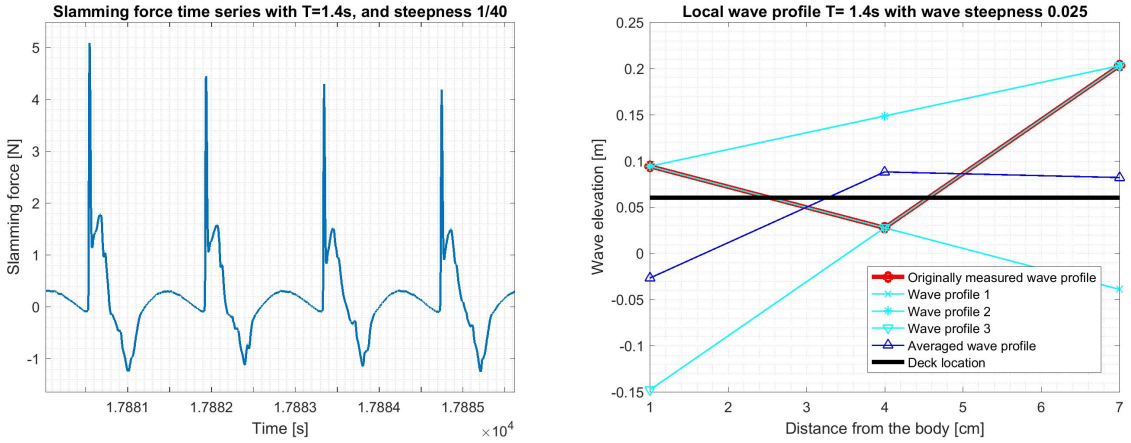

Estimation of slamming force with waves $T = 1.4s$ and steepness $1/40$. Left: Time series. Right: estimated wave profiles

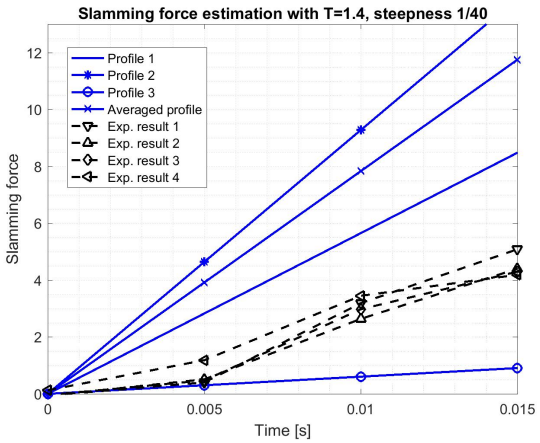

Figure 15: Estimated slamming force plotted with experimental results for time series with $T = 1.4s$ and wave steepness $1/40$

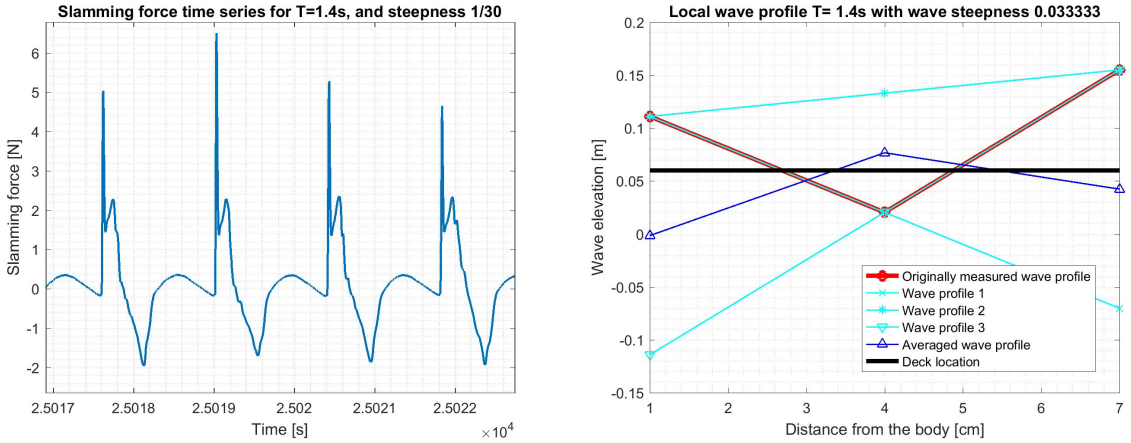

Estimation of slamming force with waves $T = 1.4s$ and steepness $1/30$. Left: Time series. Right: estimated wave profiles

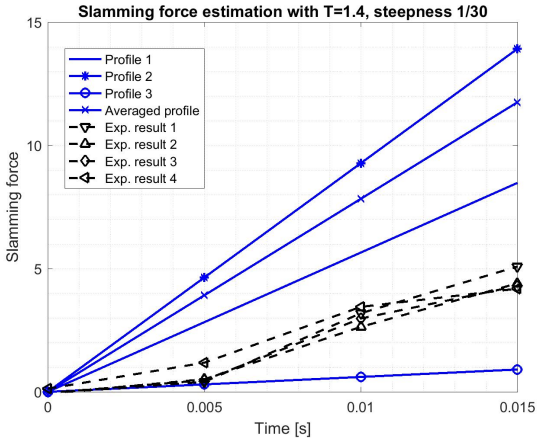

Figure 16: Estimated slamming force plotted with experimental results for time series with $T = 1.4s$ and wave steepness $1/30$

Comparison with the perforated plate

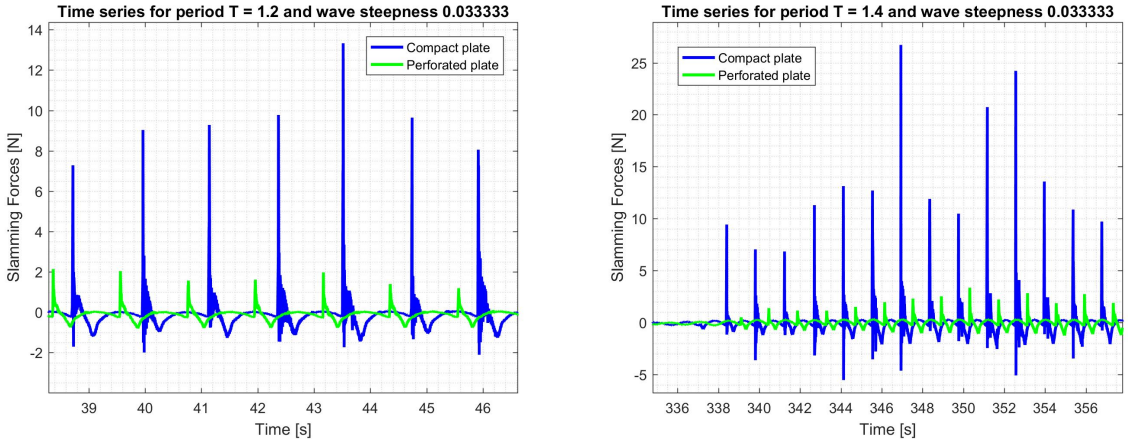

Maximum slamming force time series of test series *80000* with $H/\lambda = 1/30$ for solid and perforated plates. Green line is the perforated plate, blue is the solid plate. Left figure: with a wave period $T = 6s$. Right figure: With a wave period $T = 7s$

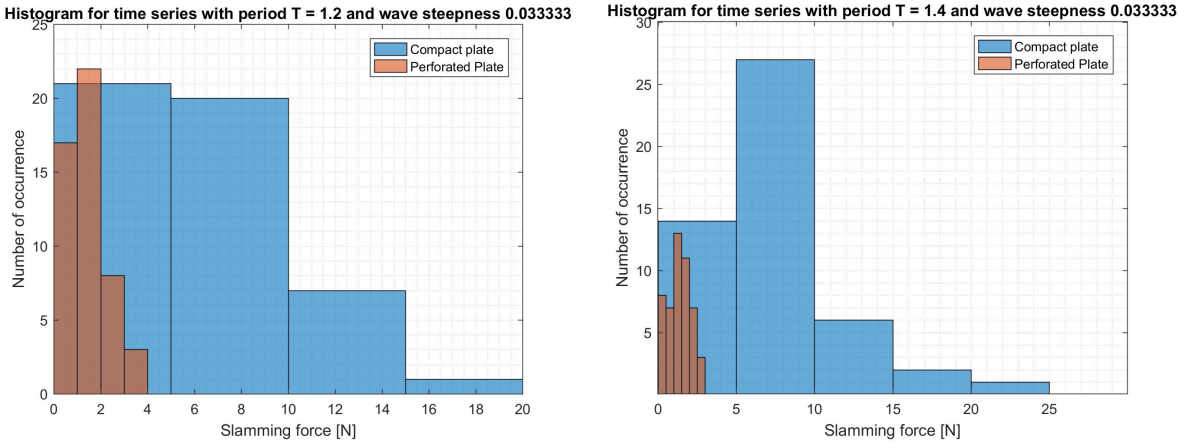

Maximum slamming force distribution of test series *80000* with $H/\lambda = 1/30$ for solid and perforated plates. The orange is the histogram for the perforated, and blue is for solid plate. Left figure: with a wave period $T = 6s$. Right figure: With a wave period $T = 7s$

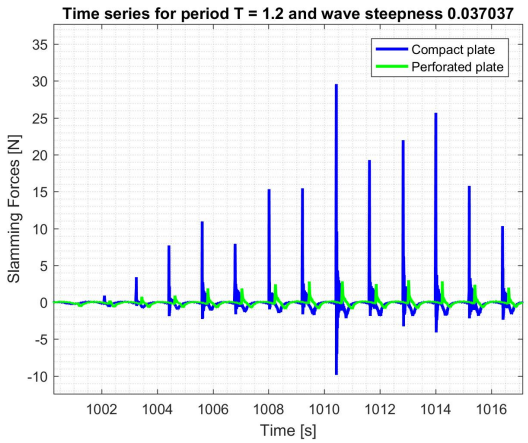

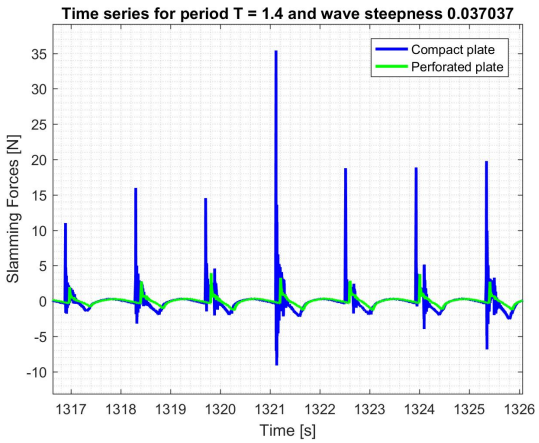

Maximum slamming force time series of test series *80000* with $H/\lambda = 1/27$ for solid and perforated plates. Green line is the perforated plate, blue is the solid plate. Left figure: with a wave period $T = 6s$. Right figure: With a wave period $T = 7s$

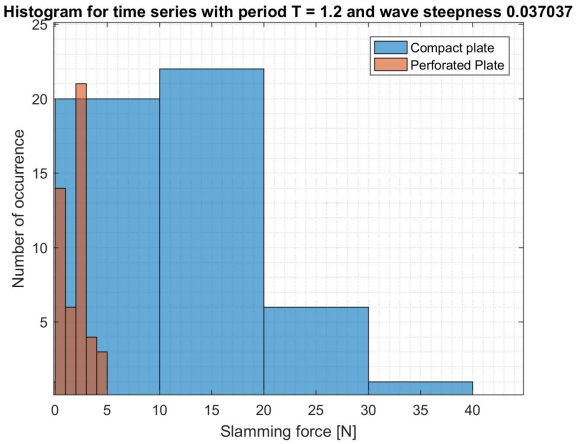

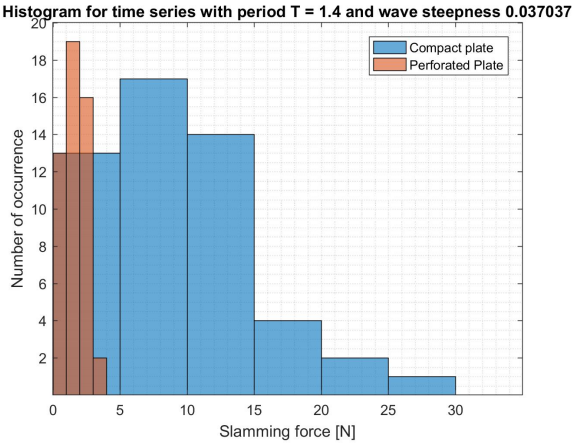

Maximum slamming force distribution of test series *80000* with $H/\lambda = 1/27$ for solid and perforated plates. The orange is the histogram for the perforated, and blue is for solid plate. Left figure: with a wave period $T = 6s$. Right figure: With a wave period $T = 7s$

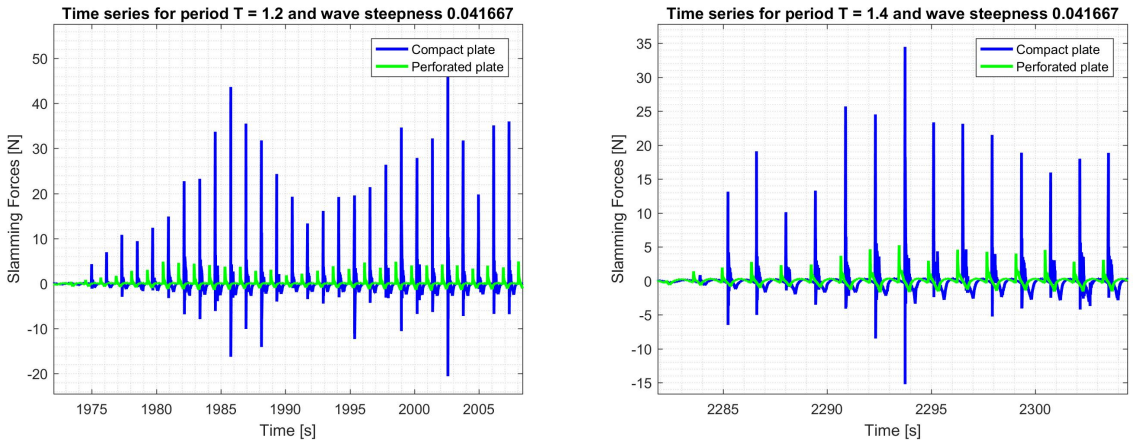

Maximum slamming force time series of test series *80000* with $H/\lambda = 1/24$ for solid and perforated plates. Green line is the perforated plate, blue is the solid plate. Left figure: with a wave period $T = 6s$. Right figure: With a wave period $T = 7s$

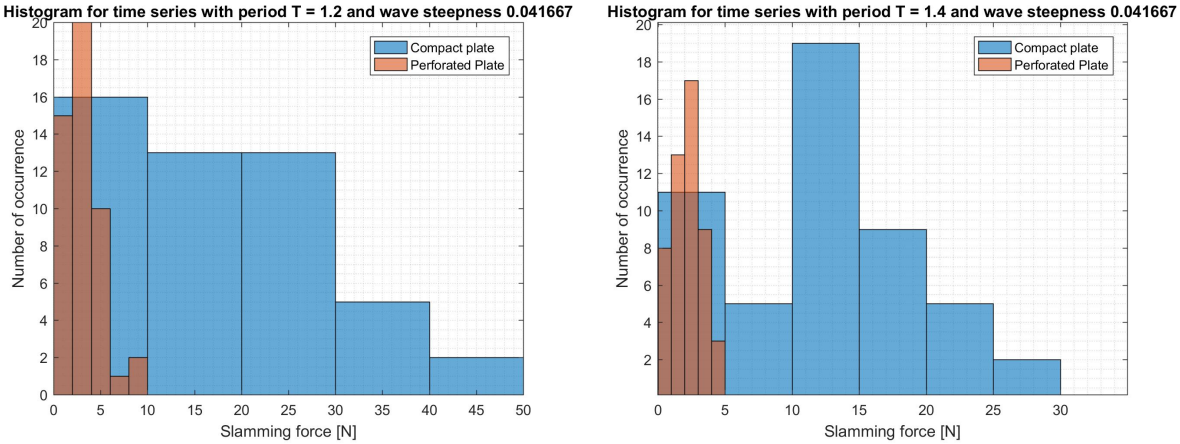

Maximum slamming force distribution of test series *80000* with $H/\lambda = 1/24$ for solid and perforated plates. The orange is the histogram for the perforated, and blue is for solid plate. Left figure: with a wave period $T = 6s$. Right figure: With a wave period $T = 7s$

C Convergence test result

The convergence test results for surge, heave and pitch performed in *WADAM*. The plots are based on the standard deviations of the motion amplitudes. This is plotted against the number of boxes, marked as N.

C.1 Finite depth analysis

The water depth is set to be $17.5m$.

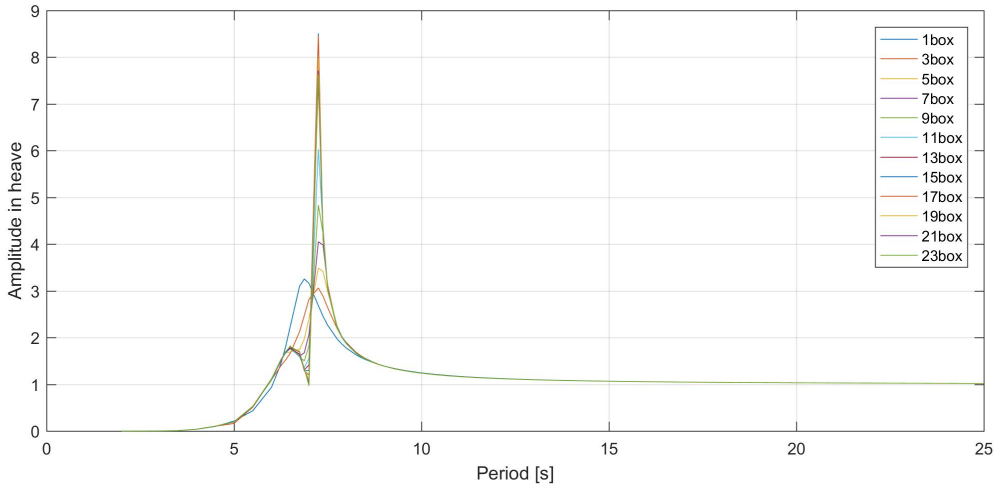

Plot of the RAO in heave obtained from different numbers of the mirroring bodies in undamped case

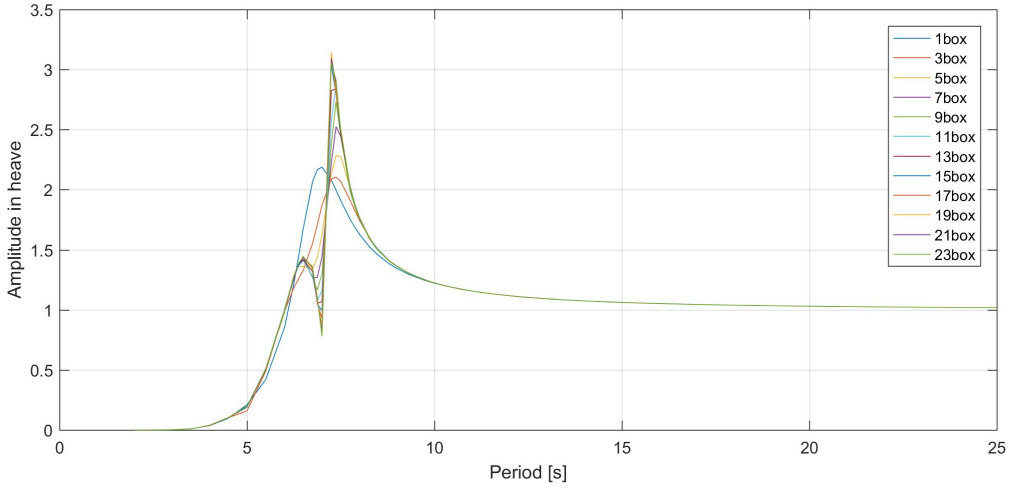

Plot of the RAO in heave obtained from different numbers of the mirroring bodies when 3% of the critical damping in heave is used

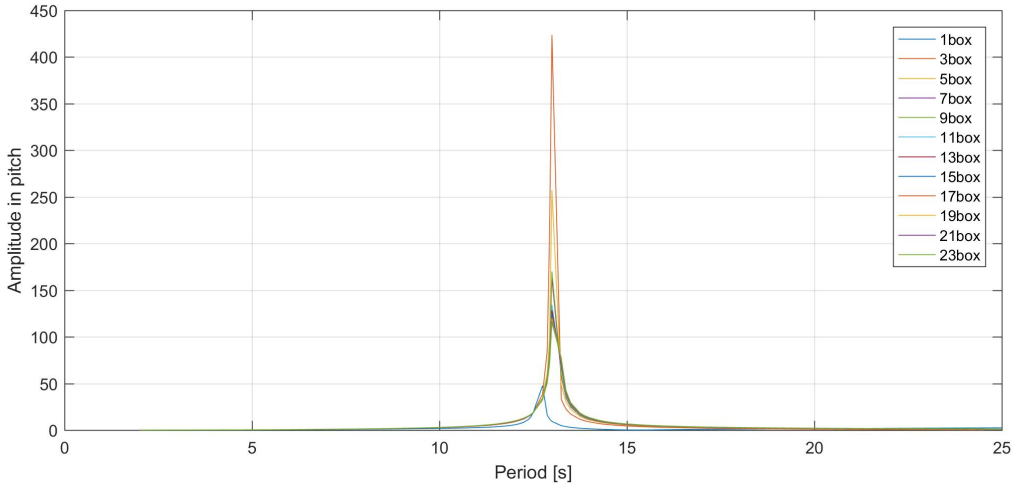

Plot of the RAO in pitch obtained from different numbers of the mirroring bodies in undamped case

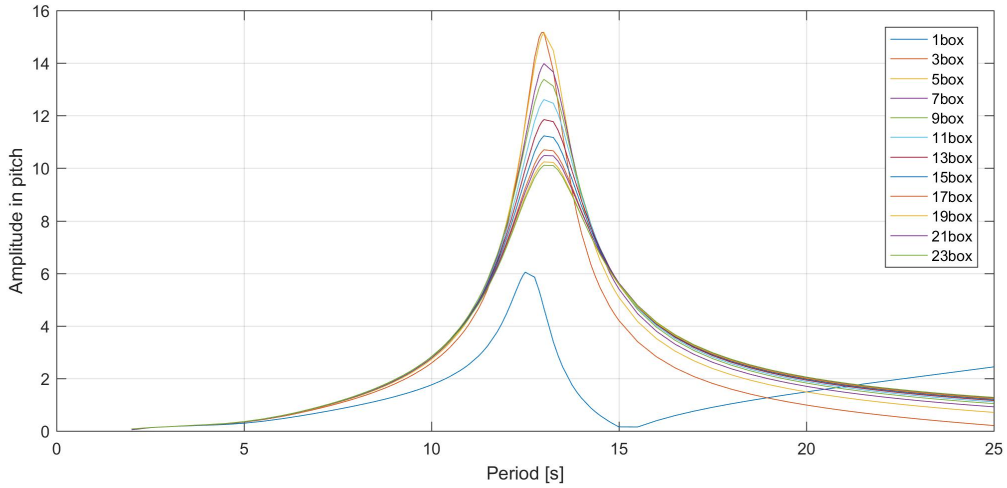

Plot of the RAO in pitch obtained from different numbers of the mirroring bodies when empirical estimated damping in pitch is used

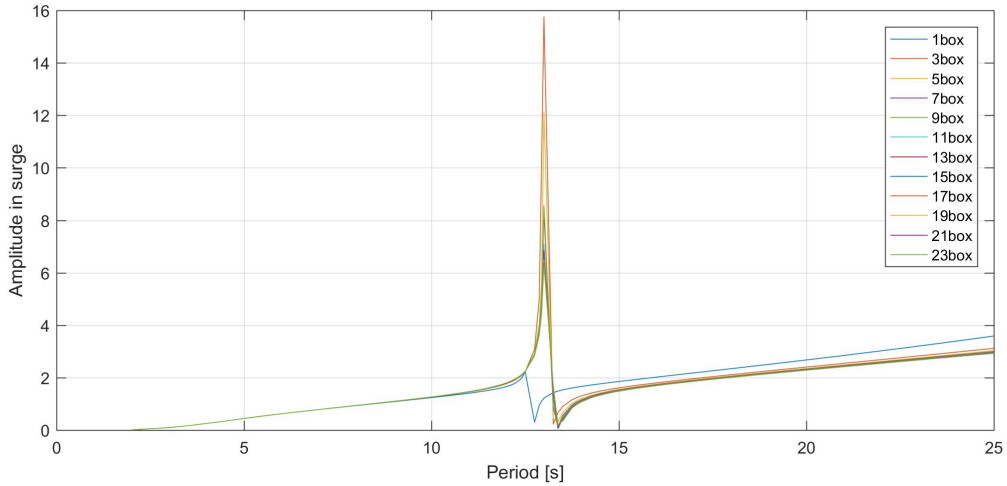

Plot of the RAO in surge obtained from different numbers of the mirroring bodies in undamped case

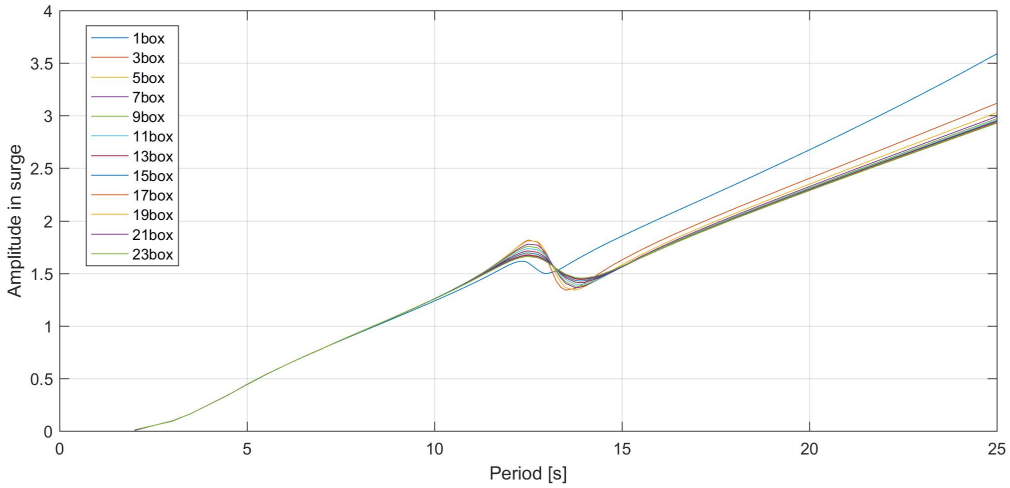

Plot of the RAO in pitch obtained from different numbers of the mirroring bodies when damping in heave and pitch motion is used

C.2 Infinite depth analysis

The water depth is set to be $10000m$ in *WADAM*.

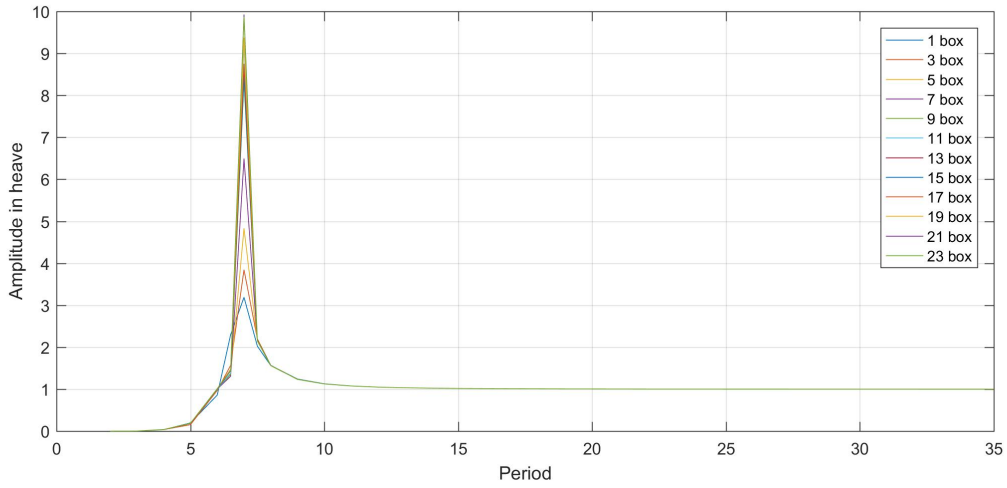

Plot of the RAO in heave obtained from different numbers of the mirroring bodies in undamped case

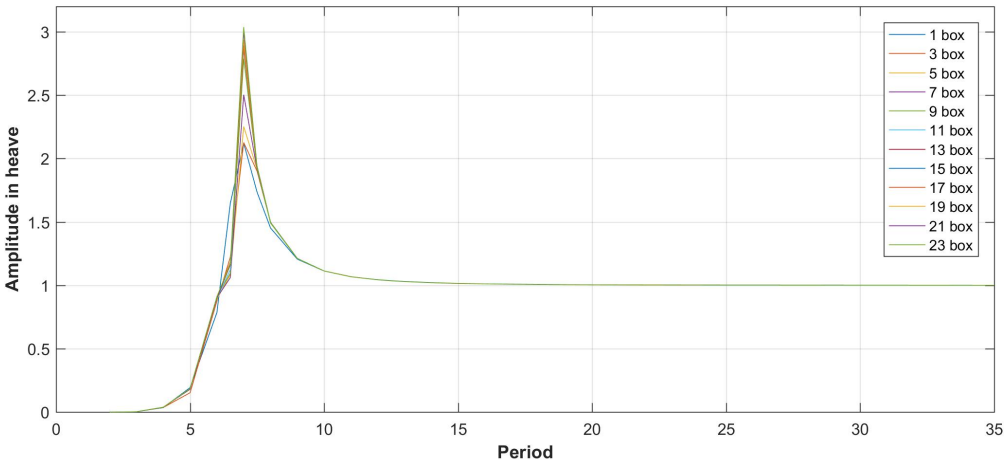

Plot of the RAO in heave obtained from different numbers of the mirroring bodies when 3% of the critical damping in heave is used

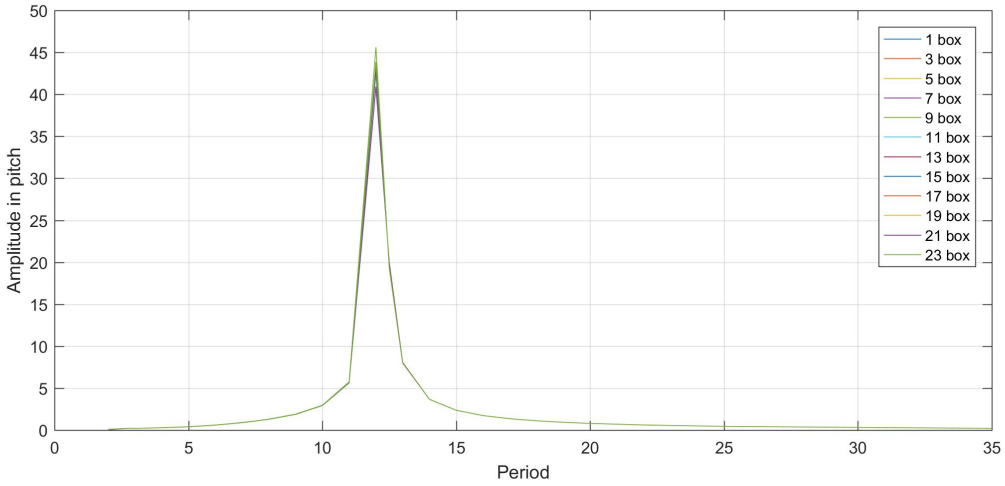

Plot of the RAO in pitch obtained from different numbers of the mirroring bodies when no external damping is added

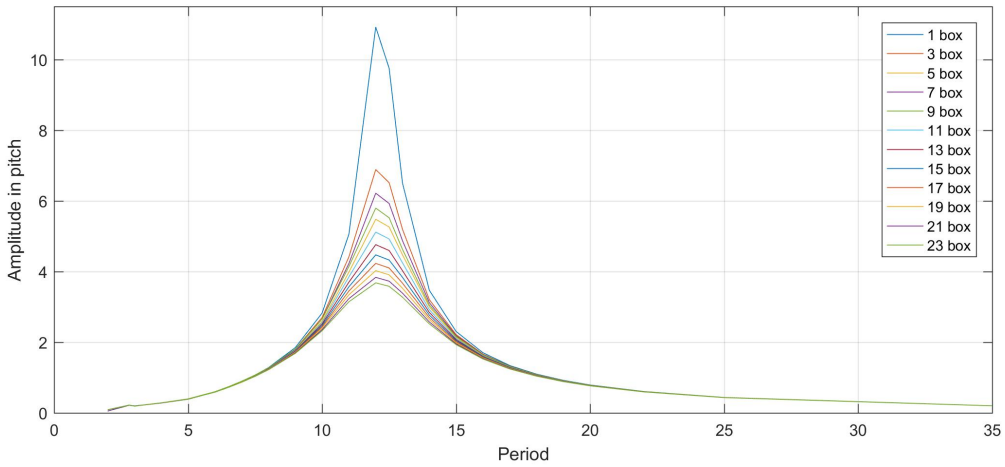

Plot of the RAO in pitch obtained from different numbers of the mirroring bodies when empirical estimated damping in pitch is used

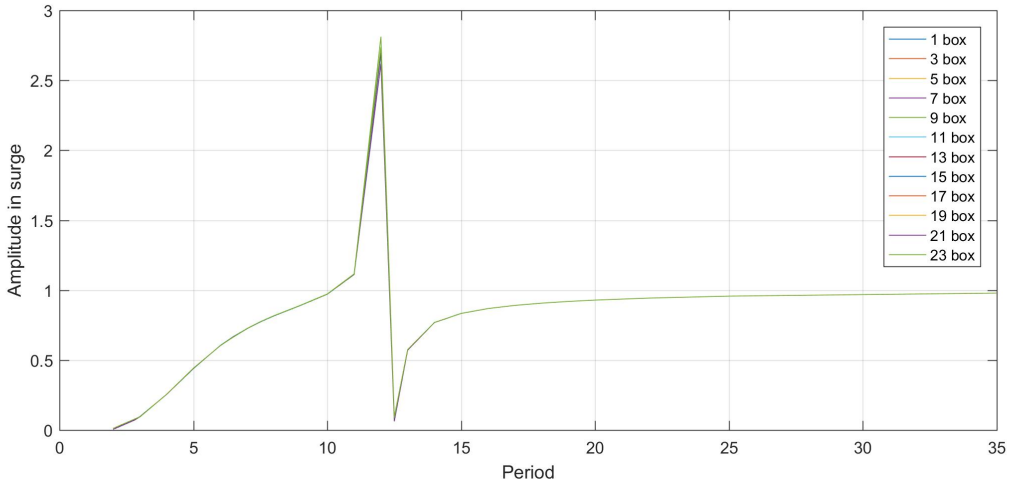

Plot of the RAO in surge obtained from different numbers of the mirroring bodies in undamped case

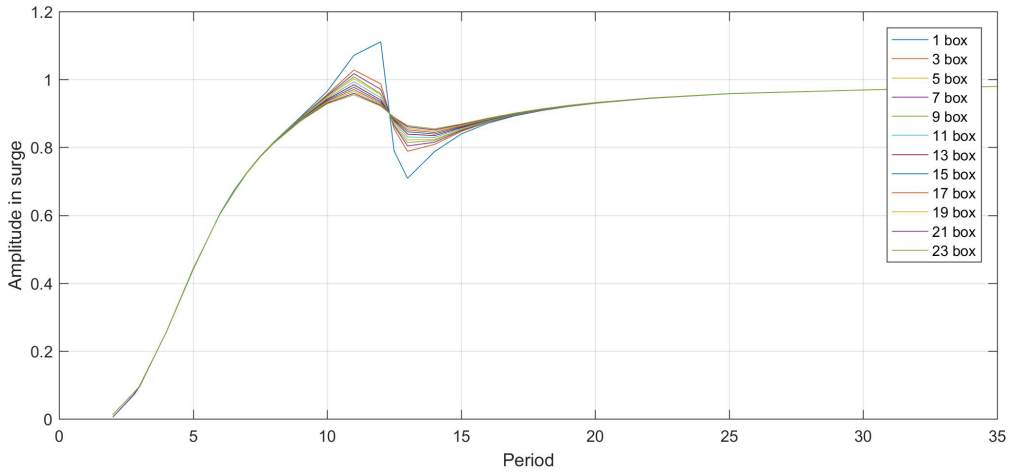

Plot of the RAO in pitch obtained from different numbers of the mirroring bodies when damping in heave and pitch motion is used